Young intermediate-mass stars
From a HIFI spectral survey
to the physics of the disk inner rim

ACADEMISCH PROEFSCHRIFT

ter verkrijging van de graad van doctor
aan de Universiteit van Amsterdam
op gezag van de Rector Magnificus
prof. dr. D. C. van den Boom
ten overstaan van een door het college voor promoties
ingestelde commissie,
in het openbaar te verdedigen in de Agnietenkapel
op dinsdag 29 januari 2013, te 12:00 uur.

door

Mihkel Kama

geboren te Tallinn, Estland

Promotiecommissie

Promotor: prof. dr. C. Dominik

Overige leden: prof. dr. C. Ceccarelli
prof. dr. A.G.G.M. Tielens
prof. dr. L.B.F.M. Waters
prof. dr. E.F. van Dishoeck
prof. dr. A. de Koter
prof. dr. L. Kaper
prof. dr. R.A.M.J. Wijers
dr. F.F.S. van der Tak

Faculteit der Natuurwetenschappen, Wiskunde en Informatica

Cover design: Erica Gorochow. Front and back imagery: OMC-2 (UKIRT/JAC)
and a disk in Orion (J. Bally & H. Throop). Spectra from Chapter 2.

Emale, vanaemale ja Oskarile

Contents

1

Introduction

"If you want to make an apple pie from scratch,
you must first invent the Universe."

Carl Sagan

How are tenuous clouds of gas in space converted to stars and their planets? This question is the domain of star formation astrophysics, and forms the context for this thesis. But the context for the question itself is another question: what is the origin and spread of life in the Universe? This existential topic is, directly and indirectly, being addressed by many branches of science. Among them, astrophysics is revealing answers to questions about the origin of the Sun and its planetary family, and of other stars and their planets. In this thesis, I investigate several aspects of the star and planet formation process, with a particular focus on the appearance and diagnostic value of molecular spectra of newborn protostars.

Atoms and molecules in star-forming gas act as probes of the physical conditions and kinematics, and control the thermal and ionization balance. Their excitation is controlled by the density, temperature and ambient radiation field, relating observed spectra to the local conditions. The chemical makeup of a gas cloud is affected by its age, but also by variations in internal and external heating, density and temperature, as well as by shocks and other processes, and large-scale motions are revealed by spectrally resolved observations. Furthermore, line emission dominates the thermal balance of the gas and thus the hydrostatic support, and magnetic fields couple to the ionized gas fraction, which is dominated by specific chemical species.

The evolving chemical composition of the gas also offers the promise of "molecular clocks", if certain abundance ratios can be found that uniquely relate to the age of a source. Finally, molecules produced in star-forming gas set the initial conditions for planet formation and may provide the precursors for the evolution of life.

Because of the wealth of information they contain, the comparative study of spectral lines in protostellar clouds across a range of parameters is one of the hottest topics in star formation. The transitions of interest are mostly in the far-infrared through

millimetre parts of the spectrum, from a hundred gigahertz to several terahertz[1]. Water vapour in the Earth's atmosphere absorbs heavily at these frequencies, mandating the use of exceptionally high and dry observing sites or, for terahertz frequencies, space telescopes. The most recent of these is the European Space Agency's *Herschel Space Observatory* mission.

With the unprecedented frequency coverage and sensitivity of *Herschel*'s HIFI spectrometer, transitions from a wide range of molecules and their excitation levels are observable at high spectral resolution. Recently, the CHESS key programme, under principal investigator Cecilia Ceccarelli, has obtained broad frequency coverage HIFI spectra of eleven protostars (Ceccarelli et al. 2010). Such long spectra have the advantage of an unbiased look at the molecular inventory as well as at the set of observable transitions for a particular species, providing many constraints for analysis. The main aims are to study each source in more detail, and to compare the spectra as a function of source luminosity and age. Much of this thesis deals with the spectrum of the intermediate-luminosity source in this sample, OMC-2 FIR 4.

Below, I summarize the evolution of matter from the state of molecular clouds in galaxies to that of stars[2] with planetary systems. The main phases and their characteristics are summarized in Fig. 1.3. I also present a brief introduction to the spectroscopic methods used in the study of molecular emission star-forming regions.

1.1 Molecular clouds – the sites of starbirth

Between the stars that form the familiar, visible contents of a galaxy, there is a low-density gas ($\hat{n} \sim 1$ cm^{-3}). This gas forms the *interstellar medium*, which is separated into an ever-evolving system of bubbles that represent phases with different density, n, and temperature, T_{kin}. Depending on the phase, the hydrogen in the gas is mainly ionized or neutral atomic, or molecular. The bulk of the molecular gas is assembled into *giant molecular clouds* (GMCs), gas complexes with typical masses of $\sim 10^5$ M$_\odot$, diameters of $10 \ldots 100$ pc, and densities and temperatures of $n_{\mathrm{H_2}} \sim 10^2$ cm^{-3} and $T_{\mathrm{kin}} \sim 10$ K, respectively. Such complexes are the main sites of star formation. Their energy balance is controlled by heating from cosmic rays, ultraviolet starlight and, in some cases, by supernova shockwaves, and by cooling through dust continuum and gas line emission. The Galaxy hosts around a thousand GMC complexes, of which examples are shown in Fig. 1.1, imaged in the molecular gas tracer, carbon monoxide. The total star formation rate in our galaxy is ~ 1.5 M$_\odot$/yr.

A positive correlation has been found between the surface density of gas, Σ_{gas}, and the star formation rate. Known as the Kennicutt-Schmidt law, this relation is valid over a wide range of conditions in different galaxies (Kennicutt & Evans 2012,

---

[1]True to the spirit of historical confusion in astronomy, millimetre-range astronomers simultaneously use frequency and wavelength units. For reference, 100 GHz is 3 mm and 1 THz is 300 μm.

[2]The star formation paradigm may seem to say that a homogeneous cloud of gas rearranges itself to form a very compact configuration, in which the final state has a much lower entropy than the initial one. That is, star formation may seem to violate the second law of thermodynamics. However, the entropy of the entire system does increase when radiation – the mechanism through which the collapsing cloud cools – is taken into account.
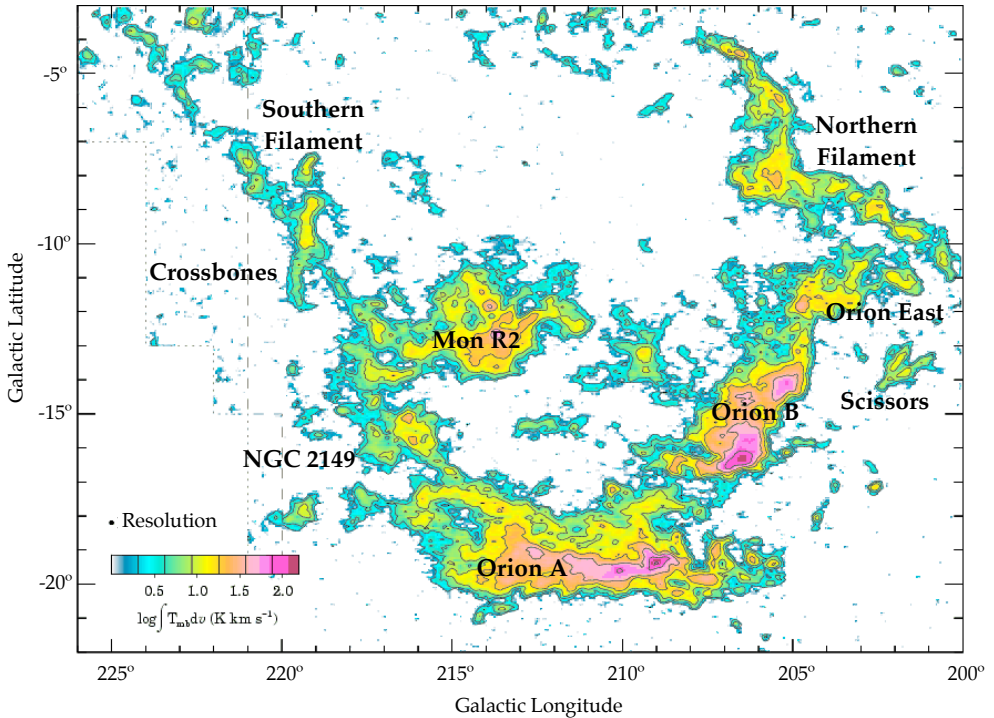
Figure 1.1: A detailed view of the filamentary giant molecular cloud complex in and around Orion. Figure adapted from Wilson et al. (2005).

and references therein).

The correlation between star formation and molecular H_2 gas complexes is due to the fact that the formation of H_2 and the formation of stars are both favoured by cold gas (Krumholz et al. 2011), so that molecular hydrogen is not necessarily a fundamental factor, but cooling is. A critical column density of around $N_{gas} = 10^{21}$ cm^{-2} is necessary for star formation (e.g. Schaye 2004; Molinari et al. 2010).

A GMC typically has a lifetime of a few times 10^7 years, after which the cloud complex has dissipated to the extent that further star formation is not possible.

1.2   The fragmentation of molecular clouds into cores

The interstellar medium is known to be turbulent. The drivers of this turbulence are Galactic rotation, which induces shearing and rotation in GMCs, supernova explosions (SNe), accretion flows bringing pristine gas from the intergalactic medium and outflows from protostars.

Supersonic turbulence in the interstellar medium gives rise to a size distribution of clumps of dense gas, which are called cores. Some of the cores become gravita-
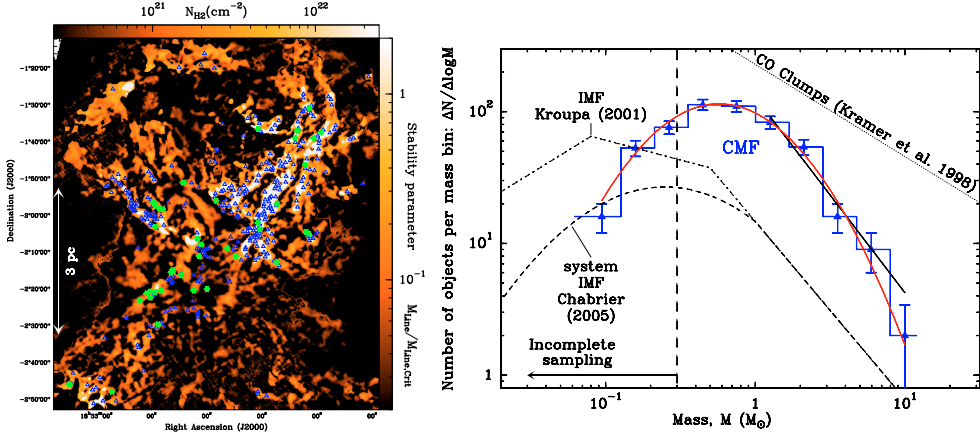
Figure 1.2: The spatial (left panel) and mass distribution (right panel) of prestellar cores in the Aquila star-forming region. *Left panel:* a column density map, overlaid with the prestellar cores identified in the region. The region has a filamentary structure, a general feature of star-forming clouds. *Right panel:* the Aquila prestellar core mass function, CMF, in comparison with the stellar mass function, IMF for single stars and multiple systems. The CMF and Kroupa IMF match in shape, with a derived core-to-star mass conversion efficiency of $\epsilon \approx 0.4$. Figures from André et al. (2010), with data references therein.

tionally bound, but many dissipate again. The large-scale appearance of the gas is filamentary, as illustrated by the left panel of Fig. 1.2, and the bound cores appear in the highest column density parts of the filaments. The hypothesis that the prestellar core mass distribution originates in turbulent motions of the gas is supported by the excellent match of the observed core mass function (CMF) with that predicted from fragmentation driven by supersonic turbulence (Padoan & Nordlund 2002), given an appropriate choice of parameters for the theory. Young stellar objects are also seen to lie along the filaments, indicating that this is where stars form. The shape of the observed CMF in nearby star-forming regions indeed corresponds, over two orders of magnitude in stellar masses, to the initial mass function (IMF) of field stars (e.g. Motte et al. 1998; Alves et al. 2007; André et al. 2010). Current results suggest that up to $30 \ldots 40\%$ of dense gas in a core is converted into stars in the star formation process.
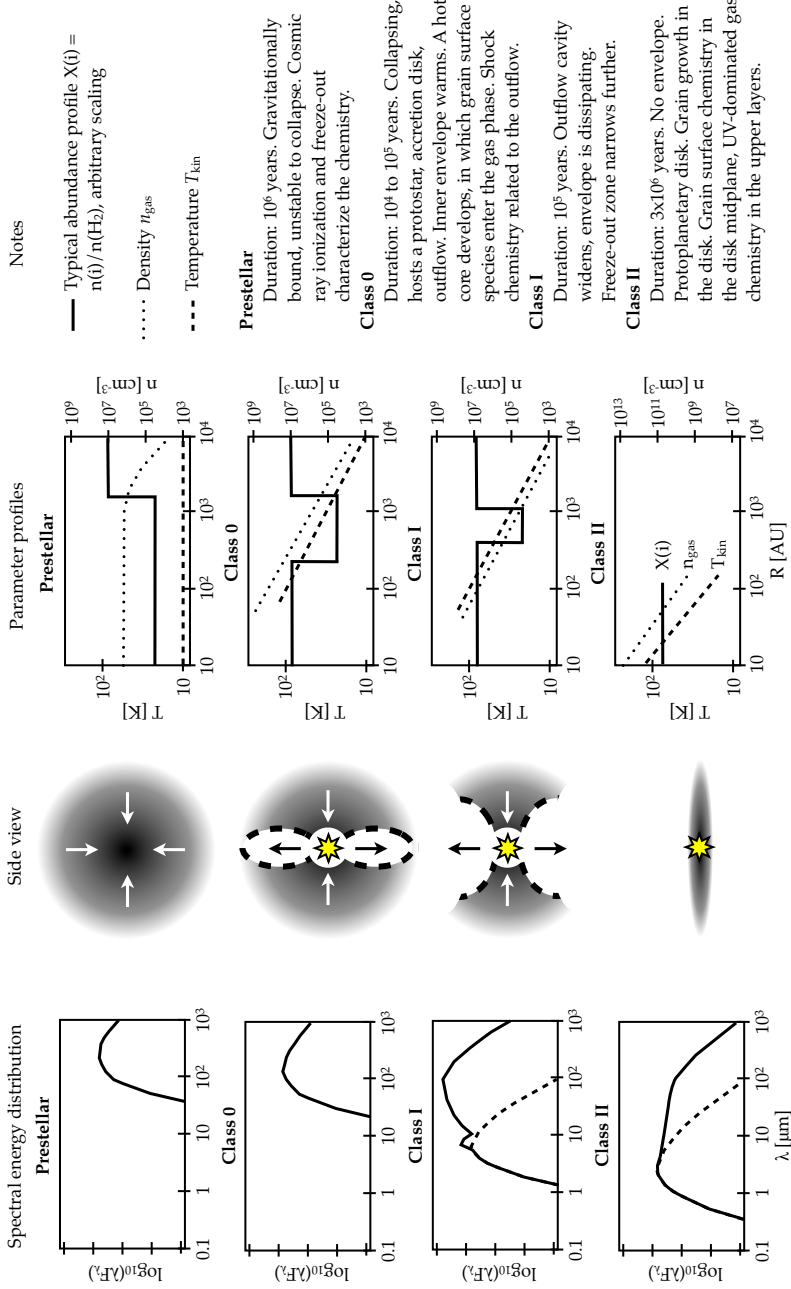
Figure 1.3: The evolutionary classes of protostars, from the prestellar to Class II stage.

1.3 From core to star

Star formation rarely happens in isolation – a single core may form multiple stars, and its evolution within a densely populated and active star-forming molecular cloud complex will not be free of external influence, such as heating and compression. However, the process is best understood in the single star case, and its description serves to illustrate important concepts which can help to understand clustered and externally modulated star formation.

If gravitationally bound, a dense core is called *prestellar*. Lacking internal energy sources, this core gradually cools and contracts. Eventually, it collapses under its own gravity and forms a protostar – or multiple protostars – near its centre and becomes a *protostellar core*. The protostar is surrounded by an accretion disk, with material fed into it from the collapsing large-scale core, and drives a bipolar outflow, which I return to in Sect. 1.3.3. The further evolution of the core is described in terms of the stages Class 0, I and II (Adams et al. 1987; Barsony 1994; McKee & Ostriker 2007). The evolutionary stages from prestellar through to Class II are illustrated in Fig. 1.3.

In the Class 0 stage, a core has formed a protostar, which is obscured by its large-scale envelope at wavelengths up to the near-infrared. The mass of the central object is smaller than that of the envelope, $M_{\mathrm{env}}/M_\star > 1$, and the spectral energy distribution is similar to that of a blackbody of $T \leq 30$ K. Class I and II objects have broader spectral energy distributions than a single-temperature blackbody, and are distinguished by having the parameter $\alpha > 0$ and < 0, respectively, where $\alpha = -\mathrm{d}\log \nu \mathrm{F}_\nu / \mathrm{d}\log \nu$ is the spectral slope between 2.2 and ~ 20 μm. Class II sources are optically visible pre main sequence stars with protoplanetary disks. I shall return to the Class II phase in Sect. 1.3.4.

Protostellar cores spend around $10^4 \dots 10^5$ years in the Class 0 stage (Andre et al. 2000; Maury et al. 2012). The Class I stage, where the envelope is dissipated, lasts $(1\dots 2)\cdot 10^5$ yr, while the Class II phase has a "half-life" of $\sim 3\cdot 10^6$ yr (Haisch et al. 2001). A typical star, with $M \lesssim 1$ $M_\odot$, reaches the main sequence after the Class I stage and stays there for $> 10^9$ yr, while high-mass stars, $M \gtrsim 10$ $M_\odot$, emerge from their envelopes already on the main sequence, lack a long Class II phase and may live for only 10^7 to 10^8 years.

1.3.1 Single star formation

A core is a clump of interstellar gas that is substantially denser than its surroundings. Observationally, a core is called *starless* if a protostar has not been detected in it. Such a core may dissolve, or it may form a star later. A core is called *prestellar* if it is gravitationally bound and close to hydrostatic equilibrium, but prone to or undergoing collapse while not yet harbouring a protostar. Many prestellar cores show asymmetries in their very narrow spectral lines, indicating infall and the onset of star formation.

Useful theoretical models exist for the structure and evolution of isolated, isothermal, hydrostatic, spherically symmetric cores. The density structure of such a core, bound by external pressure, is described by the Lane-Emden equation:
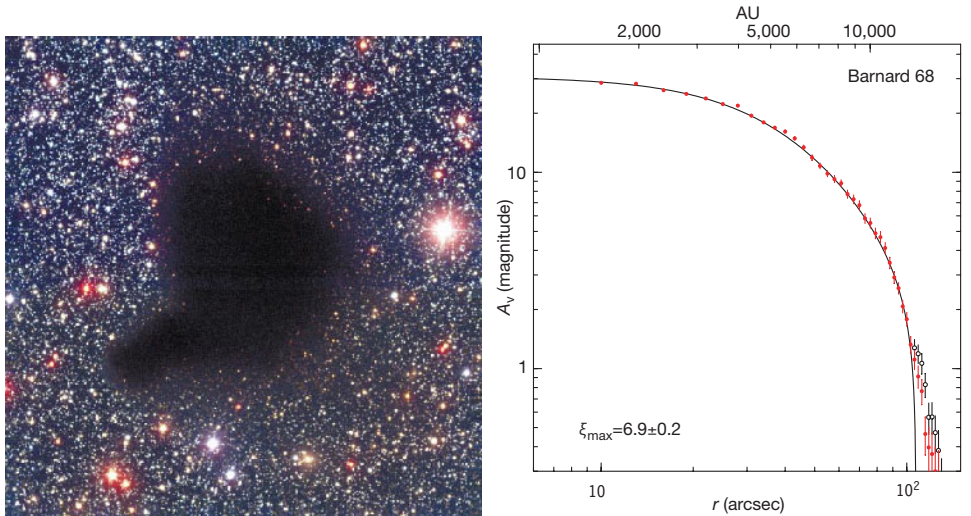
Figure 1.4: The prestellar core Barnard 68, a prime example of isolated, single star formation. *Left panel:* A B, V and I-band image showing the dark core against a field of background stars. The image scale is ∼ 30000 AU. *Right panel:* The extinction profile, equivalent to column density, of Barnard 68 (dots) compared with a fitted Bonnor-Ebert structure (line), showing excellent agreement. Figures from Alves et al. (2001).

$$\frac{1}{\xi^2}\frac{d}{d\xi}\left(\xi^2\frac{d\theta}{d\xi}\right) = -\theta^p, \tag{1.1}$$

where ξ and θ are the dimensionless radius and density whose normalization is determined by the choice of central density and polytropic equation of state, with index p, for the model. Solutions to Eq. 1.1, bounded by external pressure, are called Bonnor-Ebert spheres. Alves et al. (2001) demonstrated that the azimuthally averaged density profile of the prestellar core Barnard 68 corresponds very well to a Bonnor-Ebert structure, as shown in Fig. 1.4. The core has a mass of 2.1 $M_{\odot}$ and is seen in the left panel as a dark patch in front of a rich field of background stars. In addition to Barnard 68, a number of starless and prestellar cores are consistent with Bonnor-Ebert structures.

For a hydrostatic core to form a star, it must become unstable. It has been shown that thermally supported clouds are always unstable to collapse if their mean to outer boundary density ratio is $\hat{n}/n_{\text{out}} \geq 2.46457$, unless non-thermal pressures, such as magnetic fields, provide additional support.

1.3.2 Clustered star formation

While the theory of star formation wherein a 10^4 AU scale prestellar core contracts and forms a single star is elegant, observations show that such cases are exceptional. Most stars, 70 to 90%, form in clusters (Lada & Lada 2003), where multiple young stellar objects are born within a volume equivalent to one idealized prestellar core. Less than 10% of these clusters survive to ages of $\sim 10^8$ years, most dissipate soon after the molecular gas is dispersed and the local potential well becomes shallower. Further constraints on our understanding of the stellar birth process come from the multiplicity fraction of stars. Around half of all stars are in multiple systems (Lada 2006), although estimates vary by tens of percent. For O-stars, the multiplicity fraction is undoubtedly large, $\sim 50\%$ (Sana et al. 2012). Thus, star formation is typically messy, with multiple sub-condensations within a large core and added complexity due to the fragmentation of some sub-condensations into bound multiple star systems.

Clustered star formation produces the high-mass end of the IMF. In other words, the most massive stars, early O-type stars, are born in clusters. These are the stars that explode as supernovae, enriching the cosmos with heavy elements, and together with intermediate-mass stars generate the interstellar ultraviolet radiation field. The formation of the most massive stars is influenced by their strong radiation fields and thus differs from low-mass star formation, but it is hidden from view because of their rapid evolution, which puts massive young stars on the main sequence before their nascent protostellar cores are dissipated. Furthermore, due to the rarity of O-stars, there are fewer targets to study and they are, on average, far away ($d \gtrsim 1$ kpc).

Intermediate-mass stars, like the rare high-mass ones, also form in clusters and there are numerous examples of star formation in this mass range ($M_\star \sim 2$ to 8 M$_\odot$) in stellar nurseries within a few hundred parsecs of the Solar System. In addition to the intermediate-mass young stellar objects, these regions contain numerous low-mass ones, linking low-mass young stellar objects to high-mass ones. Observations of intermediate-mass star formation can, thus, help us to understand the birth of all stars and to characterize the transition from the single, isolated star formation case to the clustered one.

1.3.3 Outflows

Bipolar jets and outflows are a common phenomenon in accreting astrophysical systems. In the Class 0 protostar stage, all objects are thought to drive outflows (e.g. Davis et al. 2009). These extend from the extremely compact size of $\sim 10^3$ AU (e.g. Takahashi & Ho 2012) to as large as ~ 1 pc (Arce et al. 2007, and references therein) depending, among other things, on the age of the system. The outflows arise in magnetic field structures threading the innermost regions of the accretion disk and provide a way for excess angular momentum to be removed during the accretion process. Eventually, the injection of energy and momentum by an outflow into the large-scale envelope causes the protostellar core to dissipate. This contributes to bringing down the large mass accretion rate of a Class 0 protostar.

Outflows give rise to shockwaves in the medium into which the propagate. Such
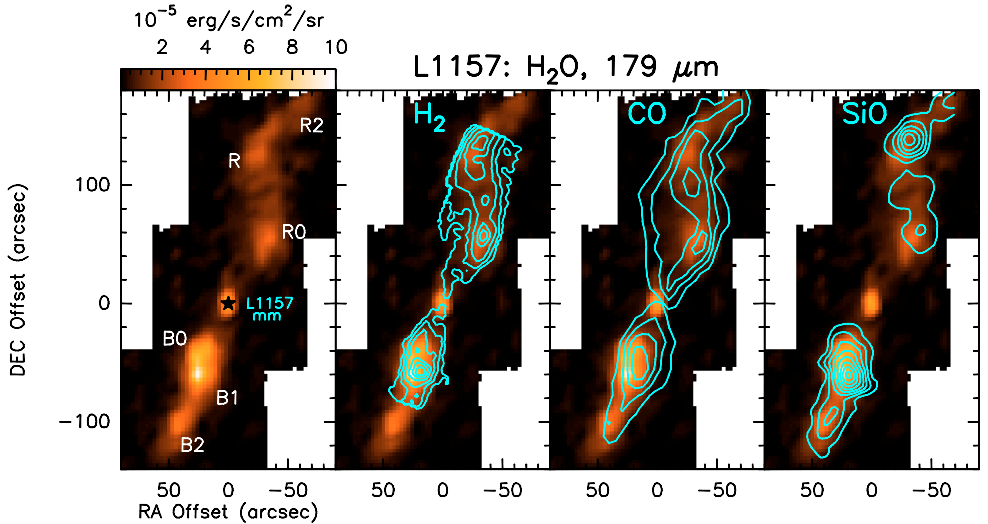
Figure 1.5: The large-scale outflow from the Class 0 protostar L1157-mm imaged in four tracers. *Left panel and background image:* the H_2O $2_{1,2} - 1_{0,1}$ line at 179 μm. *Second from left:* H_2 emission at 17 μm. *Second from right:* CO $2-1$ emission. *Right panel:* SiO $3-2$ emission, a sign of dust destruction by shocks. Figure and data from Nisini et al. (2010, and references therein).

shocks cool primarily through emission in lines of H_2, H_2O, CO, OH and OI. Water is an excellent shock tracer because both reactions in high-temperature ($T \gtrsim 300$ K) gas as well as sputtering of ice mantles from dust grains can make its abundance comparable to that of CO, $\sim 10^{-4}$ with respect to H_2. Furthermore, densities and temperatures in outflow-shocked gas are typically sufficient to excite the H_2O rotational levels. Another shock tracer is SiO, which is thought to originate in the sputtering of silicate dust grains. In Fig. 1.5, four important outflow tracers are shown. Their spatial distributions differ, illustrating the complementary diagnostic value of observing multiple tracers of the gas.

1.3.4 Disks and planets

After the clearing of most of the protostellar envelope, the newborn star becomes visible at optical wavelengths, except for in the plane of the remaining protoplanetary disk around it. This disk has a mass of the order of giant planet masses, $M_{\mathrm{disk}}/M_\star \lesssim 0.1$, is still gas-rich and facilitates a continuing low-level accretion onto the star at typical rates of $\dot{M} \sim 10^{-7 \dots -9}$ $M_\odot$/yr (Gullbring et al. 1998). The heating of protoplanetary disks has important contributions from both accretion and irradiation. Disks where accretion dominates are well described by so-called α-disk model of Shakura & Sunyaev (1973). Disks where the heating is dominated by irradiation from the central protostar are described by the model of Chiang & Goldreich (1997). In reality, both

effects contribute, with accretion dominating in the inner disk and irradiation in the outer disk. I examine the innermost regions of passively heated protoplanetary disks in Chapter 5 of this thesis, focussing on the evaporation of dust grains.

Within the protoplanetary disk, planets form, likely through collisional aggregation and possibly, in some cases, through gravitational instability. In collisional aggregation, the initially microscopic dust particles in the disk grow to macroscopic sizes by colliding and sticking, until they reach sizes large enough to start gravitationally capturing nearby material. In gravitational instability, the self-gravity of a part of the disk becomes sufficient to make that region unstable to collapse.

Following the dispersal of the heavy, gas-rich protoplanetary disk, a swarm of planetesimals – solid bodies ranging in size from some metres to thousands of kilometres – remains around a star. Such planetesimal populations are at the top of a collisional cascade that creates small dust grains which may be seen as a faint infrared excess in the spectral energy distribution of the system. These systems are called debris disks. After the dispersal of the protoplanetary disk gas and the gradual decrease in large collisions in the debris disk phase, a relatively stable planetary system may be left around a star. Over hundreds of millions of years, complex organic chemistry on planets may, in turn, lead to highly ordered self-sustaining and self-propagating systems, *life*.

Recent studies show there to be ≥ 1 planet per star in the Galaxy. The occurrence rate of planets in the 15 to 30 M_{Earth} range is $\gtrsim 50\%$ and this increases with decreasing planet mass (Mayor et al. 2011). Earth-mass planets appear to be a common by-product of starbirth, and star formation studies are helping to understand key aspects – such as the water content – of these planets. The chemical inventory of planet-forming material is related to processes in the protostellar core phase, and this is the subject of the next section.

1.4 Chemical evolution during star formation

The abundance and excitation, and therefore spectral appearance, of chemical species is very sensitive to the physical conditions in an evolving protostellar core. Chemical reactions in the gas and on dust grains depend on $n_{\mathrm{H_2}}$ and T_{kin}, and on ionization, as well as on the evolving physical structure of the core. The interplay of these factors leads to substantial variation in the relative abundances and distributions, as well as the strength of spectral features, of various species throughout the protostellar core lifetime. Some important constant factors are the dominance of molecular hydrogen, H_2, and a relatively high abundance of carbon monoxide, $CO/H_2 = X(CO) \sim 10^{-4}$. Most other important chemical species are typically present at the $X_{\mathrm{species}} \sim 10^{-9}$ level. The typical abundance profiles of chemical species at each evolutionary stage from prestellar to Class II are shown in Fig. 1.3, alongside a list of factors influencing the chemical evolution.

Ionization plays a crucial role in gas-phase chemistry. A molecular cloud is always irradiated by an interstellar ultraviolet radiation field and a flux of highly energetic particles, cosmic rays. The former give rise to a cloud surface layer where the ener-

getics and chemistry are dominated by ionizing UV photons and the H_2 abundance is low. The latter penetrate inside the cloud and are a source of an ionization fraction of $\sim 10^{-7}$ even in well-shielded regions. Such an ionization, combined with the high abundance of H_2, provides a source of the H_3^+ ion, which is an important foundation of chemistry in dense gas. Ion-neutral reaction rates have almost no temperature dependence. This makes them faster, especially in cold gas, than neutral-neutral reactions which require energy barriers to be overcome. At temperatures of a few tens of Kelvins, such as in prestellar cores and in large parts of protostellar envelopes, dense gas chemistry is characterized by ion-neutral reactions, the conversion of atomic carbon to CO, and by freeze-out of gas-phase species onto dust grains.

One of the most dramatic effects in cold temperature gas is deuteration, wherein the D to H ratio of a given molecule increases by up to several orders of magnitude above the primordial cosmic ratio of $D/H \sim 10^{-5}$. At $T \lesssim 20$ K, the reverse reaction of $H_3^+ + HD \leftrightarrow H_2D^+ + H_2$ is slower than the forward one, so deuterium enters the gas-phase reaction network in high relative abundance.

Particles can stick to dust grains for long enough to random walk around the surface, meet, and tunnel through substantial reaction barriers. Reactions that are impossible to carry out in the gas can thus occur on grains. An important example is the formation of molecular hydrogen, H_2, which cannot radiate away its binding energy on formation, making gas-phase formation inefficient. On a dust grain, the hydrogen atoms can deposit the binding energy, increasing the formation efficiency dramatically. Some other examples of molecules formed in high abundances on dust grains are H_2O, CO_2, CH_4, CH_3OH and H_2CO. This is likely the origin of the water that later gets incorporated into planets.

If the temperature rises from tens to hundreds of Kelvin, such as in the inner part of a protostellar core or under the influence of outflow shocks, various chemical species frozen out to or formed on dust grains begin to sublimate and enrich the gas. The heated inner envelopes of protostellar cores are termed *hot cores* and are characterized by evaporated ice species, such as deuterated molecules and complex organics, which may allow to trace the history of the material. As for shock-heated gas, the production of H_2O in the gas phase can become very efficient as energy barriers to two important neutral-neutral reactions can be crossed at $T \gtrsim 300$ K. Thus, while in cold gas, cosmic ray ionization leads to $X(H_2O) \sim 10^{-7}$, in hot post-shock gas $X(H_2O) \sim 10^{-6}$ to 10^{-4}, comparable to the CO abundance.

Thus, the physical structure, chemistry and spectral appearance of star-forming material are intimately linked. Next, I introduce the astrochemically best-studied region of starbirth, the Orion giant molecular cloud complex.

1.5   The Orion star-forming region

The nearest site of high-mass star formation is the Orion giant molecular cloud complex, at a distance of ~ 400 pc. As seen in Fig. 1.1, it is part of a larger system of star-forming clouds and consists itself of two main parts, Orion A and B, both with total masses $\sim 10^5$ $M_\odot$. The entire complex is around 12 Myr old, and its more
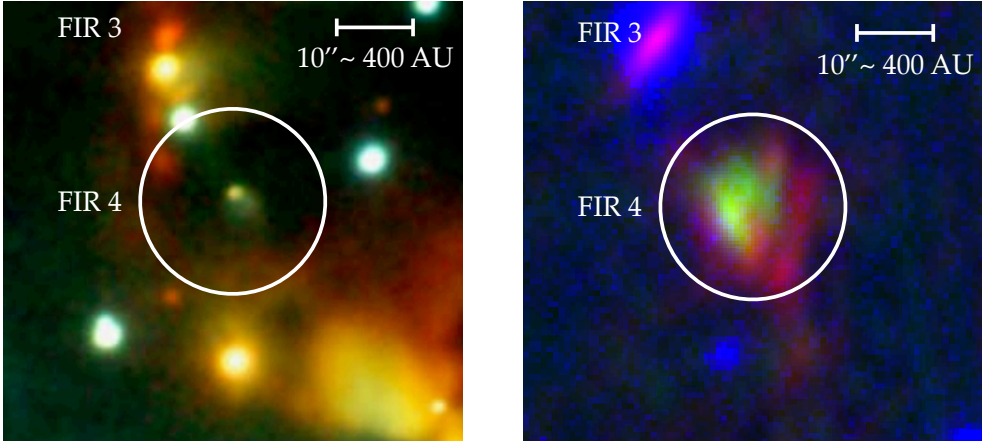
Figure 1.6: A part of the OMC-2 clustered star formation region, showing around a dozen young stellar objects of various ages. The brightest millimetre source, OMC-2 FIR 4, and the nearby FIR 3 are annotated. *Left panel:* An NOAO SQIID J, H and K-band image. A faint nebulosity is visible against the dark circular area that is the FIR 4 envelope. *Right panel:* A composite of interferometric 2 and 3 mm continuum images (green and red, López-Sepulcre et al., in prep., Shimajiri et al. 2008) and a SOFIA 37 μm image (blue, Adams et al. 2012). FIR 4 contains the bulk of the millimetre emission in the region, but is faint at mid-infrared wavelengths.

evolved massive star clusters (the OB clusters 1a, 1b and 1c) have likely already experienced around 10 to 20 supernovae, which may have compressed large parts of the Orion A cloud, thus accelerating or even causing star formation there. Orion A itself has formed thousands of stars, including the famous Trapezium cluster at the heart of the Orion Nebula. The Trapezium is home to several very massive O-stars that are the reason for a heavily enhanced interstellar ultraviolet field up to several parsecs away, heating and ionizing the surface layer of large parts of the cloud.

1.5.1   OMC-2 FIR 4

OMC-2 is a part of Orion A, around 2 pc north of the Trapezium, discovered by Gatley et al. (1974). It has a total luminosity of ~ 2000 L$_\odot$ (Thronson et al. 1978) and a mass of $\sim 10^2$ M$_\odot$ (Bally et al. 1987) and is a clustered star formation region that is home to $\sim 10^2$ low- to intermediate-mass young stellar objects, ranging in type from Class 0 through Class II (Peterson & Megeath 2008), suggesting that star formation has been occurring for longer than the 10^4 to 10^5 year ages of the current Class 0 protostars.

The brightest 1.3 mm source in OMC-2 is OMC-2 FIR 4, a Class 0 protostar shown in Fig. 1.6. The source, dark at near-infrared wavelengths (Fig. 1.6, left panel) but dominant in the millimetre continuum of cold dust (right panel), has a mass

of $30\ldots60$ M$_\odot$, making it an intermediate-mass young stellar object. The near-infrared, mid-infrared and millimetre-wavelength emission peaks are all offset from one-another by ~ 5", suggesting substructure in the source. While interferometric continuum observations at 2 and 3.3 mm have indeed revealed clumpy substructure at the 5" scale, this is dominated in brightness by one main core (Shimajiri et al. 2008, López-Sepulcre et al., submitted). The 10000 AU scale envelope is described well by a spherically symmetric power-law density and temperature profile. Multiple young stars at various evolutionary stages are within a 1' or 25000 AU radius of the nominal FIR 4 coordinates. The substructure and abundance of nearby sources underlines the clustered nature of star formation in OMC-2.

One troubling aspect is that the luminosity estimates for OMC-2 FIR 4 range from 50 to 1000 L$_\odot$ (Crimier et al. 2009; Adams et al. 2012). The use of different sized integration annuli and datasets with different spatial resolution at the crucial far-infrared and sub-millimetre wavelengths means that these numbers are not directly comparable, but the combined luminosity for the mid-infrared through millimetre wavelength sources within the FIR 4 core is likely within a factor of two of ~ 500 L$_\odot$.

OMC-2 FIR 4 is an intermediate-mass star formation laboratory with a rich sub-millimetre and millimetre spectrum, and it is currently the target of many studies. Within the CHESS key programme, a detailed investigation of its chemical diversity and structure is being carried out, employing data from the *Herschel Space Observatory*, the IRAM 30 m telescope, the James Clerk Maxwell Telescope and other instruments. In this thesis, I analyze the line-rich *Herschel*/HIFI spectrum of FIR 4.

1.6 Basics of molecular spectroscopy

Together with continuum radiation, which I do not discuss here, atomic and molecular spectral lines are the main electromagnetic source of information about astrophysical environments. In particular, the physical conditions, kinematics and composition of a medium can be determined, or at least constrained, from them. For details on what follows, I direct the reader to Goldsmith & Langer (1999) and Tielens (2005). The general principle is illustrated by a system with two energy levels, $i \in \{1, 2\}$, with energies E_i. In the context of this thesis, these typically represent rotational energy levels of simple molecules. Generally, the ratio of level populations of $\{1, 2\}$ is given by:

$$\frac{n_2}{n_1} = \frac{g_2}{g_1} \cdot \frac{\exp\left(-E_2/k_\mathrm{B}T_\mathrm{kin}\right)}{1 + n_\mathrm{cr}/n_\mathrm{gas}}, \tag{1.2}$$

where n_i and g_i are the number densities and statistical weights of levels i, T_kin is the kinetic temperature and n_gas the density of the ambient gas – usually equivalent to H$_2$. Finally, $n_\mathrm{cr} = A_{2,1}/\gamma_{2,1}$, with $A_{i+1,i}$ the Einstein A coefficient for energy level decay by spontaneous emission and $\gamma_{i+1,i}$ the rate of collisional de-excitations.

The quantity n_cr is the *critical density*, above which de-excitations are predominantly spontaneous radiative events, and below which they are predominantly collision-

driven. At $n_{\text{gas}} > n_{\text{cr}}$, local thermodynamic equilibrium (LTE) is reached. In LTE, the column density of level i, $N_i = n_i \cdot z$ where z is the radial extent of the medium, is given by

$$N_i = g_i \cdot \frac{N}{Z(T_{\text{kin}})} \cdot \exp\left(-\frac{E_i}{k_B T_{\text{kin}}}\right), \tag{1.3}$$

where Z is the temperature-dependent partition function and N the total column density of the species. The signal from a radio telescope is typically expressed in terms of antenna temperature, T_a [K]. It can be shown that, assuming LTE the antenna temperature of a spectral emission line relates to the column density of the upper level of that line as

$$T_a dv = \frac{h_P c^3 N_i A_{i,i-1}}{8\pi k_B \nu^2} \cdot \left(\frac{\Omega_s}{\Omega_a}\right) \cdot \left[\frac{1 - \exp\left(-\tau\right)}{\tau}\right], \tag{1.4}$$

where dv is the full-width half-maximum (FWHM) of the line in km·s^{-1} units, Ω_s and Ω_a the source and telescope beam solid angles on the sky. The factor in square brackets is equal to β, the escape probability for a photon in the line in an expanding spherical geometry. The optical depth, τ, of the line is approximated by

$$\tau = \frac{h_P}{dv} N_i B_{i,i-1} \left[\exp\left(\frac{h_P \nu}{k_B T_{\text{kin}}}\right) - 1\right]. \tag{1.5}$$

Making the assumptions that $\Omega_s = \Omega_a$ and $\tau \to 0$, one arrives at

$$\ln\left(\frac{N_i}{g_i}\right) = \ln\left(\frac{N}{Z(T_{\text{kin}})}\right) - \frac{E_i}{k_B T_{\text{rot}}}, \tag{1.6}$$

where T_{rot} is the rotational excitation temperature, which in LTE is equal to T_{kin}. From Eq. 1.4, one can estimate N_i directly from the spectral line. If one does this for several lines and plots them on an E_i-$\ln\left(N_i/g_i\right)$ plot, one can fit Eq. 1.6 to the plotted points to obtain T_{rot} and N from the two parameters describing the linear fit. This is called the population diagram method, which allows direct observables from spectral lines to be employed in estimating the temperature and column density of a molecule. Typically, a chemical species is not in LTE, in which case more sophisticated analyses must be carried out. One powerful, but computationally expensive alternative is to use Monte Carlo methods to calculate the population of energy levels and the radiation field, taking into account their mutual inderdependence as well as the density and temperature.

1.7   This thesis

The book you now hold in your hands represents a selection of work carried out over the past four years on various aspects of star and planet formation. The thread binding the following chapters is the formation of intermediate-mass stars: Chapters 2 through 4 deal with the analysis of the *Herschel*/HIFI spectrum of the Class 0 protostar, OMC-2 FIR 4, while Chapter 5 is dedicated to the inner regions of protoplanetary disks around Class II young stellar objects.

In Chapter 2, I present an overview of the rich HIFI sub-millimetre spectrum of OMC-2 FIR 4. Hundreds of spectral lines from several dozen molecules are detected and shown to probe a wide range of excitation conditions and kinematical components, revealing a new level of complexity in the source.

Several aspects of the HIFI spectrum of FIR 4 are explored in detail in Chapters 3 and 4. In the former, I provide evidence for a compact hot core through an analysis of over a hundred lines of a complex organic molecule produced on grain surfaces, methanol. The CH_3OH abundance with respect to hydrogen in the central few hundred astronomical units could be as high as 10^{-6}. In Chapter 4, I investigate the high-velocity wing emission of water, carbon monoxide and hydroxyl, finding good accord with an origin in shocked gas that has a high H_2O/CO ratio and a low OH/H_2O ratio, consistent with magnetized shocks with low UV-irradiation. The shocked gas has an effective source size of only ~ 1" or ~ 400 AU. Combined with archival data showing a small near-infrared nebula and an excited CO lobe, the evidence for a compact outflow in OMC-2 FIR 4 is compelling and will be followed up with interferometric observations.

In Chapter 5, I explore the structure of the inner edges of protoplanetary disks by implementing sublimation physics in a fast Monte Carlo radiative transfer code with a hydrostatic disk structure. I demonstrate that the dust evaporation region can, in optical depth terms, be very sharp or very tenuous, covering a substantial fraction of the radial extent of the inner hole in the dust distribution. Small inner rim radii are preferred for disks with diverse dust populations. The question of unexpectedly large near-infrared excess fluxes from such disk regions is addressed, but not solved, although I offer suggestions for how the excess may be explained with dusty disk models.

The comparative analysis of the CHESS spectra is only beginning, but already, new questions are arising. What is the origin of the medium, ~ 15 km $\cdot$ s^{-1}, width emission component seen in CO and H_2O lines, and in some sources other species? Does it probe the inner envelope, with accretion flows and other dynamical processes? What information is carried by lines of hydrides and hydride ions such as CH, CH^+ and SH^+? Why does the gas-phase chlorine abundance seem to be independent of shock processing, which should release depleted atoms from grains into the gas? In many cases, further work on the *Herschel* data will certainly provide answers.

It remains to be said that the process whereby the cold molecular gas of the interstellar medium is converted to stars and their accompanying planets is understood in broad terms, but plenty of challenges remain. To focus on the themes of this thesis, I bring two examples. Firstly, broadband molecular spectra are offering

an unprecedented number of constraints for our qualitative and quantitative understanding of star formation, and in many cases our conceptual and physical models of the observed sources are only beginning to catch up. Secondly, although in the case of protoplanetary disk inner rims with unusual near-infrared excesses, the observational constraints are less numerous – usually spatially unresolved fluxes and, in some cases, interferometric constraints on the location of the emitting material – they are severe in their physical implications, as the fraction of energy reprocessed by the material in the inner disk must be substantially larger than present disk models are able to easily account for.

The most important next steps in our understanding of star and planet formation will likely be taken with the millimetre inferferometer, ALMA, in the Atacama desert in Chile. This instrument allows the distributions and properties of gas and dust alike to be regularly studied at down to milli-arcsecond scales, corresponding to only an astronomical unit in the nearest star-forming regions. We may see the structure of hot cores, accretion flows deep within protostellar envelopes, the small-scale structure of outflow cavities, and the material distribution in the inner regions of protoplanetary disks, and even catch giant planets as they are forming. As always, it is an exciting time to be an astronomer.

2

The CHESS spectral survey of OMC-2 FIR 4: Herschel/HIFI observations of the 480-1902 GHz range

M. Kama, A. López-Sepulcre, C. Dominik, C. Ceccarelli, A. Fuente, E. Caux, R. Higgins, A.G.G.M. Tielens, T. Alonso-Albi

Abstract

Star formation is one of the foci of modern astrophysics. Broadband spectral surveys of star-forming regions offer a rich view of their physical, chemical and dynamical structure and evolution. The *Herschel Space Observatory* has opened up the sub-millimetre regime to such surveys, giving access to the fundamental transitions of many hydrides and to the high-energy transitions of many other species. A comparative analysis of the chemical inventories and physical processes and properties of protostars of various masses and evolutionary states is the goal of the CHESS (*Chemical HErschel Surveys of Star forming regions*) Key Programme. This paper focusses on the intermediate-mass protostar, OMC-2 FIR 4. We obtained a spectrum of OMC-2 FIR 4 in the 480 to 1902 GHz range with the HIFI spectrometer on *Herschel*, and carried out the reduction, line identification and a broad analysis of the line profile components, excitation and cooling. We detect 718 spectral lines from 40 species and isotopologues. The line flux is dominated by CO, H_2O and CH_3OH. The line profiles are complex and vary with species and upper level energy, but can be divided into four categories: quiescent gas, two broad components likely from outflows, and a foreground cloud. We find abundant evidence for warm, dense gas, as well as for an outflow in the field of view. Line flux represents 2% of the 10 $L_\odot$ luminosity detected

with HIFI in the 480 to 1250 GHz range. Of the total line flux, 63% is from CO, 12% from H_2O and 10% from CH_3OH. A comparison with similar HIFI spectra of other sources is set to provide much new insight into star formation regions, a case in point being a difference of two orders of magnitude in the relative contribution of sulphur oxides to the line cooling of Orion KL and OMC-2 FIR 4.

2.1   Introduction

With the proliferation of high-sensitivity broadband receivers, wide frequency coverage spectral surveys covering > 10 GHz are becoming the norm (e.g. Johansson et al. 1985; Blake et al. 1986b; Cernicharo et al. 1996; Schilke et al. 1997; Cernicharo et al. 2000; Caux et al. 2011). Such surveys provide comprehensive probes of the chemical inventory, excitation conditions and kinematics of sources such as protostars. Here, we present the first *Herschel*/HIFI spectral survey of an intermediate-mass protostellar core, OMC-2 FIR 4 in the Orion A molecular cloud, covering 480 to 1902 GHz.

The chemical composition of a protostar is linked to its evolutionary state and history, for example the relative abundances of the sulphur-bearing species in a protostellar core depend on the gas temperature and density, as well as the composition of the ices formed during the prestellar core phase (e.g. Wakelam et al. 2005). The chemical makeup of the gas also plays a role in the physical evolution of the protostar, for example by coupling with the magnetic field or by its role in the cooling of the gas (e.g. Goldsmith 2001). The large number of spectral lines captured by a survey places strong constraints on the excitation conditions and even spatially unresolved physical structure.

The HIFI spectrometer (de Graauw et al. 2010) on the *Herschel Space Observatory* (Pilbratt et al. 2010) has made a large part of the far-infrared or terahertz-frequency regime accessible to spectral surveys (Bergin et al. 2010; Ceccarelli et al. 2010; Crockett et al. 2010). Previous studies at these frequencies have been mostly limited to small frequency windows on the ground or, for space missions such as ISO, orders of magnitude lower spectral resolution and sensitivity than HIFI. Many hydrides and high-excitation lines of key molecules such as CO and H_2O are routinely observable while *Herschel* is operational. Spectral surveys of star forming regions with HIFI are the focus of the CHESS[1] (Ceccarelli et al. 2010) and HEXOS[2] (Bergin et al. 2010) Key Programmes. A comparison of low- to high-mass protostars, a key goal of CHESS, offers insight into the physics and chemistry of star formation through the entire stellar mass range. The intermediate-mass protostar in the CHESS sample is OMC-2 FIR 4 in Orion.

Orion is a giant molecular cloud complex at a distance of ~ 420 pc (Menten et al. 2007 found 414 ± 7 pc to the Orion Nebula Cluster and Hirota et al. 2007 437 ± 19 pc to Orion KL, consistent within the uncertainties). Various stages of star formation are represented: Orion Ia and Ib are 10 Myr old clusters, while Class 0 protostars are still abundant in the OMC-1, 2 and 3 sub-clouds. The OMC-2 cloud core contains

---

[1] `http://www-laog.obs.ujf-grenoble.fr/heberges/hs3f/`; PI Cecilia Ceccarelli.
[2] `http://www.hexos.org`, PI Edwin A. Bergin

a number of protostars, including OMC-2 FIR 4 as the dominant Class 0 object. It is among the closest intermediate-mass protostellar cores and possibly an example of triggered star formation (Shimajiri et al. 2008).

While earlier studies attributed a luminosity of 400 or 1000 $L_\odot$ to OMC-2 FIR 4 (Mezger et al. 1990; Crimier et al. 2009), recent *Herschel* and SOFIA observations found 30 to 50 $L_\odot$ (Adams et al. 2012). Adams et al. (2012) further found an envelope mass of 10 $M_\odot$ for FIR 4, while previous authors found it to be $\sim$ 30 $M_\odot$ (Mezger et al. 1990; Crimier et al. 2009) and continuum interferometry has yielded even larger estimates, 60 $M_\odot$ (Shimajiri et al. 2008). The factor of 20 difference in luminosity is certainly related to the improved spatial resolution of the *Herschel* and SOFIA data used by Adams et al. (2012), as well as their separate treatment of the bright nearby source, FIR 3, however the choices of flux integration annulus, as well as background determination, of the two groups were also different and a full explanation requires a dedicated effort in source modeling. For now, we consider OMC-2 FIR 4 an intermediate-mass Class 0 protostar with a luminosity within a factor of two of 500 $L_\odot$ and with a $2 \ldots 3$ $M_\odot$ central object, a likely precursor of a Herbig Ae star.

This paper is structured as follows: the observations, their calibration and reduction are discussed in Sect. 2.2; we summarize the quality and molecular inventory of the data and present a rotational diagram analysis in Sect. 2.3; line profile components and energetics are discussed in Sect. 2.4; and the conclusions are summarized in Sect. 2.5.

The reduced data and the list of line detections presented in this paper will be available on the CHESS Key Programme website[3] in early 2013.

2.2 Observations and data reduction

The data, presented in Fig. 2.1, were obtained with the HIFI spectrometer on the *Herschel Space Observatory* in 2010 and 2011, as part of the *Herschel*/HIFI Guaranteed-Time Key Programme CHESS (Ceccarelli et al. 2010). The spectral scan observations were carried out in Dual Beam Switch (DBS) mode, using the Wide Band Spectrometer (WBS) with a native resolution of 1.1 MHz (0.7 to 0.2 km/s). The data were downloaded from the Herschel Science Archive, re-pipelined, reduced, and then deconvolved with the HIPE software (Ott 2010a, version 6.2.0 for the SIS bands and 8.0.1 for the HEB bands). Kelvin-to-Jansky conversions were carried out with the factors given by Roelfsema et al. (2012), which is also the standard reference for other instrumental parameters.

The spectrum on which line identification was carried out was obtained by stitching together the deconvolved spectral scans and single-setting observations. In case of band overlap, the spectra were cut and stitched at the central frequency of the overlap. In principle, a lower RMS noise could be obtained for the band overlap regions by combining the data from adjacent bands, but this requires corrections for sideband gain ratio variations, which are still being characterized (see also Sect. 2.2.3).

---

[3]`http://www-laog.obs.ujf-grenoble.fr/heberges/hs3f/`.
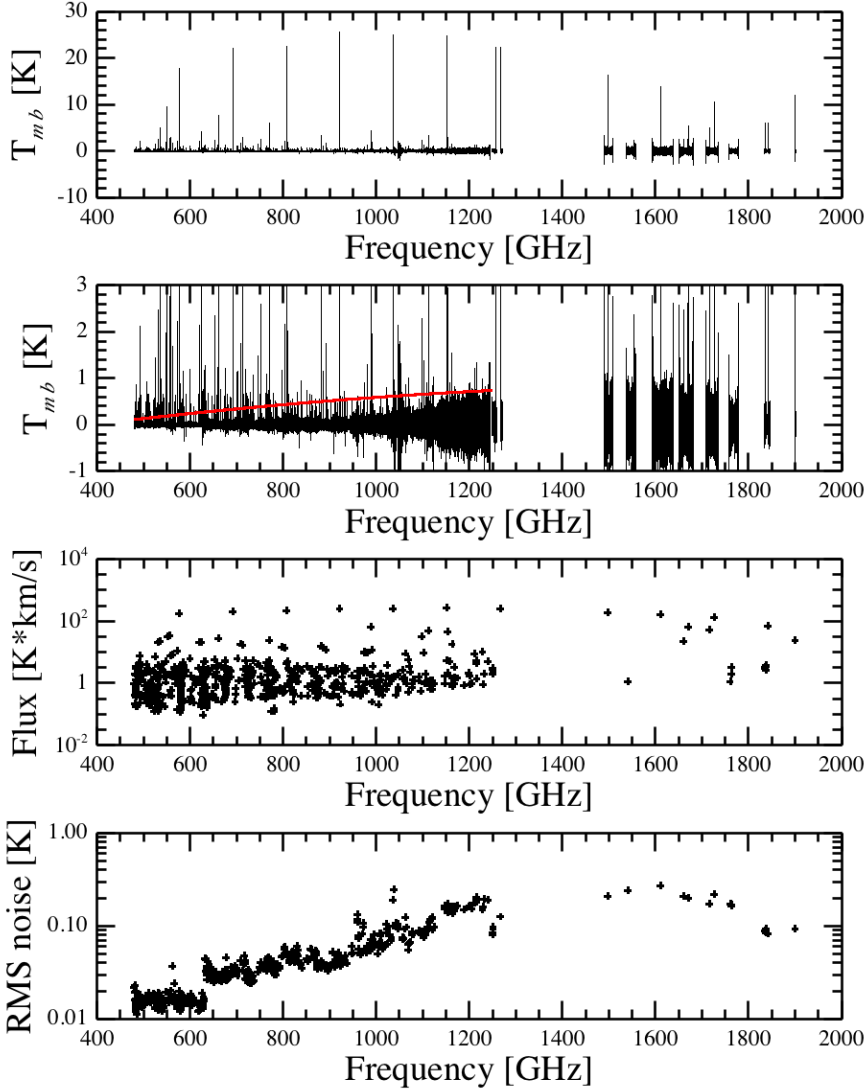
Figure 2.1: **Upper panel:** The full baseline-subtracted spectral survey at 1.1 MHz resolution. The set of bright lines towering above the rest is CO, the feature at 1901 GHz is CII. **Second panel:** The full spectral survey with a blown-up y-scale to emphasize weak lines and (black) a second-order polynomial fit to the subtracted continuum in bands 1a through 5a (red). **Third panel:** The T_{mb} scale integrated intensity of each detected transition. **Lower panel:** The local RMS noise around each detected transition.

Table 2.1: A summary of the full-band HIFI observations and of fluxes at selected standard wavelengths. The typical beam sizes, RMS noises, band-integrated fluxes and fluxes at the central frequencies are given. Except the integrated fluxes and selected wavelengths, all values are around the band centers. The notation for the band-integrated fluxes is $a(b) = a \cdot 10^b$. Due to overlap between the bands, the sum of band-integrated fluxes exceeds the total at the bottom.

Band	ν_{band} GHz	HPBW "	$\mathrm{RMS_{obs}}$ mK	Lines $\mathrm{GHz^{-1}}$	Flux $\mathrm{W \cdot m^{-2}}$	F_ν Jy
1a	520	41	16	1.9	5.4(−14)	84
1b	595	36	16	1.4	7.2(−14)	112
2a	675	31	30	1.2	1.2(−13)	141
2b	757	28	34	1.1	1.3(−13)	194
3a	830	26	45	0.7	9.3(−14)	210
3b	909	23	40	0.7	2.0(−13)	237
4a	1005	21	70	0.7	2.4(−13)	268
4b	1084	20	85	0.4	1.7(−13)	290
5a	1176	18	158	0.3	3.4(−13)	368
158 μm	1902	11			−	153
194 μm	1545	14			−	256
350 μm	857	25			−	173
450 μm	666	32			−	107
1a to 5a					1.3(−12)	

2.2.1   Data quality after reduction

After default pipelining, the data quality is already very high. However, in several bands unflagged spurious features (*spurs*) prevent the deconvolution algorithm from converging. This problem is resolved by manually flagging the spurs missed by the pipeline. The baseline level in all bands is mostly gently sloping, but has occasional noticeable ripples. The data quality after spur flagging and baseline subtraction is excellent, as seen in Fig. 2.1. Updated reductions will be provided on the CHESS KP and Herschel Science Center websites.

In bands 1 through 5, an important concern is ghosts from bright ($T_a \geq 3$ K) lines (Comito & Schilke 2002). The effect of ghosts on the overall noise properties is negligible, but they may locally imitate or damage true lines. To check this, we performed a separate reduction where bright lines are masked out and not used in the deconvolution. In bands 6 and 7, we have no ghost problems, as the signal to noise ratio of even the strongest lines is small, and ghosts are typically at the scale of double sideband intensity variations, which are $\leq 10\%$ of the peak intensity. Table 2.1 lists the measured root-mean-square (RMS) noise for the central part of each full band at 1.1 MHz resolution. Bands 6 and 7 were observed only partially, their RMS noise values can be seen in the bottom panel of Fig. 2.1.

2.2.2   Line identification

All the lines detected in the survey are summarized in Fig. 2.1, where we show the full HIFI spectrum, and the integrated flux and corresponding RMS noise level of each line. As the main detection criterion, we adopted a limit of $S \geq 5$ for the signal to noise (significance) of the integrated line flux. We use a local definition of the signal to noise ratio:

$$S = \left| \frac{\int_{i=1}^{N} \mathrm{T}_{\mathrm{mb},i} dv}{\mathrm{RMS} \cdot dv \cdot \sqrt{N}} \right|, \tag{2.1}$$

where S is the significance, the integral gives the integrated intensity, i is the channel index, $\mathrm{T}_{\mathrm{mb},i}$ is the main beam temperature of channel i and dv the channel width, N is the number of channels covered by the line, and RMS is the local RMS noise around the line, measured at a resolution of 1.1 MHz. Given $\sim 10^6$ channels in the data and a typical extent of $10 \dots 100$ channels per line, the total number of false-positives for a flux detection limit of $S = 5$ in the entire survey is negligible.

Lines in the survey were mostly identified using the JPL[4] (Pickett et al. 1998) and CDMS[5] (Müller et al. 2005) catalogues. The literature was consulted for H_2O^+. The line identification was carried out in two phases and relied on the fact that the OMC-2 FIR 4 spectrum, while relatively rich in lines, is sufficiently sparse at our sensitivity that most lines can be individually and unambiguously identified.

In phase 1, we employed the CASSIS[6] software to look for transitions of more than 80 molecules or isotopologues that had been previously reported in spectral surveys or were expected to be seen in the HIFI data. Reasonable cutoffs were applied to limit the number of transitions investigated. For example, for CH_3OH, we set $E_u < 10^3$ K, $A_{ul} > 10^{-4} s^{-1}$ and $|K_u| \leq 5$, yielding > 2000 transitions in the HIFI range. The location of each of these transitions was then visually inspected in the survey data. Once marked as a potential detection, a feature was not excluded from re-examination as a candidate for another species, with the intention of producing a conservative list of blend candidates. For suspected detections, the line flux was measured in a range covering the line and accommodating potential weak wings (typically ~ 20 km $\cdot$ s^{-1} in total). The local RMS noise was determined from two line-free nearby regions for each line, and the line flux signal-to-noise ratio was calculated from Eq. 2.1. The majority of the investigated transitions were not deemed even candidate detections, and $\sim 10\%$ of all chosen candidates turned out to be below the $S = 5$ limit. The identification process was greatly sped up by the use of the CASSIS software as well as custom HIPE scripts. Nearly all the lines reported in this paper were identified in phase 1.

In phase 2, we performed an unbiased visual inspection of all the data, looking for features significantly exceeding the local RMS noise level and not yet marked as detections in Phase 1. This process was aided by an automated line-finder that uses a sliding box to identify features exceeding $S = 3$ and 5 in the spectral data and also

---

[4]http://spec.jpl.nasa.gov/

[5]http://www.astro.uni-koeln.de/cdms/

[6]CASSIS has been developed by IRAP-UPS/CNRS, see http://cassis.irap.omp.eu.
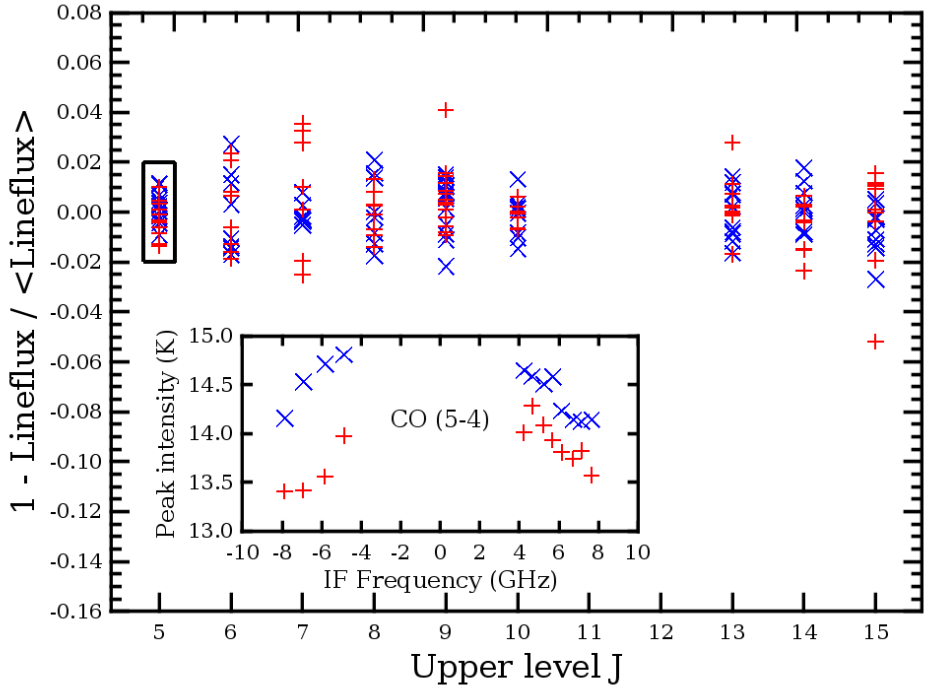
Figure 2.2: The fractional difference of the double-sideband CO line fluxes from their mean for each rotational line. The H polarization is shown in blue (x) and V in red (+). The inset shows the peak line intensity of the CO $5 - 4$ transition, highlighted in the main plot with a box, versus intermediate frequency (IF) position. Negative IF frequency denotes lower side band (LSB).

labels all previously identified lines. Phase 2 yielded a large number of candidates, of which only a handful were confirmed as line detections.

The bottom two panels of Fig. 2.1 summarize the absolute line fluxes and RMS noise values of the detected lines. All scripts used in the line identification and measurement process are available on request from the authors.

2.2.3   Flux calibration accuracy

For HIFI, instrumental effects such as the sideband gain ratios and standing waves play a dominant role in the calibration accuracy and precision (Roelfsema et al. 2012). Standing waves arise from internal reflections in the instrument and, to first order, contribute a constant $\lesssim 4\%$ to the flux calibration uncertainty across each band. The sideband gain ratio (SBR) characterizes the fraction of the total double-sideband intensity that comes from the upper or lower side band (USB, LSB). In an ideal mixer,

the USB and LSB contributions are equal, however in reality this is not exactly the case, particularly towards the edges of the receiver bands. Here, we discuss the flux calibration uncertainty in the data, using the overlaps of adjacent HIFI bands, as well as an analysis of the CO line properties at the double-sideband stage.

Of all the lines in our survey, 10% are in overlapping sections of HIFI bands, which we use to obtain a repeat measurement of their fluxes after deconvolution, and thus an estimation of the calibration and processing uncertainties. Focussing on the overlap of bands 1b and 2a, where the SBR variations are known to be large (Higgins 2011), we find that the line flux uncertainty is at the $\sim 10\%$ level, although this may depend to a substantial degree on how the data reduction is carried out.

To estimate the SBR impact in the centers of the HIFI bands, we analyze the fluxes of ^{12}CO lines in the double sideband data. In Fig. 2.2, we show the fractional difference from the mean for the integrated intensity of each CO line observed in Spectral Scan mode, i.e. with multiple LO settings. H and V polarization are shown in blue (x) and red (+), respectively. The inset in Fig. 2.2 shows the variations of the CO $(5 - 4)$ line peak intensity with LO setting, revealing a correlation with the distance of the line from the center of the intermediate frequency (IF) range, consistent with a SBR variation across the band. This correlation is similar for the other CO lines. There is also a systematic offset between the intensities in the H and V polarizations, which we do not consider. We find the relative variations from uncorrected SBRs within a band to be $\lesssim 4\%$, although other factors may contribute to the total flux uncertainty budget.

Corrections for the SBR variations are already in the pipeline for band 2a and are being characterized for all bands (Higgins et al. 2009; Higgins 2011). A more thorough analysis of the impact of SBRs as well as operations such as baselining and deconvolution on the line fluxes is needed to exploit the full potential of HIFI. This is particularly important for absorption and weak emission lines.

Table 2.2: A summary of the detected species, giving the number of detected transitions for each species, the range of upper level energies, the typical v_{lsr} and FWHM, the total line flux in K·km/s and in W·m^{-2}, where the exponential is given in brackets, and a note on the dominant line profile components. The line counts include hyperfine components and blends. Blends between species are excluded from the per-species flux sums, but included in the total line flux measured in the survey. The species are grouped similarly to Section 2.3.6. Dashes represent cases where a good single Gaussian fit was not obtained, mostly due to blending. Footnotes: [a]NH is unambiguously detected in absorption on the HCN $11-10$ line.; [b]due to a blend with CH$_3$OH on the $2-1$ line, only the H^{37}Cl $1-0$ flux is given; [c] Excluding some blended lines; [s1]Winnewisser et al. (1997); [s2]Cazzoli et al. (2004); [s3]Klapper et al. (2001); [s4]Klapper et al. (2003); [s5]Pickett et al. (2005); [s6]Johns (1985); [s7]Blake et al. (1986a); [s8]Müller et al. (2005); [s9]Mürtz et al. (1998); [s10]Müller et al. (2004); [s11]Müller et al. (2000b); [s12]Lattanzi et al. (2007); [s13]Pagani et al. (2009); [s14]Cooksy et al. (1986b); [s15]Cooksy et al. (1986a); [s16]Müller (2010); [s17]McCarthy et al. (2006); [s18]Padovani et al. (2009); [s19]Thorwirth et al. (2003); [s20]Cazzoli & Puzzarini (2005); [s21]Thorwirth et al. (2000); [s22]Klisch et al. (1995); [s23]Flores-Mijangos et al. (2004); [s24]Müller et al. (1999); [s25]Yu et al. (2010); [s26]Huang et al. (2011); [s27]Kim & Yamamoto (2003); [s28]Belov (1995); [s29]Bogey et al. (1997); [s30]Müller et al. (2000a); [s31]Brown & Müller (2009); [s32]Nolt et al. (1987); [s33]Araki et al. (2001); [s34]Brünken et al. (2004); [s35]Takano et al. (1998); [s36]Fusina et al. (1988).

Species	#	E_u range K	$\overline{v}_{lsr}$ km/s	FWHM km/s	$\int T_{mb}dv$ K·km/s	Flux W·m^{-2}	Line components
CO[s1]	11	83 …752	11.8	12.3	2.0(3)	3.6(-14)	Quiescent gas, wings.
^{13}CO[s2]	8	79 …719	11.9	4.7	1.2(2)	1.5(-15)	Quiescent gas, wings.
C^{18}O[s3]	5	79 …237	11.3	2.8	1.3(1)	1.4(-16)	Quiescent gas.
C^{17}O[s4]	3	81 …151	10.8	3.2	1.6(0)	1.4(-17)	Quiescent gas.
H$_2$O[s5]	10	53 …305	12.1	14.3	3.5(2)	7.2(-15)	Quiescent gas, wings.
H$_2^{18}$O[s6]	1	61	13.7	19.2	1.1(0)	9.1(-18)	Wings.
OH[s7]	6	270	12.7	19.1	7.3(0)	2.3(-16)	Wings.
OH^{+}[s8]	8	44 …50	–	–	-4.7(0)	-5.5(-17)	Foreground slab.
H$_2$O$^+$[s9]	1	54	8.4	2.5	-9.0(-1)	-1.6(-17)	Foreground slab.
CH$_3$OH[s10]	431	33 …659	12.2	4.7	4.9(2)	5.8(-15)	Quiescent gas.
H$_2$CO[s11]	74	97 …732	11.9	4.7	9.3(1)	9.1(-16)	Quiescent gas.

Continued from previous page

Species	#	E_u range K	$\overline{v_{lsr}}$ km/s	$\overline{FWHM}$ km/s	$\int T_{mb}dv$ K $\cdot$ km/s	Flux W $\cdot$ m^{-2}	Line components
HCO^{+}[s12]	8	90 … 389	11.5	5.4	1.0(2)	1.2(-15)	Quiescent gas, wings(?).
H^{13}CO^{+}[s12]	2	87 … 117	11.4	2.2	7.0(-1)	5.8(-18)	Quiescent gas.
N$_2$H^{+}[s13]	7	94 … 349	11.7	3.0	2.5(1)	2.9(-16)	Quiescent gas.
CI[s14]	2	24 … 63	11.9	1.8	9.4(0)	9.4(-16)	Quiescent gas.
CII[s15]	1	91	9.1	2.1	1.8(1)	5.8(-16)	Foreground slab.
CH^{+}[s16]	1	40	9.8	6.0	-2.7(0)	3.5(-17)	Foreground slab.
CH[s17]	3	26	12.7	2.5	4.4(-1)	3.6(-18)	Quiescent gas.
CCH[s18]	20	88 … 327	–	–	1.0(1)	1.2(-16)	Quiescent gas, wings.
HCN[s19]	9	89 … 447	12.3	12.1	1.0(2)	1.3(-15)^a	Quiescent gas, wings.
H^{13}CN[s20]	2	87 … 116	12.7	10.0	1.6(0)	1.3(-17)	Quiescent gas, wings.
HNC[s21]	2	91 … 122	11.6	2.6	2.0(0)	1.7(-17)	Quiescent gas.
CN[s22]	20	82 … 196	12.5	8.1	9.7(0)	9.6(-17)	Quiescent gas, wings.
NH[s23]	5	47	–	–	_^{a}	_^{a}	Quiescent gas?
NH$_3$[s25]	7	28 … 286	13.3	4.5	2.4(1)	4.1(-16)	Quiescent gas, wings.
^{15}NH$_3$[s26]	1	28	11.3	5.8	1.0(-1)	1.3(-18)	Quiescent gas.
CS[s27]	12	129 … 543	12.2	10.3	1.9(1)	1.9(-16)	Quiescent gas, wings.
C^{34}S[s27]	1	127	10.0	1.7	2.0(-1)	1.6(-18)	Quiescent gas?
H$_2$S[s28]	6	55 … 103	11.6	5.0	1.3(1)	1.7(-16)	Quiescent gas, wings?
SO[s29]	12	166 … 321	9.4	9.3	5.4(0)	4.8(-17)	Broad blue.
SO$_2$[s30]	2	65 … 379	11.1	10.0	3.0(-1)	2.2(-18)	Broad blue, quiescent gas, wings?
SH^{+}[s31]	2	25	12.6	2.8	2.0(-1)	1.5(-18)	Quiescent gas, wings?
HCl[s32]	10	30 … 90	11.4	–	4.9(0)	9.8(-17)	Quiescent gas, wings.
H^{37}Cl[s32]	10	30 … 90	11.4	–	9.5(-1)	8.6(-18)^b	Quiescent gas, wings.
H$_2$Cl^{+}[s33]	5	23 … 58	9.4	1.3	-8.2(-1)	9.3(-18)	Foreground slab.
H$_2^{37}$Cl^{+}[s33]	1	58	9.4	1.3	-3.6(-1)	-4.4(-18)	Foreground slab.
HDO[s6]	3	43 … 95	12.7	3.8	6.0(-1)	7.7(-18)	Quiescent gas, wings?

Continued from previous page

Species	#	E_u range K	$\overline{v_{lsr}}$ km/s	$\overline{FWHM}$ km/s	$\int T_{mb}dv$ K $\cdot$ km/s	Flux W $\cdot$ m^{-2}	Line components
DCN [s34]	2	97 ... 125	12.0	4.9	3.0(-1)	2.8(-18)	Quiescent gas.
ND [s35]	1	25	11.2	10.7	3.0(-1)	2.1(-18)	Quiescent gas?
NH$_2$D [s36]	2	24	11.3	2.6	6.0(-1)	4.7(-18)	Quiescent gas.
HF [s32]	1	59	10.0	2.8	-1.8(0)	-4.1(-17)	Foreground slab, quiescent gas.
All[c]	718	23 ... 752	12.0	5.4	3.4(3)	5.7(-14)	

2.3   Overview and results

2.3.1   Detected lines and species

We found and identified a total of 718 lines from 26 molecular and atomic species and 14 secondary isotopologues at or above a flux signal to noise level of 5. All the detected features were identified. The detections are summarized in Table 2.2, and a full list of lines, including a description of potential blends, is given in Appendix 2.A. Of the detected lines, 431 or 60% belong to CH_3OH. Another 74 or 10% belong to H_2CO. In comparison, from SO and SO_2 we detect only twelve and two transitions, respectively. Four deuterated isotopologues are detected: HDO, DCN, NH_2D and ND. The molecular ions include HCO^+, N_2H^+, CH^+, SH^+, H_2Cl^+, OH^+ and H_2O^+.

The upper level energies of the detected transitions range from 24 to 752 K and the typical value is $E_u \sim 100$ K, indicating that much of the emitting gas in the beam is warm or hot. Many of the transitions have very high critical densities, $n_{cr} > 10^8 cm^{-3}$, suggesting that much of the emission originates in dense gas, probably a compact region. The CO line centers are damaged by narrow emission lines in both dual beam switch reference positions. Self-absorption in H_2O and NH_3 indicates that foreground material is present at the source velocity, while blueshifted continuum absorption in OH^+, CH^+, HF and other species points to another foreground component.

In terms of integrated line intensity, CO dominates with 63% of the total line flux, H_2O is second with 12% and CH_3OH third with 10%. The line and continuum cooling are discussed in more detail in Sect. 2.4.2.

2.3.2   The continuum

While continuum emission studies are not the main goal of HIFI, the high quality of the spectra allows a continuum level to be determined for use in line modeling. For example, local wiggles of $10 \ldots 20\%$ in the baseline can mimic a continuum and distort the absorption line to continuum ratio. We provide here a global second-order polynomial fit to the continuum in bands 1a through 5a, where the data quality is highest and the frequency coverage is complete. We stitched the spectra with baselines intact and sampled every 10th channel to reduce the data volume. All spectral regions containing line detections were excluded from the fit. For a polynomial of the form

$$T_{mb}[K] = a + b \cdot \nu[GHz] + c \cdot (\nu[GHz])^2, \qquad (2.2)$$

we find the parameters to be $a = -0.51979$, $b = 0.0015261$ and $c = -4.1104 \cdot 10^{-7}$. This fit is displayed in the second panel of Fig. 2.1 and is valid in the range 480 to 1250 GHz.

2.3.3   Line profiles

There is a wealth of information in the line profiles of the detected species. Two striking examples are the different line profile components revealed by the different
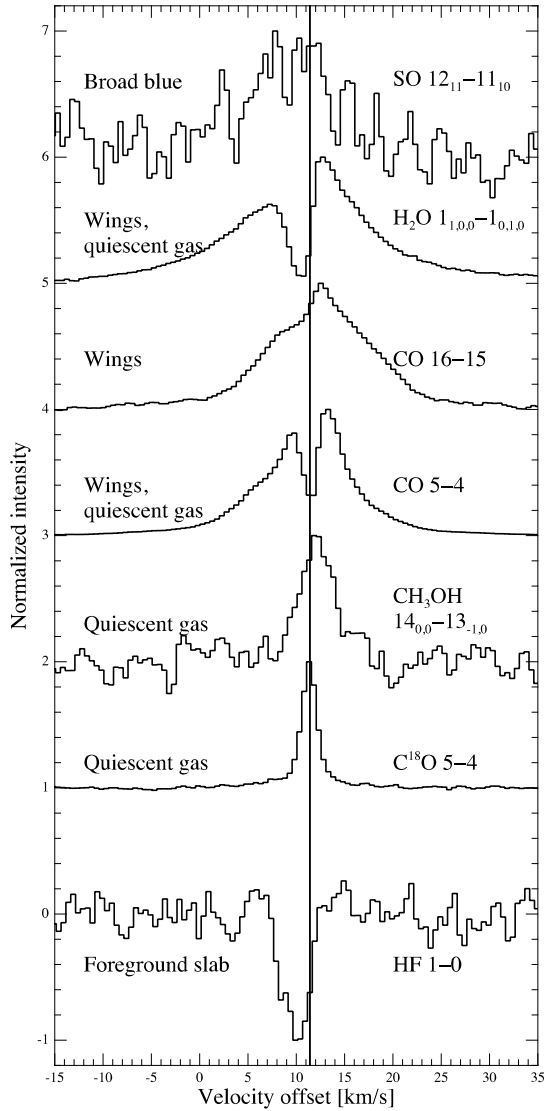
Figure 2.3: The main components of the line profiles. The solid vertical line shows the source velocity, $11.4 \text{ km} \cdot \text{s}^{-1}$. The two velocity regimes of *quiescent gas* are illustrated by $C^{18}O$ and CH_3OH. The deep, narrow absorption feature in CO is due to emission in the reference beams, while the absorption in H_2O appears to be dominated by self-absorption. The *broad blue* component is represented by SO. The HF line traces foreground material in the *foreground slab*, at $9 \text{ km} \cdot \text{s}^{-1}$, with another contribution from the *quiescent gas*. Line components not shown here are lumped in the category *other*.

Species	$E_{\rm u} < 200$ K		$E_{\rm u} > 200$ K		Notes
	$T_{\rm rot}$ [K]	N [cm^{-2}]	$T_{\rm rot}$ [K]	N [cm^{-2}]	
CO	189	$8.4 \cdot 10^{16}$	206	$9.7 \cdot 10^{16}$	Reference contamination at $E_{\rm u} < 300$ K.
^{13}CO	67	$1.3 \cdot 10^{16}$	135	$5.0 \cdot 10^{15}$	
C^{18}O	49	$2.3 \cdot 10^{15}$	–	–	
C^{17}O	37	$9.5 \cdot 10^{14}$	–	–	Two lines ($7 - 6$ is blended and removed).
HCO$^+$	73	$9.1 \cdot 10^{12}$	104	$6.3 \cdot 10^{12}$	
H^{13}CO$^+$	30	$4.2 \cdot 10^{11}$	–	–	Two lines.
HCN	84	$1.2 \cdot 10^{13}$	117	$1.2 \cdot 10^{13}$	
H^{13}CN	38	$1.0 \cdot 10^{12}$	–	–	Two lines.
DCN	28	$6.6 \cdot 10^{11}$	–	–	Two lines.

Table 2.3: Rotational diagram analyses in two upper level energy ranges, $E_{\rm u} < 200$ K and $E_{\rm u} > 200$ K. We included only species with at least two detected lines of a rarer isotopologue, and only unblended lines. Formal uncertainties for the parameters are not given, but including the effects of RMS noise and flux calibration errors, they are $\lesssim 10\%$. For several species, no transitions were detected in the higher energy range. In cases where only two transitions are fit, a note is added.

molecules and substantial changes in line parameters such as $v_{\rm lsr}$ and full-width half maximum with changing upper level energy or frequency for some molecules.

For the purposes of this paper, we distinguish the following line profile components, as illustrated in Figs. 2.3 and 2.4: the *quiescent gas*, *wings*, *broad blue*, *foreground slab* and *other*. Their nature is discussed in Sect. 2.4.1. We emphasize that this is first and foremost a morphological classification, and that the underlying spatial source structure may be more complex than is immediately apparent from the emergent line profiles.

The *quiescent gas* refers to narrow lines, $FWHM \sim 2 \ldots 6$ km$\cdot$s^{-1}. It may have at least two sub-components, one at the source velocity of 11.4 km $\cdot$ s^{-1} and another at 12.2 km$\cdot$s^{-1}. The *wings* refers to a broad component, difficult to fully disentangle but apparently centered around ~ 13 km$\cdot$s^{-1} and with $FWHM \geq 10$ km$\cdot$s^{-1}. The *broad blue* is traced by SO and is unique for its combination of blueshifted velocity and large linewidth, both ~ 9 km $\cdot$ s^{-1}. Other species may have contributions from this component. The *foreground slab* refers to narrow lines at ~ 9 km $\cdot$ s^{-1}, most of them in absorption. We use the term *other* for line profile features which do not fall in the above categories. The velocities of all components shift around by ~ 1 km$\cdot$s^{-1} with species and excitation energy, pointing to further substructure in the emitting regions, although part of this variation is certainly due to measurement uncertainties and could also be due to uncertainties of order 1 MHz in the database frequencies of some species.

Using the recently developed `HIPI` plugin for `HIPE`, we investigated spectra of the most common species for emission in the reference positions of the dual beam switch observations. For CO, CI and CII, strong emission in one or, in the case of CO, both of the HIFI dual beam switch reference positions creates artificial absorption-like features where emission is subtracted out of the on-source signal. This is evident for CO as deep, narrow dips in the line profiles, which make determining the *quiescent gas* contribution to these lines impossible. In the case of CII, the line itself peaks to the blue of the reference position emission and we judge the problem to be less severe, similarly to CI where only one reference position appears to be substantially affected. The deep self-absorption in several H_2O lines appears to be related predominantly to the source. Extended weak H_2O $1_{1,0} - 1_{0,1}$ emission is present on ~ 5' scales in OMC-2 (Snell et al. 2000), but this emission seems to peak strongly on OMC-2. Previous observations have demonstrated the large extent of uniform CO $1 - 0$ (Shimajiri et al. 2011) and CII emission (Herrmann et al. 1997), consistent with the contamination seen in the HIFI spectra.

2.3.4 Line density

In Table 2.1, we give the line density per GHz measured in each band. The typical value is 1 line GHz^{-1}. At 500 GHz, the line density is 1.9 GHz^{-1}, and at 1 THz, it is 0.7 GHz^{-1}. At 1200 GHz, the line density is only 0.3 GHz^{-1}. Clearly, the line density decreases markedly with frequency. This is due to the decreasing sensitivity of our survey and the increasing demands on temperature and density to excite high-lying rotational levels. A similar decrease for Orion KL was discussed by Crockett et al. (2010). As the line detections cover only 7% of all frequency channels at 500 GHz, a range where the highest number of transitions from CH_3OH, SO_2 and other "weed" molecules is expected, we conclude that our survey is far from the line confusion limit.

2.3.5 Rotational diagrams

The large number of transitions of various molecules covered by our survey allows us to construct and compare rotational diagrams (Goldsmith & Langer 1999), which are summarized in Table 2.3. These provide rotational excitation temperatures and LTE column densities. If the emitting medium is in LTE, and the optical depths of the lines and the source size are known, the rotational temperature is equal to the kinetic temperature. For subthermal excitation, if the source size is known, the rotational temperature gives an upper limit on $T_{\rm kin}$ and the obtained column density is generally a lower limit on the true column density. As a first guess, we assume a beam-filling emission source in all cases.

Due to its low critical density ($n \lesssim 10^6$ cm^{-3} up to $J_{\rm u} = 16$), CO is commonly assumed to be thermalized and its rarer isotopologues are mostly optically thin. However, the critical densities of species such as HCN, CS, HCO^+ etc are several orders of magnitude higher and their lines are weaker. Without isotopologue lines, optical depth effects are more difficult to assess. We thus present rotational diagram fitting results for isotopologues of CO and those other species for which at
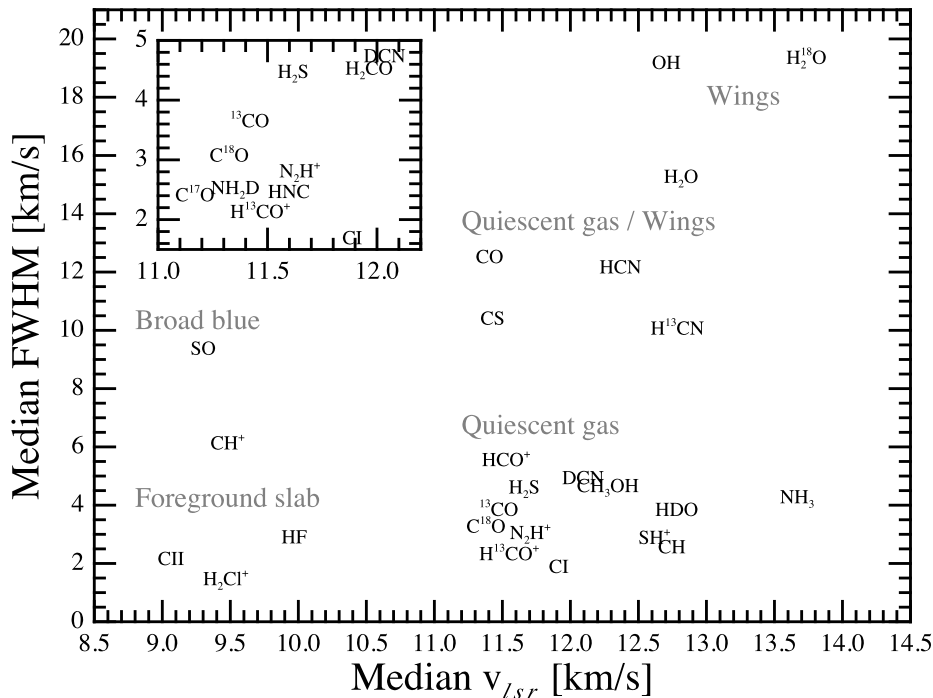
Figure 2.4: Median velocities and linewidths from Gaussian fits to lines of most detected species. Several groups emerge, which are labelled in gray and referred to throughout the paper. The inset shows a zoom of the *quiescent gas* v_{lsr} and FWHM range, to allow more species to be plotted (selected species are carried from the main panel to the inset for comparison). For a discussion, see Sect. 2.4.1.

least two transitions of a rarer isotopologue are detected and are not significantly blended. The results in Table 2.3 show the T_{rot} values to decrease with the rarity of the isotopologue, which is a sign that optical depth effects are important for the most abundant isotopologues of these species. On the other hand, the non-detection of rare isotopologues of most other species indicates that their main isotopologues likely do not have large optical depths, especially for species such as CH_3OH for which the brightest lines are quite strong.

To look for changes in the rotational temperature and column density with increasing E_{u}, we perform the analysis in two excitation regimes: $E_{\mathrm{u}} < 200$ K and $E_{\mathrm{u}} > 200$ K. The results are summarized in Table 2.3 and show that the $E_{\mathrm{u}} < 200$ K lines of all species except ^{12}CO have rotational temperatures below 100 K, while the high-lying lines, where available, give rotational temperatures $T_{\mathrm{rot}} > 100$ K. The column densities in the two regimes are typically within a factor of two of each-other.

Our previous work on a subset of the CH_3OH lines in the survey also yielded rotational temperatures > 100 K (Kama et al. 2010). If the emission is more compact than the beam, the given rotational temperatures are overestimated and the column densities underestimated.

The carbon monoxide isotopologues $C^{18}O$ and $C^{17}O$ give similar temperatures of $T_{rot} = 49$ K and 37 K, suggesting that both species trace similar regions. Including only the lower two $C^{18}O$ transitions in the fit gives $T_{rot} = 41$ K, implying that most of the difference in rotational temperatures is due to higher-excitation transitions being detected for the heavier isotopologue.

$C^{18}O$ has been observed before in OMC-2 FIR 4, from the ground. The column density we find, $N = 2.3 \cdot 10^{15}$ cm^{-2}, is almost exactly the same as that found by Castets & Langer (1995) from the $1 - 0$ and $2 - 1$ lines with with the 15 m SEST telescope, $N = 2.5 \cdot 10^{15}$ cm^{-2}. Using the IRAM 30 m telescope and the same transitions, Alonso-Albi et al. (2010) found $T_{rot} = 22$ K and $N = 4.8 \cdot 10^{15}$ cm^{-2}. For a centrally concentrated source, such an increase of average column density with decreasing beam size ($\theta_{SEST} \approx 2 \cdot \theta_{IRAM}$) is expected, although given that the true uncertainties on any column density determination are likely around a factor of two, the difference may be not significant. The different $C^{18}O$ rotational temperatures, 49 K from HIFI and 22 K from IRAM, indicate that the high-J lines preferentially probe warmer gas, consistent with our rotational diagram results in the low and high E_u regimes. The $C^{18}O$ lines in our survey could also be emitted in a region smaller than the *Herschel* beam at the lowest HIFI frequencies.

The column density ratios of HCO^+ and $H^{13}CO^+$, and HCN and $H^{13}CN$ are, respectively, 22 and 12. These small ratios suggest that the main isotopologues are optically thick and therefore their rotational temperatures are over- and column densities underestimated.

2.3.6 Comments on individual species

Here, we comment on each detected species. All quoted line parameters are from single-Gaussian fits, unless explicitly stated otherwise.

CO, ^{13}CO, $C^{18}O$, $C^{17}O$

The stitched spectrum of OMC-2 FIR 4 is dominated by the CO ladder, towering above the other lines in Fig. 2.1 and shown individually in Fig. 2.5. The peak T_{mb} values are in the range $4.4 \ldots 20.1$ K. The lines are dominated by emission in the *wings* and *quiescent gas* velocities, but up to $J_u = 11$, emission from the reference beams masks the narrower component and results in fake absorption features due to signal subtraction. With increasing J_u, the Gaussian fit velocity shifts from 11.9 to 13.3 km $\cdot$ s^{-1}. The relative contribution of the wings increases with increasing J_u level, or equivalently with decreasing beam size.

We also detect several lines of the isotopologues ^{13}CO, $C^{18}O$ and $C^{17}O$. While $C^{18}O$ and $C^{17}O$ trace the *quiescent gas* component, the ^{13}CO lines contain hints of the *wings* as seen in Fig. 2.7. From $J_u = 5$ to 11, the Gaussian linewidth of ^{13}CO
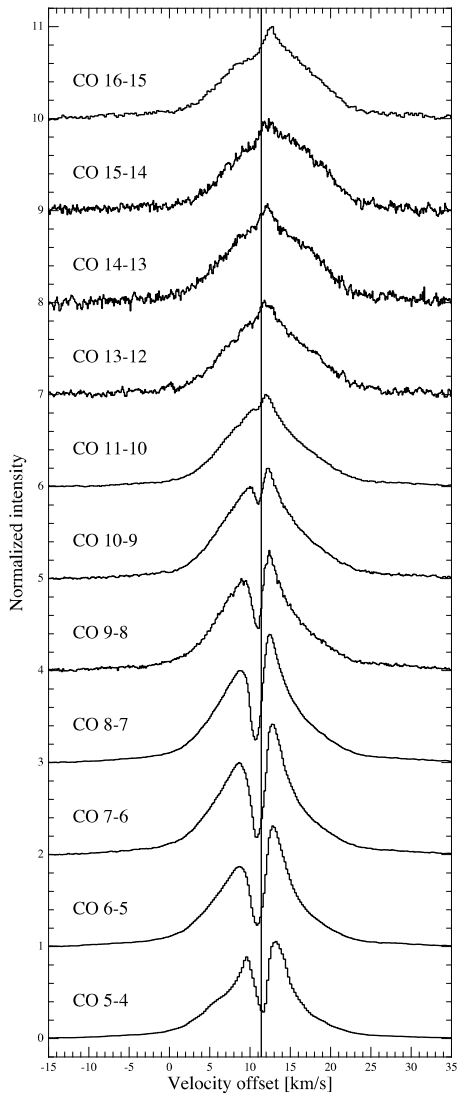
Figure 2.5: The normalized profiles of the CO lines detected in the survey, displayed with a vertical offset of unity between each profile. The solid vertical line marks the source velocity of 11.4 km·s^{-1}. The *wings* are increasingly important towards high rotational levels. Up to $J_u = 11$, the *quiescent gas* is masked by contamination in the reference beams, which causes absorption-like dips in the profiles.
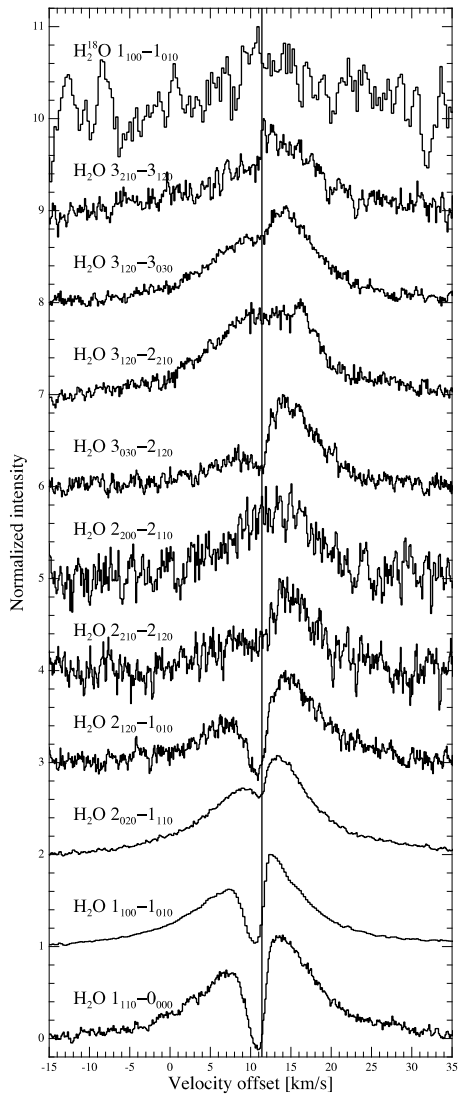
Figure 2.6: The normalized profiles of the H_2O lines detected in the survey, displayed with a vertical offset of 1 between each profile. The solid vertical line marks the source velocity of 11.4 km·s^{-1}. The narrow dips are dominated by self-absorption.

increases near-linearly from 3 km·s^{-1} to 9 km·s^{-1}. With increasing J_u, the width of the C^{18}O lines changes from 2 to 3.4 km · s^{-1}, a less pronounced change than ^{13}CO but similar to N$_2$H$^+$.

We list the C^{17}O $6-5$ line as blended with CH$_3$OH, but similar methanol transitions are not detected and the line is unusually narrow and redshifted to be a CH$_3$OH detection, suggesting the flux originates purely in the CO isotopologue. The C^{17}O $7-6$, however, has a significant flux contribution from a blended H$_2$CO line, as evidenced by the detection of formaldehyde transitions similar to the blended one.

Water: H$_2$O, OH, OH$^+$, H$_2$O$^+$

One of the key molecules observable with HIFI, water, is well detected in OMC-2 FIR 4, as seen in Figs. 2.6 and 2.8. Similarly to CO, the H$_2$O lines are self-absorbed within a ~ 0.5 km · s^{-1} blueshift from the source velocity, corresponding to the *quiescent gas* but in absorption. They also clearly display the *wings* component, Fig. 2.4 shows the H$_2$O wings are broader than those of CO and the lines are typically centered near 13 km·s^{-1}. The peak intensity of the lines does not exceed ~ 4.5 K. The single-Gaussian fit linewidths vary considerably, from 9.9 to 20.5 km·s^{-1}, although it must be kept in mind the line profiles are complex. The isotopologue H$_2^{18}$O, weakly detected, is centered at v$_{lsr}$ = 13.7 km · s^{-1} and 19.2 km · s^{-1} wide. As seen in the top panel of Fig. 2.6, the isotopologue profile is flat and weak, and thus difficult to interpret, but it appears to be as broad as H$_2$O itself. Just like CO, the H$_2$O lines point to a complex underlying velocity and excitation structure within the envelope.

The $3/2 - 1/2$ transition of OH, comprising six hyperfine components, is detected in emission and one set of hyperfine components is shown in Fig. 2.8. An LTE fit with CASSIS, including the hyperfine structure, yields v$_{lsr}$ = 12.7 and FWHM = 19.1 km/. This is consistent with the *wings* component, of which OH may be the best tracer in terms of line profile complexity. The fit is mostly useful for constraining the kinematic parameters of this species – the source size, column density and excitation temperature are not well constrained. In the best-fit model, the hyperfine components are optically thin ($\tau \lesssim 0.01$). The OH line parameters are very similar to those typical for H$_2$O and for high-J CO lines.

Multiple OH$^+$ transitions are detected in absorption at 9.3 km · s^{-1}, part of the *foreground slab* component. We also detect the H$_2$O$^+$ $1_{1,1} - 0_{0,0}$ line at 8.4 km · s^{-1}. Selected lines are presented in Fig. 2.8. These ions and the tenuous gas they probe are analyzed in a companion paper (López-Sepulcre et al., submitted).

CH$_3$OH and H$_2$CO

Lines of CH$_3$OH and H$_2$CO are shown in Fig. 2.9, although due to the enormous number of detections the only criterion for the displayed subset is to cover upper level energies from ~ 100 K through 200 K to 400 K for both species.

CH$_3$OH dominates the number of detected lines in OMC-2 FIR 4 with 431 lines, and H$_2$CO is second with 74. While the median CH$_3$OH velocity is v$_{lsr}$ is 12.2 km·s^{-1} and FWHM = 4.7 km · s^{-1}, the lines display a significant trend in v$_{lsr}$ with upper
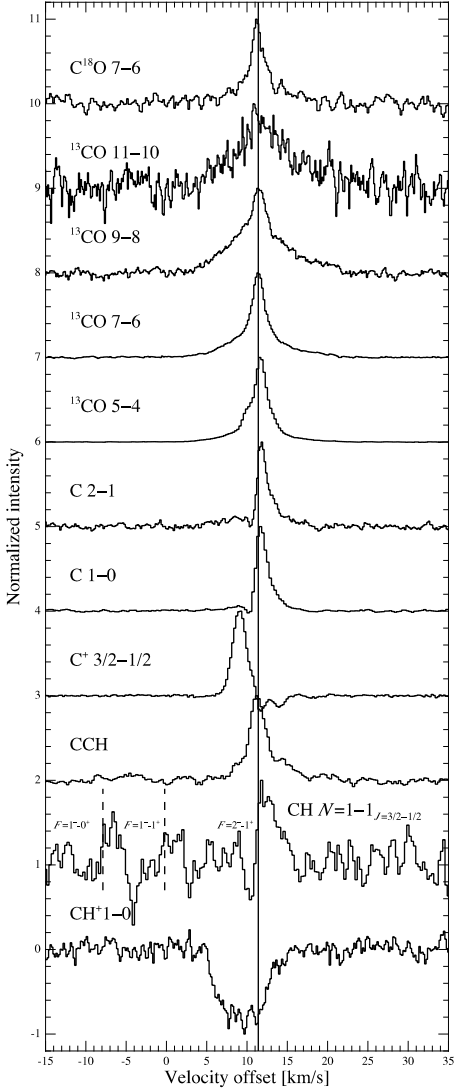
Figure 2.7: Normalized line profiles of carbon-bearing species, illustrating their different kinematics. The solid vertical line marks the source velocity of 11.4 km · s^{-1}. The short vertical dashed lines show the CH hyperfine components except the one the v$_{lsr}$ is centered on. The CII absorption at 11...15 km · s^{-1} is an artefact due to contamination in the reference spectra. The dip in CI at $\sim$ 10 km·s^{-1} as also due to reference beam contamination.
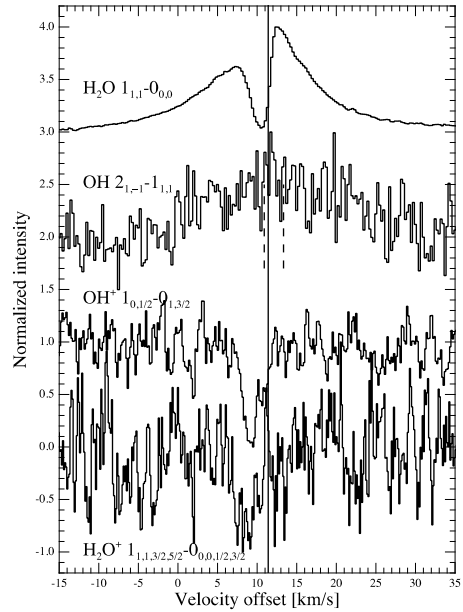
Figure 2.8: Normalized line profiles of some oxygen-bearing species, in particular relating to H$_2$O chemistry. The solid vertical line marks the source velocity of 11.4 km · s^{-1}. The short vertical dashed lines show the OH hyperfine components except the one the v$_{lsr}$ is centered on.
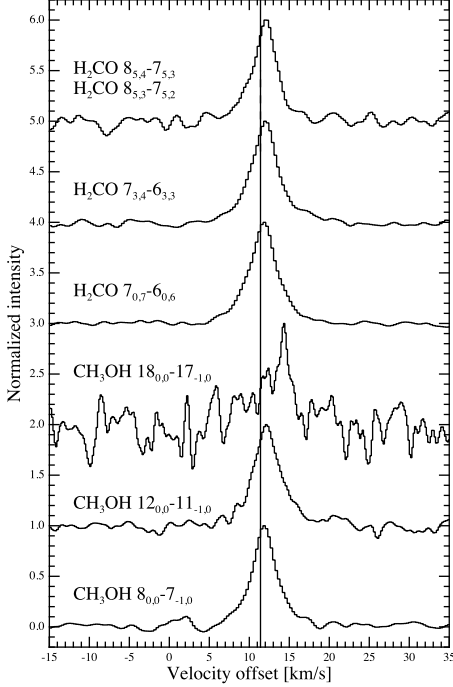
Figure 2.9: Normalized line profiles of some CH$_3$OH and H$_2$CO lines, representing, from bottom to top, upper level energies $E_u \approx$ 100 K, 200 K and 400 K for both species. The solid vertical line marks the source velocity of 11.4 km · s^{-1}.
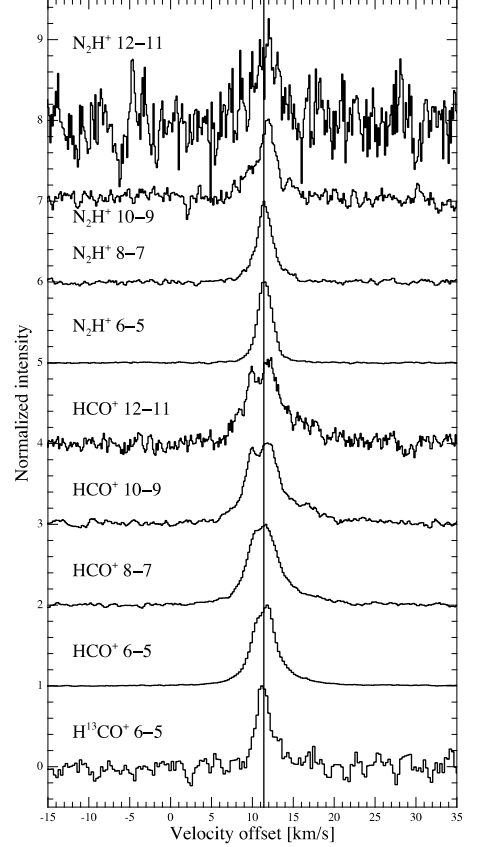
Figure 2.10: A selection of normalized line profiles of HCO$^+$ and N$_2$H$^+$, illustrating trends in the line kinematics. The solid vertical line marks the source velocity of 11.4 km · s^{-1}.

level energy: at $E_u = 50$ K, they peak at 11.8 km · s^{-1}, while by $E_u = 450$ K, the typical peak has shifted to 12.5 km · s^{-1}. This suggests the low-excitation lines are dominated by the source velocity component of the *quiescent gas*, while the redshifted ($\sim$ 12 km/s) component becomes increasingly dominant at high excitation energies. This dominance of an underlying hot component is in line with the conclusion of our previous CH$_3$OH analysis (Kama et al. 2010), where a subset of the lines was presented, including line profiles and rotational diagrams.

The H$_2$CO lines range in upper level energy from 97 K to 732 K, and the me-

dian parameters, v_{lsr} = 11.9 km·s^{-1} and FWHM = 4.7 km/s, are statistically indistinguishable from those of CH$_3$OH. The line of sight velocity trend of H$_2$CO also resembles that of CH$_3$OH.

As no isotopologues of CH$_3$OH and H$_2$CO are detected and because their excitation will be analyzed in a separate paper, we do not give rotational diagram results for these species in Table 2.3. However, the shifting of the emission peaks with upper level energy and frequency suggests these species probe multiple regions of OMC-2 FIR 4.

HCO$^+$ and N$_2$H$^+$

The HCO$^+$ and N$_2$H$^+$ lines, an overview of which can be seen in Fig. 2.10, are dominated by the *quiescent gas* component. The *wings* component appears to contribute at a low level to HCO$^+$ emission. Towards higher J levels, the HCO$^+$ lines become double-peaked, with one component near 10 km·s^{-1} and another at 12 km·s^{-1}. An examination of Fig. 2.10 shows that the double peak is relevant mostly for the highest HCO$^+$ lines, for which the critical densities are $\sim 10^8$ cm^{-3} and lower level energies > 200 K. The apparent double peak may be due to self-absorption at ~ 10 km·s^{-1}. There is no indication in the reference spectra of contamination problems for HCO$^+$. H^{13}CO$^+$ is a prime example of the *quiescent gas* component.

The N$_2$H$^+$ stays single-peaked, but at $E_{\mathrm{u}} > 200$ K ($J_{\mathrm{u}} > 9$), the peak redshifts to 12 km·s^{-1}. While the N$_2$H$^+$ lines are narrower than those of HCO$^+$ by roughly a factor of two, their widths and velocities are similar to the H^{13}CO$^+$, C^{18}O and C^{17}O lines.

Carbon: CI, CII, CH, CCH, CH$^+$

Aside from CO, a number of simple carbon-bearing species are detected. A comparison of some lines of ^{13}CO, CI, CII, CCH, CH and CH$^+$ is given in Fig. 2.7, indicating substantial variations in the line profiles.

The CI and ^{13}CO lines also correspond to the *quiescent gas*. The highest-J ^{13}CO lines show a broad base, likely the *wings*. The CI lines show an absorption dip at around 10 km·s^{-1}, which is due to emission in the reference positions and may be the cause of the slight redshift observed for CI in Fig. 2.4. The CI line fluxes from the bulk of OMC-2 FIR 4 are underestimated due to the self-absorption.

The CII line peaks at 9.5 km·s^{-1} and likely represents emission from the *foreground slab*. The CII absorption in the 11...15 km·s^{-1} velocity range is an artefact caused by emission in the reference position spectra. To estimate the amount of flux lost due to this at the line peak, we reprocessed the data with one DBS reference spectrum at a time. We established that, while the 11...15 km·s^{-1} absorption features vary strongly with the choice of reference spectrum, the 9.5 km·s^{-1} peak varies only by $\sim 10\%$, suggesting that the amount of line flux lost in this component through reference subtraction is small or that the large-scale emission at this velocity around OMC-2 is remarkably uniform. The latter is unlikely as the difference spectrum of the two reference positions shows a strong positive-negative residual, indicating a velocity offset between the components. If the extended CII emission at 9.5 km·s^{-1} in OMC-2
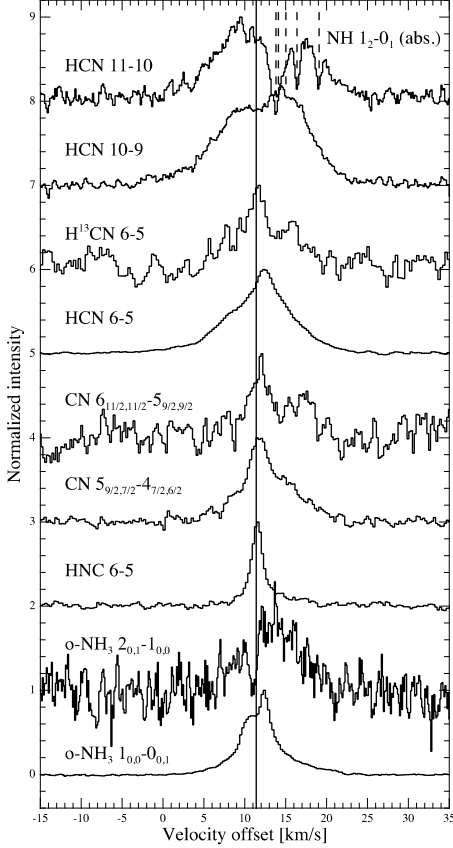
Figure 2.11: Examples of normalized line profiles of nitrogen-bearing species. The solid vertical line marks the source velocity of 11.4 km·s^{-1}. The top line profile is centered on HCN and the dashed vertical lines mark the locations of the strongest NH hyperfine components.
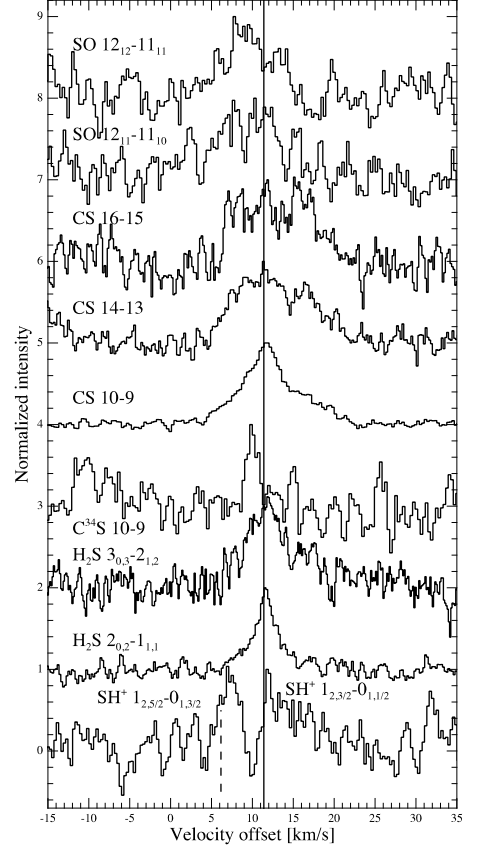
Figure 2.12: Examples of normalized line profiles of sulphur-bearing species. The solid vertical line marks the source velocity of 11.4 km · s^{-1} and the short vertical dashed line on the bottom-most line denotes the non-centered SH$^+$ hyperfine component.

is of comparable intensity to the detected peak, any intensity fluctuations must be at the $\leq 10\%$ level on a scale of 6', given a resolution of 12". Accounting for only the upper level population, we obtain a lower limit of $3.4 \cdot 10^{16}$ cm^{-2} on the CII column density towards FIR 4.

CCH is dominated by the *quiescent gas* component, but shows evidence for *other* components. The lines have a broad base which appears redshifted, perhaps indicating a contribution from the *wings*. The CH lines are dominated by redshifted *quiescent*

gas emission, close in v_lsr to the *wings* component. The parameters resemble HDO. The CH$^+$ ion absorption line is strongly saturated, leading to the increased linewidth seen in Fig. 2.4, but it is centered on the *foreground slab* component. We compare CH$^+$ and SH$^+$ in Sect. 2.3.6.

Nitrogen-bearing molecules

Aside form N$_2$H$^+$, which is covered in Sect. 2.3.6, the main detected nitrogen-bearing species are HCN, CN, HNC and the nitrogen hydrides. There are substantial differences in the profiles with species as well as with upper level energy for the nitrogen-bearing species, similarly to carbon and sulphur. In Fig. 2.11, lines of several representative nitrogen-bearing molecules are shown on a common velocity scale.

HCN, CN and HNC. Gaussian fits to the HCN lines peak at 12.1 km $\cdot$ s^{-1}. Their large linewidth, characteristic of the *wings* component, puts them close to CO and H$_2$O in Fig. 2.4. The upper level energies of the detected HCN lines range from 89 to 447 K. A rotational diagram analysis of the $E_\mathrm{u} < 200$ K lines of HCN gives T$_\mathrm{rot}$ = 84 K and N(HCN) = $1.2 \cdot 10^{13}$ cm^{-2}. The $E_\mathrm{u} > 200$ K lines give T$_\mathrm{rot}$ = 117 K and N(HCN) = $1.2 \cdot 10^{13}$ cm^{-2}. The high-lying lines, in particular, have critical densities around 10^{10} cm^{-3}, indicating that the emitting regions contain very dense and hot gas. The H^{13}CN profiles are also broad, although they show a peak corresponding to the *quiescent gas*. The rotational temperature for H^{13}CN is 38 K.

The two detected HNC lines trace the *quiescent gas* component. The CN line profiles are dominated by the *quiescent gas* component, but there is also a contribution from the *wings*, as seen in Fig. 2.11.

NH and NH$_3$.   We detect some hyperfine components of the NH $1_2 - 0_1$ transition in absorption on the HCN $11 - 10$ emission line, as shown in Fig. 2.11. The lines are close to the *quiescent gas* component velocity. The dominant hyperfine components are in absorption until below the continuum level. The ND ($1_{2,3,4}$-$0_{1,2,3}$) transition is detected in emission and is shown in Fig. 2.14.

Seven transitions of NH$_3$ are detected, covering 28 through 286 K in upper level energy. As seen in Fig. 2.11, the lines have a broad base, consistent with the *wings*, and they show narrow self-absorption near the *quiescent gas* component. We find no evidence for emission in the reference positions to be causing the absorption, but due to the relative weakness of the features this cannot be fully excluded at present. While the lines have a similar appearance to CO, H$_2$O and OH, and are centered at the same velocity, they are typically a factor of four narrower, as seen in Fig. 2.4. We return to this point in Sect. 2.4.1. The fundamental ortho-NH$_3$ line has a particularly interesting profile, with a sharp peak at 12.5 km$\cdot$s^{-1} and a plateau at $10 \dots 12$ km$\cdot$s^{-1}.

Sulphur-bearing molecules

The detected sulphur-bearing species are CS, C^{34}S, H$_2$S, SO, SO$_2$ and SH$^+$. As seen from the selection of lines in Fig. 2.12, there are significant differences between their line profiles.

The detected CS lines cover an upper level energy range of 129 K $\leq E_u \leq$ 543 K and seem similar to CO in that they may have contributions from the *quiescent gas* and the *wings*. The critical densities of the high-lying lines are $n > 10^8$ cm^{-3}, indicating the presence of dense and hot gas in the emitting regions. The C^{34}S $10-9$ line is narrow and peaks at around 10 km$\cdot$s^{-1}, likely tracing a dense, warm clump with a high CS abundance, at that velocity. The clumpy distribution of C^{34}S in OMC-2 FIR 4 is explored further by López-Sepulcre et al. (in preparation).

The H$_2$S lines are dominated by the *quiescent gas* component, but the *wings* or *broad blue* components may be present at a low level.

The SO lines are the sole clear tracer of the *broad blue* component. They cover an upper level energy range of 165 to 321 K and have critical densities of order 10^8 cm^{-3}, suggesting dense and hot gas in the emission region. It is notable that the SO lines are 9.3 km$\cdot$s^{-1} broad and peak at 9.4 km$\cdot$s^{-1}, 2 km$\cdot$s^{-1} to the blue from the OMC-2 systemic velocity. We detect only two transitions of SO$_2$, which are similar in their median properties to CO, perhaps having contributions from the *broad blue*, *quiescent gas* and *wings* components.

The detected SH$^+$ hyperfine line emission is shown in the lowest part of Fig. 2.12. The line profiles are very similar to CH, as seen in Fig. 2.4 and by comparing with the second-to-lowest panel in Fig. 2.7. The central velocity of SH$^+$ matches that of the *wings* component, but the linewidth resembles the *quiescent gas*. It is interesting to note that we detect CH$^+$ in absorption at 9.8 km$\cdot$s^{-1} and SH$^+$ in emission around 12.2 km$\cdot$s^{-1}, contrary to the strong correlation between these species seen in a sample of galactic sight-lines by Godard et al. (2012). The synthesis path of SH$^+$ is S$^+$ + H$_2$ $\rightarrow$ SH$^+$ + H, which has an activation barrier of 9860 K, more than twice the 4640 K barrier to the production of CH$^+$ via an analogous path. This may offer an explanation to our non-detection of SH$^+$ in the *foreground slab* component, but it is not immediately clear why we do not detect CH$^+$ at the same velocity as SH$^+$ – excitation and chemistry may both play a role. In the models of Bruderer et al. (2010), there are regions near a protostellar outflow base where the SH$^+$ abundance is elevated by several orders of magnitude with respect to that of CH$^+$ due to sulphur evaporation from grains.

Chlorine-bearing molecules

Lines of isotopologues containing ^{35}Cl and ^{37}Cl of two of the main chlorine-bearing molecules are detected: HCl $1-0$ and $2-1$ and H$_2$Cl$^+$ $1-0$ and $2-1$, peaking at the *quiescent gas* velocity of $\sim$ 11.4 km$\cdot$s^{-1}. There is a broad base which may be identified with the *wings* component. Several examples are shown in Fig. 2.13.

Hydrogen chloride is predicted to be the dominant gas-phase chlorine reservoir in high-extinction regions (Blake et al. 1986b; Neufeld & Wolfire 2009), consistent with the expectation that the 11.4 km$\cdot$s^{-1} component traces the large-scale envelope. On the other hand, H$_2$Cl$^+$ is predicted to be a significant carrier in photon-dominated regions, and correspondingly H$_2$Cl$^+$ is detected in absorption in the blue-shifted *foreground slab* component. The chlorine-bearing species will be the focus of an upcoming paper (Kama et al. 2012, in preparation).
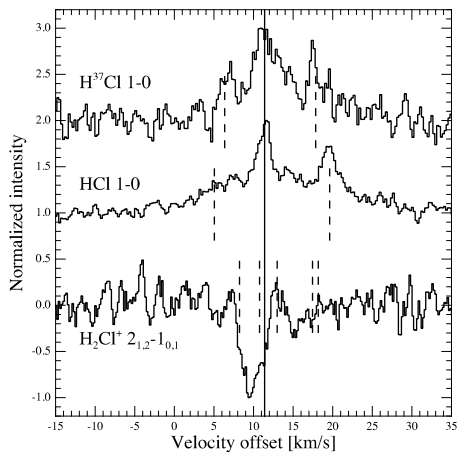
Figure 2.13: Normalized line profiles of the main detected HCl and H_2Cl^+ transitions. The solid vertical line marks the source velocity of $11.4 \text{ km} \cdot \text{s}^{-1}$.
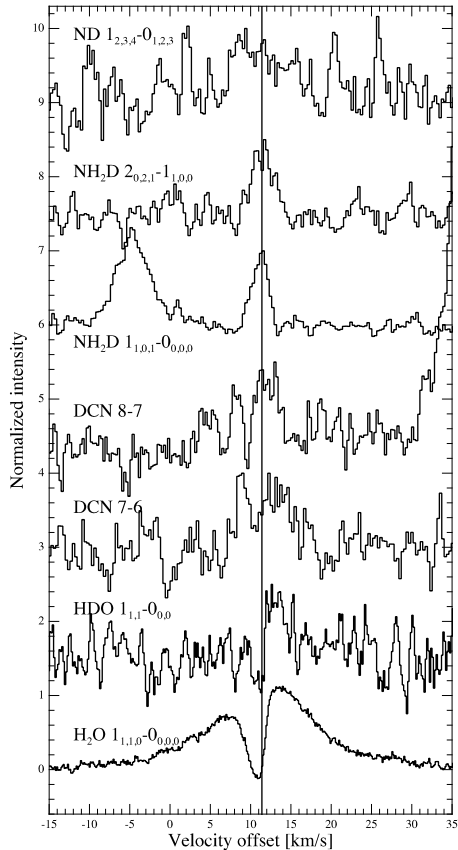
Figure 2.14: A selection of lines of deuterated species. A water line has been added for comparison with HDO. The solid vertical line marks the source velocity of $11.4 \text{ km} \cdot \text{s}^{-1}$.

Deuterated species

The HIFI survey is poor in deuterated species, the only detections are HDO, DCN, NH_2D and ND. The strongest lines are shown in Fig. 2.14. The HDO lines are very weak, therefore firm conclusions cannot be drawn, but the $1_{1,1} - 0_{0,0}$ line shown in Fig. 2.14 suggests similarities with H_2O in velocity, while the linewidth corresponds better to the *quiescent gas* component. The DCN median v_{lsr} is $12 \text{ km} \cdot \text{s}^{-1}$, consistent within the errors with HCN but with the linewidth again much narrower and corresponds to the redshifted side of the *quiescent gas* component, also traced by

CH_3OH and H_2CO. Singly deuterated ammonia, NH_2D, peaks at $v_{lsr} \approx 11.2$ km$\cdot$s^{-1} and corresponds well to other tracers of the *quiescent gas* component. The ND line is centered near the *quiescent gas* velocity but its width corresponds better to the *wings* or *broad blue* component. However, the line is weak and should be interpreted with caution.

HF

The $J = 1-0$ transition of hydrogen fluoride is detected in absorption at 10.0 km/s, and is shown in Fig. 2.3. The linewidth is 2.8 km$\cdot$s^{-1} and the estimated column density $(1.2 \pm 0.3) \cdot 10^{13}$ cm^{-2}. Modeling by López-Sepulcre et al. (submitted) suggests the presence of two different velocity components: one at 9 km $\cdot$ s^{-1}, corresponding to the *foreground slab*, and a dominant component around 11 km $\cdot$ s^{-1}, roughly the *quiescent gas* velocity.

2.4 Discussion

Much information about the kinematic, excitation and abundance structure of OMC-2 FIR 4 is encoded into the roughly 700 detected spectral lines. The source is kinematically and chemically complex. Substantial amounts of molecular gas are present in the HIFI beam at all probed scales (40"... 11" or 17000 AU... 5000 AU). We detect emission from high-J transitions of CO, CS, HCN, HCO$^+$ and other species. The high critical densities (up to $n \sim 10^9$ cm^{-3}) and rotational temperatures (up to $T_{rot} \approx 200$ K) indicate that at least some of the emitting regions are very dense and hot or able to excite such transitions via infrared pumping. We focus below on the kinematical components and the energetics, deferring more detailed analyses to future papers.

2.4.1 Interpretation of the kinematic components

We now discuss the characteristics and possible nature of the kinematic components defined in Sect. 2.3.3. We emphasize again that the features discussed are predominantly line profile components and need not have a one-to-one correspondonence with actual source components. The diversity of line profile shapes is, in any case, a clear indication of the complexity of the underlying spatial variations of composition, density, temperature and velocity.

Quiescent gas. This line profile component may have several sub-components. One, centered around $11.0 \ldots 11.5$ km $\cdot$ s^{-1}, likely corresponds to the large-scale ($\sim 10^4$ AU or 25") envelope of OMC-2 FIR 4 and matches the velocity of the bulk OMC-2 cloud (Castets & Langer 1995; Aso et al. 2000). This component is most clearly seen in C^{18}O, C^{17}O, N$_2$H$^+$ and NH$_2$D, and it appears to contribute to the emission of most detected species. The other component is centered near 12.2 km $\cdot$ s^{-1} and is best traced by CH$_3$OH, H$_2$CO and DCN.

The H$_2$O, NH$_3$ and high-J HCO$^+$ self-absorption (if HCO$^+$ is indeed self-absorbed) is blueshifted with respect to the source rest frame. One hypothesis for explaining

this blueshifted self-absorption feature is a slowly expanding layer of warm gas in the inner envelope. Similar absorption features on broad H_2O line profiles in a sample of protostars are discussed as originating in the inner envelope by Kristensen et al. (2012), who successfully reproduced such line profiles with an adaptation of the Myers et al. (1996) model, incorporating outflow emission partially obscured by an expanding layer of less excited gas.

Our previous analysis of CH_3OH lines in a subset of the present data revealed that the *quiescent gas* component is dominated at high upper level energies by a compact, hot component, which we identified with a hot core (Kama et al. 2010). The rotational diagram results for other species in Table 2.3 provide further evidence for the importance of an underlying hot component.

Wings. The broad wings are seen most clearly in OH, H_2O and CO, and likely trace at least one outflow. The existence of a broad component in the CO $3 - 2$ line was noted already by Johnstone et al. (2003). An interpretation of this component is made difficult by the projected overlap of OMC-2 FIR 4 and one lobe of an outflow from the nearby source, FIR 3 (Shimajiri et al. 2008). Given the prominence and symmetry of the wings in the high rotational lines of CO, and the broadness of the HCN and CS lines – all indicative hot or dense emitting material – the wing emission may originate in a compact outflow from FIR 4 itself (Alonso-Albi et al. 2013, in preparation).

Broad lines of OH correlate well with water and are associated with outflow shocks (Wampfler et al. 2010) and in OMC-2 FIR 4, the large width of the OH lines (FWHM = 19.1 km/s) is consistent with an outflow shock origin. Furthermore, our modeling finds the OH lines to be optically thin, so together with the highest-J CO lines, OH may be the most straightforward tracer of this outflow. As OH is centered at v_{lsr} = 12.7 km·s^{-1}, this may be the velocity of the outflow-driving central source.

In Fig. 2.4, NH_3 corresponds to the outflow tracers CO, H_2O and OH in terms of v_{lsr}, but has a typical linewidth a factor of four smaller. In the L1157-B1 outflow context, similar observations have been explained with a model where NH_3 is destroyed in a shock at velocities > 15 km · s^{-1}, while H_2O, for example, maintains its high abundance (Viti et al. 2011). Other species, such as CH_3OH and H_2CO, should also show emission at the outflow velocity, and a weak wing seems to indeed be present.

Broad blue. This component only appears clearly in lines of SO, although other species such as CO and CS do have a blue wing component that may be related. Its nature is unclear.

Foreground slab. The slab component, at $v_{lsr} \sim 9.5$ km · s^{-1}, is traced almost exclusively by absorption lines of molecular ions associated with photon-dominated regions (PDRs), such as OH^+, H_2O^+ and H_2Cl^+. The CII emission peak also corresponds to this component, as does part of the absorption in the fundamental line of HF. In addition to the set of species tracing the component, the fact that absorption is seen in low-lying lines suggests a very tenuous medium. In a companion paper (López-Sepulcre et al., submitted), we present a detailed analysis of this component, finding it to be a low-density and low-extinction ($A_v \approx 1$ mag) PDR cloud in front of OMC-2, irradiated on one side by a heavily enhanced FUV field.

Other. Aside from the above four components, there is variation in line profiles
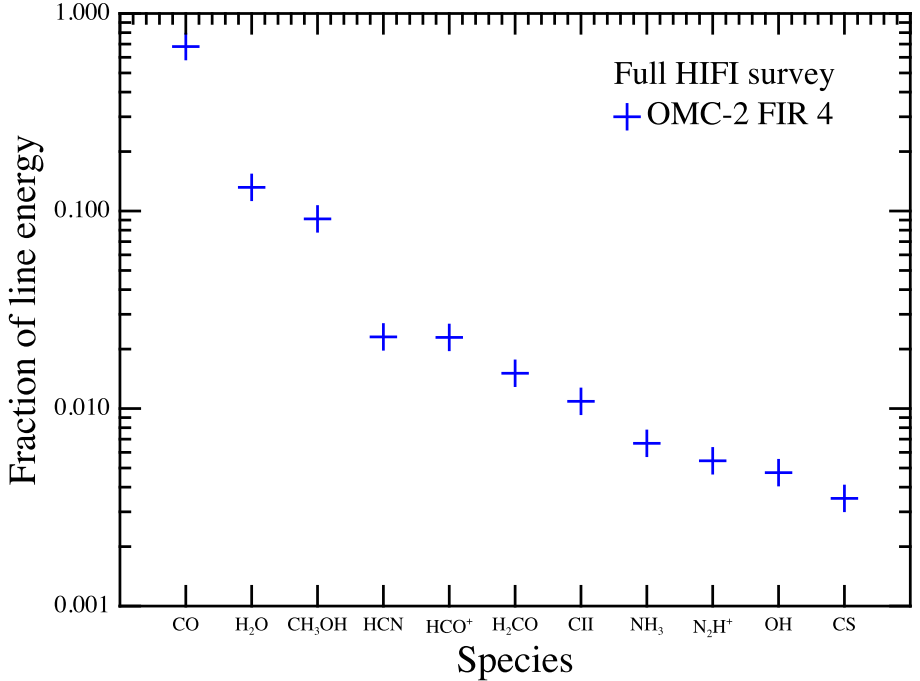
Figure 2.15: The fractional contribution of various species to the line emission from OMC-2 FIR 4. The 11 dominant cooling species, integrated across the entire 480 to 1902 GHz HIFI survey, are displayed. Note that the units are in percent of the total line flux in the HIFI survey, excluding continuum emission.

between different species, upper level energies and observing frequencies. This includes the evolution of N_2H^+ and especially HCO^+ line profiles with increasing J level (Fig. 2.10) and the plateau-and-peak profile of the fundamental ortho-NH_3 line (Fig. 2.11). Many of these line profile aspects may be sub-components of the *quiescent gas* and other aforementioned categories. A full interpretation of this variety of features, while important, is outside the scope of this paper. Pending further analyses of the HIFI data, we refer the reader to previous (Shimajiri et al. 2008) and upcoming (López-Sepulcre et al., in preparation) papers for interferometric results on the small-scale structure of OMC-2 FIR 4.

2.4.2 Line and continuum cooling

We investigated the role of molecular line emission in gas cooling by summing the integrated intensities of the detected transitions of each species. The results are given in the second-to-last column of Table 2.2, and in Fig. 2.15, we show the 11 dominant

cooling molecules. Within the frequency coverage of the survey, ^{12}CO is the dominant molecular coolant, emitting 63% of the total energy in the detected lines. The second most important is H_2O with 12% and the third is CH_3OH with 10%. Two other notable coolants are HCO^+ and HCN, both contributing 2% of the total line flux.

Due to contamination in the reference positions, the total flux in CO lines is likely underestimated by a few tens of percent, as estimated from the lack of contamination in $J_u > 11$ and a multicomponent analysis of the lower-J lines. Thus, the true contribution of CO to the line flux is likely $\sim 70 \ldots 80\%$. At the centre of the source, the contribution of H_2O to the gas cooling is higher than apparent here, if self-absorption in the intervening extended envelope is accounted for.

As the frequency coverage above 1250 GHz is not complete, the cooling contributions of some species in the HIFI range may differ from those given in Table 2.2, but for most species the total line fluxes should not differ much from their total 480 to 1902 GHz fluxes. Undetected weak lines contributing to the continuum may also introduce a small correction to the quoted numbers. The total line emission from OMC-2 FIR 4 may have a large contribution from CO, H_2O and OI lines outside the high end of the HIFI frequency range, towards the mid- and near-infrared.

It is remarkable that the sulphur oxides, SO and SO_2, contribute negligibly to the line cooling in OMC-2 FIR 4, in striking difference from Orion KL, as discussed in Sect. 2.4.2.

To measure the relative importance of line and continuum cooling, we integrated the spectra with baselines intact in the fully frequency sampled region of the survey (bands 1a through 5a or 480 to 1250 GHz), obtaining a flux of $1.7 \cdot 10^{-12}$ W $\cdot$ m^{-2}. Of this, only $3.6 \cdot 10^{-14}$ W $\cdot$ m^{-2} or 2% is in lines. In their 300 GHz range study of five low- to intermediate-luminosity protostars including OMC-2 FIR 4, Johnstone et al. (2003) found lines to contribute $< 8\%$ of the measured continuum in their entire sample, consistent with our terahertz-range result. Assuming a distance of 437 pc, the flux we measure with HIFI between 480 and 1250 GHz corresponds to a luminosity of ~ 10 L$_\odot$, of which 0.2 L$_\odot$ is line emission.

Comparison with other sources

As a detailed comparison with other sources is outside the scope of this paper, we provide here an initial view.

In Fig. 2.16, we compare the relative line cooling in the 795 through 903 GHz range in OMC-2 FIR 4 and Orion KL, a well-studied strong line and continuum emitter. The numbers here are not to be confused with the results for the entire survey given above. The selected species contain the seven most important coolants for either source. H_2O is not considered in this comparison as it has no lines in the 795 to 903 GHz range. In OMC-2 FIR 4 in this range, CO emission contains 60% of the line energy, followed by CH_3OH with 20%, HCN with 8% and HCO^+ with 7%. In Orion KL, SO_2 dominates with 24% of the energy, followed by CH_3OH with 22%, CO with 16% and SO with 12%.

While the sulphur oxides contribute at the $10 \ldots 20\%$ level to line cooling in Orion KL, in OMC-2 FIR 4 both contribute $\leq 0.1\%$ in the 795 to 903 GHz range,
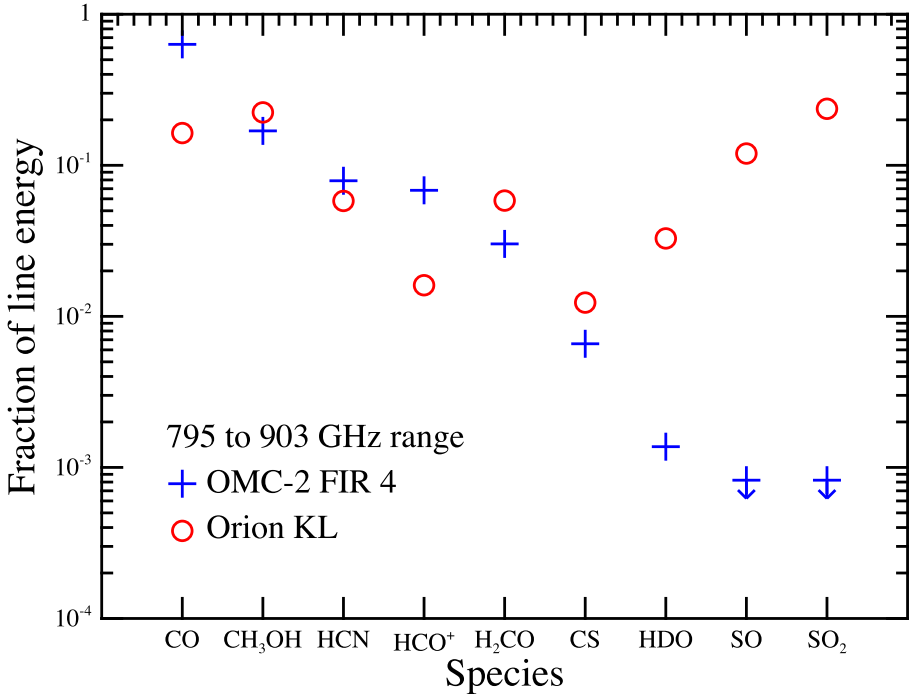
Figure 2.16: Line cooling in the 795 – 903 GHz range in two sources in Orion. The symbols mark the percentage of line emission in each dominant cooling species in OMC-2 FIR 4 (crosses, this work) and in Orion KL (circles, Comito et al. 2005). The upper limits are 5σ. Note that the units are in percent of all line flux within the 795 to 903 GHz range, excluding continuum emission.

a difference of at least two orders of magnitude. This may be due to an exceptional contribution of energetic shocks in Orion KL. A similar scarcity of sulphur oxides in comparison to Orion KL has been reported before in samples of low- as well as high-mass protostars (Johnstone et al. 2003; Schilke et al. 2006). In addition to shocks, factors such as the thermal evolution of the gas and dust may also play an important role in abundance variations of sulphur-bearing molecules (Wakelam et al. 2004, 2005). The difference of peak velocity we observe between SO and CH$_3$OH, ~ 2 km$\cdot$s^{-1}, suggests that SO emission in OMC-2 FIR 4 is dominated by a spatially distinct region, a result seen also in Sagittarius B2 (Nummelin et al. 2000).

The nature and heating processes of Orion KL are currently under debate in the community and our comparison once again confirms the exceptional nature of this source. It must be kept in mind that the quoted Orion KL observations were carried out with the Caltech Submillimeter Observatory, with a beam roughly a third the

size of that of *Herschel* at equivalent frequencies, therefore beam dilution effects may be important and the above comparison should be repeated with the HIFI survey of that source (Crockett et al. 2012, in preparation). The accelerating publication of HIFI spectral surveys and line observations of a number of other protostars (e.g. Caux et al. 2012, in preparation, but see also other papers from the CHESS, HEXOS and WISH Key Programmes) will soon allow more, and more detailed, comparative analyses to be made, across molecular species as well as protostellar properties.

2.5   Conclusions

- We present a *Herschel*/HIFI spectral survey of OMC-2 FIR 4 in the range 480 to 1901 GHz, one of the first spectral surveys of a protostar in the terahertz regime.

- We find 718 lines in the survey, originating from 26 different molecular and atomic species and tracing a large range of excitation conditions, with $24 \leq E_{\mathrm{u}} \leq 752$ K.

- The line profiles have contributions from the large-scale envelope of OMC-2 FIR 4, at least one outflow, a newly discovered foreground PDR and other components. The broad outflow emission has a redshifted offset of 1.5 km$\cdot$s^{-1} from the source velocity. Narrow, blue-shifted self-absorption on broad emission lines of H_2O, NH_3, and possibly HCO^+, may originate in an expanding layer in the inner envelope. Broad, blue-shifted SO lines trace a new component of unclear nature.

- The cooling budget of OMC-2 FIR 4 between 480 and 1250 GHz is dominated by continuum radiation, with lines contributing 2%. The total flux received in this range is $1.7 \cdot 10^{-12}$ W$\cdot$m^{-2} or ~ 10 L$_\odot$ at 437 pc.

- Of all the detected line flux, 63% is from ^{12}CO, 12% from H_2O and 10% from CH_3OH. Every other species contributes at the $\leq 2\%$ level.

- The dominant cooling molecules in OMC-2 FIR 4 and Orion KL are similar, but the relative role of SO and SO_2 in the energy budget of OMC-2 FIR 4 is two orders of magnitude smaller than in Orion KL, indicating a substantial difference in the role of shocks or in the thermal evolution.

- In terms of composition and dominant chemical species, OMC-2 FIR 4 is well in line with results for other protostars from ground-based instruments. It is thus a nearby intermediate-mass star formation laboratory for which an exceptional spectral dataset is now available.

2.A   Detected transitions

Here, we present a frequency-sorted table of the transitions detected in the survey. Line profile parameters (v_{lsr}, FWHM, T_{mb}) are not given for the lines which are blended. Blending is indicated by a `B:` in the final column, followed by an identification of the blended line (only one `B:` line is given also for multiple overlapping blends). For some species, such as OH and SH$^+$, the line parameters were determined by fitting models of the hyperfine line profile to the data, these results can be seen in Table 2.2 and Fig. 2.4.

ν GHz (1)	Species (2)	Transition (3)	ν_rest GHz (4)	E_u K (5)	A_ul rad/s (6)	Gaussian fit v_lsr km/s (7)	FWHM km/s (8)	T_mb K (9)	from moments v_lsr km/s (10)	Flux K km/s (11)	RMS mK (12)	Blend(**B**) / Notes (13)
480.269	CH$_3$OH	$3_2 - 3_1$	480.269	51.64	4.89e-04	12.26	5.20	0.21	11.75	1.01	22	
481.504	CH$_3$OH	$2_2 - 2_1$	481.504	44.67	3.94e-04	11.36	3.64	0.20	13.34	0.42	23	
481.916	C^{34}S	$10_0 - 9_0$	481.916	127.23	2.38e-03	10.01	1.68	0.10	10.29	0.21	19	
482.282	CH$_3$OH	$10_0 - 9_0$	482.282	140.60	5.02e-04	11.80	3.61	0.49	11.89	1.93	16	
482.959	CH$_3$OH	$10_{-1} - 9_{-1}$	482.959	133.15	5.00e-04	11.82	3.82	0.81	11.82	3.09	15	
483.141	CH$_3$OH	$10_0 - 9_0$	483.141	127.60	5.05e-04	11.73	3.72	0.87	11.80	3.48	17	
483.389	CH$_3$OH	$10_2 - 9_2$	483.389	165.35	4.89e-04	12.22	5.07	0.16	11.46	0.81	20	
483.472	CH$_3$OH	$10_{-4} - 9_{-4}$	483.472	215.55	6.30e-04	12.65	5.21	0.05	12.10	0.18	15	
483.539	CH$_3$OH	$10_4 - 9_4$	483.539	207.99	6.31e-04						14	**B**: CH$_3$OH ($10_4 - 9_4$)
483.539	CH$_3$OH	$10_4 - 9_4$	483.539	207.99	6.31e-04						14	**B**: CH$_3$OH ($10_4 - 9_4$)
483.551	CH$_3$OH	$10_3 - 9_3$	483.551	177.46	6.82e-04						14	**B**: CH$_3$OH ($10_4 - 9_4$)
483.556	CH$_3$OH	$10_{-3} - 9_{-3}$	483.556	190.37	6.87e-04						14	**B**: CH$_3$OH ($10_4 - 9_4$)
483.566	CH$_3$OH	$10_3 - 9_3$	483.566	177.46	6.82e-04						14	**B**: CH$_3$OH ($10_4 - 9_4$)
483.686	CH$_3$OH	$10_1 - 9_1$	483.686	148.73	7.60e-04						13	**B**: CH$_3$OH ($10_3 - 9_3$)
483.697	CH$_3$OH	$10_3 - 9_3$	483.697	175.39	6.85e-04						13	**B**: CH$_3$OH ($10_1 - 9_1$)
483.761	CH$_3$OH	$10_2 - 9_2$	483.761	165.40	4.90e-04	12.16	4.09	0.13	13.30	0.51	16	
484.005	CH$_3$OH	$2_2 - 2_1$	484.005	44.67	4.01e-04						14	
484.023	CH$_3$OH	$10_2 - 9_2$	484.023	149.97	4.83e-04						12	**B**: CH$_3$OH ($10_2 - 9_2$)
484.072	CH$_3$OH	$10_{-2} - 9_{-2}$	484.072	153.63	4.89e-04	11.92	4.25	0.23	11.55	0.94	13	**B**: CH$_3$OH ($2_2 - 2_1$)
485.263	CH$_3$OH	$3_2 - 3_1$	485.263	51.64	5.05e-04	11.74	4.33	0.24	11.16	1.10	16	
485.418	H$_2$Cl$^+$	$1_{1,1,5/2} - 0_{0,0,3/2}$	485.418	23.30	1.59e-03	8.26	2.82	-0.05	8.80	-0.18	11	
486.941	CH$_3$OH	$4_2 - 4_1$	486.941	60.92	5.51e-04	11.57	4.40	0.30	11.29	1.27	16	
487.532	CH$_3$OH	$10_1 - 9_1$	487.532	143.28	5.15e-04	12.02	3.84	0.49	11.94	2.00	17	
489.037	CH$_3$OH	$5_2 - 5_1$	489.037	72.53	5.79e-04	11.90	3.88	0.31	12.29	1.27	17	
489.751	CS	$10 - 9$	489.751	129.29	2.51e-03	11.92	8.28	0.58	12.19	4.34	18	
491.551	CH$_3$OH	$6_2 - 6_1$	491.551	86.46	6.00e-04	11.88	4.65	0.25	12.18	1.11	17	
491.935	SO$_2$	$7_{4,4} - 6_{3,3}$	491.935	65.01	9.49e-04						18	**B**: H$_2$CO ($7_{1,7} - 6_{1,6}$)
491.968	H$_2$CO	$7_{1,7} - 6_{1,6}$	491.968	106.31	3.44e-03						18	**B**: SO$_2$ ($7_{4,4} - 6_{3,3}$)
492.161	C	$1 - 0$	492.161	23.62	7.99e-08	11.90	1.81	2.12	11.88	4.74	18	
492.279	CH$_3$OH	$4_1 - 3_0$	492.279	37.55	3.83e-04	11.69	4.15	0.87	11.77	3.47	17	
493.699	CH$_3$OH	$5_3 - 4_2$	493.699	84.62	6.62e-04	11.67	3.72	0.63	11.93	2.44	14	
493.734	CH$_3$OH	$5_3 - 4_2$	493.734	84.62	6.62e-04	11.59	3.71	0.65	11.69	2.56	15	
494.455	NH$_2$D	$1_{1,0,1} - 0_{0,0,0}$	494.455	23.73	9.95e-04	11.19	2.21	0.20	11.23	0.42	14	
494.482	CH$_3$OH	$7_2 - 7_1$	494.482	102.70	6.18e-04	11.79	5.06	0.26	11.84	1.30	14	
495.173	CH$_3$OH	$7_0 - 6_{-1}$	495.173	78.08	3.21e-04	11.71	3.68	0.51	11.85	1.94	15	
496.924	CH$_3$OH	$14_0 - 13_1$	496.924	256.14	3.26e-04	12.34	4.62	0.10	11.72	0.35	13	
497.828	CH$_3$OH	$8_2 - 8_1$	497.828	121.27	6.36e-04	11.90	4.61	0.24	12.51	1.29	14	
501.589	CH$_3$OH	$9_2 - 9_1$	501.589	142.15	6.54e-04	11.93	3.98	0.20	12.23	0.87	14	
504.294	CH$_3$OH	$7_1 - 6_0$	504.294	86.05	3.53e-04	11.72	4.01	0.50	11.08	2.09	15	
505.565	H$_2$S	$2_{2,1} - 2_{1,2}$	505.565	79.37	2.40e-04	11.29	3.83	0.16	11.39	0.48	16	
505.762	CH$_3$OH	$10_2 - 10_1$	505.762	165.35	6.73e-04	11.95	4.16	0.18	10.08	0.62	18	
505.834	H$_2$CO	$7_{0,7} - 6_{0,6}$	505.834	97.44	3.82e-03	11.75	4.42	0.93	11.51	4.03	18	
506.153	CH$_3$OH	$11_1 - 10_2$	506.153	174.27	2.34e-04	12.05	4.16	0.10	13.58	0.32	18	
506.825	DCN	$7 - 6$	506.825	97.30	6.33e-03	12.04	6.78	0.05	11.91	0.24	15	
509.146	H$_2$CO	$7_{2,6} - 6_{2,5}$	509.146	144.93	3.58e-03	11.70	4.51	0.47	11.94	2.28	16	
509.292	HDO	$1_{1,0} - 1_{0,1}$	509.292	46.76	2.32e-03						16	**B**: H$_2$CO ($7_{6,1} - 6_{6,0}$)

ν GHz (1)	Species (2)	Transition (3)	ν_rest GHz (4)	E_u K (5)	A_{ul} rad/s (6)	v_{lsr} km/s (7)	FWHM km/s (8)	T_{mb} K (9)	v_{lsr} km/s (10)	Flux K km/s (11)	RMS mK (12)	Blend(**B**) / Notes (13)
						Gaussian fit			*from moments*			
509.306	H$_2$CO	$7_{6,1} - 6_{6,0}$	509.306	520.81	1.03e-03						17	**B:** HDO ($1_{1,0} - 1_{0,1}$)
509.306	H$_2$CO	$7_{6,2} - 6_{6,1}$	509.306	520.81	1.03e-03						16	**B:** HDO ($1_{1,0} - 1_{0,1}$)
509.562	H$_2$CO	$7_{5,3} - 6_{5,2}$	509.562	391.84	1.91e-03						17	**B:** H$_2$CO ($7_{5,2} - 6_{5,1}$)
509.562	H$_2$CO	$7_{5,2} - 6_{5,1}$	509.562	391.84	1.91e-03						17	**B:** H$_2$CO ($7_{5,3} - 6_{5,2}$)
509.565	CH$_3$OH	$10_2 - 9_1$	509.565	149.97	4.07e-04						19	**B:** H$_2$CO ($7_{5,3} - 6_{5,2}$)
509.830	H$_2$CO	$7_{4,4} - 6_{4,3}$	509.830	286.17	2.63e-03						17	**B:** H$_2$CO ($7_{4,3} - 6_{4,2}$)
509.830	H$_2$CO	$7_{4,3} - 6_{4,2}$	509.830	286.17	2.63e-03						19	**B:** H$_2$CO ($7_{4,4} - 6_{4,3}$)
510.156	H$_2$CO	$7_{3,5} - 6_{3,4}$	510.156	203.89	3.20e-03	11.88	4.08	0.66	11.94	2.89	16	
510.238	H$_2$CO	$7_{3,4} - 6_{3,3}$	510.238	203.90	3.20e-03	11.93	4.19	0.66	12.41	2.77	16	
510.345	CH$_3$OH	$11_2 - 11_1$	510.345	190.86	6.94e-04	12.02	4.28	0.13	12.13	0.44	15	
512.427	NH$_2$D	$2_{0,2,1} - 1_{1,0,0}$	512.427	47.75	1.57e-04	11.49	3.00	0.10	11.07	0.19	17	
513.076	H$_2$CO	$7_{2,5} - 6_{2,4}$	513.076	145.35	3.66e-03	11.92	4.40	0.47	11.67	2.26	18	
514.853	SO	$12_{11} - 11_{10}$	514.853	167.59	1.82e-03	9.30	12.17	0.08	9.01	0.68	16	
515.170	CH$_3$OH	$16_0 - 15_1$	515.170	315.21	4.10e-04	12.05	4.31	0.29	12.58	1.08	17	
515.335	CH$_3$OH	$12_2 - 12_1$	515.335	218.69	7.16e-04	12.57	5.69	0.11	12.83	0.53	15	
516.335	SO	$12_{12} - 11_{11}$	516.335	174.22	1.83e-03	9.32	7.38	0.08	9.33	0.45	16	
517.354	SO	$12_{13} - 11_{12}$	517.354	165.78	1.86e-03	9.05	12.09	0.08	8.12	0.73	17	
517.970	H^{13}CN	$6 - 5$	517.970	87.01	6.65e-03	12.14	8.87	0.14	13.50	0.96	16	
519.188	SO$_2$	$29_{1,29} - 28_{0,28}$	519.188	379.20	1.91e-03	11.50	12.03	0.03	10.09	0.27	16	
520.179	CH$_3$OH	$2_{-2} - 1_{-1}$	520.179	32.86	9.76e-04	11.78	4.78	0.53	12.21	2.39	17	
520.460	H^{13}CO$^+$	$6 - 5$	520.460	87.43	1.14e-02	11.38	2.42	0.17	12.03	0.45	16	
520.728	CH$_3$OH	$13_2 - 13_1$	520.728	248.84	7.40e-04	11.73	2.85	0.10	10.82	0.49	19	
522.077	ND	$1_{2,3,4} - 0_{1,2,3}$	522.077	25.06	1.07e-03	11.17	10.67	0.04	11.30	0.27	16	
523.274	CH$_3$OH	$14_{-1} - 13_0$	523.274	248.93	6.27e-04	11.91	3.70	0.44	12.40	1.63	18	
523.972	CCH	$6_{13/2,7} - 5_{11/2,6}$	523.972	88.02	4.58e-04						18	**B:** CCH ($6_{13/2,6} - 5_{11/2,5}$)
523.972	CCH	$6_{13/2,6} - 5_{11/2,5}$	523.972	88.02	4.53e-04						17	**B:** CCH ($6_{13/2,7} - 5_{11/2,6}$)
524.003	CH$_3$OH	$15_{-4} - 15_{-3}$	524.003	366.32	1.06e-03	13.46	2.91	0.05	12.75	0.13	16	
524.034	CCH	$6_{11/2,6} - 5_{9/2,5}$	524.034	88.04	4.51e-04						18	**B:** CCH ($6_{11/2,5} - 5_{9/2,4}$)
524.035	CCH	$6_{11/2,5} - 5_{9/2,4}$	524.035	88.04	4.43e-04						18	**B:** CCH ($6_{11/2,6} - 5_{9/2,5}$)
524.269	CH$_3$OH	$13_{-4} - 13_{-3}$	524.269	299.06	7.10e-04	11.27	3.18	0.06	10.40	0.27	16	
524.385	CH$_3$OH	$12_{-4} - 12_{-3}$	524.385	268.91	7.03e-04	11.75	9.29	0.06	12.57	0.30	17	
524.489	CH$_3$OH	$11_{-4} - 11_{-3}$	524.489	241.07	6.94e-04	12.58	5.52	0.07	10.77	0.29	17	
524.666	CH$_3$OH	$9_{-4} - 9_{-3}$	524.666	192.34	6.64e-04	11.60	3.35	0.08	11.36	0.25	16	
524.740	CH$_3$OH	$8_{-4} - 8_{-3}$	524.740	171.46	6.39e-04	12.11	5.90	0.10	11.18	0.46	16	
524.805	CH$_3$OH	$7_{-4} - 7_{-3}$	524.805	152.90	6.03e-04	11.85	4.81	0.11	12.12	0.49	17	
524.861	CH$_3$OH	$6_{-4} - 6_{-3}$	524.861	136.65	5.49e-04	11.79	3.96	0.14	11.19	0.56	15	
524.908	CH$_3$OH	$5_{-4} - 5_{-3}$	524.908	122.72	4.62e-04	12.01	3.85	0.11	11.56	0.40	15	
524.947	CH$_3$OH	$4_{-4} - 4_{-3}$	524.947	111.12	3.08e-04	11.81	4.16	0.08	11.30	0.24	16	
525.666	H$_2$CO	$7_{1,6} - 6_{1,5}$	525.666	112.79	4.20e-03	11.82	4.92	1.45	11.92	7.14	13	
526.039	SH$^+$	$1_{2,3/2} - 0_{1,1/2}$	526.039	25.25	7.99e-04						13	**B:** SH$^+$ ($1_{2,5/2} - 0_{1,3/2}$)
526.048	SH$^+$	$1_{2,5/2} - 0_{1,3/2}$	526.048	25.25	9.59e-04						13	**B:** SH$^+$ ($1_{2,3/2} - 0_{1,1/2}$)
526.520	CH$_3$OH	$14_2 - 14_1$	526.520	281.29	7.66e-04	12.51	5.67	0.08	13.03	0.37	16	
527.053	CH$_3$OH	$11_1 - 10_1$	527.053	166.37	6.54e-04	11.97	3.86	0.38	12.23	1.41	16	
527.171	CH$_3$OH	$15_3 - 15_2$	527.171	326.28	8.92e-04	13.07	4.81	0.05	12.99	0.14	17	
527.658	CH$_3$OH	$14_3 - 14_2$	527.658	291.46	8.88e-04	11.99	8.39	0.06	12.97	0.34	17	

ν GHz (1)	Species (2)	Transition (3)	ν_{rest} GHz (4)	E_u K (5)	A_{ul} rad/s (6)	Gaussian fit v_{lsr} km/s (7)	FWHM km/s (8)	T_{mb} K (9)	from moments v_{lsr} km/s (10)	Flux K km/s (11)	RMS mK (12)	Blend(**B**) / Notes (13)
528.177	CH$_3$OH	$13_3 - 13_2$	528.177	258.96	8.81e-04	12.51	3.74	0.07	10.58	0.24	17	
528.683	CH$_3$OH	$12_3 - 12_2$	528.683	228.78	8.74e-04	12.10	4.01	0.07	14.11	0.25	17	
529.143	CH$_3$OH	$11_3 - 11_2$	529.143	200.92	8.64e-04	12.53	4.11	0.09	11.63	0.37	15	
529.540	CH$_3$OH	$10_3 - 10_2$	529.540	175.39	8.52e-04	12.15	5.06	0.12	13.36	0.48	16	
529.867	CH$_3$OH	$9_3 - 9_2$	529.867	152.17	8.37e-04	12.37	5.20	0.13	12.30	0.64	16	
530.123	CH$_3$OH	$8_3 - 8_2$	530.123	131.28	8.18e-04	11.81	4.89	0.14	12.36	0.63	14	
530.184	CH$_3$OH	$11_0 - 10_0$	530.184	166.05	6.69e-04	12.00	3.72	0.48	11.94	1.80	16	
530.316	CH$_3$OH	$7_3 - 7_2$	530.316	112.71	7.93e-04	12.33	4.76	0.19	12.84	0.74	15	
530.455	CH$_3$OH	$6_3 - 6_2$	530.455	96.46	7.58e-04	12.13	4.78	0.18	11.73	0.78	13	
530.549	CH$_3$OH	$5_3 - 5_2$	530.549	82.53	7.04e-04	12.17	5.77	0.18	11.26	0.91	13	
530.610	CH$_3$OH	$4_3 - 4_2$	530.610	70.93	6.14e-04	12.18	5.04	0.16	11.91	0.79	14	
530.647	CH$_3$OH	$3_3 - 3_2$	530.647	61.64	4.37e-04	12.37	6.05	0.15	12.33	0.78	15	
531.079	CH$_3$OH	$11_{-1} - 10_{-1}$	531.079	158.64	6.69e-04	11.89	3.98	0.85	11.49	3.48	14	
531.319	CH$_3$OH	$11_0 - 10_0$	531.319	153.10	6.75e-04	11.87	4.02	0.91	12.02	3.67	18	
531.636	CH$_3$OH	$11_2 - 10_2$	531.636	190.87	6.58e-04	12.25	4.23	0.18	12.22	0.70	19	
531.716	HCN	$6 - 5$	531.716	89.32	7.20e-03	12.04	9.01	2.47	11.51	21.07	19	
531.772	CH$_3$OH	$11_{-4} - 10_{-4}$	531.772	241.07	8.70e-04	12.56	5.97	0.06	12.06	0.15	17	
531.829	CH$_3$OH	$11_4 - 10_4$	531.829	249.18	8.75e-04	12.27	5.90	0.04	11.80	0.13	18	
531.866	CH$_3$OH	$11_{-3} - 10_{-3}$	531.866	215.90	9.34e-04						17	**B:** CH$_3$OH ($11_3 - 10_3$)
531.869	CH$_3$OH	$11_3 - 10_3$	531.869	202.98	9.27e-04						17	**B:** CH$_3$OH ($11_{-3} - 10_{-3}$)
531.870	CH$_3$OH	$11_4 - 10_4$	531.870	233.52	8.72e-04						16	**B:** CH$_3$OH ($11_{-3} - 10_{-3}$)
531.871	CH$_3$OH	$11_4 - 10_4$	531.871	233.52	8.72e-04						15	**B:** CH$_3$OH ($11_{-3} - 10_{-3}$)
531.893	CH$_3$OH	$11_3 - 10_3$	531.893	202.98	6.26e-04						18	**B:** CH$_3$OH ($11_{-3} - 10_{-3}$)
532.031	CH$_3$OH	$11_1 - 10_1$	532.031	174.27	6.86e-04	11.94	4.00	0.35	11.89	1.37	17	
532.069	CH$_3$OH	$11_3 - 10_3$	532.069	200.92	6.28e-04	11.98	4.38	0.11	11.88	0.48	16	
532.133	CH$_3$OH	$11_2 - 10_2$	532.133	190.94	6.60e-04	11.77	3.68	0.14	11.55	0.45	15	
532.466	CH$_3$OH	$11_2 - 10_2$	532.466	175.53	6.51e-04	12.00	4.14	0.43	12.28	1.75	14	
532.567	CH$_3$OH	$11_{-2} - 10_{-2}$	532.567	179.19	1.18e-03	12.00	3.74	0.23	11.20	0.92	18	
532.707	CH$_3$OH	$15_2 - 15_1$	532.707	316.05	2.07e-04						17	**B:** CH ($^2\Pi\,1_{1,0,3/2,1} - 1_{-1,0,1/2,1}$)
532.722	CH	$^2\Pi\,1_{1,0,3/2,1} - 1_{-1,0,1/2,1}$	532.722	25.73	2.07e-04						19	**B:** CH ($^2\Pi\,1_{1,0,3/2,2} - 1_{-1,0,1/2,1}$)
532.724	CH	$^2\Pi\,1_{1,0,3/2,2} - 1_{-1,0,1/2,1}$	532.724	25.73	6.21e-04						19	**B:** CH ($^2\Pi\,1_{1,0,3/2,1} - 1_{-1,0,1/2,1}$)
535.062	HCO$^+$	$6 - 5$	535.062	89.88	1.25e-02	11.46	3.81	5.05	12.04	22.76	14	
536.191	CH$_3$OH	$11_1 - 10_1$	536.191	169.01	6.89e-04	12.01	4.05	0.56	11.67	2.23	15	
536.761	CH	$^2\Pi\,1_{-1,0,3/2,2} - 1_{1,0,1/2,1}$	536.761	25.76	6.38e-04	12.74	2.48	0.09	11.96	0.21	18	
538.571	CH$_3$OH	$5_1 - 4_0$	538.571	49.06	4.93e-04	11.80	4.47	0.99	11.99	4.19	14	
538.689	CS	$11 - 10$	538.689	155.15	3.35e-03	12.12	9.38	0.49	12.17	4.07	14	
539.282	CH$_3$OH	$16_2 - 16_1$	539.282	353.12	8.24e-04	12.33	4.79	0.04	11.35	0.22	12	
540.922	CH$_3$OH	$15_0 - 14_1$	540.922	290.74	4.21e-04	12.63	4.12	0.10	12.72	0.35	17	
542.001	CH$_3$OH	$6_3 - 5_2$	542.001	98.55	3.99e-04	11.85	3.99	0.66	11.90	2.73	15	
542.082	CH$_3$OH	$6_3 - 5_2$	542.082	98.55	7.93e-04	11.79	3.99	0.65	11.74	2.60	14	
543.076	CH$_3$OH	$8_0 - 7_{-1}$	543.076	96.61	4.54e-04	11.89	3.92	0.55	12.05	2.31	13	
543.898	HNC	$6_{0,0} - 5_{0,0}$	543.898	91.37	8.04e-03	11.54	2.20	0.58	12.39	1.62	14	
546.239	CH$_3$OH	$17_2 - 17_1$	546.239	392.50	1.27e-03	12.06	8.99	0.06	12.49	0.17	16	
547.676	H$_2^{18}$O	$1_{1,0} - 1_{0,1}$	547.676	60.46	3.29e-03	13.69	19.19	0.09	13.78	1.09	19	
548.831	C^{18}O	$5 - 4$	548.831	79.02	1.06e-05	11.34	2.02	1.99	11.39	5.10	16	

ν GHz (1)	Species (2)	Transition (3)	ν_{rest} GHz (4)	E_u K (5)	A_{ul} rad/s (6)	Gaussian fit v_{lsr} km/s (7)	Gaussian fit FWHM km/s (8)	T_{mb} K (9)	from moments v_{lsr} km/s (10)	from moments Flux K km/s (11)	RMS mK (12)	Blend(**B**) / Notes (13)
550.926	^{13}CO	$5-7_0$	550.926	79.33	1.07e-05	11.60	3.09	9.64	11.47	31.33	16	
553.146	CH$_3$OH	$8_1 - 7_0$	553.146	104.62	4.63e-04	11.73	4.20	0.47	11.39	1.82	16	
554.055	CH$_3$OH	$12_1 - 11_2$	554.055	202.12	4.63e-04	12.09	3.28	0.10	13.46	0.41	15	
556.936	H$_2$O	$1_{1,0,0} - 1_{0,1,0}$	556.936	60.96	3.46e-03	11.36	20.54	2.38	11.71	33.72	19	
558.087	SO	$13_{12} - 12_{11}$	558.087	194.37	2.32e-03	9.78	9.17	0.08	9.44	0.59	20	
558.345	CH$_3$OH	$11_2 - 10_1$	558.345	175.53	5.16e-04	12.10	3.66	0.51	11.99	1.76	17	
558.967	N$_2$H$^+$	$6-5$	558.967	93.90	1.16e-02	11.55	2.24	3.02	11.61	7.71	16	
559.319	SO	$13_{13} - 12_{12}$	559.319	201.07	2.34e-03	9.98	5.49	0.07	7.86	0.40	16	
560.178	SO	$13_{14} - 12_{13}$	560.178	192.66	2.37e-03	10.93	11.15	0.07	13.07	0.60	17	
561.712	C^{17}O	$5_{5/2} - 4_{7/2}$	561.712	80.88	1.20e-07	11.18	2.52	0.49	10.33	1.58	15	
561.899	H$_2$CO	$8_{1,8} - 7_{1,7}$	561.899	133.28	5.20e-03	11.98	4.74	1.70	11.90	8.38	37	
566.730	CN	$5_{9/2,11/2} - 4_{7/2,9/2}$	566.730	81.59	1.98e-03						16	**B:** CN ($5_{9/2,7/2} - 4_{7/2,5/2}$)
566.731	CN	$5_{9/2,7/2} - 4_{7/2,5/2}$	566.731	81.59	1.86e-03						16	**B:** CN ($5_{9/2,11/2} - 4_{7/2,9/2}$)
566.731	CN	$5_{9/2,9/2} - 4_{7/2,7/2}$	566.731	81.59	1.88e-03						16	**B:** CN ($5_{9/2,11/2} - 4_{7/2,9/2}$)
566.947	CN	$5_{11/2,11/2} - 4_{9/2,9/2}$	566.947	81.64	1.96e-03						18	**B:** CN ($5_{11/2,13/2} - 4_{9/2,11/2}$)
566.947	CN	$5_{11/2,13/2} - 4_{9/2,11/2}$	566.947	81.64	2.03e-03						24	**B:** CN ($5_{11/2,11/2} - 4_{9/2,9/2}$)
566.947	CN	$5_{11/2,9/2} - 4_{9/2,7/2}$	566.947	81.65	1.95e-03						16	**B:** CN ($5_{11/2,11/2} - 4_{9/2,9/2}$)
568.566	CH$_3$OH	$3_{-2} - 2_{-1}$	568.566	39.83	1.01e-03	11.90	4.96	0.63	12.58	2.87	16	
568.783	CH$_3$OH	$17_0 - 16_1$	568.783	354.54	5.62e-04	12.09	3.84	0.25	11.64	1.00	15	
572.113	^{15}NH$_3$	$1_{0,0} - 0_{0,1}$	572.113	28.00	1.57e-03	12.83	5.76	0.04	11.49	0.15	13	
572.498	o-NH$_3$	$1_{0,0} - 0_{0,1}$	572.498	27.48	1.57e-03	11.79	5.28	2.22	12.31	10.80	14	
572.899	CH$_3$OH	$15_{-1} - 14_0$	572.899	283.64	8.61e-04	12.02	3.92	0.36	11.77	1.55	14	
574.868	CH$_3$OH	$12_1 - 11_1$	574.868	193.96	8.53e-04	12.24	4.44	0.32	12.46	1.48	13	
576.268	CO	$5-4$	576.268	82.98	1.22e-05	11.37	11.91	17.74	10.82	171.01	20	
576.708	H$_2$CO	$8_{0,8} - 7_{0,7}$	576.708	125.12	5.70e-03	11.94	4.76	0.67	12.20	3.32	13	
578.006	CH$_3$OH	$12_0 - 11_0$	578.006	193.79	8.70e-04	12.12	3.90	0.47	11.86	1.87	13	
579.085	CH$_3$OH	$2_2 - 1_1$	579.085	44.67	1.23e-03	11.80	4.71	0.49	12.27	2.15	14	
579.151	CH$_3$OH	$12_{-1} - 11_{-1}$	579.151	186.43	8.72e-04	12.06	3.77	0.88	11.99	3.43	13	
579.201	DCN	$8-7$	579.201	125.10	9.52e-03	12.04	2.93	0.05	12.19	0.11	12	
579.460	CH$_3$OH	$12_0 - 11_0$	579.460	180.91	8.79e-04	11.96	3.98	0.88	11.93	3.47	12	
579.858	CH$_3$OH	$12_2 - 11_2$	579.858	218.69	8.62e-04	12.26	4.67	0.16	12.78	0.80	13	
579.921	CH$_3$OH	$2_2 - 1_1$	579.921	44.67	1.24e-03	11.71	5.07	0.47	11.60	2.31	13	
580.033	CH$_3$OH	$12_{-5} - 11_{-5}$	580.033	305.00	1.08e-03						14	**B:** CH$_3$OH ($12_5 - 11_5$)
580.058	CH$_3$OH	$12_5 - 11_5$	580.058	318.90	1.09e-03						13	**B:** CH$_3$OH ($12_{-5} - 11_{-5}$)
580.058	CH$_3$OH	$12_5 - 11_5$	580.058	318.90	1.09e-03						13	**B:** CH$_3$OH ($12_{-5} - 11_{-5}$)
580.059	CH$_3$OH	$12_{-4} - 11_{-4}$	580.059	268.91	1.16e-03						14	**B:** CH$_3$OH ($12_3 - 11_5$)
580.126	CH$_3$OH	$12_4 - 11_4$	580.126	277.02	1.17e-03						16	**B:** CH$_3$OH ($12_3 - 11_3$)
580.163	CH$_3$OH	$12_{-3} - 11_{-3}$	580.163	243.74	1.23e-03						14	**B:** CH$_3$OH ($12_4 - 11_4$)
580.176	CH$_3$OH	$12_3 - 11_3$	580.176	230.83	1.22e-03						13	**B:** CH$_3$OH ($12_{-3} - 11_{-3}$)
580.195	CH$_3$OH	$12_4 - 11_4$	580.195	261.37	1.16e-03						17	**B:** CH$_3$OH ($12_{-3} - 11_{-3}$)
580.196	CH$_3$OH	$12_4 - 11_4$	580.196	261.37	1.16e-03						16	**B:** CH$_3$OH ($12_{-3} - 11_{-3}$)
580.213	CH$_3$OH	$12_3 - 11_3$	580.213	230.83	1.22e-03						15	**B:** CH$_3$OH ($12_4 - 11_4$)
580.369	CH$_3$OH	$12_1 - 11_1$	580.369	202.12	8.94e-04	12.02	4.16	0.30	12.07	1.33	15	
580.442	CH$_3$OH	$12_3 - 11_3$	580.442	228.78	8.29e-04	11.99	4.51	0.11	12.13	0.37	16	
580.502	CH$_3$OH	$12_2 - 11_2$	580.502	218.80	8.64e-04	12.10	3.95	0.15	12.26	0.54	15	

ν GHz (1)	Species (2)	Transition (3)	ν_{rest} GHz (4)	E_u K (5)	A_{ul} rad/s (6)	*Gaussian fit* v_{lsr} km/s (7)	FWHM km/s (8)	T_{mb} K (9)	*from moments* v_{lsr} km/s (10)	Flux K km/s (11)	RMS mK (12)	Blend(**B**) / Notes (13)
580.903	CH$_3$OH	$12_2 - 11_2$	580.903	203.41	8.53e-04	11.94	4.06	0.44	11.99	1.84	14	
581.092	CH$_3$OH	$12_{-2} - 11_{-2}$	581.092	207.08	8.63e-04	12.02	4.77	0.21	11.21	1.10	15	
581.612	H$_2$CO	$8_{2,7} - 7_{2,6}$	581.612	172.84	5.49e-03	11.83	4.42	0.38	11.74	1.74	16	
581.750	H$_2$CO	$8_{7,2} - 7_{7,1}$	581.750	700.86	1.37e-03						17	**B:** H$_2$CO ($8_{7,1} - 7_{7,0}$)
581.750	H$_2$CO	$8_{7,1} - 7_{7,0}$	581.750	700.86	1.37e-03						17	**B:** H$_2$CO ($8_{7,2} - 7_{7,1}$)
582.071	H$_2$CO	$8_{6,3} - 7_{6,2}$	582.071	548.74	2.57e-03						14	**B:** H$_2$CO ($8_{6,2} - 7_{6,1}$)
582.071	H$_2$CO	$8_{6,2} - 7_{6,1}$	582.071	548.74	2.57e-03						15	**B:** H$_2$CO ($8_{6,3} - 7_{6,2}$)
582.382	H$_2$CO	$8_{5,4} - 7_{5,3}$	582.382	419.79	3.58e-03						15	**B:** H$_2$CO ($8_{5,3} - 7_{5,2}$)
582.382	H$_2$CO	$8_{5,3} - 7_{5,2}$	582.382	419.79	3.58e-03						16	**B:** H$_2$CO ($8_{5,4} - 7_{5,3}$)
582.723	H$_2$CO	$8_{4,5} - 7_{4,4}$	582.723	314.14	4.42e-03						18	**B:** H$_2$CO ($8_{4,4} - 7_{4,3}$)
582.724	H$_2$CO	$8_{4,4} - 7_{4,3}$	582.724	314.14	4.42e-03						18	**B:** H$_2$CO ($8_{4,5} - 7_{4,4}$)
583.145	H$_2$CO	$8_{3,6} - 7_{3,5}$	583.145	231.88	5.07e-03	12.02	4.38	0.56	12.39	2.60	16	
583.309	H$_2$CO	$8_{3,5} - 7_{3,4}$	583.309	231.89	5.08e-03	11.96	4.60	0.56	12.08	2.70	17	
584.147	CH$_3$OH	$16_0 - 15_1$	584.147	327.63	7.81e-04	12.51	4.52	0.09	10.74	0.32	17	
584.450	CH$_3$OH	$6_1 - 5_0$	584.450	62.87	6.25e-04	11.98	4.28	1.15	11.88	4.59	16	
584.822	CH$_3$OH	$12_1 - 11_1$	584.822	197.08	8.98e-04	12.03	4.09	0.51	11.99	2.22	18	
587.454	H$_2$CO	$8_{2,6} - 7_{2,5}$	587.454	173.55	5.66e-03	11.96	4.35	0.36	11.95	1.68	16	
587.616	CS	$12 - 11$	587.616	183.35	4.36e-03	12.10	10.32	0.39	12.39	3.75	17	
590.278	CH$_3$OH	$7_3 - 6_2$	590.278	114.79	9.50e-04	11.78	4.08	0.67	12.06	2.52	16	
590.440	CH$_3$OH	$7_3 - 6_2$	590.440	114.79	9.50e-04	11.84	4.13	0.66	11.66	2.67	15	
590.791	CH$_3$OH	$9_0 - 8_{-1}$	590.791	117.46	6.23e-04	12.01	4.15	0.61	11.89	2.54	16	
599.927	HDO	$2_{1,1} - 2_{0,2}$	599.927	95.23	3.45e-03	12.03	5.05	0.07	11.12	0.25	15	
600.331	H$_2$CO	$8_{1,7} - 7_{1,6}$	600.331	141.61	6.34e-03	12.00	5.14	1.20	12.18	6.12	17	
601.258	SO	$14_{13} - 13_{12}$	601.258	223.23	2.92e-03	7.39	11.75	0.06	7.14	0.36	17	
601.849	CH$_3$OH	$13_1 - 12_2$	601.849	232.29	4.07e-04	11.91	5.35	0.13	12.37	0.58	15	
602.233	CH$_3$OH	$9_1 - 8_0$	602.233	125.52	5.95e-04	11.86	3.84	0.45	12.05	1.68	19	
602.292	SO	$14_{14} - 13_{13}$	602.292	229.97	2.93e-03	9.58	8.56	0.06	11.27	0.27	17	
603.021	SO	$14_{15} - 13_{14}$	603.021	221.61	2.96e-03	8.39	9.41	0.05	8.02	0.32	14	
604.268	H^{13}CN	$7 - 6$	604.268	116.01	1.07e-02	13.24	11.10	0.09	13.59	0.62	16	
607.175	H^{13}CO$^+$	$7 - 6$	607.175	116.57	1.84e-02	11.48	2.07	0.11	12.24	0.24	17	
607.216	CH$_3$OH	$12_2 - 11_1$	607.216	203.41	6.42e-04	12.07	3.75	0.39	12.65	1.43	16	
611.267	CCH	$7_{15/2,7} - 6_{13/2,6}$	611.267	117.35	7.29e-04						15	**B:** CCH ($7_{15/2,8} - 6_{13/2,7}$)
611.267	CCH	$7_{15/2,8} - 6_{13/2,7}$	611.267	117.36	7.36e-04						15	**B:** CCH ($7_{15/2,7} - 6_{13/2,6}$)
611.330	CCH	$7_{13/2,7} - 6_{11/2,6}$	611.330	117.38	7.27e-04						16	**B:** CCH ($7_{13/2,6} - 6_{11/2,5}$)
611.330	CCH	$7_{13/2,6} - 6_{11/2,5}$	611.330	117.38	7.18e-04						15	**B:** CCH ($7_{13/2,7} - 6_{11/2,6}$)
616.980	CH$_3$OH	$4_{-2} - 3_{-1}$	616.980	49.12	1.11e-03	12.00	5.09	0.66	12.37	3.16	12	
620.304	HCN	$7 - 6$	620.304	119.09	1.16e-02	12.26	10.13	2.15	11.88	21.23	12	
622.568	CH$_3$OH	$18_0 - 17_1$	622.568	396.17	7.52e-04	12.22	4.98	0.21	13.18	1.07	14	
622.659	CH$_3$OH	$13_1 - 12_1$	622.659	223.85	1.09e-03	12.33	4.62	0.34	12.42	1.57	14	
622.774	CH$_3$OH	$16_{-1} - 15_0$	622.774	320.63	1.16e-03	12.16	4.18	0.34	12.78	1.50	15	
624.208	HCO$^+$	$7 - 6$	624.208	119.84	2.01e-02	11.36	4.32	4.10	11.75	21.10	16	
624.964	H^{37}Cl	$1_{3/2} - 0_{3/2}$	624.964	29.99	1.16e-03						15	**B:** H^{37}Cl ($1_{5/2} - 0_{3/2}$)
624.978	H^{37}Cl	$1_{5/2} - 0_{3/2}$	624.978	29.99	1.16e-03						14	**B:** H^{37}Cl ($1_{3/2} - 0_{3/2}$)
624.988	H^{37}Cl	$1_{1/2} - 0_{3/2}$	624.988	30.00	1.16e-03						15	**B:** H^{37}Cl ($1_{5/2} - 0_{3/2}$)
625.749	CH$_3$OH	$13_0 - 12_0$	625.749	223.82	1.11e-03	12.14	3.79	0.43	12.00	1.58	15	

ν GHz	Species	Transition	ν_rest GHz	E_u K	A_{ul} rad/s	Gaussian fit		T_{mb} K	from moments		RMS mK	Blend(**B**) / Notes
						v_{lsr} km/s	FWHM km/s		v_{lsr} km/s	Flux K km/s		
(1)	(2)	(3)	(4)	(5)	(6)	(7)	(8)	(9)	(10)	(11)	(12)	(13)
625.902	HCl	$1_{3/2} - 0_{3/2}$	625.902	30.04	1.17e-03						13	**B:** HCl $(1_{5/2} - 0_{3/2})$
625.919	HCl	$1_{5/2} - 0_{3/2}$	625.919	30.04	1.17e-03						15	**B:** HCl $(1_{3/2} - 0_{3/2})$
625.932	HCl	$1_{1/2} - 0_{3/2}$	625.932	30.04	1.17e-03						14	**B:** HCl $(1_{3/2} - 0_{3/2})$
626.555	CH$_3$OH	$17_0 - 16_1$	626.555	366.79	9.51e-04						15	**B:** CH$_3$OH $(13_4 - 12_4)$
626.555	CH$_3$OH	$13_4 - 12_4$	626.555	573.97	1.49e-03						15	**B:** CH$_3$OH $(17_0 - 16_1)$
626.626	CH$_3$OH	$3_2 - 2_1$	626.626	51.64	1.23e-03	11.70	4.87	0.56	11.70	2.52	19	
627.170	CH$_3$OH	$13_{-1} - 12_{-1}$	627.170	216.53	1.11e-03	12.04	4.14	0.73	12.40	3.24	15	
627.558	CH$_3$OH	$13_0 - 12_0$	627.558	211.03	1.12e-03	11.97	4.14	0.76	12.25	3.17	14	
628.052	CH$_3$OH	$13_2 - 12_2$	628.052	248.84	1.10e-03	12.15	4.73	0.16	13.01	0.64	15	
628.330	CH$_3$OH	$13_{-4} - 12_{-4}$	628.330	299.06	1.51e-03	11.72	2.69	0.08	13.04	0.40	13	
628.409	CH$_3$OH	$13_4 - 12_4$	628.409	307.18	1.51e-03	12.42	3.89	0.04	13.17	0.10	14	
628.445	CH$_3$OH	$13_{-3} - 12_{-3}$	628.445	273.90	1.59e-03						14	**B:** CH$_3$OH $(13_3 - 12_3)$
628.470	CH$_3$OH	$13_3 - 12_3$	628.470	260.99	1.06e-03						13	**B:** CH$_3$OH $(13_{-3} - 12_{-3})$
628.470	CH$_3$OH	$13_3 - 12_3$	628.470	260.99	1.58e-03						14	**B:** CH$_3$OH $(13_{-3} - 12_{-3})$
628.512	CH$_3$OH	$13_4 - 12_4$	628.512	291.53	1.51e-03						14	**B:** CH$_3$OH $(13_4 - 12_4)$
628.513	CH$_3$OH	$13_4 - 12_4$	628.513	291.53	1.51e-03						13	**B:** CH$_3$OH $(13_4 - 12_4)$
628.525	CH$_3$OH	$13_4 - 12_3$	628.525	261.00	1.58e-03						13	**B:** CH$_3$OH $(13_4 - 12_4)$
628.696	CH$_3$OH	$13_1 - 12_1$	628.696	232.29	1.14e-03	12.12	4.12	0.29	12.42	1.15	14	
628.816	CH$_3$OH	$13_3 - 12_3$	628.816	258.96	1.07e-03	12.39	6.48	0.09	12.92	0.46	13	
628.869	CH$_3$OH	$13_2 - 12_2$	628.869	248.98	1.11e-03	12.04	4.66	0.14	11.79	0.62	14	
629.140	CH$_3$OH	$3_2 - 2_1$	629.140	51.64	1.25e-03	11.73	4.26	0.58	11.67	2.35	17	
629.322	CH$_3$OH	$13_2 - 12_2$	629.322	233.61	1.09e-03	12.05	4.25	0.41	12.44	1.68	17	
629.652	CH$_3$OH	$13_{-2} - 12_{-2}$	629.652	237.30	1.11e-03	12.20	4.84	0.19	12.65	0.90	16	
629.921	CH$_3$OH	$7_1 - 6_0$	629.921	78.97	7.78e-04	12.02	4.18	1.19	12.10	4.96	16	
631.703	H$_2$CO	$9_{1,9} - 8_{1,8}$	631.703	163.60	7.46e-03	11.95	4.86	0.96	11.85	4.96	44	
633.423	CH$_3$OH	$13_1 - 12_1$	633.423	227.48	1.15e-03	12.29	3.68	0.43	12.73	1.66	43	
634.511	HNC	$7_{0,0} - 6_{0,0}$	634.511	121.82	1.29e-02	11.66	2.95	0.15	14.11	0.42	33	
636.193	CH$_3$OH	$16_4 - 16_3$	636.193	395.93	2.23e-03						31	**B:** CH$_3$OH $(13_4 - 13_3)$
636.197	CH$_3$OH	$13_4 - 13_3$	636.197	291.53	2.14e-03						32	**B:** CH$_3$OH $(16_4 - 16_3)$
636.199	CH$_3$OH	$17_4 - 17_3$	636.199	435.37	2.25e-03						31	**B:** CH$_3$OH $(16_4 - 16_3)$
636.274	CH$_3$OH	$9_4 - 9_3$	636.274	184.79	1.95e-03						35	**B:** CH$_3$OH $(10_4 - 10_3)$
636.279	CH$_3$OH	$10_4 - 10_3$	636.279	207.99	2.02e-03						31	**B:** CH$_3$OH $(9_4 - 9_3)$
636.281	CH$_3$OH	$11_4 - 11_3$	636.281	233.52	2.07e-03						30	**B:** CH$_3$OH $(9_4 - 9_3)$
636.291	CH$_3$OH	$9_4 - 9_3$	636.291	184.79	1.96e-03						31	**B:** CH$_3$OH $(9_4 - 9_3)$
636.299	CH$_3$OH	$12_4 - 12_3$	636.299	261.36	2.11e-03						32	**B:** CH$_3$OH $(9_4 - 9_3)$
636.303	CH$_3$OH	$8_4 - 8_3$	636.303	163.90	1.87e-03						31	**B:** CH$_3$OH $(9_4 - 9_3)$
636.312	CH$_3$OH	$8_4 - 8_3$	636.312	163.90	1.87e-03						31	**B:** CH$_3$OH $(9_4 - 9_3)$
636.334	CH$_3$OH	$7_4 - 7_3$	636.334	145.33	1.76e-03						27	**B:** CH$_3$OH $(8_4 - 8_3)$
636.337	CH$_3$OH	$7_4 - 7_3$	636.337	145.33	1.76e-03						33	**B:** CH$_3$OH $(8_4 - 8_3)$
636.364	CH$_3$OH	$6_4 - 6_3$	636.364	129.09	1.60e-03						37	**B:** CH$_3$OH $(6_4 - 6_3)$
636.366	CH$_3$OH	$6_4 - 6_3$	636.366	129.09	1.60e-03						37	**B:** CH$_3$OH $(7_4 - 7_3)$
636.393	CH$_3$OH	$5_4 - 5_3$	636.393	115.16	1.34e-03						31	**B:** CH$_3$OH $(6_4 - 6_3)$
636.394	CH$_3$OH	$5_4 - 5_3$	636.394	115.16	1.34e-03						34	**B:** CH$_3$OH $(6_4 - 6_3)$
636.523	CH$_3$OH	$15_4 - 15_3$	636.523	358.81	2.21e-03						35	**B:** CS $(13 - 12)$
636.532	CS	$13 - 12$	636.532	213.90	5.56e-03						35	**B:** CH$_3$OH $(15_4 - 15_3)$

ν GHz (1)	Species (2)	Transition (3)	ν_{rest} GHz (4)	E_u K (5)	A_{ul} rad/s (6)	Gaussian fit v_{lsr} km/s (7)	FWHM km/s (8)	T_{mb} K (9)	from moments v_{lsr} km/s (10)	Flux K km/s (11)	RMS mK (12)	Blend(**B**) / Notes (13)
638.280	CH_3OH	$10_0 - 9_{-1}$	638.280	140.60	8.35e−04	12.26	3.96	0.51	13.03	2.05	42	
638.524	CH_3OH	$8_3 - 7_2$	638.524	133.36	1.13e−03	11.97	3.93	0.60	11.28	2.45	41	
638.818	CH_3OH	$8_3 - 7_2$	638.818	133.36	1.13e−03	11.98	3.91	0.68	11.14	2.80	35	
645.254	SO	$15_{15} - 14_{14}$	645.254	260.94	3.62e−03	11.61	9.64	0.09	11.15	0.36	36	
645.875	SO	$15_{16} - 14_{15}$	645.875	252.60	3.65e−03	8.79	6.64	0.14	10.00	0.43	34	
647.082	H_2CO	$9_{0,9} - 8_{0,8}$	647.082	156.18	8.10e−03	11.80	4.91	0.63	11.69	3.10	28	
649.540	CH_3OH	$14_1 - 13_2$	649.540	264.78	5.20e−04						27	**B:** CH_3OH ($14_1 - 13_2$)
649.540	CH_3OH	$14_1 - 13_2$	649.540	264.78	7.71e−04						26	**B:** CH_3OH ($14_1 - 13_2$)
651.617	CH_3OH	$10_1 - 9_0$	651.617	148.73	7.51e−04	11.87	4.46	0.43	11.96	1.93	25	
652.096	N_2H^+	$7 - 6$	652.096	125.19	1.87e−02	11.49	2.24	2.34	11.72	5.79	30	
653.970	H_2CO	$9_{2,8} - 8_{2,7}$	653.970	204.23	7.96e−03	11.95	3.88	0.37	12.01	1.58	31	
654.463	H_2CO	$9_{7,3} - 8_{7,2}$	654.463	732.27	3.32e−03						32	**B:** H_2CO ($9_{7,2} - 8_{7,1}$)
654.463	H_2CO	$9_{7,2} - 8_{7,1}$	654.463	732.27	3.32e−03						32	**B:** H_2CO ($9_{7,3} - 8_{7,2}$)
655.212	H_2CO	$9_{5,5} - 8_{5,4}$	655.212	451.24	5.83e−03						31	**B:** H_2CO ($9_{5,4} - 8_{5,3}$)
655.212	H_2CO	$9_{5,4} - 8_{5,3}$	655.212	451.24	5.83e−03						30	**B:** H_2CO ($9_{5,5} - 8_{5,4}$)
655.640	H_2CO	$9_{4,6} - 8_{4,5}$	655.640	345.60	6.77e−03						28	**B:** H_2CO ($9_{4,5} - 8_{4,4}$)
655.644	H_2CO	$9_{4,5} - 8_{4,4}$	655.644	345.60	6.77e−03						28	**B:** H_2CO ($9_{4,6} - 8_{4,5}$)
656.165	H_2CO	$9_{3,7} - 8_{3,6}$	656.165	263.37	7.52e−03						30	**B:** CH_3OH ($13_2 - 12_1$)
656.169	CH_3OH	$13_2 - 12_1$	656.169	233.61	7.87e−04						30	**B:** H_2CO ($9_{3,7} - 8_{3,6}$)
656.465	H_2CO	$9_{3,6} - 8_{3,5}$	656.465	263.40	7.53e−03	11.85	4.78	0.52	11.51	2.34	29	
658.553	$C^{18}O$	$6 - 5$	658.553	110.63	1.86e−05	11.39	2.22	1.23	11.65	3.46	27	
661.067	^{13}CO	$6 - 5$	661.067	111.05	1.88e−05	11.54	3.22	7.72	11.39	28.65	28	
662.209	H_2CO	$9_{2,7} - 8_{2,6}$	662.209	205.33	8.27e−03	12.09	5.29	0.27	12.39	1.39	26	
665.442	CH_3OH	$5_{-2} - 4_{-1}$	665.442	60.73	1.27e−03	12.00	4.91	0.77	12.10	3.66	30	
668.117	CH_3OH	$18_0 - 17_1$	668.117	408.23	7.64e−04	12.54	3.67	0.09	12.89	0.25	25	
670.423	CH_3OH	$14_1 - 13_1$	670.423	256.02	1.36e−03	12.04	4.71	0.28	12.26	1.35	29	
672.903	CH_3OH	$17_{-1} - 16_0$	672.903	359.92	1.53e−03	12.10	4.25	0.31	11.80	1.32	29	
673.416	CH_3OH	$14_0 - 13_0$	673.416	256.11	1.38e−03	12.32	4.69	0.33	12.88	1.52	28	
673.746	CH_3OH	$4_2 - 3_1$	673.746	60.92	1.34e−04	11.70	4.62	0.62	11.40	2.91	30	
674.009	$C^{17}O$	$6_{7/2} - 5_{9/2}$	674.009	113.23	8.37e−08						32	**B:** CH_3OH ($14_1 - 13_1$)
674.017	CH_3OH	$14_1 - 13_1$	674.017	568.00	2.06e−03						32	**B:** $C^{17}O$ ($6_{7/2} - 5_{9/2}$)
674.791	CH_3OH	$14_2 - 13_2$	674.791	541.67	2.02e−03						31	**B:** H_2CO ($9_{1,8} - 8_{1,7}$)
674.810	H_2CO	$9_{1,8} - 8_{1,7}$	674.810	173.99	9.09e−03						32	**B:** CH_3OH ($14_2 - 13_2$)
674.991	CH_3OH	$8_1 - 7_0$	674.991	97.38	9.56e−04	12.09	4.69	1.22	11.80	5.55	33	
675.135	CH_3OH	$14_{-1} - 13_{-1}$	675.135	248.94	1.39e−03	12.13	4.25	0.69	12.11	2.97	31	
675.613	CH_3OH	$14_0 - 13_0$	675.613	243.45	1.40e−03	12.23	4.23	0.70	12.10	3.07	29	
675.773	CH_3OH	$3_3 - 2_2$	675.773	61.64	2.56e−03	12.35	5.22	0.51	19.36	1.54	33	
676.215	CH_3OH	$14_2 - 13_2$	676.215	281.29	1.38e−03	12.08	6.04	0.14	13.24	0.65	31	
676.495	CH_3OH	$14_5 - 13_5$	676.495	379.68	1.23e−03						32	**B:** CH_3OH ($19_0 - 18_1$)
676.499	CH_3OH	$19_0 - 18_1$	676.499	440.09	9.84e−04						34	**B:** CH_3OH ($14_5 - 13_5$)
676.585	CH_3OH	$14_{-4} - 13_{-4}$	676.585	331.54	1.29e−03	12.42	4.24	0.11	12.55	0.40	31	
676.749	CH_3OH	$14_3 - 13_3$	676.749	293.47	1.34e−03	12.17	4.18	0.15	11.66	0.48	28	
676.822	CH_3OH	$14_4 - 13_4$	676.822	324.01	1.30e−03						31	**B:** CH_3OH ($14_4 - 13_4$)
676.824	CH_3OH	$14_4 - 13_4$	676.824	324.01	1.30e−03						31	**B:** CH_3OH ($14_4 - 13_4$)
676.830	CH_3OH	$14_3 - 13_3$	676.830	293.48	1.34e−03						30	**B:** CH_3OH ($14_4 - 13_4$)

ν GHz (1)	Species (2)	Transition (3)	ν_{rest} GHz (4)	E_u K (5)	A_{ul} rad/s (6)	Gaussian fit v_{lsr} km/s (7)	FWHM km/s (8)	T_{mb} K (9)	from moments v_{lsr} km/s (10)	Flux K km/s (11)	RMS mK (12)	Blend(**B**) / Notes (13)
677.013	CH$_3$OH	$14_1 - 13_1$	677.013	264.78	1.43e-03	12.19	4.25	0.24	11.36	0.93	31	
677.191	CH$_3$OH	$14_3 - 13_3$	677.191	291.46	1.35e-03						29	**B:** CH$_3$OH $(14_2 - 13_2)$
677.233	CH$_3$OH	$14_2 - 13_2$	677.233	281.49	1.39e-03						26	**B:** CH$_3$OH $(14_3 - 13_3)$
677.710	CH$_3$OH	$14_2 - 13_2$	677.710	266.14	1.37e-03	12.17	4.09	0.37	12.40	1.53	46	
678.253	CH$_3$OH	$14_{-2} - 13_{-2}$	678.253	269.85	1.39e-03	12.09	6.15	0.27	13.01	1.13	29	
678.785	CH$_3$OH	$4_2 - 3_1$	678.785	60.93	1.37e-03	11.90	4.52	0.65	11.94	2.78	27	
680.047	CN	$6_{11/2,13/2} - 5_{9/2,11/2}$	680.047	114.23	3.50e-03						31	**B:** CN $(6_{11/2,9/2} - 5_{9/2,7/2})$
680.047	CN	$6_{11/2,9/2} - 5_{9/2,7/2}$	680.047	114.22	3.36e-03						31	**B:** CN $(6_{11/2,13/2} - 5_{9/2,11/2})$
680.047	CN	$6_{11/2,11/2} - 5_{9/2,9/2}$	680.047	114.22	3.38e-03						31	**B:** CN $(6_{11/2,13/2} - 5_{9/2,11/2})$
680.264	CN	$6_{13/2,13/2} - 5_{11/2,11/2}$	680.264	114.29	3.47e-03						31	**B:** CN $(6_{13/2,15/2} - 5_{11/2,13/2})$
680.264	CN	$6_{13/2,15/2} - 5_{11/2,13/2}$	680.264	114.29	3.56e-03						30	**B:** CN $(6_{13/2,11/2} - 5_{11/2,11/2})$
680.264	CN	$6_{13/2,11/2} - 5_{11/2,9/2}$	680.264	114.29	3.46e-03						31	**B:** CN $(6_{13/2,13/2} - 5_{11/2,11/2})$
681.990	CH$_3$OH	$14_1 - 13_1$	681.990	260.21	1.43e-03	12.32	4.86	0.44	12.23	2.06	29	
685.435	CS	$14 - 13$	685.435	246.79	6.96e-03						31	**B:** CH$_3$OH $(11_0 - 10_{-1})$
685.505	CH$_3$OH	$11_0 - 10_{-1}$	685.505	166.05	1.10e-03						29	**B:** CS $(14 - 13)$
686.732	CH$_3$OH	$9_3 - 8_2$	686.732	154.25	1.34e-03	12.10	4.16	0.59	12.21	2.44	30	
687.225	CH$_3$OH	$9_3 - 8_2$	687.225	154.25	1.34e-03	11.83	4.45	0.59	12.02	2.42	31	
687.303	H$_2$S	$2_{0,2} - 1_{1,1}$	687.303	54.70	9.32e-04	11.64	3.82	0.44	12.38	1.59	36	
691.473	CO	$6 - 5$	691.473	116.16	2.14e-05	11.30	13.00	22.13	11.03	204.50	31	
697.146	CH$_3$OH	$15_1 - 14_2$	697.146	299.59	6.56e-04	11.37	1.86	0.16	12.21	0.25	37	
698.545	CCH	$8_{17/2,8} - 7_{15/2,7}$	698.545	150.88	1.10e-03						33	**B:** CCH $(8_{17/2,9} - 7_{15/2,8})$
698.545	CCH	$8_{17/2,9} - 7_{15/2,8}$	698.545	150.88	1.11e-03						31	**B:** CCH $(8_{17/2,8} - 7_{15/2,7})$
698.607	CCH	$8_{15/2,8} - 7_{13/2,7}$	698.607	150.91	1.10e-03						34	**B:** CCH $(8_{17/2,8} - 7_{15/2,7})$
698.607	CCH	$8_{15/2,7} - 7_{13/2,6}$	698.607	150.91	1.09e-03						33	**B:** CCH $(8_{17/2,8} - 7_{15/2,7})$
701.367	CH$_3$OH	$11_1 - 10_0$	701.367	174.27	9.33e-04						29	**B:** H$_2$CO $(10_{1,10} - 9_{1,9})$
701.370	H$_2$CO	$10_{1,10} - 9_{1,9}$	701.370	197.26	1.03e-02						31	**B:** CH$_3$OH $(11_1 - 10_0)$
705.182	CH$_3$OH	$14_2 - 13_1$	705.182	266.14	9.56e-04	12.09	4.56	0.29	11.77	1.18	33	
708.877	HCN	$8 - 7$	708.877	153.11	1.74e-02	12.37	11.01	1.74	11.57	18.75	42	
713.341	HCO$^+$	$8 - 7$	713.341	154.07	3.02e-02	11.35	4.79	2.98	11.87	16.69	33	
713.982	CH$_3$OH	$6_{-2} - 5_{-1}$	713.982	74.66	1.45e-03	11.85	4.81	0.67	11.56	2.92	39	
716.938	H$_2$CO	$10_{0,10} - 9_{0,9}$	716.938	190.58	1.11e-02	11.97	3.99	0.34	12.04	1.38	48	
718.159	CH$_3$OH	$15_1 - 14_1$	718.159	290.49	1.68e-03	12.46	4.35	0.19	12.04	0.78	43	
718.436	CH$_3$OH	$4_{-4} - 3_{-3}$	718.436	111.12	3.06e-03	11.75	4.56	0.43	11.60	1.90	40	
719.665	CH$_3$OH	$9_1 - 8_0$	719.665	118.08	1.16e-03	12.17	4.46	1.20	12.32	5.38	27	
720.441	CH$_3$OH	$5_2 - 4_1$	720.441	72.53	1.50e-03	11.92	4.90	0.69	12.36	3.49	32	
721.011	CH$_3$OH	$15_0 - 14_0$	721.011	290.74	1.70e-03	12.60	4.61	0.33	12.89	1.23	26	
723.040	CH$_3$OH	$15_{-1} - 14_{-1}$	723.040	283.64	1.71e-03	12.21	4.25	0.57	12.01	2.50	28	
723.280	CH$_3$OH	$18_{-1} - 17_0$	723.280	401.50	1.98e-03	12.48	5.37	0.25	13.39	1.08	30	
723.619	CH$_3$OH	$15_0 - 14_0$	723.619	278.18	1.72e-03	12.13	4.27	0.62	11.70	2.52	31	
724.122	CH$_3$OH	$4_3 - 3_2$	724.122	70.93	2.56e-03	12.26	5.38	0.55	12.55	2.77	31	
724.345	CH$_3$OH	$15_2 - 14_2$	724.345	316.05	1.71e-03	12.26	5.00	0.14	11.30	0.51	34	
725.013	CH$_3$OH	$15_3 - 14_3$	725.013	328.26	2.47e-03	12.67	5.12	0.13	12.85	0.36	34	
725.122	CH$_3$OH	$15_4 - 14_4$	725.122	358.81	2.39e-03						31	**B:** CH$_3$OH $(15_4 - 14_4)$
725.126	CH$_3$OH	$15_4 - 14_4$	725.126	358.81	2.39e-03						31	**B:** CH$_3$OH $(15_4 - 14_4)$

ν GHz	Species	Transition	ν_{rest} GHz	E_u K	A_{ul} rad/s	Gaussian fit v_{lsr} km/s	FWHM km/s	T_{mb} K	from moments v_{lsr} km/s	Flux K km/s	RMS mK	Blend(**B**) / Notes
(1)	(2)	(3)	(4)	(5)	(6)	(7)	(8)	(9)	(10)	(11)	(12)	(13)
725.126	CH$_3$OH	$15_3 - 14_3$	725.126	328.28	2.47e-03						31	**B:** CH$_3$OH $(15_4 - 14_4)$
725.316	CH$_3$OH	$15_1 - 14_1$	725.316	299.59	1.76e-03	12.15	3.98	0.23	12.21	0.72	32	
725.565	CH$_3$OH	$15_3 - 14_3$	725.565	326.28	2.48e-03						24	**B:** CH$_3$OH $(15_2 - 14_2)$
725.594	CH$_3$OH	$15_2 - 14_2$	725.594	316.31	1.72e-03						26	**B:** CH$_3$OH $(15_3 - 14_3)$
726.052	CH$_3$OH	$15_2 - 14_2$	726.052	300.98	1.70e-03	12.47	4.62	0.35	12.13	1.53	28	
726.208	H$_2$CO	$10_{2,9} - 9_{2,8}$	726.208	239.08	1.11e-02	12.23	5.16	0.20	12.65	0.86	29	
726.899	CH$_3$OH	$15_{-2} - 14_{-2}$	726.899	304.74	1.72e-03	12.11	4.34	0.15	13.64	0.44	32	
728.054	H$_2$CO	$10_{5,6} - 9_{5,5}$	728.054	486.18	8.72e-03						25	**B:** H$_2$CO $(10_{5,5} - 9_{5,4})$
728.054	H$_2$CO	$10_{5,5} - 9_{5,4}$	728.054	486.18	8.72e-03						26	**B:** H$_2$CO $(10_{5,6} - 9_{5,5})$
728.583	H$_2$CO	$10_{4,7} - 9_{4,6}$	728.583	380.57	9.78e-03						25	**B:** H$_2$CO $(10_{4,6} - 9_{4,5})$
728.592	H$_2$CO	$10_{4,6} - 9_{4,5}$	728.592	380.57	9.78e-03						25	**B:** H$_2$CO $(10_{4,7} - 9_{4,6})$
728.862	CH$_3$OH	$5_2 - 4_1$	728.862	72.53	1.55e-03	11.82	4.85	0.71	12.68	3.20	28	
729.213	H$_2$CO	$10_{3,8} - 9_{3,7}$	729.213	298.36	1.06e-02	12.14	5.10	0.33	13.15	1.48	24	
729.725	H$_2$CO	$10_{3,7} - 9_{3,6}$	729.725	298.42	1.06e-02	12.05	4.21	0.35	12.11	1.56	25	
730.520	CH$_3$OH	$15_1 - 14_1$	730.520	295.27	1.77e-03						28	**B:** CH$_3$OH $(20_0 - 19_1)$
730.550	CH$_3$OH	$20_0 - 19_1$	730.550	486.30	1.26e-03						26	**B:** CH$_3$OH $(15_1 - 14_1)$
731.596	SO	$17_{18} - 16_{17}$	731.596	320.77	5.32e-03	8.98	8.66	0.07	9.29	0.33	24	
732.432	CH$_3$OH	$12_0 - 11_{-1}$	732.432	193.79	1.42e-03	12.21	4.38	0.51	12.59	2.33	28	
734.324	CS	$15 - 14$	734.324	282.04	8.58e-03	11.44	11.05	0.19	11.48	1.90	26	
734.894	CH$_3$OH	$10_3 - 9_2$	734.894	177.46	1.58e-03	11.88	5.03	0.53	12.02	2.50	25	
735.673	CH$_3$OH	$10_3 - 9_2$	735.673	177.46	1.58e-03	12.06	4.47	0.54	11.70	2.22	25	
736.034	H$_2$S	$2_{1,2} - 1_{0,1}$	736.034	55.10	1.33e-03	11.65	5.27	1.07	12.04	5.30	29	
737.343	H$_2$CO	$10_{2,8} - 9_{2,7}$	737.343	240.72	1.16e-02	11.84	4.94	0.25	11.65	1.01	26	
745.210	N$_2$H$^+$	$8 - 7$	745.210	160.96	2.81e-02	11.51	2.60	1.49	11.65	4.09	32	
749.072	H$_2$CO	$10_{1,9} - 9_{1,8}$	749.072	209.94	1.25e-02	12.06	5.59	0.66	12.47	3.49	36	
751.551	CH$_3$OH	$12_1 - 11_0$	751.551	202.12	1.14e-03	12.16	4.38	0.40	12.56	1.61	35	
752.312	CH$_3$OH	$7_{-5} - 7_{-4}$	752.312	189.00	2.35e-03	12.23	7.29	0.10	11.84	0.37	41	
754.222	CH$_3$OH	$15_2 - 14_1$	754.222	300.98	1.15e-03	12.14	3.83	0.25	10.93	1.02	36	
762.636	H$_2$CO	$7_{-2} - 6_{-1}$	762.636	90.91	1.66e-03	12.04	4.96	0.69	11.37	2.99	38	
762.676	CH$_3$OH	$13_{-3} - 13_{-2}$	762.676	273.90	2.31e-03	12.03	4.79	0.11	12.56	0.31	39	
763.883	CH$_3$OH	$12_{-3} - 12_{-2}$	763.883	243.74	2.32e-03	12.67	2.80	0.14	12.74	0.44	33	
763.951	CH$_3$OH	$8_5 - 9_4$	763.951	221.45	4.87e-04						38	**B:** CH$_3$OH $(8_5 - 9_4)$
763.951	CH$_3$OH	$8_5 - 9_4$	763.951	221.45	4.87e-04						40	**B:** CH$_3$OH $(8_5 - 9_4)$
763.953	CH$_3$OH	$10_1 - 9_0$	763.953	141.08	1.39e-03						40	**B:** CH$_3$OH $(8_5 - 9_4)$
764.812	CH$_3$OH	$11_{-3} - 11_{-2}$	764.812	215.90	2.31e-03	12.02	4.95	0.17	10.19	0.59	37	
765.513	CH$_3$OH	$10_{-3} - 10_{-2}$	765.513	190.37	2.30e-03	12.31	10.55	0.15	12.11	0.95	34	
765.866	CH$_3$OH	$16_1 - 15_1$	765.866	327.24	2.04e-03	12.54	5.19	0.23	13.24	0.87	42	
766.028	CH$_3$OH	$9_{-3} - 9_{-2}$	766.028	167.16	2.28e-03	12.19	5.33	0.23	11.29	0.84	38	
766.396	CH$_3$OH	$8_{-3} - 8_{-2}$	766.396	146.28	2.24e-03	12.11	6.61	0.23	13.59	1.16	42	
766.648	CH$_3$OH	$7_{-3} - 7_{-2}$	766.648	127.71	2.18e-03	12.28	5.61	0.23	12.65	1.24	39	
766.710	CH$_3$OH	$6_2 - 5_1$	766.710	86.46	1.69e-03	11.94	4.75	0.66	11.69	2.69	42	
766.761	CH$_3$OH	$5_{-4} - 4_{-3}$	766.761	122.72	3.13e-03	11.67	3.99	0.49	11.79	1.92	42	
766.810	CH$_3$OH	$6_{-3} - 6_{-2}$	766.810	111.46	2.10e-03	11.97	5.32	0.29	12.03	1.03	45	
766.908	CH$_3$OH	$5_{-3} - 5_{-2}$	766.908	97.53	1.96e-03	11.89	3.00	0.31	11.14	0.75	43	
766.960	CH$_3$OH	$4_{-3} - 4_{-2}$	766.960	85.92	2.54e-03						39	**B:** CH$_3$OH $(3_{-3} - 3_{-2})$

ν GHz (1)	Species (2)	Transition (3)	ν_rest GHz (4)	E_u K (5)	A_{ul} rad/s (6)	Gaussian fit v_{lsr} km/s (7)	FWHM km/s (8)	T_{mb} K (9)	from moments v_{lsr} km/s (10)	Flux K km/s (11)	RMS mK (12)	Blend(**B**) / Notes (13)
766.982	CH$_3$OH	$3_{-3} - 3_{-2}$	766.982	76.64	1.81e-03	11.31	3.19	0.75	11.07	2.51	38	**B:** CH$_3$OH ($4_{-3} - 4_{-2}$)
768.252	C^{18}O	$7 - 6$	768.252	147.50	2.98e-05	12.31	5.03	0.29	13.59	1.09	46	
768.540	CH$_3$OH	$16_0 - 15_0$	768.540	327.63	2.06e-03						44	
770.886	CH$_3$OH	$16_{-1} - 15_{-1}$	770.886	320.63	3.08e-03						36	**B:** H$_2$CO ($11_{1,11} - 10_{1,10}$)
770.896	H$_2$CO	$11_{1,11} - 10_{1,10}$	770.896	234.26	1.37e-02						36	**B:** CH$_3$OH ($16_{-1} - 15_{-1}$)
771.184	^{13}CO	$7 - 6$	771.184	148.06	3.01e-05	11.37	3.58	5.96	11.29	23.54	36	
771.576	CH$_3$OH	$16_0 - 15_0$	771.576	315.21	2.10e-03	12.32	4.08	0.51	11.87	2.06	35	
772.454	CH$_3$OH	$5_3 - 4_2$	772.454	82.53	2.70e-03	12.74	6.21	0.54	12.98	3.45	40	
773.259	CH$_3$OH	$16_3 - 15_3$	773.259	365.37	2.03e-03	11.95	5.15	0.14	10.96	0.40	38	
773.416	CH$_3$OH	$16_3 - 15_3$	773.416	365.40	3.01e-03	11.97	5.04	0.18	12.87	0.65	38	
773.602	CH$_3$OH	$16_1 - 15_1$	773.602	336.72	2.13e-03	12.72	3.31	0.18	12.16	0.50	40	
773.893	CH$_3$OH	$19_{-1} - 18_0$	773.893	445.37	2.53e-03	12.29	5.36	0.17	13.28	0.66	35	
773.941	CH$_3$OH	$16_3 - 15_3$	773.941	363.43	3.03e-03						35	**B:** CH$_3$OH ($16_2 - 15_2$)
773.950	CH$_3$OH	$16_2 - 15_2$	773.950	353.45	3.10e-03						35	**B:** CH$_3$OH ($16_3 - 15_3$)
774.333	CH$_3$OH	$16_2 - 15_2$	774.333	338.14	2.07e-03	12.01	3.24	0.27	11.15	0.71	39	
775.596	CH$_3$OH	$16_{-2} - 15_{-2}$	775.596	341.96	2.10e-03	11.74	3.82	0.13	11.03	0.39	41	
779.009	CH$_3$OH	$16_1 - 15_1$	779.009	332.65	2.15e-03						40	**B:** CH$_3$OH ($13_0 - 12_{-1}$)
779.031	CH$_3$OH	$13_0 - 12_{-1}$	779.031	223.82	1.82e-03						40	**B:** CH$_3$OH ($16_1 - 15_1$)
779.380	CH$_3$OH	$6_2 - 5_1$	779.380	86.46	1.78e-03	11.85	5.08	0.68	11.72	2.60	41	
780.039	H$_2^{37}$Cl$^+$	$2_{1,2,5/2} - 1_{0,1,5/2}$	780.039	57.66	1.78e-03	9.38	1.15	-0.11	5.17	-0.38	35	**B:** H$_2$Cl$^+$ ($2_{1,2,7/2} - 1_{0,1,5/2}$)
781.609	H$_2$Cl$^+$	$2_{1,2,5/2} - 1_{0,1,5/2}$	781.609	57.75	1.79e-03						32	**B:** H$_2$Cl$^+$ ($2_{1,2,7/2} - 1_{0,1,5/2}$)
781.622	H$_2$Cl$^+$	$2_{1,2,5/2} - 1_{0,1,3/2}$	781.622	57.75	4.17e-03						30	**B:** H$_2$Cl$^+$ ($2_{1,2,5/2} - 1_{0,1,5/2}$)
781.627	H$_2$Cl$^+$	$2_{1,2,7/2} - 1_{0,1,5/2}$	781.627	57.75	5.96e-03						31	**B:** H$_2$Cl$^+$ ($2_{1,2,5/2} - 1_{0,1,5/2}$)
781.628	CH$_3$OH	$2_{1,2,1/2} - 1_{0,1,1/2}$	781.628	57.75	4.96e-03						30	**B:** H$_2$Cl$^+$ ($2_{1,2,5/2} - 1_{0,1,5/2}$)
783.002	CH$_3$OH	$11_3 - 10_2$	783.002	202.98	1.85e-03	12.08	4.39	0.51	12.39	2.13	33	
783.199	CS	$16 - 15$	783.199	319.62	1.04e-02	11.74	10.51	0.17	12.10	1.27	32	
784.177	CH$_3$OH	$11_3 - 10_2$	784.177	202.99	1.86e-03	12.16	4.21	0.47	12.24	1.89	35	
784.693	CH$_3$OH	$21_0 - 20_1$	784.693	534.79	1.60e-03	12.66	3.86	0.17	13.62	0.61	30	
785.802	CCH	$9_{19/2,9} - 8_{17/2,8}$	785.802	188.59	1.58e-03						35	**B:** CCH ($9_{19/2,10} - 8_{17/2,9}$)
785.802	CCH	$9_{19/2,10} - 8_{17/2,9}$	785.802	188.59	1.59e-03						35	**B:** CCH ($9_{19/2,9} - 8_{17/2,8}$)
786.280	C^{17}O	$7_{9/2} - 6_{11/2}$	786.280	150.96	6.36e-08						39	**B:** H$_2$CO ($11_{0,11} - 10_{0,10}$)
786.285	H$_2$CO	$11_{0,11} - 10_{0,10}$	786.285	228.32	1.47e-02						39	**B:** C^{17}O ($7_{9/2} - 6_{11/2}$)
793.336	CN	$7_{13/2,15/2} - 6_{11/2,13/2}$	793.336	152.30	5.64e-03						35	**B:** CN ($7_{13/2,11/2} - 6_{11/2,9/2}$)
793.336	CN	$7_{13/2,11/2} - 6_{11/2,9/2}$	793.336	152.30	5.48e-03						35	**B:** CN ($7_{13/2,15/2} - 6_{11/2,13/2}$)
793.337	CN	$7_{13/2,13/2} - 6_{11/2,11/2}$	793.337	152.30	5.51e-03						35	**B:** CN ($7_{13/2,15/2} - 6_{13/2,13/2}$)
793.553	CN	$7_{15/2,15/2} - 6_{13/2,13/2}$	793.553	152.38	5.61e-03						36	**B:** CN ($7_{15/2,17/2} - 6_{13/2,15/2}$)
793.553	CN	$7_{15/2,17/2} - 6_{13/2,15/2}$	793.553	152.38	5.71e-03						37	**B:** CN ($7_{15/2,15/2} - 6_{13/2,13/2}$)
793.554	CN	$7_{15/2,13/2} - 6_{13/2,11/2}$	793.554	152.38	5.59e-03						35	**B:** CN ($7_{15/2,15/2} - 6_{13/2,13/2}$)
797.433	HCN	$9 - 8$	797.433	191.38	2.49e-02	12.44	11.93	1.17	11.62	14.60	47	
798.313	H$_2$CO	$11_{2,10} - 10_{2,9}$	798.313	277.39	1.49e-02	9.62	6.16	0.16	11.56	0.49	49	
802.241	CH$_3$OH	$13_1 - 12_0$	802.241	232.29	1.38e-03	12.31	2.47	0.26	11.51	0.52	58	
802.282	H$_2$CO	$11_{3,9} - 10_{3,8}$	802.282	336.87	1.45e-02	11.82	3.20	0.26	14.49	0.51	57	
802.458	HCO$^+$	$9 - 8$	802.458	192.59	4.33e-02	11.55	5.42	2.17	11.90	13.19	57	
803.112	H$_2$CO	$11_{3,8} - 10_{3,7}$	803.112	336.96	1.45e-02	12.27	3.64	0.23	13.57	0.77	59	

ν GHz (1)	Species (2)	Transition (3)	ν_{rest} GHz (4)	E_u K (5)	A_{ul} rad/s (6)	Gaussian fit v_{lsr} km/s (7)	FWHM km/s (8)	T_{mb} K (9)	from moments v_{lsr} km/s (10)	Flux K km/s (11)	RMS mK (12)	Blend(**B**) / Notes (13)
803.239	CH$_3$OH	$16_2 - 15_1$	803.239	338.14	1.38e-03	12.25	5.16	0.17	10.65	0.57	56	
806.652	CO	$7 - 6$	806.652	154.88	3.42e-05	11.27	13.27	22.59	11.34	211.46	49	
807.866	CH$_3$OH	$11_1 - 10_0$	807.866	166.37	1.65e-03						51	**B:** CH$_3$OH ($11_1 - 10_0$)
807.866	CH$_3$OH	$11_1 - 10_0$	807.866	166.37	1.65e-03						50	**B:** CH$_3$OH ($11_1 - 10_0$)
809.342	C	$2 - 1$	809.342	62.46	2.67e-07	11.98	1.80	2.02	11.80	4.90	47	
811.445	CH$_3$OH	$8_{-2} - 7_{-1}$	811.445	109.49	1.88e-03	12.38	5.11	0.66	13.48	2.98	49	
812.550	CH$_3$OH	$7_2 - 6_1$	812.550	102.70	1.92e-03	12.16	5.05	0.60	12.76	2.70	43	
812.831	H$_2$CO	$11_{2,9} - 10_{2,8}$	812.831	279.73	1.57e-02	11.93	8.71	0.13	10.00	0.77	41	
813.542	CH$_3$OH	$17_1 - 16_1$	813.542	366.29	2.45e-03	13.96	8.69	0.18	14.74	0.99	43	
815.071	CH$_3$OH	$6_{-4} - 5_{-3}$	815.071	136.65	3.31e-03	11.91	4.39	0.51	11.92	1.76	41	
816.011	CH$_3$OH	$17_0 - 16_0$	816.011	366.79	2.48e-03	12.10	5.39	0.22	14.33	1.20	46	
818.669	CH$_3$OH	$17_{-1} - 16_{-1}$	818.669	359.92	2.50e-03	12.67	4.15	0.34	12.24	1.28	51	
819.479	CH$_3$OH	$17_0 - 16_0$	819.479	354.54	2.51e-03	12.39	4.04	0.38	10.76	1.47	53	
820.499	CH$_3$OH	$17_2 - 16_2$	820.499	392.50	3.71e-03	12.12	12.87	0.14	11.54	0.59	50	
820.762	CH$_3$OH	$6_3 - 5_2$	820.762	96.46	2.93e-03	12.17	5.18	0.56	12.91	2.31	52	
821.698	CH$_3$OH	$17_3 - 16_3$	821.698	404.83	3.64e-03	12.77	3.44	0.21	13.96	0.44	43	
821.869	CH$_3$OH	$17_1 - 16_1$	821.869	376.17	2.56e-03	12.44	3.75	0.20	12.86	0.50	45	
822.301	CH$_3$OH	$17_2 - 16_2$	822.301	392.92	3.73e-03	12.31	3.45	0.13	12.28	0.25	45	
822.540	CH$_3$OH	$17_2 - 16_2$	822.540	377.62	2.49e-03	12.29	4.45	0.21	12.16	0.59	46	
823.083	H$_2$CO	$11_{1,10} - 10_{1,9}$	823.083	249.44	1.67e-02	12.08	4.32	0.45	11.95	1.94	42	
824.343	CH$_3$OH	$17_{-2} - 16_{-2}$	824.343	381.52	2.53e-03	12.73	2.85	0.18	12.25	0.44	41	
825.276	CH$_3$OH	$14_0 - 13_{-1}$	825.276	256.14	2.28e-03	12.17	4.45	0.38	11.83	1.56	41	
827.454	CH$_3$OH	$17_1 - 16_1$	827.454	372.37	2.58e-03	12.68	5.47	0.23	11.41	1.11	53	
829.891	CH$_3$OH	$4_4 - 3_3$	829.891	103.56	7.63e-03						50	**B:** CH$_3$OH ($4_4 - 3_3$)
829.891	CH$_3$OH	$4_4 - 3_3$	829.891	103.56	7.63e-03						50	**B:** CH$_3$OH ($4_4 - 3_3$)
830.349	CH$_3$OH	$7_2 - 6_1$	830.349	102.72	2.05e-03	12.04	5.30	0.69	12.45	3.16	50	
831.045	CH$_3$OH	$12_3 - 11_2$	831.045	230.83	2.14e-03	11.99	4.97	0.44	11.71	1.68	60	
832.057	CS	$17 - 16$	832.057	359.56	1.25e-02	10.80	12.31	0.22	9.32	1.15	56	
832.754	CH$_3$OH	$12_3 - 11_2$	832.754	230.83	2.16e-03	12.13	3.95	0.41	13.20	1.11	48	
835.138	CH$^+$	$1 - 0$	835.138	40.08	6.36e-03	9.46	6.04	-0.51	9.78	-2.81	40	
838.307	N$_2$H$^+$	$9 - 8$	838.307	201.19	4.03e-02	11.77	2.88	0.94	11.43	2.60	40	
838.902	CH$_3$OH	$22_0 - 21_1$	838.902	585.57	1.99e-03	13.44	5.05	0.14	14.81	0.39	39	
840.276	H$_2$CO	$12_{1,12} - 11_{1,11}$	840.276	274.58	1.79e-02	12.10	5.22	0.46	12.32	2.40	36	
851.415	CH$_3$OH	$12_1 - 11_0$	851.415	193.96	1.95e-03	12.48	4.59	0.75	12.63	3.50	44	
852.177	CH$_3$OH	$17_2 - 16_1$	852.177	377.62	1.65e-03	11.88	2.85	0.15	11.92	0.39	42	
853.504	CH$_3$OH	$14_1 - 13_0$	853.504	264.78	1.65e-03	12.23	5.38	0.21	13.23	0.79	42	
857.959	CH$_3$OH	$8_2 - 7_1$	857.959	121.27	2.18e-03	12.14	4.72	0.67	12.61	2.83	57	
860.459	CH$_3$OH	$9_{-2} - 8_{-1}$	860.459	130.40	2.13e-03	12.20	4.89	0.65	12.23	2.77	55	
861.186	CH$_3$OH	$18_1 - 17_1$	861.186	407.62	2.92e-03	12.72	9.93	0.14	10.91	0.99	46	
863.365	H$_2$CO	$7_{-4} - 6_{-3}$	863.365	152.89	3.57e-03	11.81	5.52	0.41	12.23	2.19	47	
863.431	CH$_3$OH	$18_0 - 17_0$	863.431	408.23	2.94e-03	11.61	4.67	0.18	11.75	0.58	47	
866.388	CH$_3$OH	$18_{-1} - 17_{-1}$	866.388	401.50	2.97e-03	12.98	7.75	0.28	13.04	1.68	44	
867.327	CH$_3$OH	$18_0 - 17_0$	867.327	396.17	2.99e-03	12.18	4.60	0.31	13.90	0.94	46	
869.038	CH$_3$OH	$7_3 - 6_2$	869.038	112.71	3.21e-03	12.35	5.12	0.55	11.85	2.26	54	
869.973	CH$_3$OH	$18_3 - 17_3$	869.973	446.59	4.34e-03	12.23	5.05	0.18	11.44	0.47	52	

ν GHz (1)	Species (2)	Transition (3)	ν_{rest} GHz (4)	E_u K (5)	A_{ul} rad/s (6)	Gaussian fit v_{lsr} km/s (7)	FWHM km/s (8)	T_{mb} K (9)	from moments v_{lsr} km/s (10)	Flux K km/s (11)	RMS mK (12)	Blend(**B**) / Notes (13)
870.273	H₂CO	$12_{2,11} - 11_{2,10}$	870.273	319.16	1.94e-02	10.94	3.73	0.22	14.29	0.78	50	
870.664	CH₃OH	$18_2 - 17_2$	870.664	419.41	4.39e-03						52	**B:** CH₃OH $(18_3 - 17_3)$
870.691	CH₃OH	$18_3 - 17_3$	870.691	444.68	4.36e-03						53	**B:** CH₃OH $(18_2 - 17_2)$
871.152	CH₃OH	$15_0 - 14_{-1}$	871.152	290.74	2.84e-03	12.73	4.79	0.39	13.15	1.75	49	
873.036	CCH	$10_{21/2,10} - 9_{19/2,9}$	873.036	230.49	2.18e-03						38	**B:** CCH $(10_{21/2,11} - 9_{19/2,10})$
873.036	CCH	$10_{21/2,11} - 9_{19/2,10}$	873.036	230.49	2.19e-03						38	**B:** CCH $(10_{21/2,10} - 9_{19/2,9})$
873.138	CH₃OH	$18_{-2} - 17_{-2}$	873.138	423.43	3.01e-03	12.75	8.22	0.19	12.15	0.95	39	
873.775	H₂CO	$12_{5,8} - 11_{5,7}$	873.775	566.55	1.67e-02						34	**B:** H₂CO $(12_{5,7} - 11_{5,6})$
873.776	H₂CO	$12_{5,7} - 11_{5,6}$	873.776	566.55	1.67e-02						35	**B:** H₂CO $(12_{5,8} - 11_{5,7})$
875.366	H₂CO	$12_{3,10} - 11_{3,9}$	875.366	378.88	1.91e-02	12.26	4.08	0.18	10.37	0.55	37	
875.735	CH₃OH	$21_{-1} - 20_0$	875.735	539.96	3.97e-03	12.58	4.12	0.11	14.24	0.38	36	
875.852	CH₃OH	$18_1 - 17_1$	875.852	414.40	3.07e-03	12.56	3.54	0.21	14.72	0.56	38	
876.649	H₂CO	$12_{3,9} - 11_{3,8}$	876.649	379.03	1.92e-02	12.04	4.84	0.15	12.46	0.68	38	
877.922	C¹⁸O	$8 - 7$	877.922	189.64	4.47e-05	11.44	3.23	0.39	11.63	1.38	37	
878.226	CH₃OH	$5_4 - 4_3$	878.226	115.16	7.60e-03						37	**B:** CH₃OH $(5_4 - 4_3)$
878.227	CH₃OH	$5_4 - 4_3$	878.227	115.16	7.60e-03						40	**B:** CH₃OH $(5_4 - 4_3)$
879.013	CH₃OH	$13_3 - 12_2$	879.013	260.99	2.48e-03	12.19	4.77	0.26	13.30	1.05	37	
880.899	CS	$18 - 17$	880.899	401.83	1.49e-02	10.13	12.56	0.18	7.68	1.25	39	
881.273	¹³CO	$8 - 7$	881.273	190.36	4.52e-05	11.29	5.07	3.35	11.50	15.76	42	
881.421	CH₃OH	$13_3 - 12_2$	881.421	261.00	2.50e-03	11.96	3.72	0.33	12.23	1.21	38	
881.782	CH₃OH	$8_2 - 7_1$	881.782	121.29	2.37e-03	11.94	4.76	0.72	12.19	3.28	35	
885.971	HCN	$10 - 9$	885.971	233.90	3.44e-02	12.56	12.24	1.16	12.30	14.07	40	
888.629	H₂CO	$12_{2,10} - 11_{2,9}$	888.629	322.37	2.07e-02	11.90	7.51	0.11	12.87	0.47	37	
891.557	HCO⁺	$10 - 9$	891.557	235.38	5.97e-02	11.42	5.52	1.76	12.14	11.66	38	
893.639	HDO	$1_{1,1} - 0_{0,0}$	893.639	42.89	8.35e-03	13.42	2.47	0.14	14.96	0.41	37	
894.614	CH₃OH	$13_1 - 12_0$	894.614	223.84	2.27e-03	12.49	4.44	0.61	12.24	2.76	36	
896.805	H₂CO	$12_{1,11} - 11_{1,10}$	896.805	292.48	2.17e-02	12.01	5.10	0.32	12.11	1.75	33	
900.972	CH₃OH	$18_2 - 17_1$	900.972	419.41	1.96e-03	11.65	4.10	0.11	14.36	0.37	37	
902.935	CH₃OH	$9_2 - 8_1$	902.935	142.15	2.47e-03	12.36	5.24	0.51	12.94	2.41	36	
905.404	CH₃OH	$15_1 - 14_0$	905.404	299.59	1.94e-03	11.90	4.81	0.24	11.48	0.77	52	
906.593	CN	$8_{15/2,17/2} - 7_{13/2,15/2}$	906.593	195.81	8.51e-03						53	**B:** CN $(8_{15/2,13/2} - 7_{13/2,11/2})$
906.593	CN	$8_{15/2,13/2} - 7_{13/2,11/2}$	906.593	195.81	8.34e-03						53	**B:** CN $(8_{15/2,17/2} - 7_{13/2,15/2})$
909.045	OH⁺	$1_{0,1/2} - 0_{1,1/2}$	909.045	43.63	5.23e-03	8.75	3.45	-0.13	10.90	-0.44	40	
909.159	OH⁺	$1_{0,1/2} - 0_{1,3/2}$	909.159	43.63	1.05e-02	9.36	2.74	-0.23	8.74	-0.72	40	
909.508	H₂CO	$13_{1,13} - 12_{1,12}$	909.508	318.23	2.28e-02	12.12	4.33	0.39	15.05	0.89	39	
909.738	CH₃OH	$10_{-2} - 9_{-1}$	909.738	153.63	2.38e-03	12.36	4.97	0.51	13.19	2.16	36	
910.808	CH₃OH	$19_0 - 18_0$	910.808	451.94	3.45e-03	12.39	6.07	0.16	12.40	1.01	37	
911.642	CH₃OH	$8_{-4} - 7_{-3}$	911.642	171.46	3.89e-03	11.84	5.29	0.43	11.97	2.10	44	
912.109	CH₃OH	$3_{-3} - 2_{-2}$	912.109	76.64	5.85e-03	12.18	6.01	0.50	12.38	2.97	39	
914.044	CH₃OH	$19_{-1} - 18_{-1}$	914.044	445.37	3.49e-03	12.37	4.39	0.26	11.91	1.06	38	
915.117	CH₃OH	$19_0 - 18_0$	915.117	440.09	3.51e-03	12.34	4.04	0.21	13.27	0.75	43	
916.652	CH₃OH	$16_0 - 15_{-1}$	916.652	327.63	3.49e-03	12.52	3.78	0.29	12.66	1.01	47	
917.270	CH₃OH	$8_3 - 7_2$	917.270	131.28	3.53e-03	12.67	6.11	0.48	12.19	2.46	50	
918.699	CH₃OH	$19_2 - 18_2$	918.699	463.50	3.49e-03	11.83	4.01	0.15	16.89	0.36	51	
921.800	CO	$8 - 7$	921.800	199.11	5.13e-05	11.27	12.91	25.68	11.55	248.50	48	

ν GHz (1)	Species (2)	Transition (3)	ν_{rest} GHz (4)	E_u K (5)	A_{ul} rad/s (6)	Gaussian fit v_{lsr} km/s (7)	FWHM km/s (8)	T_{mb} K (9)	from moments v_{lsr} km/s (10)	Flux K km/s (11)	RMS mK (12)	Blend(**B**) / Notes (13)
923.588	H$_2$CO	$13_{0,13} - 12_{0,12}$	923.588	313.69	2.39e-02	12.02	4.23	0.14	2.44	0.21	37	
924.198	CH$_3$OH	$19_1 - 18_1$	924.198	458.76	3.61e-03	12.58	5.26	0.15	12.36	0.63	39	
926.555	CH$_3$OH	$6_4 - 5_3$	926.555	129.09	7.85e-03						39	**B:** CH$_3$OH ($6_4 - 5_3$)
926.555	CH$_3$OH	$6_4 - 5_3$	926.555	129.09	7.85e-03						40	**B:** CH$_3$OH ($6_4 - 5_3$)
926.893	CH$_3$OH	$14_3 - 13_2$	926.893	293.47	4.20e-03	11.38	5.90	0.30	10.89	1.57	43	
929.723	CS	$19 - 18$	929.723	446.45	1.75e-02	9.76	9.64	0.17	7.18	0.95	45	
930.198	CH$_3$OH	$14_3 - 13_2$	930.198	293.48	2.87e-03	12.25	4.19	0.26	15.94	0.56	44	
931.386	N$_2$H$^+$	$10 - 9$	931.386	245.89	5.56e-02	11.65	4.01	0.71	10.30	3.03	45	
933.693	CH$_3$OH	$9_2 - 8_1$	933.693	142.19	2.73e-03	11.84	5.21	0.55	11.14	2.52	48	
937.478	CH$_3$OH	$14_1 - 13_0$	937.478	256.02	2.64e-03	12.46	5.78	0.54	12.50	2.94	40	
947.476	CH$_3$OH	$10_2 - 9_1$	947.476	165.35	2.78e-03	12.27	4.42	0.51	12.86	1.69	61	
948.454	H$_2$CO	$13_{3,11} - 12_{3,10}$	948.454	424.40	2.46e-02	12.28	4.27	0.19	13.30	0.51	50	
950.365	H$_2$CO	$13_{3,10} - 12_{3,9}$	950.365	424.65	2.47e-02	11.88	4.86	0.19	9.89	0.41	51	
959.346	CH$_3$OH	$11_{-2} - 10_{-1}$	959.346	179.19	2.65e-03	13.42	3.57	0.46	12.00	1.71	134	
959.901	CH$_3$OH	$9_{-4} - 8_{-3}$	959.901	192.34	4.26e-03	12.86	9.23	0.45	15.27	1.50	117	
960.471	CH$_3$OH	$4_{-3} - 3_{-2}$	960.471	85.92	5.57e-03	11.70	7.30	0.63	11.38	2.51	110	
961.635	CH$_3$OH	$20_{-1} - 19_{-1}$	961.635	491.52	4.07e-03	13.44	3.60	0.26	14.43	0.50	74	
961.777	CH$_3$OH	$17_0 - 16_{-1}$	961.777	366.79	4.25e-03	12.71	4.27	0.29	13.14	0.77	79	
962.848	CH$_3$OH	$20_0 - 19_0$	962.848	486.30	4.10e-03	11.83	3.68	0.27	9.72	1.14	57	
965.448	CH$_3$OH	$9_3 - 8_2$	965.448	152.17	3.90e-03	12.52	5.11	0.49	12.93	2.53	50	
966.507	CH$_3$OH	$20_3 - 19_3$	966.507	537.04	6.00e-03						50	**B:** CH$_3$OH ($20_1 - 19_1$)
966.515	CH$_3$OH	$20_1 - 19_1$	966.515	508.38	6.19e-03						52	**B:** CH$_3$OH ($20_3 - 19_3$)
970.199	H$_2$CO	$13_{1,12} - 12_{1,11}$	970.199	339.05	2.76e-02	10.78	4.87	0.21	10.49	0.67	82	
971.804	OH$^+$	$1_{2,5/2} - 0_{1,3/2}$	971.804	46.64	1.82e-02						108	**B:** OH$^+$ ($1_{2,3/2} - 0_{1,1/2}$)
971.805	OH$^+$	$1_{2,3/2} - 0_{1,1/2}$	971.805	46.65	1.52e-02						107	**B:** OH$^+$ ($1_{2,5/2} - 0_{1,3/2}$)
972.489	CH$_3$OH	$20_1 - 19_1$	972.489	505.43	4.21e-03	12.78	2.83	0.32	10.76	0.60	99	
974.462	NH	$1_{2,5/2,3/2} - 0_{1,3/2,1/2}$	974.462	46.77	5.04e-03						55	**B:** NH ($1_{2,3/2,3/2} - 0_{1,1/2,1/2}$)
974.471	NH	$1_{2,5/2,5/2} - 0_{1,3/2,3/2}$	974.471	46.77	5.66e-03						55	**B:** NH ($1_{2,3/2,3/2} - 0_{1,1/2,1/2}$)
974.475	NH	$1_{2,3/2,3/2} - 0_{1,1/2,1/2}$	974.475	46.77	3.38e-03						57	**B:** NH ($1_{2,5/2,3/2} - 0_{1,3/2,1/2}$)
974.478	NH	$1_{2,5/2,7/2} - 0_{1,3/2,5/2}$	974.478	46.77	6.94e-03						55	**B:** NH ($1_{2,3/2,3/2} - 0_{1,3/2,1/2}$)
974.479	NH	$1_{2,3/2,5/2} - 0_{1,1/2,3/2}$	974.479	46.78	6.01e-03						56	**B:** NH ($1_{2,5/2,3/2} - 0_{1,3/2,1/2}$)
974.487	HCN	$11 - 10$	974.487	280.67	4.59e-02						55	**B:** NH ($1_{2,5/2,3/2} - 0_{1,3/2,1/2}$)
974.673	CH$_3$OH	$15_3 - 14_2$	974.673	328.26	3.24e-03	11.58	2.14	0.30	12.29	0.70	57	
974.877	CH$_3$OH	$7_4 - 6_3$	974.877	145.33	8.28e-03						56	**B:** CH$_3$OH ($7_4 - 6_3$)
974.878	CH$_3$OH	$7_4 - 6_3$	974.878	145.33	8.28e-03						57	**B:** CH$_3$OH ($7_4 - 6_3$)
978.529	CS	$20 - 19$	978.529	493.42	2.04e-02						51	**B:** H$_2$CO ($14_{1,14} - 13_{1,13}$)
978.592	H$_2$CO	$14_{1,14} - 13_{1,13}$	978.592	365.20	2.84e-02						56	**B:** CS ($20 - 19$)
979.110	CH$_3$OH	$15_3 - 14_2$	979.110	328.28	3.28e-03	12.45	4.62	0.27	13.72	1.08	53	
980.025	CH$_3$OH	$15_1 - 14_0$	980.025	290.49	3.04e-03	12.68	4.52	0.54	12.62	2.15	61	
980.636	HCO$^+$	$11 - 10$	980.636	282.44	7.98e-02	11.44	6.14	1.30	12.38	9.31	54	
986.098	CH$_3$OH	$10_2 - 9_1$	986.098	165.40	3.13e-03	12.48	4.40	0.53	12.88	1.87	63	
987.560	C^{18}O	$9 - 8$	987.560	237.03	6.38e-05	11.01	3.37	0.36	13.23	0.96	54	
987.927	H$_2$O	$2_{0,2,0} - 1_{1,1,0}$	987.927	100.85	5.85e-03	12.37	16.39	4.47	13.22	66.59	72	
991.329	^{13}CO	$9 - 8$	991.329	237.94	6.45e-05	11.32	6.92	1.96	11.58	11.49	65	
991.580	CH$_3$OH	$11_2 - 10_1$	991.580	190.87	3.12e-03	12.27	5.28	0.44	12.13	1.90	59	

ν GHz (1)	Species (2)	Transition (3)	ν_{rest} GHz (4)	E_u K (5)	A_{ul} rad/s (6)	Gaussian fit v_{lsr} km/s (7)	FWHM km/s (8)	T_{mb} K (9)	from moments v_{lsr} km/s (10)	Flux K km/s (11)	RMS mK (12)	Blend(**B**) / Notes (13)
991.660	H$_2$CO	$14_{0,14} - 13_{0,13}$	991.660	361.28	2.97e-02	12.21	2.46	0.16	13.32	0.24	56	
993.108	H$_2$S	$3_{0,3} - 2_{1,2}$	993.108	102.76	3.73e-03	11.67	5.99	0.46	13.82	3.41	64	
994.217	CH$_3$OH	$5_{-5} - 4_{-4}$	994.217	158.83	9.26e-03	12.18	6.32	0.27	12.10	0.99	62	
995.492	o-NH$_3$	$4_{0,1} - 4_{3,1}$	995.492	285.60	3.87e-08	13.49	0.94	0.31	11.30	1.23	80	
997.873	CH$_3$OH	$20_2 - 19_1$	997.873	509.89	2.76e-03	12.74	6.56	0.20	13.32	0.72	68	
1002.779	H$_2$S	$3_{1,3} - 2_{0,2}$	1002.779	102.82	3.87e-03	10.88	3.42	0.24	9.49	0.63	50	
1005.455	CH$_3$OH	$21_0 - 20_0$	1005.455	546.18	4.66e-03	14.58	0.44	0.17	10.93	0.46	64	
1005.642	CH$_3$OH	$10_4 - 10_3$	1005.642	223.65	5.06e-03	12.41	7.31	0.21	13.73	0.78	60	
1006.028	CH$_3$OH	$7_4 - 7_3$	1006.028	160.99	4.45e-03						63	**B**: CH$_3$OH $(6_4 - 6_3)$
1006.081	CH$_3$OH	$6_4 - 6_3$	1006.081	144.75	4.04e-03						63	**B**: CH$_3$OH $(7_4 - 7_3)$
1006.111	CH$_3$OH	$5_4 - 5_3$	1006.111	130.82	3.40e-03						64	**B**: CH$_3$OH $(7_4 - 7_3)$
1006.125	CH$_3$OH	$4_4 - 4_3$	1006.125	119.21	2.26e-03						60	**B**: CH$_3$OH $(7_4 - 7_3)$
1006.540	CH$_3$OH	$18_0 - 17_{-1}$	1006.540	408.23	5.12e-03	13.49	5.14	0.39	13.95	1.09	67	
1008.139	CH$_3$OH	$10_{-4} - 9_{-3}$	1008.139	215.55	4.69e-03	12.16	9.13	0.39	12.16	1.75	84	
1008.812	CH$_3$OH	$5_{-3} - 4_{-2}$	1008.812	97.53	5.63e-03	11.93	4.85	0.60	10.17	2.02	79	
1009.358	CH$_3$OH	$12_{-2} - 11_{-1}$	1009.358	207.08	2.91e-03	12.22	4.80	0.44	12.07	1.32	84	
1011.325	CH$_3$OH	$17_1 - 16_0$	1011.325	376.17	2.60e-03	13.22	4.04	0.23	13.61	0.61	66	
1013.563	CH$_3$OH	$10_3 - 9_2$	1013.563	175.39	4.29e-03						57	**B**: CH$_3$OH $(10_3 - 9_2)$
1013.563	CH$_3$OH	$10_3 - 9_2$	1013.563	175.39	4.29e-03						57	**B**: CH$_3$OH $(10_3 - 9_2)$
1020.720	CH$_3$OH	$21_1 - 20_1$	1020.720	554.42	4.88e-03	12.61	4.32	0.22	9.44	1.00	62	
1022.271	CH$_3$OH	$16_1 - 15_0$	1022.271	327.24	3.49e-03	12.53	5.29	0.45	12.47	1.76	86	
1022.338	CH$_3$OH	$16_3 - 15_2$	1022.338	365.37	3.67e-03	12.88	5.12	0.25	12.96	0.64	106	
1023.193	CH$_3$OH	$8_4 - 7_3$	1023.193	163.90	8.84e-03						63	**B**: CH$_3$OH $(8_4 - 7_3)$
1023.197	CH$_3$OH	$8_4 - 7_3$	1023.197	163.90	8.84e-03						64	**B**: CH$_3$OH $(8_4 - 7_3)$
1024.443	N$_2$H$^+$	$11 - 10$	1024.443	295.06	7.43e-02	11.97	3.30	0.49	10.05	1.78	94	
1027.314	CS	$21 - 20$	1027.314	542.72	2.37e-02	6.56	7.50	0.26	7.44	0.98	81	
1028.180	CH$_3$OH	$16_3 - 15_2$	1028.180	365.40	3.73e-03	13.00	8.45	0.28	13.03	1.42	79	
1032.998	OH$^+$	$1_{1,1/2} - 0_{1,1/2}$	1032.998	49.58	1.41e-02						70	**B**: OH$^+$ $(1_{1,3/2} - 0_{1,1/2})$
1033.004	OH$^+$	$1_{1,3/2} - 0_{1,1/2}$	1033.004	49.58	3.53e-03						70	**B**: OH$^+$ $(1_{1,1/2} - 0_{1,1/2})$
1033.112	OH$^+$	$1_{1,1/2} - 0_{1,3/2}$	1033.112	49.58	7.03e-03						74	**B**: OH$^+$ $(1_{1,3/2} - 0_{1,3/2})$
1033.119	OH$^+$	$1_{1,3/2} - 0_{1,3/2}$	1033.119	49.58	1.76e-02						75	**B**: OH$^+$ $(1_{1,1/2} - 0_{1,3/2})$
1035.247	CH$_3$OH	$12_2 - 11_1$	1035.247	218.69	3.48e-03	12.07	5.07	0.44	14.69	1.41	99	
1036.912	CO	$9 - 8$	1036.912	248.88	7.33e-05	11.27	12.44	25.10	11.59	257.05	188	
1039.015	CH$_3$OH	$11_2 - 10_1$	1039.015	190.94	3.59e-03	12.31	5.07	0.87	13.97	1.57	249	
1042.522	CH$_3$OH	$6_{-5} - 5_{-4}$	1042.522	172.76	9.19e-03	11.24	2.30	0.51	9.30	0.41	108	
1047.427	CCH	$12_{25/2,13} - 11_{23/2,12}$	1047.427	326.85	3.81e-03						105	**B**: CCH $(12_{25/2,12} - 11_{23/2,11})$
1047.427	CCH	$12_{25/2,12} - 11_{23/2,11}$	1047.427	326.85	3.79e-03						98	**B**: CCH $(12_{25/2,13} - 11_{23/2,12})$
1047.490	CCH	$12_{23/2,12} - 11_{21/2,11}$	1047.490	326.88	3.79e-03						93	**B**: CCH $(12_{25/2,13} - 11_{23/2,12})$
1047.490	CCH	$12_{23/2,11} - 11_{21/2,10}$	1047.490	326.88	3.78e-03						92	**B**: CCH $(12_{25/2,13} - 11_{23/2,12})$
1056.355	CH$_3$OH	$11_{-4} - 10_{-3}$	1056.355	241.07	5.17e-03	12.57	5.51	0.37	11.87	1.35	72	
1057.118	CH$_3$OH	$6_{-3} - 5_{-2}$	1057.118	111.46	5.86e-03	11.90	5.93	0.60	12.65	2.57	75	
1059.859	CH$_3$OH	$13_{-2} - 12_{-1}$	1059.859	237.30	3.16e-03	12.09	2.65	0.39	13.04	1.41	73	
1061.609	CH$_3$OH	$11_3 - 10_2$	1061.609	200.92	4.72e-03	13.11	6.04	0.37	13.34	1.49	92	
1062.981	HCN	$12 - 11$	1062.981	331.69	5.98e-02	12.39	14.47	0.87	11.62	9.19	124	
1064.237	CH$_3$OH	$17_1 - 16_0$	1064.237	366.29	3.98e-03	12.44	4.49	0.38	6.89	1.01	97	

ν GHz (1)	Species (2)	Transition (3)	ν_{rest} GHz (4)	E_u K (5)	A_{ul} rad/s (6)	*Gaussian fit* v_{lsr} km/s (7)	FWHM km/s (8)	T_{mb} K (9)	*from moments* v_{lsr} km/s (10)	Flux K km/s (11)	RMS mK (12)	Blend(**B**) / Notes (13)
1069.694	HCO$^+$	$12-11$	1069.694	333.78	1.04e-01	11.54	5.94	1.01	12.39	5.86	56	
1069.874	CH$_3$OH	17_3-16_2	1069.874	404.80	4.14e-03	12.86	4.01	0.24	12.27	0.53	63	**B**: CH$_3$OH (9_4-8_3)
1071.505	CH$_3$OH	9_4-8_3	1071.505	184.79	9.51e-03						65	**B**: CH$_3$OH (9_4-8_3)
1071.514	CH$_3$OH	9_4-8_3	1071.514	184.79	9.52e-03						66	
1072.837	H$_2$S	$2_{2,1}-1_{1,0}$	1072.837	79.37	4.13e-03	12.33	7.48	0.39	12.63	2.29	67	
1076.834	CH$_3$OH	5_5-4_4	1076.834	170.89	1.07e-02	12.37	3.69	0.36	11.74	1.01	87	
1077.437	CH$_3$OH	17_3-16_2	1077.437	404.83	6.26e-03	12.68	4.80	0.30	7.95	0.72	81	
1078.477	CH$_3$OH	13_2-12_1	1078.477	248.84	3.88e-03	12.31	5.31	0.41	14.13	1.27	80	
1090.816	CH$_3$OH	$7_{-5}-6_{-4}$	1090.816	189.00	9.37e-03	12.40	6.75	0.29	11.49	1.18	84	
1092.463	CH$_3$OH	12_2-11_1	1092.463	218.80	4.09e-03	11.86	4.63	0.55	11.93	1.66	90	
1095.063	CH$_3$OH	20_0-19_{-1}	1095.063	497.93	7.23e-03	12.40	4.12	0.30	10.53	0.56	83	
1097.365	H$_2$O	$3_{1,2,0}-3_{0,3,0}$	1097.365	249.44	1.64e-02	12.66	15.63	2.30	12.51	32.89	87	
1101.350	^{13}CO	$10-9$	1101.350	290.79	8.86e-05	11.34	7.95	1.38	11.92	9.39	75	
1104.547	CH$_3$OH	$12_{-4}-11_{-3}$	1104.547	268.91	5.69e-03	12.42	4.69	0.35	13.76	0.95	92	
1105.370	CH$_3$OH	$7_{-3}-6_{-2}$	1105.370	127.71	6.21e-03	12.43	5.05	0.60	12.28	1.94	80	
1105.944	CH$_3$OH	18_1-17_0	1105.944	407.62	4.51e-03	13.06	3.33	0.40	13.04	1.14	85	
1109.585	CH$_3$OH	12_3-11_2	1109.585	228.78	5.18e-03	12.74	5.21	0.40	12.23	1.16	97	
1110.941	CH$_3$OH	$14_{-2}-13_{-1}$	1110.941	269.85	3.40e-03	12.73	4.87	0.37	15.03	0.96	93	
1113.343	H$_2$O	$1_{1,1,0}-0_{0,0,0}$	1113.343	53.43	1.84e-02	12.63	20.54	3.28	12.31	48.58	94	
1115.204	H$_2$O$^+$	$1_{1,1,3/2,5/2}-0_{0,0,1/2,3/2}$	1115.204	53.52	3.10e-02	8.40	2.50	-0.29	9.66	-0.89	110	
1116.986	CH$_3$OH	23_1-22_1	1116.986	659.32	6.41e-03	13.80	5.58	0.46	14.80	0.65	119	
1117.477	N$_2$H$^+$	$12-11$	1117.477	348.69	9.68e-02	11.78	3.48	0.50	12.37	1.23	115	
1119.813	CH$_3$OH	10_4-9_3	1119.813	207.99	1.03e-02						122	**B**: CH$_3$OH (10_4-9_3)
1119.831	CH$_3$OH	10_4-9_3	1119.831	207.99	1.03e-02						123	**B**: CH$_3$OH (10_4-9_3)
1121.269	CH$_3$OH	14_2-13_1	1121.269	281.29	4.30e-03	12.23	4.55	0.25	13.31	0.65	91	
1125.143	CH$_3$OH	6_5-5_4	1125.143	184.82	1.55e-02	12.32	10.90	0.26	13.98	1.00	99	
1146.464	CH$_3$OH	13_2-12_1	1146.464	248.98	4.66e-03	12.56	4.31	0.56	12.12	1.74	153	
1147.415	CH$_3$OH	19_1-18_0	1147.415	451.23	5.10e-03	14.11	4.21	0.53	14.20	1.00	165	
1151.449	HCN	$13-12$	1151.449	386.95	7.63e-02	12.19	13.51	0.71	9.67	5.43	152	
1151.985	CO	$10-9$	1151.985	304.17	1.01e-04	11.40	11.47	24.84	12.12	267.41	162	
1153.127	H$_2$O	$3_{1,2,0}-2_{2,1,0}$	1153.127	249.44	2.67e-03	12.08	16.13	2.96	12.86	46.14	172	
1153.549	CH$_3$OH	$8_{-3}-7_{-2}$	1153.549	146.28	6.64e-03	12.72	5.36	0.56	14.31	2.07	140	
1157.499	CH$_3$OH	13_3-12_2	1157.499	258.96	5.66e-03	12.52	7.96	0.56	14.14	1.68	144	
1158.727	HCO$^+$	$13-12$	1158.727	389.39	1.33e-01	12.16	7.63	0.91	13.42	5.12	154	
1162.706	CH$_3$OH	$15_{-2}-14_{-1}$	1162.706	304.74	3.61e-03	11.58	7.87	0.40	12.68	0.99	160	
1162.912	H$_2$O	$3_{2,1,0}-3_{1,2,0}$	1162.912	305.25	2.28e-02	12.91	14.45	1.56	14.58	18.18	137	
1163.624	CH$_3$OH	15_2-14_1	1163.624	316.05	4.75e-03	13.47	3.23	0.50	15.97	0.80	136	
1168.118	CH$_3$OH	11_4-10_3	1168.118	233.52	7.51e-03						161	**B**: CH$_3$OH (11_4-10_3)
1168.150	CH$_3$OH	11_4-10_3	1168.150	233.52	7.51e-03						152	**B**: CH$_3$OH (11_4-10_3)
1168.452	p-NH$_3$	$2_{1,0}-1_{1,1}$	1168.452	57.21	1.21e-02	13.06	8.38	0.83	15.39	3.35	148	
1173.435	CH$_3$OH	7_5-6_4	1173.435	201.06	1.57e-02	10.30	7.77	0.52	8.37	1.45	165	
1188.672	CH$_3$OH	20_1-19_0	1188.672	497.13	5.75e-03	12.69	4.05	0.44	13.88	0.84	151	
1199.599	CH$_3$OH	4_4-3_3	1199.599	119.21	1.48e-02	12.58	7.28	0.54	12.52	2.13	160	
1200.855	CH$_3$OH	$14_{-4}-13_{-3}$	1200.855	331.54	6.89e-03	12.02	4.54	0.61	12.09	0.94	160	
1201.630	CH$_3$OH	$9_{-3}-8_{-2}$	1201.630	167.16	7.15e-03	11.89	4.04	0.79	14.51	1.71	167	

continued from previous page

ν GHz (1)	Species (2)	Transition (3)	ν_{rest} GHz (4)	E_u K (5)	A_{ul} rad/s (6)	Gaussian fit v_{lsr} km/s (7)	FWHM km/s (8)	T_{mb} K (9)	from moments v_{lsr} km/s (10)	Flux K km/s (11)	RMS mK (12)	Blend(**B**) / Notes (13)
1205.368	CH$_3$OH	$14_3 - 13_2$	1205.368	291.46	6.15e-03	13.24	3.64	0.48	15.28	0.96	153	
1211.330	^{13}CO	$11 - 10$	1211.330	348.93	1.18e-04	11.97	9.03	1.22	12.62	8.77	176	
1214.853	o-NH$_3$	$2_{0,1} - 1_{0,0}$	1214.853	85.78	1.81e-02	13.79	7.57	1.34	12.97	5.54	183	**B:** CH$_3$OH ($16_{-2} - 15_{-1}$)
1215.246	p-NH$_3$	$2_{1,1} - 1_{1,0}$	1215.246	58.32	1.36e-02						195	**B:** p-NH$_3$ ($2_{1,1} - 1_{1,0}$)
1215.261	CH$_3$OH	$16_{-2} - 15_{-1}$	1215.261	341.96	5.60e-03						204	
1216.420	CH$_3$OH	$12_4 - 11_3$	1216.420	261.36	8.14e-03	12.11	5.62	0.60	12.91	1.40	190	
1228.789	H$_2$O	$2_{2,0,0} - 2_{1,1,0}$	1228.789	195.91	1.88e-02	12.93	12.80	1.00	12.61	10.18	148	
1229.740	CH$_3$OH	$21_1 - 20_0$	1229.740	545.31	6.45e-03	11.30	2.25	0.54	12.22	0.90	160	
1232.476	HF	$1 - 0$	1232.476	59.15	2.42e-02	9.98	2.82	-0.99	9.33	-2.00	195	
1239.890	HCN	$14 - 13$	1239.890	446.45	9.55e-02	12.19	14.59	0.73	11.23	5.02	191	
1249.559	H^{37}Cl	$2_{3/2} - 1_{1/2}$	1249.559	89.97	4.65e-03						83	**B:** H^{37}Cl ($2_{3/2} - 1_{5/2}$)
1249.569	H^{37}Cl	$2_{3/2} - 1_{5/2}$	1249.569	89.96	5.58e-04						83	**B:** H^{37}Cl ($2_{3/2} - 1_{1/2}$)
1249.571	H^{37}Cl	$2_{1/2} - 1_{1/2}$	1249.571	89.97	9.30e-03						85	**B:** H^{37}Cl ($2_{3/2} - 1_{1/2}$)
1249.573	H^{37}Cl	$2_{7/2} - 1_{5/2}$	1249.573	89.97	1.12e-02						83	**B:** H^{37}Cl ($2_{3/2} - 1_{1/2}$)
1249.573	H^{37}Cl	$2_{5/2} - 1_{3/2}$	1249.573	89.96	7.82e-03						83	**B:** H^{37}Cl ($2_{3/2} - 1_{1/2}$)
1249.582	H^{37}Cl	$2_{3/2} - 1_{3/2}$	1249.582	89.97	5.95e-03						82	**B:** H^{37}Cl ($2_{3/2} - 1_{1/2}$)
1249.584	CH$_3$OH	$10_{-3} - 9_{-2}$	1249.584	190.37	1.14e-02						84	**B:** H^{37}Cl ($2_{3/2} - 1_{1/2}$)
1249.595	H^{37}Cl	$2_{1/2} - 1_{3/2}$	1249.595	89.97	1.86e-03						84	**B:** H^{37}Cl ($2_{3/2} - 1_{1/2}$)
1251.434	HCl	$2_{5/2} - 1_{3/2}$	1251.434	90.10	3.36e-03						96	**B:** HCl ($2_{5/2} - 1_{1/2}$)
1251.434	HCl	$2_{3/2} - 1_{3/2}$	1251.434	90.10	4.67e-03						97	**B:** HCl ($2_{5/2} - 1_{5/2}$)
1251.447	HCl	$2_{3/2} - 1_{1/2}$	1251.447	90.10	5.61e-04						96	**B:** HCl ($2_{5/2} - 1_{5/2}$)
1251.450	HCl	$2_{1/2} - 1_{1/2}$	1251.450	90.10	9.34e-03						96	**B:** HCl ($2_{5/2} - 1_{5/2}$)
1251.452	HCl	$2_{5/2} - 1_{3/2}$	1251.452	90.10	7.85e-03						96	**B:** HCl ($2_{5/2} - 1_{5/2}$)
1251.464	HCl	$2_{3/2} - 1_{3/2}$	1251.464	90.10	5.98e-03						97	**B:** HCl ($2_{5/2} - 1_{5/2}$)
1251.481	HCl	$2_{1/2} - 1_{3/2}$	1251.481	90.10	1.87e-03						94	**B:** HCl ($2_{5/2} - 1_{5/2}$)
1267.014	CO	$11 - 10$	1267.014	364.97	1.34e-04	11.66	11.29	22.38	12.16	247.42	126	
1496.923	CO	$13 - 12$	1496.923	503.14	2.20e-04	12.19	12.02	16.44	12.39	192.13	209	
1541.843	CH$_3$OH	$20_2 - 19_1$	1541.843	525.23	1.06e-02	14.84	2.56	1.06	15.09	1.14	241	
1611.794	CO	$14 - 13$	1611.794	580.50	2.74e-04	12.32	12.54	13.90	12.49	165.51	273	
1661.008	H$_2$O	$2_{1,0} - 2_{1,1,0}$	1661.008	194.10	3.06e-02	14.52	10.99	2.48	13.35	22.30	210	
1669.905	H$_2$O	$2_{1,2,0} - 1_{0,1,0}$	1669.905	114.38	5.60e-02	15.24	14.58	5.53	13.44	66.52	200	
1716.770	H$_2$O	$3_{0,3,0} - 2_{1,2,0}$	1716.770	196.77	5.06e-02	15.01	9.91	4.92	13.48	53.86	175	
1726.603	CO	$15 - 14$	1726.603	663.36	3.35e-04	13.05	12.34	10.49	12.73	135.76	221	
1760.486	^{13}CO	$16 - 15$	1760.486	718.70	3.57e-04	16.15	3.95	0.40	15.14	1.15	172	
1763.601	p-NH$_3$	$3_{1,0} - 2_{1,1}$	1763.601	142.96	5.28e-02	13.83	2.13	0.56	22.16	3.22	166	
1763.823	p-NH$_3$	$3_{2,0} - 2_{2,1}$	1763.823	126.97	3.30e-02	13.83	2.95	0.60	11.47	2.05	169	
1834.736	OH	$^2\Pi\, 2_{1,-1,0,1} - 1_{1,1,0,1}$	1834.736	269.76	2.12e-02						89	**B:** OH ($^2\Pi\, 2_{1,-1,0,2} - 1_{1,1,0,1}$)
1834.747	OH	$^2\Pi\, 2_{1,-1,0,2} - 1_{1,1,0,1}$	1834.747	269.76	6.36e-02						89	**B:** OH ($^2\Pi\, 2_{1,-1,0,1} - 1_{1,1,0,1}$)
1834.750	OH	$^2\Pi\, 2_{1,-1,0,1} - 1_{1,1,0,0}$	1834.750	269.76	4.24e-02						89	**B:** OH ($^2\Pi\, 2_{1,-1,0,1} - 1_{1,1,0,1}$)
1837.747	OH	$^2\Pi\, 2_{1,1,0,1} - 1_{1,-1,0,1}$	1837.747	270.14	2.13e-02						85	**B:** OH ($^2\Pi\, 2_{1,1,0,2} - 1_{1,-1,0,1}$)
1837.817	OH	$^2\Pi\, 2_{1,1,0,2} - 1_{1,-1,0,1}$	1837.817	270.14	6.40e-02						88	**B:** OH ($^2\Pi\, 2_{1,1,0,1} - 1_{1,-1,0,1}$)
1837.837	OH	$^2\Pi\, 2_{1,1,0,1} - 1_{1,-1,0,0}$	1837.837	270.14	4.27e-02						93	**B:** OH ($^2\Pi\, 2_{1,1,0,1} - 1_{1,-1,0,1}$)
1841.346	CO	$16 - 15$	1841.346	751.73	4.05e-04	12.60	12.45	6.08	12.32	69.82	83	
1900.537	C$^+$	$3/2 - 1/2$	1900.537	91.21	2.32e-06	9.07	2.08	11.99	8.84	24.14	94	

3

The methanol lines and hot core of OMC-2 FIR 4

M. Kama, C. Dominik, S. Maret, F. van der Tak, E. Caux, C. Ceccarelli, A. Fuente, N. Crimier, S. Lord and the CHESS, Herschel and HIFI teams

Abstract

In contrast with numerous studies on the physical and chemical structure of low- and high-mass protostars, much less is known about their intermediate-mass counterparts, a class of objects that could help to elucidate the mechanisms of star formation on both ends of the mass range. We present the first results from a rich HIFI spectral dataset on an intermediate-mass protostar, OMC-2 FIR 4, obtained in the CHESS (*Chemical HErschel Surveys of Star forming regions*) key programme. The more than 100 methanol lines detected between 554 and 961 GHz cover a range in upper level energy of 40 to 540 K. Our physical interpretation focusses on the hot core, but likely the cold envelope and shocked regions also play a role in reality, because an analysis of the line profiles suggests the presence of multiple emission components. An upper limit of 10^{-6} is placed on the methanol abundance in the hot core, using a population diagram, large-scale source model and other considerations. This value is consistent with abundances previously seen in low-mass hot cores. Furthermore, the highest energy lines at the highest frequencies display asymmetric profiles, which may arise from infall around the hot core.

3.1   Introduction

Intermediate-mass, and therefore intermediate-luminosity protostars offer insights into the physical and chemical differences between the formation of low- and high-mass stars, but questions about their chemistry and dominant gas-heating mechanisms

remain only partly answered.

Deep in the interior of a protostellar core, energy is released by a forming protostar. This energy heats the surrounding gas by dust-mediated and UV photon heating, as well as through shocks caused by protostellar outflows. The respective roles of these mechanisms as a function of protostar luminosity and the effects of heating on protostar evolution, are under intense study (e.g. Spaans et al. 1995; Doty et al. 2006; Bruderer et al. 2009), with the role of shocks and UV photons in low- and intermediate-luminosity sources emphasized by recent *Herschel* Space Observatory results (Fich et al. 2010; van Kempen et al. 2010). Sub-millimeter molecular line emission is a versatile probe of the physical and chemical conditions in these heated regions, the *hot cores*, revealing the initial conditions for forming stars and planetary systems. Hot cores are compact (sizes < 0.1pc), warm (T > 100K), and show evidence of complex chemistry (Kurtz et al. 2000; Ceccarelli et al. 2007). The two main paths to this complexity are gas-phase and grain-surface reactions (e.g. Garrod et al. 2008). During the gradual warm-up of grains in a hot core, species formed on them in earlier evolutionary phases react and the products are later released into the gas phase. Observable chemical differences include a methanol–formaldehyde abundance ratio, which increases with decreasing protostar luminosity (Cazaux et al. 2003; Bottinelli et al. 2004, 2007).

We present *Herschel*/HIFI sub-millimeter observations of methanol line emisson toward the intermediate-mass protostar OMC-2 FIR 4[1], attributing part of the emission to a hot core. With a luminosity of 1000 $L_\odot$ (Crimier et al. 2009, hereafter Crim09) and a distance of only 440 pc (Hirota et al. 2007), the protostar OMC-2 FIR 4 is an excellent laboratory to study hot core chemistry in the intermediate mass regime. A structure model, constrained by 7.5″ to 14.8″ resolution dust-continuum maps and the broadband spectral energy distribution, was made for OMC-2 FIR 4 by Crim09. The uncertainties in the properties of the central component are large, but the model suggests a hot core radius of R_{Crim} = 440 AU and densities above $\sim 5 \cdot 10^6$ cm^{-3}. At $\sim$1″ resolution, FIR 4 is seen to consist of several clumps, which may be forming a cluster of protostars (Shimajiri et al. 2008, hereafter Shim08). Some of this activity may be triggered by an outflow from the nearby source OMC-2 FIR 3.

Methanol is a powerful diagnostic of the physical and chemical conditions in protostellar sources (van der Tak et al. 2000; Leurini et al. 2004, 2007; Maret et al. 2005; Wang et al. 2010), and is used to that end here. A careful analysis of methanol is also important for recovering the other species which CH$_3$OH lines often blend with.

3.2   Observations

The source OMC-2 FIR 4 was observed with the HIFI spectrograph on the ESA *Herschel* Space Observatory (Pilbratt et al. 2010), using only the wide band spectrometer (WBS) (de Graauw et al. 2010), covering bands 1b (554.5 to 636.5 GHz), 2b (714.1 to 801 GHz), and 3b (858.0 to 961.0 GHz). The WBS native resolution is 1.1MHz. The data were taken in dual beam switch (DBS) spectral scan mode with a redundancy of

---

[1]SIMBAD entry: [MWZ90] OMC-2 FIR 4
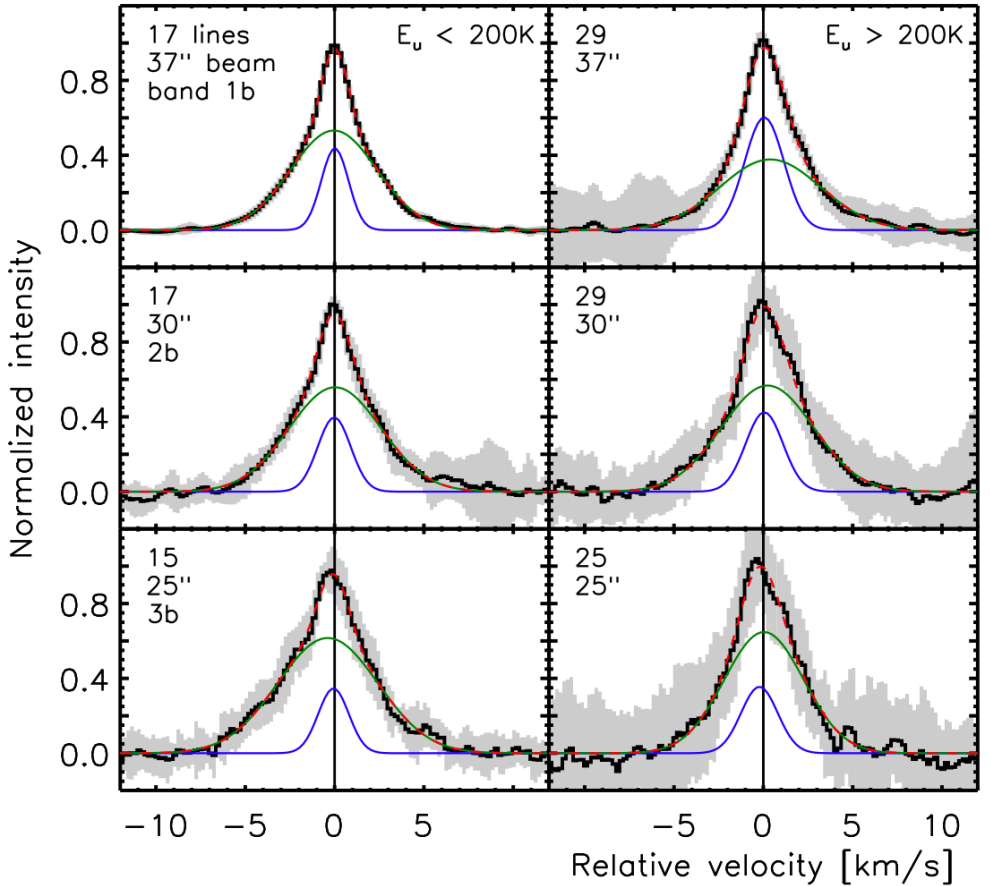
Figure 3.1: Averaged CH$_3$OH line profiles in the E$_u$ ≤ 200K (left) and E$_u$ ≥ 200K (right) ranges, for bands 1b (top), 2b (middle) and 3b (bottom). The gray area marks the biased weighted standard deviation of the sample of normalized profiles. The two fitted Gaussians (blue, green) and their sum (dashed red line) are given.

four. More observations, expected later in 2010, will cover most of HIFI's frequency range. Median baseline subtraction and sideband deconvolution were performed with the HIPE 2 software (Ott 2010a). A frequency-dependent main beam efficiency within three percent of 0.70 and a calibration uncertainty of 15% were used in calculating line fluxes. For a detailed review of HIFI's in-orbit performance, see Roelfsema et al. (2010).

The data quality in 1b is superb, whereas 2b and 3b are significantly influenced by spurious features, "spurs", introduced by the local oscillator electronics, which act to increase noise in the single-sideband spectra and can damage spectral line profiles.

Combining the H and V polarizations, the RMS outside the bright lines is $T_a^\star = 10$ mK in 1b, 21 mK in 2b, and 26 mK in 3b.

3.3   Results

Preliminary data processing reveals 91 lines from 17 species in band 1b, and similar numbers in 2b and 3b, establishing OMC-2 FIR 4 as a relatively line-rich protostar (see also the review by Ceccarelli et al. in this volume). Methanol lines are advantageous to study in OMC-2 FIR 4 because they are abundant, cover a large range of excitation conditions, and are straightforward to measure because the spectrum is less crowded than in higher luminosity hot sources, in which more levels of more species can be significantly excited. Out of the hundreds of CH_3OH transitions in each band, we detect 46 lines in band 1b, 46 in 2b, and 40 in 3b, with a range of 40 K $\leq E_u \leq$ 540 K in excitation energy. Identification made use of the JPL database[2], with methanol data by Xu et al. (2008). This paper discusses lines detected with $> 4\sigma$ confidence and not blended or damaged by spurs.

3.3.1   Line profiles

Average line profiles were calculated in two energy ranges, $E_u \leq 200$ K and $E_u \geq 200$ K, for each observed band. These six average profiles are presented in Fig. 3.1, with the number of lines and relevant beam sizes given. Before averaging, each line profile was resampled to an 0.2 km·s^{-1} resolution grid with origin at the rest frequency, fitted by a single Gaussian and normalized by the intensity at the fit center. Distinguishing between the core ($|v| < 2$ km/s) and wings ($|v| > 2$ km/s) of a profile, we note that the cores of the average line profiles seem to show a broadening trend with decreasing beam size and increasing E_u. Also, the wings are weaker in the higher energy regime than in the lower.

Two-component blind Gaussian fits were made for the average profiles in each energy range and band. The fits systematically separate into a narrow and broad component, the widths and central locations of which are given in Table 3.1. The superiority of a two-Gaussian fit to that of a single Gaussian, as well as the trends mentioned in the previous paragraph, strongly suggest the presence of at least two physical emission components with different beam filling factors, as discussed in Sect. 3.4.

3.3.2   Population diagram and LTE modelling

The detection of 132 CH_3OH lines covering 500K in upper level energy presents an excellent opportunity to perform a population diagram analysis (Goldsmith & Langer 1999) to study the excitation conditions. In Fig. 3.2 we present the population diagram for the observed methanol lines. Line fluxes were obtained from single-Gaussian fits.

---

[2]The catalogue is available on-line at http://spec.jpl.nasa.gov.

E_u range	Fit	FWHM [km/s] (bands 1b, 2b, 3b)
$\leq$ 200 K	1	(1.52, 1.84, 1.72) $\pm$ (0.01, 0.08, 0.08)
	2	(4.84, 5.16, 5.62) $\pm$ (0.03, 0.11, 0.07)
$\geq$ 200 K	1	(2.22, 2.08, 2.06) $\pm$ (0.04, 0.11, 0.28)
	2	(5.68, 5.16, 4.44) $\pm$ (0.13, 0.13, 0.24)

E_u range	Fit	Gaussian centre [km/s]
$\leq$ 200 K	1	(0.02, -0.02, -0.06) $\pm$ (0.01, 0.03, 0.04)
	2	(-0.04, 0.03, -0.38) $\pm$ (0.01, 0.04, 0.04)
$\geq$ 200 K	1	(0.05, 0.05, -0.22) $\pm$ (0.02, 0.04, 0.10)
	2	(0.39, 0.23, 0.04) $\pm$ (0.05, 0.05, 0.10)

Table 3.1: Widths and central velocities of the two Gaussian fit components ("Fit") to each average line profile in Fig. 3.1.

Part of the vertical scatter in Fig. 3.2 is due to optical depth, estimated from LTE modelling to contribute $\Delta \ln (N_u/g_u) \leq 0.37$. Another factor is beam dilution, which contributes up to $\Delta \ln (N_u/g_u) \approx 2 \ln (37''/25'') \approx 0.8$ for a point source observed at the spectral edges of bands 1b and 3b. However, most of the scatter is due to differences in thermalization conditions for CH_3OH transitions with different upper level K quantum numbers. We assume the K-ladders with the lowest n_{cr}, e.g. $K_u = 0$, approach LTE, as they thermalize below the densities expected for the hot core from the Crim09 model and are seen to lie close to each other, forming the upper envelope of the diagram. The $K_u = -3$ ladder, which has a critical density of $n_{cr} \approx 10^9 cm^{-3}$, forms the lower envelope, well below most detected ladders ($-4 \leq K_u \leq 4$).

Excitation temperatures and column densities from linear fitting are given in Table 3.2 for the ladder likely closest to LTE, $K_u = 0$. The fit to the A state is shown in Fig. 3.2 and yields $T_{rot} = (145 \pm 12)$K and $N_A = (2.2 \pm 0.5) \cdot 10^{14} cm^{-2}$. Fitting the E state gives $T_{rot} = (120 \pm 8)$K and $N_A = (1.4 \pm 0.3) \cdot 10^{14} cm^{-2}$. A fit to the $K_u = -3$ ladder gives $T_{rot} = (66 \pm 2)$K. This low value is likely mostly due to subthermal excitation, but optical depth and beam dilution may also play a role, as explained earlier.

A two-component LTE model was made with the CASSIS software[3], treating methanol as a single species. The model envelope and hot core have methanol abundances of $2 \cdot 10^{-9}$ and 10^{-6}, line widths of 3 km/s and apparent diameters of $20.0''$ and $3.5''$, respectively. Source sizes, H_2 column densities, and excitation temperatures were taken to be consistent with the Crim09 source model, as well as with the observed T_{rot} values in Table 3.2, and are discussed in Sect. 3.4. Table 3.2 gives the column densities and excitation temperatures we used as input to the model and the simulated observables derived from it. The simulated population diagram, including the *Herschel*/HIFI beam efficiency, is shown as the inset in Fig. 3.2. Optical depth

---

[3]CASSIS has been developed by CESR-UPS/CNRS (http://cassis.cesr.fr).
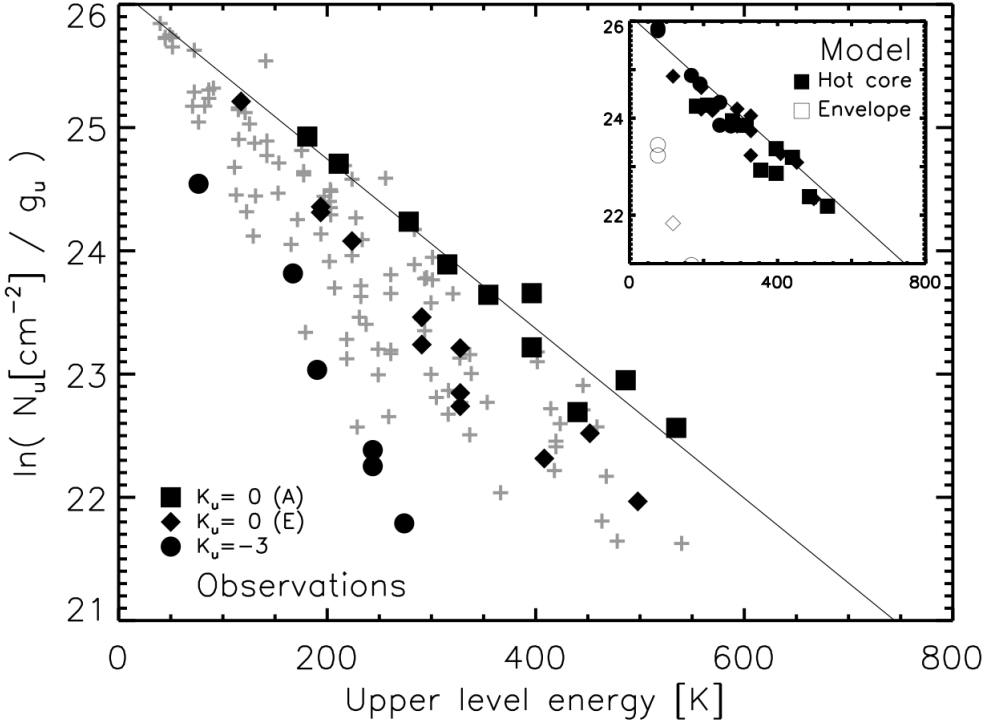
Figure 3.2: Observed and modelled (inset) CH_3OH population diagrams, plotting column density, divided by statistical weight, versus upper level energy for detected lines from all observed HIFI bands. Most transitions are given as crosses, but the $K_u = 0$ ladders for A and E states are indicated by filled squares and diamonds, and $K_u = -3$ by filled circles. The inset gives the synthetic population diagram from our LTE model for $K_u = 0$ and -3, with solid and open symbols representing the hot core and envelope contributions. The linear fit to the observed $K_u = 0$ A state lines is shown on both plots.

in the modelled lines is typically $0.01 \ldots 0.80$. The LTE conditions align transitions from all K-ladders, decreasing scatter in the simulated diagram.

The model was adjusted to reproduce the $K_u = 0$ lines, which led to a solution where the hot core dominates the line fluxes, as seen in the inset of Fig. 3.2. As the T_{rot} values in Table 3.2 show, a linear fit to the simulated observations yields results different from the model input. This is due to optical depth, blending, and beam dilution effects. The T_{rot} derived from the simulation is sensitive to factor two changes in input line width at the 10% level due to optical depth effects. Owing to the high upper level energies of the detected $K_u = 0$ transitions, the envelope emission only influences the derived T_{rot} at the 1% level in the model. It is not clear that LTE is a valid assumption even for the $K_u = 0$ ladder, and thus a more

Approach	Component	T [K] (type)	$N_{meth}[cm^{-2}]$
Population	$K_u = 0(A)$	145±12 (rot)	$(2.2 \pm 0.5) \cdot 10^{14}$
diagram	$K_u = 0(E)$	120±8 (rot)	$(1.4 \pm 0.3) \cdot 10^{14}$
LTE model	Envelope	40 (exc)	$2 \cdot 10^{14}$
input	Hot core	120 (exc)	$6 \cdot 10^{16}$
LTE simu-	$K_u = 0(A)$	164 (rot)	$1.4 \cdot 10^{14}$
lated obs.	$K_u = 0(E)$	168 (rot)	$1.7 \cdot 10^{14}$

Table 3.2: From the top: the rotational temperatures and methanol column densities derived from the observed population diagram; the input excitation temperatures and column densities of the LTE model; the rotational temperatures and column densities derived from the modelled population diagram.

comprehensive, non-LTE modelling effort is underway. Preliminary results suggest the hot core density is higher than in the Crim09 best-fit model.

3.4 Discussion

The source OMC-2 FIR 4 is a line-rich protostar with a high degree of chemical and physical complexity. The hundreds of CH_3OH transitions that are detectable with HIFI cover a wide range of excitation conditions and offer unprecedented spectral constraints on the structure of protostellar cores.

Previous knowledge (Jørgensen et al. 2006, Shim08, Crim09) suggests OMC-2 FIR 4 is dominated by three components: a large-scale, cool envelope $\sim 10^4$ AU across; a compact hot core $\sim 10^2$ AU across; and the outflow from FIR 3, in particular a suspected blue-shifted spot resulting from its interaction with the FIR 4 envelope. The hot core gives rise to a dominant part of the emission in all lines in our LTE model, but the changes in line profiles through Fig. 3.1 imply reality is more complex. The envelope may contribute significantly to the lowest excitation lines, and shocks from regions such as where the FIR 3 outflow strikes FIR 4 (Shim08) are likely to be important.

The effects of the hot core radius and H_2 column density on the line fluxes are degenerate if the lines are optically thin, as they are in our LTE model. Thus, an upper limit on the former and lower limit on the latter will result in an upper limit on the methanol abundance. Attributing the luminosity of FIR 4, 10^3 $L_\odot$, to the central protostar and assuming grain mantle evaporation at 100 K, one finds an upper limit of $R_{core} \approx 760$ AU for $0.1\mu m$ olivine grains. More realistic radiative transfer would decrease this value. At 440 pc, 760 AU extends $\sim 1.75''$ on the sky, which is adopted as the core radius in the model.

To reproduce the observed $K_u = 0$ line fluxes with LTE at an assumed $T_{exc} = 120$K, we need a column density of $N(CH_3OH) = 6 \cdot 10^{16} cm^{-2}$ in the model hot core. Integrating the Crim09 H_2 density distribution from 100 to $R_{Crim} = 440$ AU, one

obtains $N(H_2) \approx 6 \cdot 10^{22} cm^{-2}$. The source model was based on low-resolution maps, and the core is poorly constrained and excludes the inner 100 AU. We thus take the H_2 column density as a lower limit and, adopting it in the LTE model, conclude that the obtained CH_3OH abundance $X_{core} = 10^{-6}$ is a conservative upper limit. The highest abundance seen in low-mass hot cores is $2 \cdot 10^{-6}$ (Jørgensen et al. 2005). If the hot core does not dominate the line emission in reality, smaller hot core sizes and methanol column densities, as well as higher rotational temperatures, may be consistent with the data. Presently, the abundance of methanol in the envelope is very poorly constrained. We set it to $2 \cdot 10^{-9}$ in the LTE model, consistent with the factor $10^{2...3}$ abundance jump seen in hot cores (van der Tak et al. 2000; Maret et al. 2005).

The hot core density is broadly constrained to be between 10^6 and 10^8 cm^{-3} by this early analysis. Lower and higher values would be difficult to reconcile with the large-scale density profile, furthermore the population diagram suggests the K ladders with the lowest n_{cr} may approach LTE while those with the highest n_{cr} clearly deviate from it. Typical kinetic temperatures well in the ≥ 100 K hot core regime are implied by the obtained rotational temperatures of $T_{rot} \approx (120 \ldots 145)$ K. Shock contributions from the FIR 3-FIR 4 interaction spot as well as the hot core itself need to be considered before drawing further conclusions about the temperature structure.

An intriguing feature is the appearance of an asymmetry in the $E_u \geq 200$ K lines, as seen in Fig. 3.1. Because these lines should be dominated by the hot core emission, the profiles observed could represent the blue asymmetric profile expected for infalling gas (e.g. Walker et al. 1994), implying we may be seeing collapse in the central regions. To clarify whether infall, shocks, or other phenomena are responsible for the asymmetry, interferometry as well as further analysis of the *Herschel*/HIFI data, in particular the $^{13}CH_3OH$ lines, will be employed.

We note the difference in column density of the $K_u = 0$ transitions of the A and E states in Table 3.2. Whether it is truly significant will be explored in a future paper. Also, early results from an analysis of formaldehyde in OMC-2 FIR 4 will be presented in a companion paper (Crimier et al., in prep.).

4

Compact, water-rich shocks in OMC-2 FIR 4

M. Kama, C. Dominik, A.G.G.M. Tielens, C. Ceccarelli, A. López-Sepulcre, E. Caux, A. Fuente, T. Alonso-Albi

Abstract

Outflows from protostars play an important role in star formation, transporting angular momentum, dispersing protostellar envelopes and driving turbulence in interstellar gas. Water, H_2O, has been predicted and observed to be a sensitive tracer of gas shocked by such outflows, and its emission lines provide strong constraints on the gas properties. We aim to characterize the high-velocity wings of H_2O, CO and OH lines towards OMC-2 FIR 4, to better understand the role of outflows in the cluster-forming OMC-2 region in Orion. To accomplish this, we observed a large set of transitions of H_2O, CO and OH with the HIFI spectrometer on the *Herschel Space Observatory* and isolated the high-velocity wings as tracers of shocked gas. The line wing fluxes were fitted with non-LTE models to obtain the gas parameters and column densities. The water line ratios were compared with a grid of shock models. The shocked gas has an equivalent source size of 0.8" $\approx$ 340 AU. The main parameters are $n_{H_2} \sim 5 \cdot 10^5$ cm^{-3} and $T_{\mathrm{kin}} \approx 500$ K, and the column densities $N(H_2O)/\mathrm{dv} \approx 1.3 \cdot 10^{17}$ cm^{-2}/(km·s^{-1}) and $N(CO)/\mathrm{dv} \approx 1.5 \cdot 10^{17}$ cm^{-2}/(km·s^{-1}). We find abundance ratios $H_2O/CO \approx 0.9$ and $OH/H_2O \lesssim 0.3$. The column density ratios are consistent with shock models as well as with recent estimates of the cosmic ray ionization rate around OMC-2, and constrain the external UV irradiation of the post-shock gas to be at most comparable to the internal one. The high-velocity wings of H_2O and high-J CO towards OMC-2 FIR 4 originate in arcsecond-scale regions of gas processed by shocks, with flux ratios well reproduced by models of C-shocks. Our findings support the presence of a compact outflow in OMC-2 FIR 4. Sensitive observations of the high-velocity wings of HCN and CO with $\lesssim 5''$ resolution will

allow to test this hypothesis.

4.1   Introduction

In the current star formation paradigm, bipolar outflows play an important role within the first $\sim 10^5$ yr of the formation of low-mass stars (Bachiller 1996; Arce & Sargent 2006; Bally et al. 2007). The outflows help remove excess angular momentum in the accretion of gas onto the central protostar, contribute to the dissipation of the protostellar envelope by injecting energy and momentum into it, and help to drive turbulence in the interstellar medium. Surveys suggest that nearly all Class 0 protostars are driving outflows on some scale (e.g. Davis et al. 2009). In this paper, we use *Herschel*/HIFI observations of high-velocity emission from H_2O and CO to study the conditions in outflow-shocked gas towards OMC-2 FIR 4, an intermediate-mass protostar in the Orion A complex.

On spatial scales of $\geq 10^4$ AU, molecular outflows are often seen in CO emission, particularly in high-velocity ($\Delta v \gtrsim 10$ km/s) line wings that are seen in most protostellar sources (e.g. Zhang et al. 2005) and are not easily explained by other dynamical processes, such as turbulence or infall. Shocked clumps of gas along the outflow axis are seen in near-infrared ro-vibrational lines of H_2 (e.g. Caratti o Garatti et al. 2006) and in (sub-)millimetre lines of the grain destruction tracer, SiO (e.g. Martin-Pintado et al. 1992; Nisini et al. 2007). These shocked regions typically have a size of order $10^2 \ldots 10^3$ AU. In some sources, the outflows themselves are very compact – the intermediate-mass protostars NGC 1333 IRAS4B and OMC-3 MMS 6 have outflow lobes extending only $\sim 10^3$ AU (Di Francesco et al. 2001; Takahashi & Ho 2012).

Another diagnostic tool of interstellar shocks is water, H_2O. As the shock temperature exceeds a few hundred kelvin, neutral-neutral reactions involving O, H_2, OH and H can proceed rapidly (Baulch 1972), producing abundances up to $[H_2O]/[H_2] = X(H_2O) \sim 10^{-4}$ (Kaufman & Neufeld 1996). Water also has a high critical density due to its strong radiative transitions. Typical outflow shocked gas is sufficiently hot ($T_{kin} \sim 200 \ldots 1000$ K) and dense ($n_{H_2} \sim 10^5$ cm^{-3} in protostellar envelopes) to favour H_2O production and excitation.

Water can also be produced on dust grain surfaces in cold, $T_{kin} \lesssim 100$ K, environments, where it can reach an abundance of $X(H_2O) \sim 10^{-4}$. Heating or shock sputtering is required to release this water into the gas phase and increase the abundance similarly to the high-temperature reactions. The pure gas-phase production of H_2O at low temperatures yields low abundances, of order 10^{-7}. Photodissociation (van Dishoeck & Black 1988; Crovisier 1989; van Dishoeck et al. 2006), which produces OH from water, and freeze-out can lower the H_2O abundance. In hot, well-shielded gas, $X(H_2O)/X(CO) \sim 1$, while in cold gas it can be as low as $X(H_2O)/X(CO) \sim 10^{-4}$. Some recent models of the protostellar envelope and outflow cavity system combine results from the modelling of quiescent envelopes, photon-dominated regions and shocks (Visser et al. 2012). According to these models, $> 99\%$ of the H_2O line flux from such a system comes from shocked gas, while $20 \ldots 80\%$ of the high-J CO emission

traces shocked and UV-irradiated gas, with relative contributions varying from source to source.

Water is the dominant absorber of infrared radiation in the Earth's atmosphere (e.g. Dickinson & Cicerone 1986), and thus high sensitivity observations of H_2O transitions from astronomical objects typically require the use of space telescopes. Previous advances from ODIN, SWAS and ISO are now being complemented by a stream of results from the *Herschel Space Observatory*. The high abundance of H_2O in outflow-shocked gas has been repeatedly confirmed by observations (e.g. Ceccarelli et al. 1999; Nisini et al. 1999; Lefloch et al. 2010; Bergin & van Dishoeck 2012; Herczeg et al. 2012) and many recent *Herschel* results are reviewed in van Dishoeck et al. (2011). The HIFI heterodyne spectrometer on *Herschel* offers an unprecedented combination of frequency coverage, sensitivity and spectral and spatial resolution ($d\nu/\nu \approx 10^6$, $\theta \approx 11'' \ldots 40''$), allowing velocity-resolved observations of many H_2O lines. We present an analysis of *Herschel*/HIFI observations of the high-velocity wings of H_2O, CO and OH towards the protostar OMC-2 FIR 4.

We begin by presenting the source in Sect. 4.2, and the data in Sect. 4.3 and 4.4. The analysis approach and results are described in Sect. 4.5. We discuss the implications in Sect. 4.6 and summarize our conclusions in Sect. 4.7. Finally, Appendix 4.A presents the results of line wing fitting which are not used in our analysis, but may prove useful in comparisons with other sources.

4.2 The OMC-2 FIR 4 core

OMC-2 is an intermediate-mass star-forming clump in the Orion region (Gatley et al. 1974), at a distance of ~ 420 pc (Hirota et al. 2007; Menten et al. 2007). It hosts a small group of sources ranging from Class 0 protostars to T Tauri stars, making it a cluster- or association-forming clump. Here, we focus on a part of the Southern half of OMC-2, shown in Fig. 4.1. On scales of 3 arcminutes, the average hydrogen density in this subclump is $n_H \sim 4 \cdot 10^5$ cm^{-3} (Mezger et al. 1990). The Class 0 protostar OMC-2 FIR 4 is the dominant millimetre source (Chini et al. 1997), while the Class I source OMC-2 FIR 3 dominates at $\sim 50 \ldots 100$ μm (Pendleton et al. 1986).

A model of the large-scale structure of the OMC-2 FIR 4 protostellar core was presented by Crimier et al. (2009), giving an envelope mass of 30 $M_\odot$ and a luminosity of $L = 10^3$ $L_\odot$. More recently, based on new SOFIA and *Herschel* data, Adams et al. (2012) found $L = 50$ $L_\odot$, a mass accretion rate of $\dot{M}_{acc} \sim 10^{-4}$ $M_\odot$/yr and an inclination $i = 50°$. A discussion of the large disagreement in luminosity is outside the scope of this paper, but a useful paragraph can be found in López-Sepulcre et al. (submitted). We consider OMC-2 FIR 4 an intermediate-mass protostar with a luminosity likely within a factor of two of 500 $L_\odot$.

The CHESS *Herschel*/HIFI spectral survey of OMC-2 FIR 4 has revealed a rich molecular sub-millimetre spectrum (Ceccarelli et al. 2010, Kama et al., submitted) and the existence of a hot core like central region (Kama et al. 2010). Continuum interferometry has revealed several chemically diverse sub-cores within the $\sim 10^4$ AU radius FIR 4 core (Shimajiri et al. 2008, López-Sepulcre et al., in prep.), although
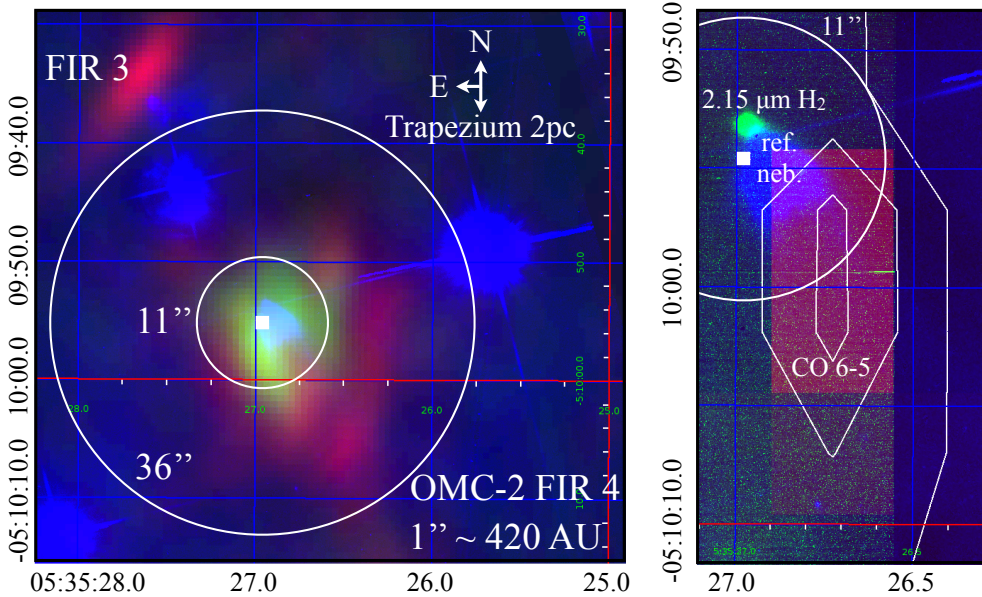
Figure 4.1: The OMC-2 FIR 4 core and its vicinity. The white square marks the nominal source position. *Left panel:* Continuum interferometric images at 3.3 mm and 2 mm (red and green, Shimajiri et al. 2008, López-Sepulcre et al., in prep.) and an archival Hubble Space Telescope 0.814 μm image (blue, PI D.Padgett). The white circles mark two characteristic HIFI beam sizes, 36" and 11". The nearby source FIR 3, a likely outflow-driving source, is also marked. *Right panel:* A close-up of the 0.814 μm nebula (blue): a CSO map of CO $6-5$ emission (white contours at 150, 200 and 250 K·km·s^{-1} and large red pixels, PI M.Houde) and a VLT/NACO 2.15 μm image (green, PI T.Stanke) showing H_2 emission. White circles and blue data as in the left panel. The right panel data are discussed in Sect. 4.6.

one sub-core clearly dominates the mass and millimetre emission.

Observations of CO and H_2O lines have shown the presence of broad wings (Johnstone et al. 2003; Shimajiri et al. 2008, Kama et al., submitted), extending to ± 25 km·s^{-1} from the central $v_{\rm lsr} \approx 11.4$ km·s^{-1}, which indicate the presence of an outflow towards FIR 4. Emission from shocked gas in this outflow is the subject of this paper. The outflow source is unclear and is discussed in Sect. 4.6.3.

4.3 Observations and data reduction

The *Herschel*/HIFI observations of OMC-2 FIR 4 were carried out in 2010 and 2011 as part of the guaranteed-time Key Programme CHESS[1], PI Cecilia Ceccarelli, and

---

[1] http://www-laog.obs.ujf-grenoble.fr/heberges/hs3f/

covered a number of transitions of H_2O, CO, OH and their isotopologues.

HIFI (de Graauw et al. 2010) is a high-sensitivity far-infrared heterodyne spectrometer on the *Herschel Space Observatory* (Pilbratt et al. 2010), with a range of $480 \ldots 1900$ GHz and spectral resolution of $d\nu/\nu \sim 10^6$. The observations were carried out in Dual Beam Switch mode, using the Wide Band Spectrometer (WBS) with a native resolution of 1.1 MHz (~ 0.7 to 0.2 km/s). The data were reduced with the Herschel Interactive Processing Environment (`HIPE`, Ott 2010b) software[2], versions 6.2.0 and 8.0.1. We used telescope and spectrometer parameters and performance estimates, including a line flux calibration uncertainty of 10%, from Roelfsema et al. (2012).

We extracted lines of H_2O, CO, OH and their isotopologues from the CHESS survey data, including eight o-H_2O, seven p-H_2O and one $H_2^{18}O$ lines; the ^{12}CO rotational ladder from $J_u = 5$ through 16, excluding 12; the ^{13}CO ladder from $J_u = 5$ through 11, and additionally 14 and 16; and two hyperfine triplets of OH, at 1834 and 1837 GHz. The lines are summarized in Table 4.2. The continuum is detected at the few hundred millikelvin level and a fitting formula for it is presented in Chapter 2.

Both fundamental H_2O lines lie in overlaps of HIFI bands: o-H_2O in bands 1a and 1b, and p-H_2O in 4b and 5a. To combine the spectra, sideband gain ratio (SBR) corrections must be applied but were only available for band 5 at the time of analysis. Accordingly, the p-H_2O $1_{1,1} - 0_{0,0}$ line was scaled down by 3% in band 5. Its band 4 flux was scaled down by 7% to match the band 5 value. Correction factors for bands 1a and 1b were provided ahead of official release by the HIFI Instrument Control Centre[3]. The o-H_2O $1_{1,0} - 1_{0,1}$ line was scaled down by 4% in band 1a and by 12% in 1b. For both lines, the data were then noise-weighted and averaged. The other lines were not corrected for SBRs, but allowance is made for this in the flux calibration error budget.

The analysis in this paper relies on emission in the high-velocity line wings, which may be affected by baseline subtraction as the wings have a low intensity but are extended in velocity. To quantify this, we baselined several lines multiple times, varying the baseline polynomial order, and found variations in the fluxes from 1% to 8%. We generalized this to a 5% baselining uncertainty on the line wing fluxes. This is an overestimate for the strongest line wings.

In the CO lines up to $J_u = 11$, and in some lines of H_2O, a narrow dip is observed near the line centre. This was determined to be due to contaminating emission at the reference positions in the case of CO, but source-related in the case of H_2O, as discussed in the next section.

4.4   Line profiles in the HIFI spectra

The H_2O spectra used in this work are shown in Fig. 4.2, while the CO, $H_2^{18}O$ and OH lines are presented in Kama et al. (submitted). Fluxes and other parameters for all lines used in our analysis are given in Table 4.2. A flux measurement confidence

---

[2] `http://herschel.esac.esa.int/HIPE_download.shtml`
[3] `http://herschel.esac.esa.int/esupport/`

level of 3σ was adopted as the detection criterion. In the case of a non-detection a flux of zero, with the corresponding measurement uncertainty, was used in the χ^2 calculation.

Herschel/HIFI observations of various sets of H_2O lines have previously been presented for a range of sources, including low-mass protostars in NGC 1333 (Kristensen et al. 2010), L1448 (Kristensen et al. 2011) and Serpens (Goicoechea et al. 2012); the intermediate-mass protostar NGC 7129 FIRS 2 (Johnstone et al. 2010); several high-mass protostars and energetic sources (Chavarría et al. 2010; Marseille et al. 2010; Melnick et al. 2010; van der Tak et al. 2010; Wyrowski et al. 2010); and pure outflow shocks (e.g. Lefloch et al. 2010). In terms of line profile shapes, the H_2O emission in OMC-2 FIR 4 resembles those in most other HIFI targets, in particular with regards to the presence of high-velocity line wings. Broken down into Gaussian components, the H_2O lines consist of a broad (FWHM $\sim 20\ldots 40$ km/s) and medium (~ 10 km/s) emission component and a narrow (FWHM $\sim 3\ldots 6$ km/s) self-absorption component. With the recent *Herschel*/HIFI observations referred to above, these components have been discovered to be typical of H_2O in low- through high-mass protostars. The detection of all lines in emission is more characteristic of low- than high-mass protostars.

The broad line wings most likely originate in shocks in an outflow. The medium component has also been linked to shocks (Kristensen et al. 2010), but ones originating in denser gas and likely related to processes in the innermost envelope around the protostar. The narrow component, seen in absorption, traces quiescent, cold large-scale envelope material.

The CO lines are very similar to those of H_2O in terms of the broad and medium emission components. The line centres are difficult to interpret due to contaminating narrowband emission in both reference positions for lines up to $J_u = 11$. This was verified by examining a calibrated difference of the reference spectra with the HIPE plugin `HIPI`[4]. The ^{13}CO lines and the line wings are not affected. In the case of H_2O, no evidence of strong contamination was found in the reference spectra for o-H_2O $1_{1,0} - 1_{0,1}$ and p-H_2O $1_{1,1} - 0_{0,0}$, and self-absorption was found to be a common feature in o-H_2O spectra of protostars observed with SWAS (Franklin et al. 2008). We thus consider it real in OMC-2 FIR 4, as well. It is prominent in all H_2O lines up to $E_u = 162$ K (o-H_2O $3_{0,3} - 2_{1,2}$). In higher lines, a smaller dip appears at $\sim 10\ldots 11$ km $\cdot$ s^{-1}. This dip is typically well fitted as a weak Gaussian absorption feature, however overlapping emission peaks could also form similar profiles.

The spatial structure underlying the H_2O and CO emission in OMC-2 FIR 4 is complex, as indicated by interferometric observations of clumps on 5" to 10" scales (Shimajiri et al. 2008, López-Sepulcre et al., submitted) and by the diversity of line profiles from different chemical species (Kama et al., submitted). We thus postpone the analysis of the H_2O line centres until a better description of the source structure on small scales is available. A companion paper will present a detailed model of the CO emission from the envelope (Alonso-Albi et al., in prep.).

The o-H_2O $5_{3,2} - 4_{4,1}$ line at 620 GHz is likely detected due to the excellent sensi-

---

[4]Available by default with the HIPE 10 release.
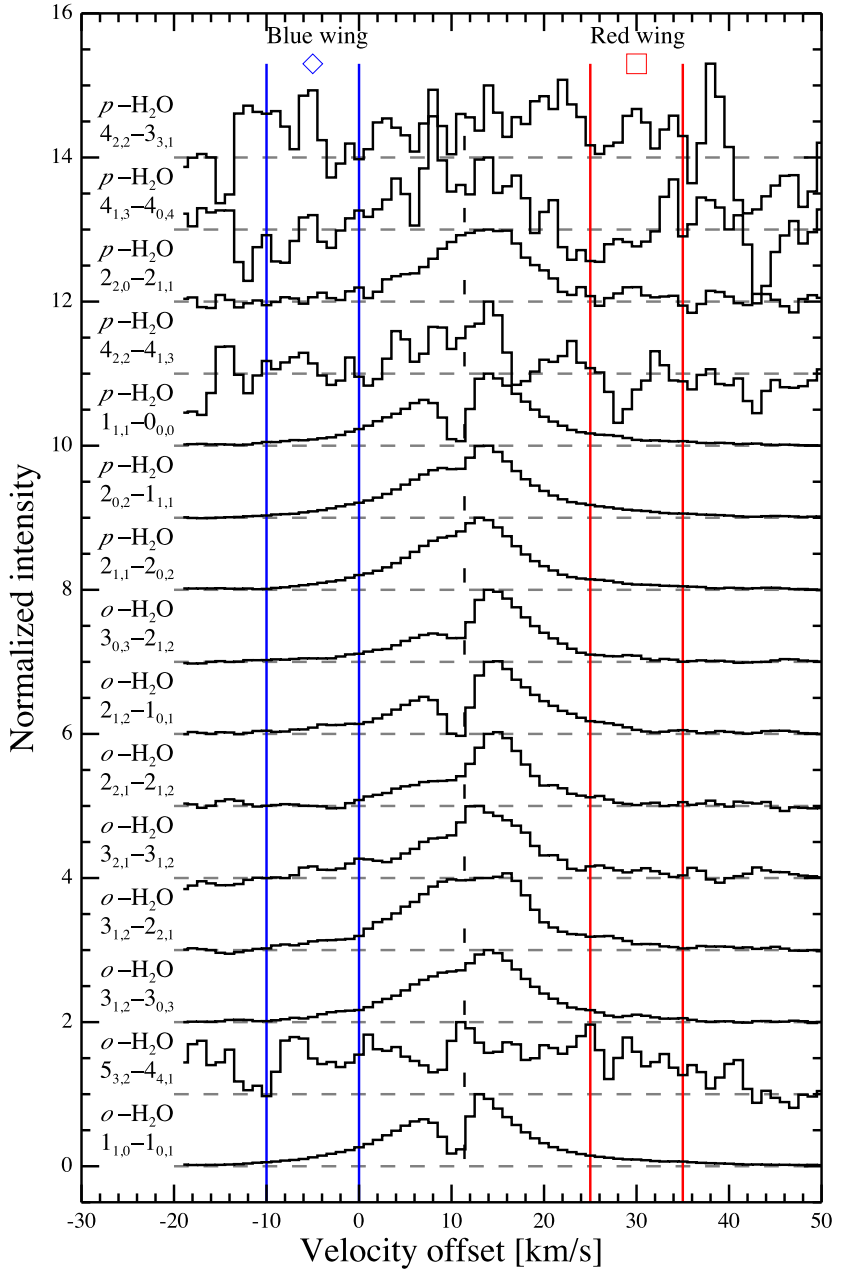
Figure 4.2: Transitions of H_2O observed towards OMC-2 FIR 4 and used in this work. The profiles are binned to $1 \ km \cdot s^{-1}$ and normalized. A vertical offset of one is applied for clarity and a dashed line denotes the systemic velocity of 11.4 km/s. For the line parameters, see Table 4.2.
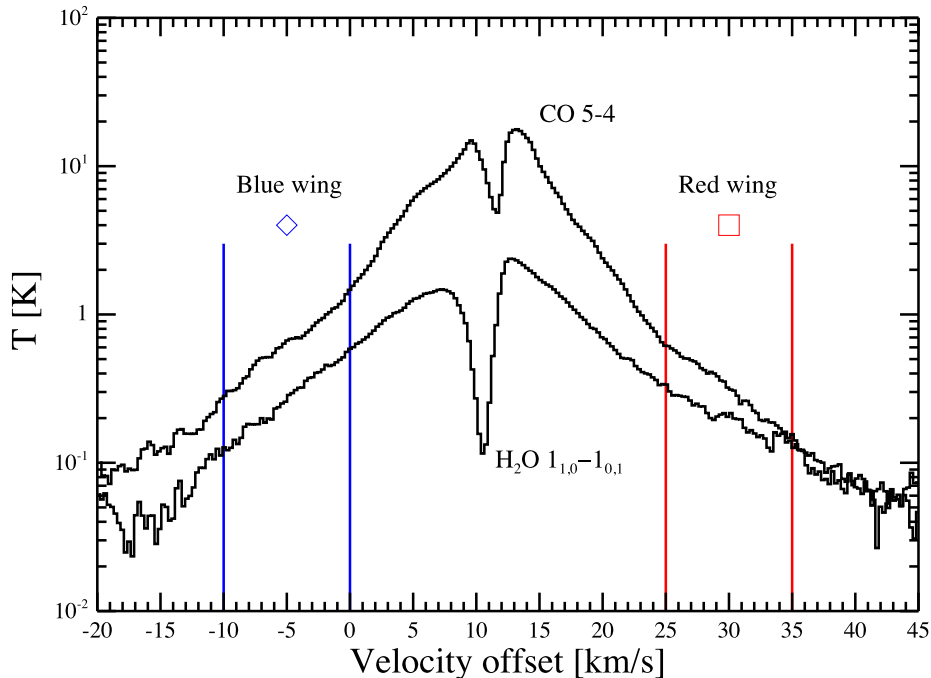
Figure 4.3: The CO $5-4$ and the o-H_2O $1_{1,0} - 1_{0,1}$ line, plotted on a logarithmic intensity scale to emphasize the exponential-like wing profiles. The H_2O/CO intensity ratio increases with velocity. Vertical blue and red lines indicate the velocity intervals used for the line flux integration. The diamond and square symbols are used throughout the paper.

tivity and stability of HIFI in band 1. As seen in Fig. 4.2, it has a very low intensity but is highly significant in flux terms due to its great width, which is dominated by the broad component. The feature is present regardless of baseline subtraction and represents a substantial excursion from the usual baseline variation in band 1. It may represent the extremely high velocity component sometimes seen in CO observations of outflows (Bachiller et al. 1990), in which case it is unclear why our CO data do not show this component more prominently.

It was recently discovered that the high-velocity wings of CO and H_2O in the outflow shock, L1157-B1, are described by a sum of three exponential functions of the form $T_{mb} \propto \exp(|v/v_0|)$, where v_0 is a fitting parameter (Lefloch et al. 2012). In Fig. 4.3, we show the lowest-lying HIFI CO and H_2O lines from OMC-2 FIR 4 on a log-linear scale to point out that, within the chosen velocity regimes, these are also well-described by such functions, which are straight lines on this scale. In Appendix 4.A, we also give the fitted v_0 values for all the H_2O and CO lines, for the
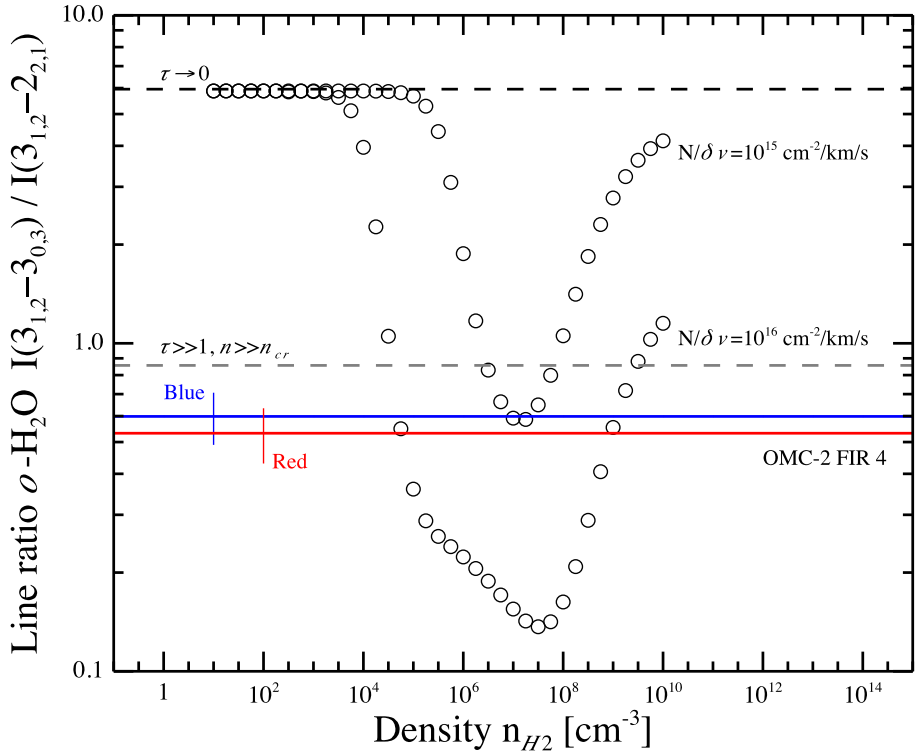
Figure 4.4: The o-H$_2$O $3_{1,2} - 3_{0,3}$ and $3_{1,2} - 2_{2,1}$ line flux ratio as a column density diagnostic. The dashed lines give the theoretical ratios for the optically thin (5.9) and the thermalized very high optical depth (0.86) case. Black circles show sets of RADEX models for two $N(o$-H$_2$O$)/\delta v$ values as a function of $n_{\mathrm{H_2}}$ at $T_{\mathrm{kin}} = 500$ K. The blue and red lines give the values observed for OMC-2 FIR 4 in the blue and red wings, with vertical bars giving 3σ uncertainties.

blue and red wings. Within the fitting errors, most of the studied line wings are of similar shape. The fits are provided for reference, but we do not pursue this approach further in this work.

For our analysis, described next, we integrate the flux separately in either wing.

4.5   Analysis

To determine the typical properties of the gas giving rise to the high-velocity emission, we analyze two velocity intervals: $-10\ldots0$ and $25\ldots35$ km$\cdot$s^{-1}. As Fig. 4.7 shows, the relative contributions of the wings in these intervals are consistent within the
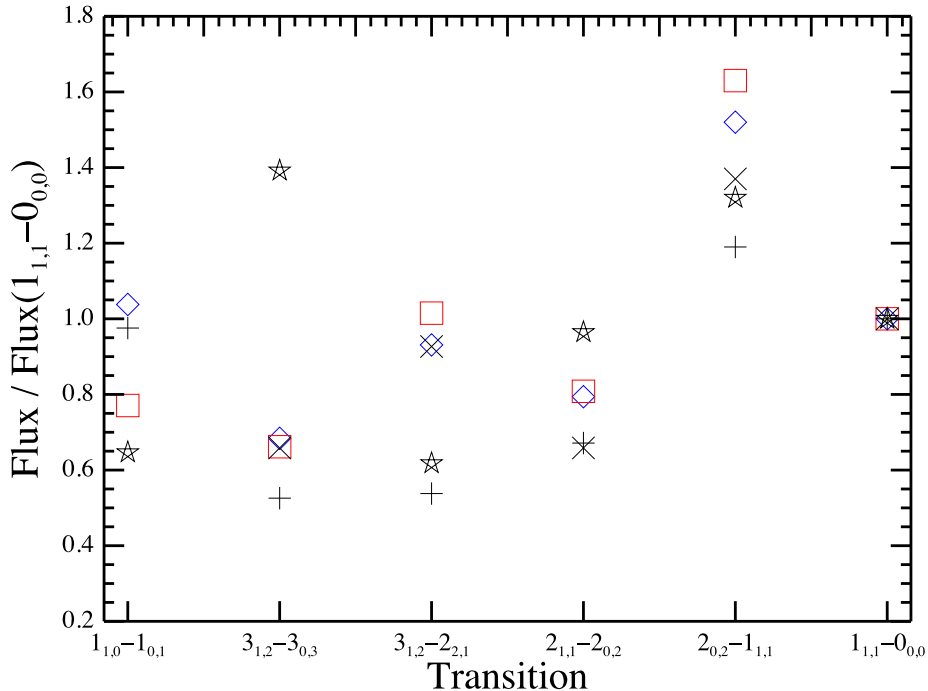
Figure 4.5: High-velocity emission in a selection of water lines from a sample of protostars. Shown are the blue and red wing Kelvin-scale fluxes for OMC-2 FIR 4 (blue diamonds, red squares; this work), Gaussian fits for L1448-MM (upright crosses; Kristensen et al. 2011) and NGC 1333 IRAS 2A (diagonal crosses; Kristensen et al. 2010), as well as the integrated $H_2^{18}O$ fluxes for Orion-KL (stars; Melnick et al. 2010). Each source is normalized to its $1_{1,1} - 0_{0,0}$ line flux. The ratio of lines from the $3_{1,2}$ level can be interpreted with Fig. 4.4.

uncertainties, implying they originate in physically similar components that can, as a first attempt, be modelled with one set of parameters, with the benefit of an increased number of constraints.

4.5.1   The column density of water

$N(H_2O)$ is constrained by the ratio of the o-H_2O $3_{1,2} - 3_{0,3}$ and $3_{1,2} - 2_{2,1}$ lines, at 1097.365 and 1153.127 GHz, as shown in Fig. 4.4. The lines share an upper level, and have very different radiative decay rates ($1.648 \cdot 10^{-2}$ s^{-1} and $2.634 \cdot 10^{-3}$ s^{-1}, respectively) and collision rates. These features make this line flux ratio sensitive to $N(o$-$H_2O)$ and to n_{H_2}. Beam dilution does not substantially affect this, as the

Table 4.1: Results of the RADEX model fitting of the H_2O and CO wings. The uncertainties on the fitted parameters are obtained from Gaussian fits to the $\min{(\chi^2)}$ curve for that parameter. Notes: [a] – collision rates from (Faure & Josselin 2008) used for $T_{\mathrm{kin}} > 1500$ K.

Parameter	Best fit range	Grid range	Units
n_{H_2}	$10^{4.7\pm0.5}$	$10^{2.5}\ldots10^{8.5}$	cm^{-3}
T_{kin}	500 ± 300	$20\ldots3000^{a}$	K
θ	0.8 ± 0.3	$0.2\ldots60$	$''$
$N(o\text{-}H_2O)/\delta v$	$10^{17.0\pm0.5}$	$10^{14}\ldots10^{18}$	$\mathrm{cm}^{-2}/\,\mathrm{km/s}$
$N(CO)/\delta v$	$10^{17.2\pm0.2}$	$10^{14}\ldots10^{18}$	$\mathrm{cm}^{-2}/\,\mathrm{km/s}$
$N(OH)/\delta v$	$\lesssim 3\cdot10^{16}$	$10^{13}\ldots10^{18}$	$\mathrm{cm}^{-2}/\,\mathrm{km/s}$

transition frequencies are similar.

In Fig. 4.4, we plot several theoretical values and numerical models for this line ratio and compare them with the observations of OMC-2 FIR 4. Circles show RADEX models for $N(o\text{-}H_2O)/\delta v = 10^{15}\ \mathrm{cm}^{-2}/(\mathrm{km\cdot s^{-1}})$ and $\sim 10^{16}\ \mathrm{cm}^{-2}/(\mathrm{km\cdot s^{-1}})$, with $T_{\mathrm{kin}} = 500$ K. At the lowest densities, the models converge to the optically thin limit, the ratio of $A_{\mathrm{ul}}\cdot\nu_{\mathrm{ul}}$ values (black dashed line). The theoretical high optical depth and local thermodynamic equilibrium limit (gray dashed line) is reached with even higher column densities, $\sim 10^{17}\ \mathrm{cm}^{-2}/(\mathrm{km\cdot s^{-1}})$ (not shown). Higher gas temperatures push the valleys in the RADEX curves to the lower left, n_{H_2} and the ratio decrease by $\sim 10\ldots20\%$ if the temperature is raised from 500 to 2000 K. Our observations (blue and red lines with 3σ errorbars) constrain the column density of $o\text{-}H_2O$ per unit velocity in both wings to be $\gtrsim 10^{15}\ \mathrm{cm}^{-2}/(\mathrm{km\cdot s^{-1}})$. Many H_2O lines are optically thick at the column densities implied for OMC-2 FIR 4, making them sensitive also to the source size, θ.

In Fig. 4.5, we compare the OMC-2 FIR 4 blue and red wing fluxes (blue diamonds and red squares) with values, usually from broad Gaussian fits, for other sources: L1448-MM (upright crosses; Kristensen et al. 2011) and NGC 1333 IRAS 2A (diagonal crosses; Kristensen et al. 2010), and the $H_2^{18}O$ fluxes for Orion-KL (stars; Melnick et al. 2010). For each source, the fluxes are normalized to the corresponding $1_{1,1}-0_{0,0}$ line. Differences in the transitions originating in the $3_{1,2}$ level indicate differences of an order of magnitude or more in $N(o\text{-}H_2O)/\delta v$ between the sources. Orion KL stands out in this respect with a line ratio of around two. It is the only source for which $H_2^{18}O$ is plotted, and this isotopologue is more optically thin as it has an abundance ~ 450 times below H_2O. Within the presented subsample of bright lines, OMC-2 FIR 4 is most similar to NGC 1333 IRAS 2A.

4.5.2 RADEX modeling

Flux measurements for the H_2O, CO and OH line wing regions analyzed in this work are summarized in the two rightmost columns of Table 4.2. To determine the

properties of the emitting gas, we compared the observations with a grid of models with the publicly available RADEX[5] code (van der Tak et al. 2007). Molecular data are taken from the LAMDA[6] (Schöier et al. 2005), JPL[7] (Pickett et al. 1998) and CDMS[8] (Müller et al. 2005) databases and include collision rates for H_2O (Dubernet et al. 2009; Faure & Josselin 2008), CO (Yang et al. 2010) and OH (Offer et al. 1994). Given n_{H_2}, T_{kin}, a column density of the target molecule and a geometry, which we assume to be a face-on slab, the code calculates non-LTE level populations and emergent line fluxes. The parameter ranges of the grid are given in Table 4.1.

We do not consider infrared pumping via ro-vibrational transitions. As the typical dust temperature in OMC-2 FIR 4 is small, $\sim 20\ldots50$ K, and no emission is detected from vibrationally excited H_2O, this should not introduce major errors.

We assume the water ortho to para spin state ratio to be $o/p = 3$, the thermalized H_2 value at $T_{kin} \gtrsim 200$ K, except at lower temperatures, where we fit only for o-H_2O. For the $H_2O/H_2^{18}O$ ratio, we adopt 450, based on the range given in Wilson & Rood (1994). For CO, we adopt a $^{12}CO/^{13}CO$ isotope ratio of 50 (Liszt & Ziurys 2012). Higher ratios, such as 63 (Langer & Penzias 1993), were found to provide a poor match to the ^{12}CO and ^{13}CO lines. As all the ^{13}CO wings are weak or not detected, the ratio has little effect on the modeling. We use the cosmic carbon abundance of $\sim 3\cdot10^{-4}$ (Cardelli et al. 1996) as an upper limit on the CO abundance in interstellar gas.

The same grid of n_{H_2}, T_{kin} and source sizes (θ) was used to model a wide range of H_2O and CO column densities. All the CO lines can be fitted with a single model, however we did not use these results as the high-J CO lines typically arise in the same gas as H_2O, while low-J CO emission is thought to trace gas with different properties (e.g. Visser et al. 2012). Therefore, we only use the CO lines with $J_u \geq 11$ together with H_2O in the model fitting. In Fig. 4.7, all the CO lines are shown to verify the model for consistency.

4.5.3 RADEX results

The best-fit model to both H_2O and high-J CO, with $\chi^2_{red} = 2.1$, is shown alongside the observations in Fig. 4.7 and the parameters are summarized in Table 4.1, with uncertainties corresponding to the $\chi^2_{red} \lesssim 2.5$ range. The χ^2 surface for n_{H_2} and T_{kin} is shown in Fig. 4.6. The best fit model is the same if only H_2O is used to constrain it.

We find $n_{H_2} = 10^{4.7\pm0.5}$ cm^{-3}, $T_{kin} = (500 \pm 300)$ K and a source size of $\theta = (0.8\pm0.3)$". The o-H_2O column density in the best-fit model is $N(o$-$H_2O)/\delta v = 10^{17}$ cm^{-2} / km $\cdot$ s^{-1}, equivalent to $N(H_2O)/\delta v = 1.3 \cdot 10^{17}$ cm^{-2} / km $\cdot$ s^{-1}, and the CO column density $N(CO)/\delta v = 1.5 \cdot 10^{17}$ cm^{-2} / km $\cdot$ s^{-1}. Using these values, we find $H_2O/CO \approx 0.9$. If the total CO abundance is of order $\sim 10^{-4}$, as expected for dense molecular gas, this implies $X(H_2O) \sim 10^{-4}$. Using the best-fit

---

[5]RADEX: `home.strw.leidenuniv.nl/~moldata/radex.html`
[6]LAMDA: `home.strw.leidenuniv.nl/~moldata`
[7]JPL: `http://spec.jpl.nasa.gov/`
[8]CDMS: `http://www.astro.uni-koeln.de/cdms/`
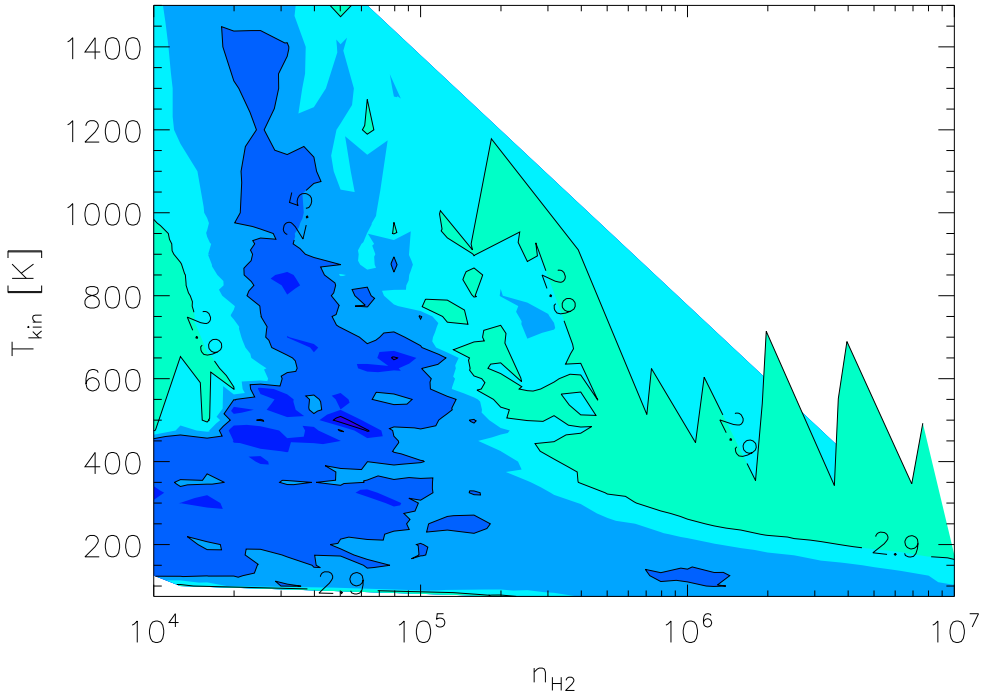
Figure 4.6: A contour map of the χ^2 for the H_2O-CO models as a function of n_{H_2} and T_{kin}, where darker colour indicates a smaller χ^2. Only $\min(\chi^2)$ is shown for each n_{H_2}-T_{kin} pair, hiding the other three model parameters $[N(H_2O), N(CO), \theta]$. Contour lines are drawn for $\chi^2_{\text{red}} = 2.1$ (small patch at $T_{\text{kin}} \sim 500$ K, $n_{H_2} \sim 10^{4.7}$ cm^{-3}), 2.5 and 2.9. The colour levels go in χ^2_{red} steps of 0.2. The roughness of the contours originates in the discrete sampling of the model parameters.

model parameters and a 3σ flux upper limit of ~ 200 mK·km·s^{-1} in each high-velocity wing, we determined an upper limit of $N(\text{OH}) \lesssim 3 \cdot 10^{16}$ cm^{-2} / km·s^{-1}, giving OH/$H_2O \lesssim 0.3$.

For CO, the modelled optical depth is around unity for the lines near $J_u = 11$, and below unity for the lower and higher ones. The wings of the H_2O lines with $E_u < 400$ K are optically thick ($\tau \sim 10^1 \ldots 10^3$). To verify the RADEX results at such high optical depths, we used the best-fit model parameters with a spherical geometry in RADEX and in the 1D Monte Carlo code, RATRAN[9] (Hogerheijde & van der Tak 2000). The output fluxes are consistent within a factor of two.

---

[9]`http://www.sron.rug.nl/∼vdtak/ratran/frames.html`
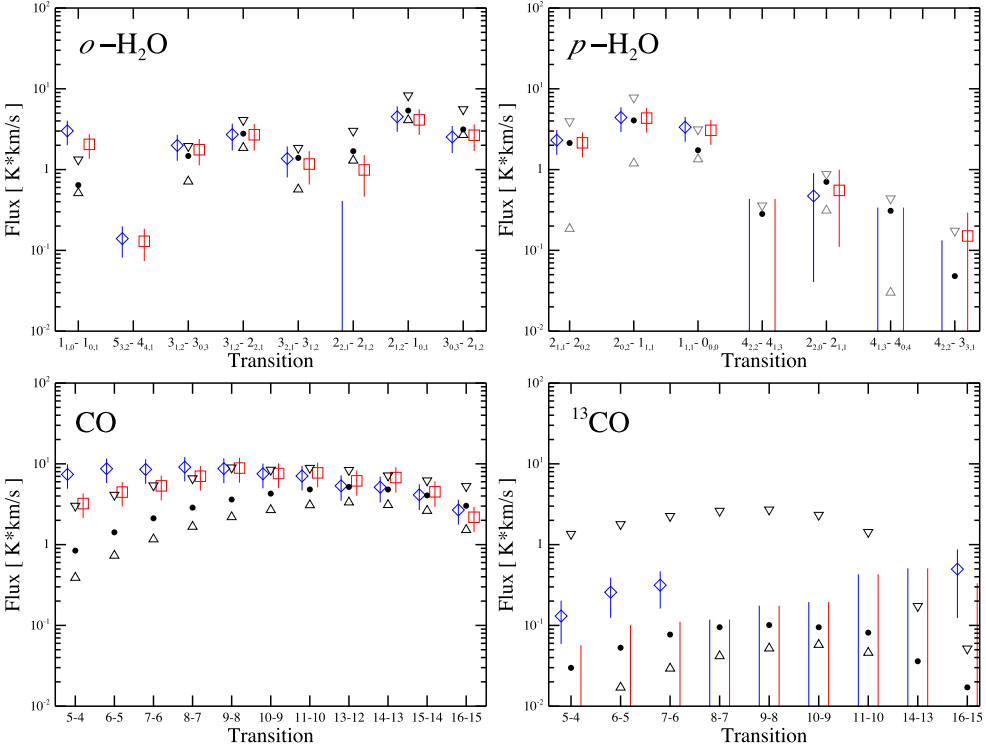
Figure 4.7: The o-H_2O (top left panel) and p-H_2O (top right panel) line fluxes in the blue (blue diamonds) and red (red squares) wings. Overplotted are the best-fit RADEX model fluxes (filled black circles) and the extreme fluxes for each line for models within $\chi^2_{\mathrm{red}} = 2.5$ (up- and down pointing black triangles). The flux uncertainties are 3σ and include the RMS noise, instrumental flux calibration and baselining errors. Symbolless vertical lines indicate 3σ upper limits. The model values are always below the plot range for the o-H_2O $5_{3,2} - 4_{4,1}$ line. For the best-fit model, $\chi^2_{\mathrm{red}} = 2.1$.

4.5.4   Comparison with shock models

Magnetized shocks in molecular clouds fall into two broad categories: "continuous" and "jump", or C- and J-shocks (Draine 1980). Both are shocks propagating through a weakly ionized gas permeated by a magnetic field. In a C-shock, the magnetic field perpendicular to the shock velocity vector is strong enough for ambipolar diffusion to heat the gas ahead of the neutral density wave, causing a smoothing-out of the thermodynamic variables. In a J-shock, the perpendicular magnetic field component is weaker and the thermodynamic variables are discontinuous. The temperatures reach up to $\sim 10^5$ K in J-shocks, and up to $\sim 10^3$ K in C-shocks.

As a check on our RADEX results and on the interpretation of the high-velocity
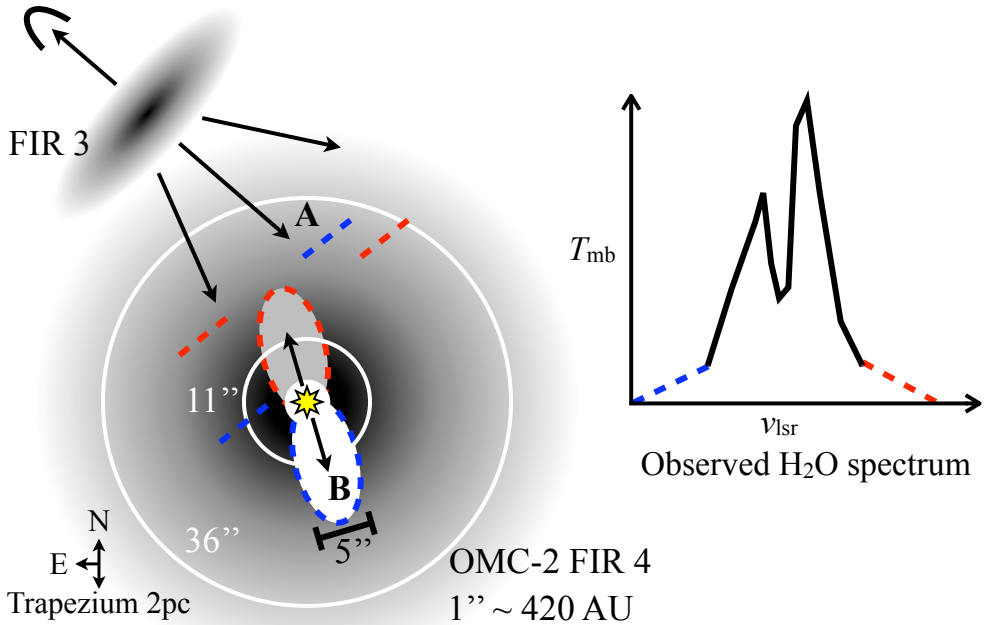
Figure 4.8: A schematic showing two hypotheses of the origin of the high-velocity wings. **A**: an outflow from FIR 3 interacting with the FIR 4 envelope, with straight dashed lines representing small shocks across the envelope, and **B:** a compact outflow from FIR 4, with dashed ellipses representing shocks along the outflow cavity walls. The scale roughly corresponds to Fig. 4.1 and the white circles show the largest and smallest HIFI beams for our data. An illustration of a typical H_2O line profile shows the correspondence between the shocks and the line profile regions analyzed in this work.

wings as being shocked gas, we determined the best fit in the small grid of C- and J-shock models by Flower & Pineau Des Forêts (2010). These authors sampled pre-shock densities of $2 \cdot 10^4$ and $2 \cdot 10^5$ cm^{-3}, and shock velocities of 10, 20, 30, 40 km·s^{-1} (for C-shocks) and 10, 20, 30 km · s^{-1} (for J-shocks). They calculated the density, temperature and chemical structure of the shocks and simulated the emergent flux for a large set of CO and H_2O lines.

We performed a chi-squared minimization on the line flux ratios. The observations were beam-diluted using the $\theta = 0.8$" source size determined in the previous section. All three best-fitting shock models are C-shocks in a medium with a pre-shock density of $2 \cdot 10^5$ cm^{-3}. The minimum is $\chi_{red}' = 1.6$, for a shock velocity of 40 km · s^{-1}. Shocks of 30 km·s^{-1} and 20 km·s^{-1} have χ_{red}' values of a factor of a few larger, but all the other models have chi-squared values two or more orders of magnitude larger than the best-fitting model.

Even though the Flower & Pineau Des Forêts (2010) model grid is very coarse, it suggests a match with a C-shock of $v \geq 20$ km · s^{-1}, propagating in a gas with

pre-shock density $\sim 10^5$ cm^{-3}. This is of the same order as the post-shock density found in the previous subsection, suggesting a relatively low compression factor of the gas, but follow-up work is needed to understand if this explanation is sufficient to explain the density found from RADEX modeling.

4.6 Discussion

4.6.1 Physical properties of the shocked gas

We derive the properties $n_{H_2} \sim 5 \cdot 10^4$ cm^{-3} and $T_{kin} \approx 500$ K (see Table 4.1) for the source of the analysed emission. A comparison of our observations with the advanced shock models of Flower & Pineau Des Forêts (2010) shows consistency with a fast, $v \gtrsim 20$ km$\cdot$s^{-1} C-shock model in gas with a pre-shock density $\sim 10^5$ cm^{-3}, as described in Sect. 4.5.4.

Properties similar to those found here were derived for the high-velocity component of the outflow shock L1157-B1 by Lefloch et al. (2010), with $n_{H_2} \sim (1.0 \dots 3.0) \cdot 10^4$ cm^{-3}. The relatively low density of shocked gas in the two sources suggests either a very low pre-shock density ($\sim 10^4$ cm^{-3}) or a relatively low shock velocity ($v \lesssim 20$ km/s). Our line wing analysis extends from ± 13 to ± 23 km$\cdot$s^{-1} away from the OMC-2 rest velocity. This implies that the fastest projected shock velocity entering directly into our analysis is ~ 20 km$\cdot$s^{-1}. From the shock model comparison, the lowest velocities consistent with our observations are also 20 km$\cdot$s^{-1}. Together with the low compression needed to explain the density we find, this velocity is preferred over significantly higher velocities.

If the shock velocity is actually 40 km$\cdot$s^{-1} along the outflow axis, the axis would be inclined $\sim 60°$ to the line of sight, consistent with the inclination of $50°$ determined for the envelope and disk components by Adams et al. (2012). Even faster shocks must contribute part of the emission at the highest velocities, as the line wings continue beyond the range analyzed here.

The best-fit shocked gas density range is consistent with the average density in the OMC-2 clump, $\sim 10^5$ cm^{-3}, but is below the values encountered in the FIR 4 envelope structure from Crimier et al. (2009), which has densities in excess of $8 \cdot 10^5$ cm^{-3} within the beam sizes of interest. As noted above, the pre-shock density must have been even lower than the fitted value. That such densities are missing in the source model may be due to an azimuthally averaged density profile masking local lower-density regions. The existence of an outflow cavity itself also implies a gradient in density from envelope values to the rarefied gas in the outflow. Or, the relatively low n_{H_2} we find might be explained by shocks in the surface layer of the OMC-2 clump, where the FIR 3 outflow, discussed in Sect. 4.6.3, may be interacting with low-density gas.

The source size of $\theta = 0.8$" characterizes the typical beam-filling factor per unit velocity over the 10 km$\cdot$s^{-1} wing intervals analyzed here. We have no a priori reason to assume that the different velocity bins overlap in projected location on the sky, however. Also, the total intensity of an H$_2$O line at each velocity is likely the sum of

a number of smaller, low-intensity optically thick emission sources which sum up to form a smooth line wing. The velocity-integrated beam-filling factor of the shocked gas could correspond to several arcseconds.

The $o-$ and p-H_2O fundamental lines, and the o-H_2O $5_{3,2} - 4_{4,1}$, are always underproduced by the best-fit models, as seen in Fig. 4.7. The fundamental lines are the easiest to excite, with $E_u < 100$ K. They likely trace larger volumes of gas than the other H_2O lines. Indeed, fitting only the water lines with $E_u < 200$ K allows to reproduce the fundamental lines and gives a best-fit $T_{kin} \approx 250$ K and a source size $\theta \approx 3$". The SWAS spectrum analyzed by Franklin et al. (2008) shows that o-H_2O $1_{1,0} - 1_{0,1}$ has a high-velocity blue wing of intensity a few tens of mK in a ~ 4' beam.

The $5_{3,2} - 4_{4,1}$ line, with $E_u \sim 700$ K, is the highest-lying line in our sample by ~ 300 K, and may therefore trace hotter gas than most of the emission in the other lines. It is underproduced by the best-fit models. As seen in Fig. 4.7, the p-H_2O $4_{1,3} - 4_{0,4}$ line does not have substantial flux in either wing, but the models match the 3σ upper limits, suggesting that the line wings are just below detectability.

If the high-J CO emission has contributions from sources other than the H_2O-bearing gas, our results allow for $N(H_2O)/N(CO) \gtrsim 1$, but this ratio is not expected to reach much above unity due to elemental abundance limitations. Aside from shocks, the high-J emission can trace UV-heated gas. Modelling of NGC 1333 IRAS 2A suggests that shock- and UV-heated gas contribute roughly equally to the CO $11 \leq J_u \leq 16$ emission in that source (Visser et al. 2012). NGC 1333 IRAS 2A is similar to OMC-2 FIR 4 in terms of high-velocity H_2O emission (Fig. 4.5) and it is possible that the role of UV-heating is also similar. As we show in the next subsection, molecular abundance arguments support the conclusion that any UV radiation in the gas is predominantly locally produced. An analysis of the *Herschel*/PACS spectrum of OMC-2 FIR 4 by the HOPS Key Programme (PI T.Megeath), should help to better quantify the shock and UV contributions to CO emission in this source.

While the properties of the H_2O and CO line wings are broadly consistent with the single-component model employed here, the above discussion on the underestimated fundamental line fluxes, as well as the flux of the highest-lying water line, suggests that a range of gas properties must be invoked for a full understanding of the emission. Within our errorbars, the velocity dependence of the derived gas properties cannot be studied with much certainty, but a future analysis, covering more of the lines, may provide more detail. For CO, the emission closer to the line centre yields a larger best-fit effective source size, consistent with the expectation that lower-velocity gas is more widespread than high-velocity material.

Some uncertainties are hidden in our assumptions about the geometry of the source (a face-on slab) and its position within the HIFI beam (central). The pointing uncertainty for HIFI is $2''$ (Roelfsema et al. 2012) and should not introduce substantial variations in the line fluxes for a $> 12''$ beam. The parameter $N(H_2O)$ is constrained by the o-H_2O $3_{1,2} - 3_{0,3}$ / $3_{1,2} - 2_{2,1}$ ratio to be $\gtrsim 10^{15}$ cm^{-2} / km $\cdot$ s^{-1}. The same ratio constrains $(10^2 < n_{H_2} < 10^7)$ cm^{-3}, but it is not very sensitive to T_{kin}. Some off-centre emission may be cut out in the smallest beams, in particular if the wings represent the sum of many smaller areas with similar properties.

4.6.2 Chemical properties of the shocked gas

We find column density ratios of $H_2O/CO \approx 0.9$ and $OH/H_2O \lesssim 0.3$. The H_2O/CO ratio of unity is in excellent agreement with expectations from shock models, which predict the oxygen left over from CO formation to be driven into H_2O at $T_{kin} \gtrsim 300$ K (Kaufman & Neufeld 1996; Wardle 1999; Flower & Pineau Des Forêts 2010). $H_2O/CO \approx 0.9$ is also consistent with observations of other sources, for example the high-velocity wings in NGC 1333 (Kristensen et al. 2010). Several studies have shown the H_2O/CO ratio to increase with velocity for low-J lines (Franklin et al. 2008; Kristensen et al. 2010, 2012), but for high-J the ratio appears to be constant (Yildiz et al., in preparation). Our analysis is averaged over a part of the high-velocity wings and does not yet explicitly address this question.

The ratio of $OH/H_2O \lesssim 0.3$ in OMC-2 FIR 4 is also consistent with shock models. Models of C-shocks by Wardle (1999) focussed on oxygen chemistry and included a local UV-field due to cosmic ray intercations with H_2. For a pre-shock density of $n_{H_2} = 10^4$ cm^{-3}, a shock velocity $v = 25$ km·s^{-1}, a cosmic ray ionization rate of $\xi = 3 \cdot 10^{-16}$ s^{-1}, Wardle found a post-shock $n_{H_2} \sim 10^5$ cm^{-3} and an OH/H_2O ratio of 0.1. The column densities scale as $N(OH) \propto \xi^{0.5}$ and $N(H_2O) \neq f(\xi)$. Interestingly, López-Sepulcre et al. (submitted) recently found $\xi = 3 \cdot 10^{-16}$ s^{-1} for a diffuse cloud in the close foreground of the OMC-2 clump. Such an ionization rate, likely due to cosmic rays and other high-energy particles, near OMC-2 FIR 4 implies that our upper limit of 0.3 on OH/H_2O may be close to the true ratio. This, in turn, would imply that additional UV sources are not needed for the post-shock production of OH in the high-velocity gas.

From a lower limit of $OH/H_2O > 0.028$ for the broad emission component associated with the massive protostar W3 IRS 5, Wampfler et al. (2011) concluded that some amount of UV-photodissociation of shocked gas was necessary to explain the observations.

An analysis similar to that presented here for OMC-2 FIR 4 was carried out by Herczeg et al. (2012) on a large set of far-infrared H_2O, CO and OH lines observed towards NGC 1333 IRAS4B with *Herschel*/PACS. This study found ratios $H_2O/CO \sim 2$ and $OH/H_2O \sim 0.1$. These observations were not spectrally resolved, however, and thus represent an average for that source.

The blue high-velocity wing of a species not considered in the present analysis, hydrogen cyanide, is prominent in all lines of that species in the HIFI spectrum of OMC-2 FIR 4. Models suggest HCN can be abundant and observable in post-shock gas (Neufeld & Dalgarno 1989a,b) and observations confirm this (e.g. Bachiller & Perez Gutierrez 1997). This molecule is one target of our follow-up work, where the two wings are treated as separate entities, as they must originate in spatially distinct regions and the HCN detection is suggestive of at least some difference in the chemistry or in the excitation or viewing conditions. We note that the OMC-3 MMS 6 compact outflow, described in Sect. 4.6.3, is traced more clearly by HCN than CO emission (Takahashi & Ho 2012).

4.6.3   The origin of the outflow shocks

To the best of our knowledge, no arcminute-scale and sub-arcminute resolution CO maps of OMC-2 exist that would have sufficient sensitivity to probe the spatial distribution of wings at velocities as high as those seen in the HIFI spectra studied here. The Shimajiri et al. (2008) CO $3 - 2$ line wing maps (their Fig. 1) are formally integrated to very high velocities, but the on-source CO spectrum (their Fig. 2) shows that the wings are noisy and the fluxes are dominated by lower velocities, making it difficult to draw conclusions about the spatial distribution of the highest velocity emission.

In Fig 4.8, we illustrate two possible scenarios for the origin of the high-velocity wings. In hypothesis **A**, the emission arises as the sum of a large number of small-scale shocks in the outer envelope, which arise from the interaction of an external outflow with the OMC-2 FIR 4 core. The blue- and redshifted wings might then originate at the front- and backside of the FIR 4 core, respectively. In hypothesis **B**, the high-velocity wings arise as the sum of small-scale shocks in a compact outflow cavity in the FIR 4 envelope. Of course, in reality, both could also contribute. We will now describe the background of these hypotheses.

There are strong indications that the Class I source OMC-2 FIR 3, located $\sim$ $30''$ North-East of FIR 4, drives the large-scale outflow whose North-Eastern lobe is observed in blue- and redshifted CO and in knots of H_2, and whose South-Western lobe has been proposed to be ploughing into OMC-2 FIR 4 and triggering star formation there (Shimajiri et al. 2008; Davis et al. 2009). A redshifted structure corresponding to the S-W lobe is visible in interferometric maps of CO $1 - 0$ (Williams et al. 2003). It ends abruptly on reaching an unresolved blueshifted CO $1 - 0$, $3 - 2$ and SiO $2 - 1$ core near the centre of OMC-2 FIR 4 (Shimajiri et al. 2008).

Of the lines analyzed in this work, some with $\nu > 1600$ GHz have relatively weak wings. For example, the p-H_2O $4_{1,3} - 4_{0,4}$ line wings have no detected flux, and the CO $16 - 15$ wings fall below the best-fit model. If some of the shocked gas falls outside the $12''$ beam, e.g. the wings are the sum of many small-scale shocks, a large-scale driver is suggested, such as the OMC-2 FIR 3 outflow interacting with the FIR 4 envelope over a large area. However, the wings of o-H_2O lines at ~ 1600 GHz are well reproduced by the models, suggesting that the bulk of the shocked gas is within the smallest HIFI beams.

Mapping of OMC-2 in various tracers has not yielded clear evidence for an outflow from OMC-2 FIR 4 itself. An elongated 3.6 cm radio continuum source of $13''x \leq 6''$ size, possibly related to an outflow, has been imaged in the source (Reipurth et al. 1999) but could also be due to an HII region around a 700 $L_\odot$ B4-type star (López-Sepulcre et al., in prep.).

A near-infrared nebulosity $\sim 5''$ across has been observed well within the OMC-2 FIR 4 envelope radius, $\sim 5''$ North-West of the mid-infrared and sub-millimetre peaks (Bally et al. 2006; Takahashi et al. 2008; Davis et al. 2009). The continuum-subtracted 2.2 μm H_2 emission image of Yu et al. (1997) also shows a compact emission source at this location, a strong sign of outflow shocks. All groups suggested this to be related to outflow activity, but the nebula has never been studied in detail.

We examined archival Hubble Space Telescope[10] and VLT/NACO[11] data, confirming the conical reflection nebula to be $5''$ across in the 814 nm Hubble image and identifying a point source, likely H_2, at the tip of the cone in the 2.15 μm NACO image. As seen in Fig. 4.1, the cone opens along a line that passes just West of the sub-millimetre source. The extended 814 nm source is consistent with a reflection nebulosity, while the point-like 2.15 μm source could be a young stellar object or a bow shock emitting in H_2 vibrational lines.

Archival maps of the CO $6-5$ transition[12] show a strong peak within a roughly 5"x10" area that matches the blueshifted low-J CO and SiO core, showing a strong blue wing within this region but not outside it. As seen in Fig. 4.1, the tip of the CO structure overlaps with the visible and near-infrared nebulosity. The redshifted wing originates from slightly North-East, in a region that falls partly within the HIFI beam even at high J levels. The high-J red wing could be the same material traced by the Williams et al. (2003) CO $1-0$ interferometry described above.

An illustrative case to compare OMC-2 FIR 4 with is that of another intermediate-mass Class 0 protostar in Orion, OMC-3 MMS 6. Searches in the CO $1-0$ (Williams et al. 2003) and $3-2$ (Takahashi et al. 2008) lines found no evidence for an outflow, while H_2 emission is associated with the source (Stanke et al. 2002; Davis et al. 2009). Nevertheless, sub-arcsecond resolution observations of millimetre CO and HCN lines have recently revealed a very compact bipolar outflow in OMC-3 MMS 6, with lobes only $\sim$ 2" across (Takahashi & Ho 2012).

Thus, while not conclusive, the optical and near-infrared data is consistent with the existence of a very compact, elliptical outflow cavity in the FIR 4 envelope. The scales associated with the point source and the nebulosity, $\sim$ 1" and $\sim 5''$, are consistent with the small beam-filling factor derived for the shocked gas by our analysis. There is, to the best of our knowledge, no CO or HCN interferometry of sufficient spatial resolution and sensitivity to rule out an outflow in FIR 4 as compact as that found in MMS 6, or to determine if the high-velocity material relates to the FIR 3 outflow. The CHESS HIFI dataset of OMC-2 FIR 4 reveals that the HCN $6-5$ through $10-9$ lines have high-velocity wings, in particular significant emission in the $-10\ldots0$ km$\cdot$s^{-1} range. This may be an indication of a high-density high-velocity component. Arcsecond-scale interferometry of HCN and CO high-velocity wings will allow to resolve the origin of the shocked gas studied here.

4.7 Conclusions

- The H_2O line profiles in OMC-2 FIR 4 show several components: a broad ($\sim$ 20$\ldots$40 km/s) and medium ($\sim$ 10 km/s) emission component and a narrow (3$\ldots$6 km/s) self-absorption component. Such components are commonly seen in H_2O lines in protostars.

- The subset of H_2O lines in common between OMC-2 FIR 4 and a sample of other

---

[10]Proposal ID 10603, PI D.Padgett.

[11]Programme 082.C-0873(A), PI T.Stanke.

[12]Caltech Submillimeter Observatory, PI M.Houde.

protostellar sources has overall similar flux ratios. Orion KL is the only source for which $H_2^{18}O$ is compared instead of H_2O, leading to line ratios characteristic of more optically thin emission.

- The high-velocity post-shock gas in OMC-2 FIR 4 has a density of $\sim 5 \cdot 10^4$ cm^{-3} and a temperature of ~ 500 K, with an effective source size of 0.8" or 340 AU. The column density of water is $N(H_2O) \approx 1.3 \cdot 10^{17}$ cm^{-2}/(km $\cdot$ s^{-1}), and the emission is correspondingly very optically thick. Furthermore, $N(CO) \approx 1.5 \cdot 10^{17}$ cm^{-2}/(km $\cdot$ s^{-1}). We find abundance ratios $H_2O/CO \approx 0.9$ and $OH/H_2O \lesssim 0.3$.

- The observed line wing flux ratios match models of C-shocks with $\Delta v \geq 20$ km $\cdot$ s^{-1}.

- Our findings are consistent with the existence of a compact outflow in OMC-2 FIR 4, although sensitive, high spatial resolution follow-up observations of the high-velocity wings of CO and HCN are needed to determine the exact location and origin of the outflow shocks.

Table 4.2: Lines of H_2O and OH observed towards OMC-2 FIR 4. The total line fluxes, F_{total}, are integrated over the entire line profile. Fluxes in the blue and red wings, F_{blue} and F_{red}, are integrated in the ranges $-10\ldots0$ km $\cdot$ s^{-1} and $25\ldots35$ km $\cdot$ s^{-1}, respectively. The flux uncertainties and upper limits correspond to 3σ RMS noise. Parameters for the ortho and para isomers of H_2O are from the VASTEL database, by Charlotte Vastel, available as part of the CASSIS software. For the two sets of three blended OH hyperfine components, the frequency and Einstein coefficient of the strongest of each triplet is given.

Species	Transition	Freq. [GHz]	E_u [K]	A_{ul} [s^{-1}]	Beam ["]	T_{mb} [K]	RMS [mK]	F_{total} [K·km/s]	F_{blue} [K·km/s]	F_{red} [K·km/s]
o-H_2O	$1_{1,0}-1_{0,1}$	556.936	26.7	$3.45 \cdot 10^{-3}$	38.1	2.4	14	34.25 ± 0.24	3.02 ± 0.06	1.05 ± 0.06
o-H_2O	$2_{1,2}-1_{0,1}$	1669.905	80.1	$5.59 \cdot 10^{-2}$	12.7	5.5	206	67.96 ± 1.38	4.51 ± 0.43	4.13 ± 0.43
o-H_2O	$2_{2,1}-2_{1,2}$	1661.008	159.9	$3.06 \cdot 10^{-2}$	12.8	2.5	204	22.00 ± 0.93	< 0.41	0.99 ± 0.41
o-H_2O	$3_{0,3}-2_{1,2}$	1716.770	162.5	$5.04 \cdot 10^{-2}$	12.3	4.9	188	54.36 ± 1.20	2.53 ± 0.36	2.66 ± 0.36
o-H_2O	$3_{1,2}-2_{2,1}$	1153.127	215.2	$2.66 \cdot 10^{-3}$	18.4	2.8	159	45.94 ± 1.11	2.71 ± 0.40	2.70 ± 0.40
o-H_2O	$3_{1,2}-3_{0,3}$	1097.365	215.2	$1.64 \cdot 10^{-2}$	19.3	2.3	92	33.48 ± 0.75	1.99 ± 0.25	1.76 ± 0.25
o-H_2O	$3_{2,1}-3_{1,2}$	1162.912	271.0	$2.28 \cdot 10^{-2}$	18.2	1.5	140	17.58 ± 1.00	1.37 ± 0.33	1.17 ± 0.33
o-H_2O	$5_{3,2}-4_{4,1}$	620.701	697.8	$1.09 \cdot 10^{-4}$	34.2	0.01	11	1.27 ± 0.12	0.14 ± 0.03	0.13 ± 0.03
p-H_2O	$1_{1,1}-0_{0,0}$	1113.343	53.4	$1.84 \cdot 10^{-2}$	19.1	2.8	64	49.07 ± 0.96	2.91 ± 0.15	2.66 ± 0.15
p-H_2O	$2_{0,2}-1_{1,1}$	987.927	100.8	$5.84 \cdot 10^{-3}$	21.5	4.5	48	66.64 ± 0.48	4.41 ± 0.12	4.34 ± 0.12
p-H_2O	$2_{1,1}-2_{0,2}$	752.033	136.9	$7.04 \cdot 10^{-3}$	28.2	2.6	41	38.45 ± 0.45	2.31 ± 0.12	2.15 ± 0.12
p-H_2O	$2_{2,0}-2_{1,1}$	1228.789	195.9	$1.87 \cdot 10^{-2}$	17.3	1.0	171	11.03 ± 1.23	0.47 ± 0.40	0.55 ± 0.40
p-H_2O	$4_{1,3}-4_{0,4}$	1602.219	396.4	$3.72 \cdot 10^{-2}$	13.2	0.9	166	2.19 ± 0.93	< 0.34	< 0.34
p-H_2O	$4_{2,2}-4_{1,3}$	1207.639	454.3	$2.84 \cdot 10^{-2}$	17.6	0.6	184	1.22 ± 1.32	< 0.43	< 0.43
p-H_2O	$4_{2,2}-3_{3,1}$	916.172	454.3	$5.66 \cdot 10^{-4}$	23.1	0.1	49	0.87 ± 0.42	< 0.13	0.15 ± 0.12
$H_2^{18}O$	$1_{1,0}-1_{0,1}$	547.676	60.5	$3.29 \cdot 10^{-3}$	38.7	0.05	19	1.07 ± 0.07	0.07 ± 0.02	0.09 ± 0.02
CO	$5-4$	576.268	83.0	$1.22 \cdot 10^{-5}$	36.8	12.9	18	171.27 ± 0.21	7.40 ± 0.06	3.22 ± 0.06
CO	$6-5$	691.473	116.2	$2.14 \cdot 10^{-5}$	30.7	14.4	33	204.33 ± 0.36	8.70 ± 0.09	4.47 ± 0.09
CO	$7-6$	806.652	154.9	$3.42 \cdot 10^{-5}$	26.3	14.6	66	211.73 ± 0.63	8.52 ± 0.18	5.33 ± 0.18
CO	$8-7$	921.800	199.1	$5.13 \cdot 10^{-5}$	23.0	17.2	36	248.59 ± 0.30	9.11 ± 0.09	7.03 ± 0.09

Species	Transition	Freq. [GHz]	E_u [K]	A_{ul} [s^{-1}]	Beam ["]	T_{mb} [K]	RMS [mK]	F_{total} [K·km/s]	F_{blue} [K·km/s]	F_{red} [K·km/s]
CO	$9-8$	1036.912	248.9	$7.33 \cdot 10^{-5}$	20.4	17.9	204	257.70 ± 1.98	8.73 ± 0.51	8.87 ± 0.51
CO	$10-9$	1151.985	304.2	$1.01 \cdot 10^{-4}$	18.4	20.1	140	267.18 ± 1.20	7.52 ± 0.33	7.59 ± 0.33
CO	$11-10$	1267.014	365.0	$1.34 \cdot 10^{-4}$	16.7	18.0	135	248.41 ± 0.87	7.07 ± 0.30	7.74 ± 0.30
CO	$13-12$	1496.923	503.1	$2.20 \cdot 10^{-4}$	14.2	12.2	211	192.08 ± 1.56	5.34 ± 0.45	6.16 ± 0.45
CO	$14-13$	1611.794	580.5	$2.74 \cdot 10^{-4}$	13.2	10.3	276	167.21 ± 1.89	5.13 ± 0.57	6.76 ± 0.57
CO	$15-14$	1726.603	663.4	$3.35 \cdot 10^{-4}$	12.3	7.4	212	136.87 ± 1.41	4.13 ± 0.43	4.51 ± 0.43
CO	$16-15$	1841.346	751.7	$4.05 \cdot 10^{-4}$	11.5	4.4	86	69.74 ± 0.45	2.69 ± 0.15	2.18 ± 0.15
^{13}CO	$5-4$	550.926	79.3	$1.07 \cdot 10^{-5}$	36.8	12.9	18	34.43 ± 0.12	0.13 ± 0.06	< 0.06
^{13}CO	$6-5$	661.067	111.1	$1.88 \cdot 10^{-5}$	30.7	14.4	33	28.74 ± 0.24	0.26 ± 0.10	< 0.10
^{13}CO	$7-6$	771.184	148.1	$3.01 \cdot 10^{-5}$	26.3	14.6	66	23.51 ± 0.24	0.31 ± 0.11	< 0.11
^{13}CO	$8-7$	881.273	190.4	$4.52 \cdot 10^{-5}$	23.0	17.2	36	15.67 ± 0.27	< 0.12	< 0.12
^{13}CO	$9-8$	991.329	237.9	$6.45 \cdot 10^{-5}$	20.4	17.9	204	11.23 ± 0.42	< 0.18	< 0.18
^{13}CO	$10-9$	1151.985	290.8	$8.86 \cdot 10^{-5}$	18.4	20.1	140	9.44 ± 0.48	< 0.19	< 0.19
^{13}CO	$11-10$	1267.014	348.9	$1.18 \cdot 10^{-4}$	16.7	18.0	135	9.11 ± 1.02	< 0.43	< 0.43
^{13}CO	$14-13$	1611.794	555.0	$2.41 \cdot 10^{-4}$	13.2	10.3	276	0.45 ± 1.11	< 0.51	< 0.51
^{13}CO	$16-15$	1841.346	718.7	$3.57 \cdot 10^{-4}$	11.5	4.4	86	1.39 ± 0.72	0.50 ± 0.33	< 0.33
OH	$2_{1,-1} - 1_{1,1}$	1834.747	269.8	$6.36 \cdot 10^{-2}$	11.6	0.2	9	2.29 ± 0.45	< 0.18	< 0.18
OH	$2_{1,1} - 1_{1,-1}$	1837.817	270.1	$6.40 \cdot 10^{-2}$	11.5	0.2	9	6.48 ± 0.45	< 0.15	< 0.15

4.A   A comparison of H_2O and CO line wings

As noted in Sect. 4.4, the wings of H_2O and CO lines of OMC-2 FIR 4 follow a similar exponential profile to those seen in L1157-B1 by Lefloch et al. (2012). The general form for the functions which can be added to produce the line profiles is $T_{mb} \propto \exp\left(|v/v_0|\right)$, where v_0 is a fitting parameter. In Fig. 4.A.1, we show the v_0 parameters from fits to the blue and red wings of H_2O and CO in OMC-2 FIR 4. Horizontal lines are drawn at $v_0 = 10$ to guide the eye.

The parameter values found by Lefloch et al. (2012) were $v_0 = 12.5$, 4.4 and 2.0, where the largest v_0 value described the highest velocities and corresponded to the highest temperature (~ 210 K). Our single-function fits to the $-10 \ldots 0$ and $25 \ldots 35$ km $\cdot$ s^{-1} ranges give v_0 values reasonably similar to the Lefloch et al. values, suggesting that further analysis with two-function fits is worthwhile for a more detailed comparison with L1157.
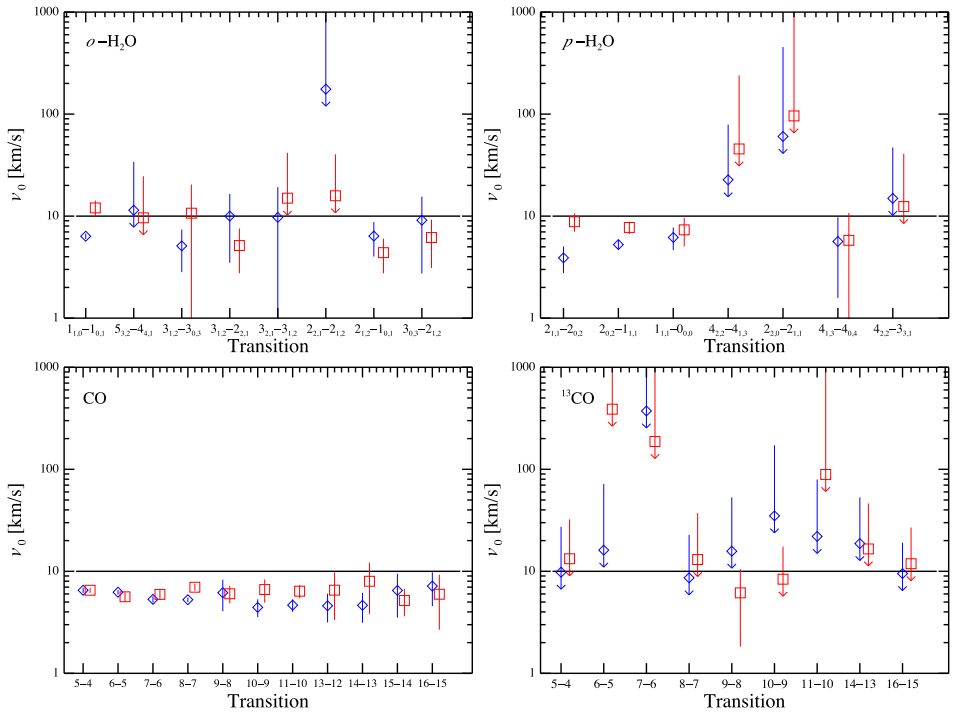
Figure 4.A.1: Fit parameters to the H$_2$O and CO line wings in the blue $(-10\ldots0$ km $\cdot$ s^{-1}, blue diamonds) and red $(25\ldots35$ km $\cdot$ s^{-1}, red squares) intervals analyzed in this paper. Each point has 3σ errorbars. The parameter v_0 defines the function $T_{\mathrm{mb}} \propto \exp\left(-|v/v_0|\right)$, where v is the velocity coordinate in the line. For comparison, the horizontal line marks $v_0 = 10$ km $\cdot$ s^{-1}.

The inner rim structures of protoplanetary discs

M. Kama, M. Min, C. Dominik

Abstract

The inner boundary of protoplanetary discs is structured by the dramatic opacity changes at the transition from the dust-containing to a dust-free zone. This paper explores the variety and limits of inner rim structures in passively heated dusty discs. For this study, we implemented detailed sublimation physics in a fast Monte Carlo radiative transfer code. We show that the inner rim in dusty discs is not an infinitely sharp wall but a diffuse region which may be narrow or wide. Furthermore, high surface densities and large silicate grains as well as iron and corundum grains decrease the rim radius, from a 2.2AU radius for small silicates around a $47L_\odot$ Herbig Ae star typically to 0.4AU and as close as 0.2AU. A passive disc with grain growth and a diverse dust composition must thus have a small inner rim radius. Finally, an analytical expression is presented for the rim location as a function of dust, disc and stellar properties.

5.1 Introduction

The inner regions of protoplanetary discs are the birthplaces of terrestrial planets. Understanding their nature and diversity is key to our picture of the formation of planetary systems.

This paper uses Monte Carlo radiative transfer modelling and detailed sublimation physics to explore the inner rim structures of passive dust discs, and their merits in reconciling theory with observation.

T Tauri and Herbig Ae/Be stars have prominent infrared excesses in their spectral energy distributions (SEDs), due to the presence of protoplanetary discs. The existence of such discs is known observationally through statistics of photometric colours (Adams et al. 1987; Rydgren & Zak 1987; Calvet et al. 1992; Lada & Adams 1992), spectral fitting (Kenyon & Hartmann 1987), imaging (McCaughrean & O'dell 1996; Burrows et al. 1996), interferometry (Mannings & Sargent 1997), and is inferred from studies of the Solar System and exoplanets. Based on broadband SEDs, discs are classified as either self-shadowed or flaring (Kenyon & Hartmann 1987; Meeus et al. 2001; Dullemond & Dominik 2004) and their temperature structure can be approximated with two layers to explain solid-state silicate emission bands (Chiang & Goldreich 1997). In the inner regions of discs, dust sublimates. The location where starlight reaches an optical depth of unity in the dust is referred to as the inner rim. The dust sublimation temperature is around 1500K, so the inner rim radiates in the near-infrared.

In this paper, we use a new Monte Carlo radiative transfer code to study the effects of various physical parameters on the inner rim structure of protoplanetary discs. Our motivation is outlined in Section 5.2. Dust sublimation, backwarming and other theoretical aspects are introduced in Section 5.3 and the results are presented in Section 5.4. A discussion and conclusions follow in Sections 5.5 and 5.6.

5.2   Observational and physical motivation

Herbig Ae/Be stars typically show excess near-infrared (NIR, $\lambda \approx 1.25 \ldots 7 \mu m$) emission, corresponding to temperatures of $\sim 1500K$. Most fractional NIR excesses, $f_{NIR} = L_{NIR}/L_\star$, form a rising histogram from $f_{NIR} \approx 0.02$ to 0.22 and are well reproduced by models including dust sublimation in a hydrostatic disc (Dullemond et al. 2001; Isella & Natta 2005, hereafter DDN01 and IN05). Larger excesses, e.g. $f_{NIR} = 0.23$ and 0.25 for AB Aur and WW Vul (Natta et al. 2001), and $f_{NIR} = 0.32$ for HD 142527 (Dominik et al. 2003), have proven impossible to reproduce with existing models without introducing unrealistic assumptions about the rim scaleheight or dust sublimation temperature.

Herbig Ae/Be and T Tauri stars have been shown to follow a $R_{rim} \propto L_\star^{1/2}$ law for inner rim radii measured in the NIR regime (Monnier et al. 2005; Millan-Gabet et al. 2007), thought to coincide with the dust rim. Most Herbig Ae/Be rims in this sample have been shown to be scattered within expected limits (Monnier et al. 2005) for a radius determined by dust sublimation, consistent with an optically thin inner hole. Some Herbig Be stars, with $L_\star > 10^3 L_\odot$, conform to models where the inner hole is optically thick in the midplane and the rim radii are consequently smaller. Gas undergoing accretion onto the star has been assumed as the inner hole opacity source in these cases.

The presence of a smooth, extended hot emission component interior to the dust sublimation radius has been deduced for several systems from interferometric observations (Eisner et al. 2007; Tannirkulam et al. 2008b,a; Kraus et al. 2008; Isella et al. 2008). A hot emission component in the inner hole has recently gained further support
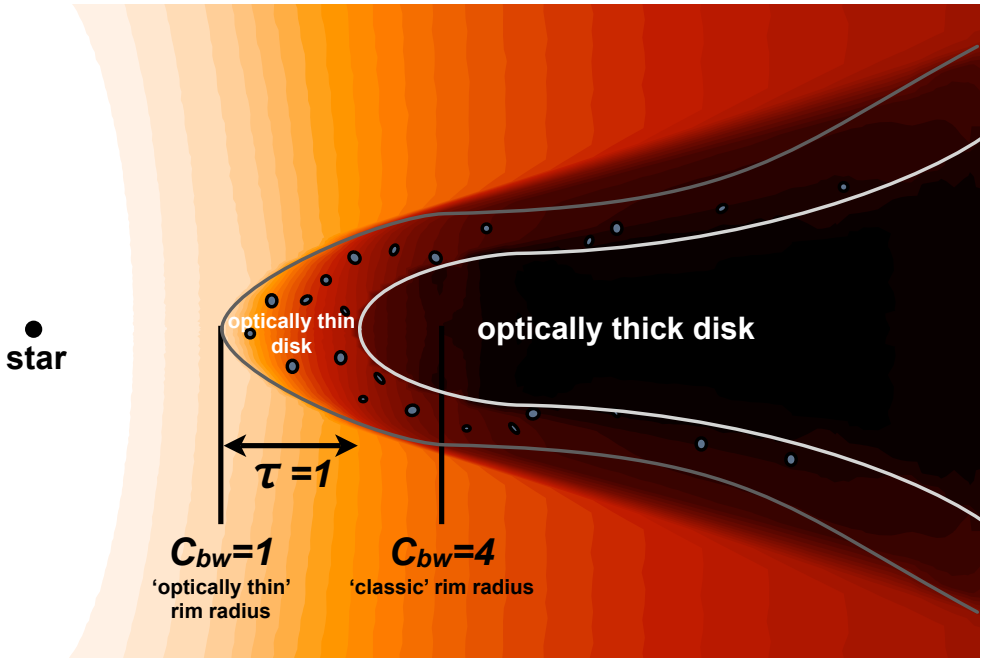
Figure 5.2.1: A schematic of the inner few AU of a disc. The colour map indicates the temperature, from < 300K (*dark*) to > 2000K (*white*). At the optically thin radius, $C_{bw} = 1$, dust can begin to condense. The classical rim, at $C_{bw} = 4$, is a maximally backwarmed dust wall. The actual rim, i.e. $\tau = 1$ surface, is between these limits and preceded by an optically thin zone.

from spatially resolved spectroscopy (Najita et al. 2009; Eisner et al. 2009).

Meanwhile, the physico-chemical parameter space of dust rim models has been little explored in terms of variations in global inner disc properties (surface density profile, composition) and dust type (astronomical silicate has been the standard opacity and homogeneous spheres the particle shape). The complex geometry and high optical depth of protoplanetary discs can now be studied with fast Monte Carlo radiative transfer codes (Min et al. 2009), providing further incentive to incorporate more detailed physics to clarify the limits of dusty rim models.

5.3 Methods

We consider models of passive discs, with temperature structures dominated by irradiation from the central star, and no accretional heating. (For a broader review of disc models, we refer the reader to Dullemond et al. 2007). The modern paradigm in passive disc models was developed by Chiang & Goldreich (1997, hereafter CG97). In this approach, the disc consists of a cool midplane and a hot surface layer. Such

models are highly successful in reproducing the general form and solid state bands of young star SEDs, but not the NIR excess, as emission from the dust sublimation region is not considered.

Any realistic dust species will sublimate at or below a temperature of $T_{subl} \sim$ 1500K, corresponding to an emission maximum around $2\mu m$. In a disc, this implies a radius inside which no dust can exist. Terminating the CG97 density distribution at such a radius results in a dust wall that is exposed to direct starlight, becomes hot and "puffs up" (Natta et al. 2001, and DDN01). Backwarming, explained later, pushes the sublimation location to larger radii. The DDN01 models explain the NIR excess, but the emission is very inclination dependent, an effect contradicted by observations.

A semi-analytical treatment including a gas density dependent sublimation temperature was applied successfully in explaining observed SEDs and deriving important properties such as characteristic grain sizes (IN05 and Isella et al. 2006). The rim surface was shown to be curved rather than wall-like, due to the dependence of the sublimation temperature on gas density (IN05). Isella et al. (2006) successfully fitted the SEDs and interferometric rim radii of four out of five Herbig Ae stars with IN05 models. In most cases, the best fits required astronomical silicate grains of $\geq 1.2\mu m$ size. However, the modelled rim radii were larger than those obtained by Eisner et al. (2004) by up to a factor of three, and simultaneously fitting the SED and rim radius of AB Aur was unsuccessful.

In a passive disc, the structure of the inner rim is determined by the stellar parameters, the surface density, cooling efficiencies and sublimation temperatures of the dust species, and by backwarming. Because the dust temperature and hydrostatic structure are also intimately coupled in a non-trivial geometry, finding static, stable solutions in terms of dust temperature structure is a difficult task, for which Monte Carlo radiative transfer is well suited.

Monte Carlo radiative transfer has been used to extend the IN05 models to two grain sizes in thermal contact (Tannirkulam et al. 2007). It was shown that grain growth, specifically the presence of grains of different sizes and settling of large grains, strongly curves the inner rim. A comparison with these results is made in Section 5.5.

5.3.1   The bulk gas and vapour densities

The total amount of gas in a disc is referred to as the bulk gas in this paper. The *bulk gas density* determines the amount of dust present if a fixed gas to dust mass ratio, e.g. $f_{gd} = 100$, is assumed. Dust grains always contribute some particles to the gas phase. These do not appreciably change the gas mass but do maintain the gas-grain equilibrium, with gas phase particles of the dust species sticking onto a grain and balancing its evaporation. If all of a given dust species must be in the gas phase to maintain this equilibrium, we call its density the *vapour density*. In reality, many gas-phase species may combine to maintain the gas-grain equilibrium of any solid species. As at most a few species exist simultaneously in our models, we generally neglect this fact, with some exceptions (see Sect. 5.5.2).
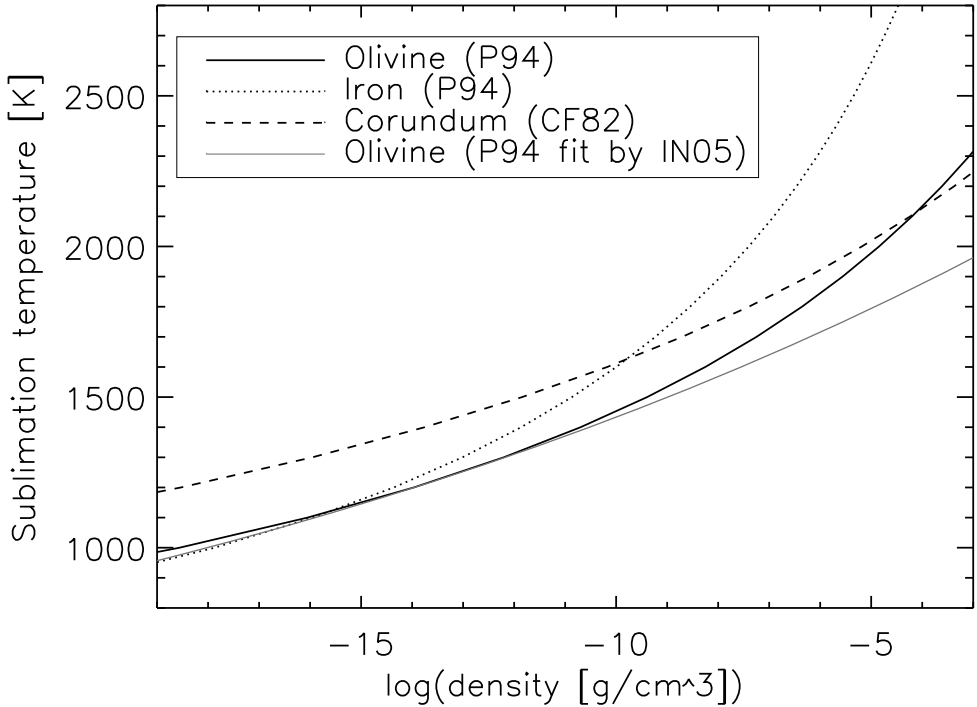
Figure 5.3.1: Sublimation curves of the species used in this work. The vapour density of the species is used. At low vapour densities, corundum is the most refractory, whereas at higher values iron is relatively more refractory. At least one of the two species is always relatively more refractory than olivine. The expression for the curves is given in Eq. 5.1, and the fitting parameters in Table 5.1. The IN05 fitting formula has been abundance-corrected for this plot, otherwise it would lie ~ 50K below our curve for any olivine vapour density (see Appendix 5.B). For astronomical silicate and forsterite, the olivine sublimation curve was used in modelling.

5.3.2 Dust sublimation

The temperature of a dust grain is determined by its wavelength-dependent opacity, and by the intensity and spectrum of the radiation field responsible for the heating. The cooling efficiency, given by $\epsilon = \kappa'_{\mathrm{P}}(\mathrm{T_{dust}})/\kappa'_{\mathrm{P}}(\mathrm{T_\star}) = C_{abs}(T_{dust})/C_{abs}(T_\star)$, is a ratio between the Planck mean opacity of the dust species at its own temperature to that at the stellar temperature, or for a single grain the ratio of absorption cross sections. In an identical stellar radiation field, a grain with a large ϵ will achieve radiative equilibrium at a lower temperature than a grain with a small ϵ, and generally epsilon increases with grain size.

For a grain to be stable, the particle flux excaping from its surface must be balanced by the flux coming onto it from the gas phase. If the temperature gets too

high, the grain will sublimate. The first rim models assumed that this would occur at T_{subl} = const, e.g. DDN01 used 1500K. Generally, the sublimation temperature of a dust species is a function of the partial pressure of its gas phase component, T_{subl} = f(P). The ideal gas equation of state can be used to replace the partial pressure P of the species with a function of its temperature and its vapour density, ρ_{vapour}. Loosely following Zemansky (1968), the vapour density at saturation pressure is given by the Clausius-Clapeyron equation:

$$\log\left(\rho_{vapour}\right) = B - \frac{A}{T_{subl}} - \log\left(T_{subl}^{-C}\right), \tag{5.1}$$

where A, B and C are thermodynamical quantities that can be fitted using laboratory measurements[1].

We take C = −1 and obtain A and B from a published table of evaporation temperatures with corresponding bulk gas densities and abundances (Pollack et al. 1994, P94). The resulting parameters for Eq. 5.1, alongside those obtained from other sources, are summarized in Table 5.1. In fitting the P94 data, the partial pressure of each species was expressed through its abundance and molecular mass, and the bulk gas density. Parameters from other sources were converted (see Eq.2 of Lamy (1974) and Eq.10 of Cameron & Fegley (1982)). The table also gives T_{subl} at $\rho_{vapour} = 10^{-12}$g/cm^3 and references for each species, with boldface denoting the species used in this study.

Sublimation curves of the main species used in this work are shown in Fig. 5.3.1. At vapour densities of $10^{-12...-10}$g/cm^3, olivine sublimates at around 1300K, iron at 1400K and corundum at 1500K. Corundum must have an abundance < 1% of the total dust mass and thus will necessarily have a much lower partial density than olivine or iron.

---

[1]Thermodynamically, A = ΔH$/\ln(10)$, where ΔH is the enthalpy of vapourization, and C = $(c_0'''/R - 1)$. The molar heat capacity has been broken into constant and temperature-dependent components, $c_P''' = c_0''' + c_i'''$. In addition, B = $B_1 + \log(k/\mu m_p)$, where B_1 is given by

$$B_1 = \frac{1}{\ln(10)}\left(\int_0^T \left[\frac{\int_0^T c_i'''dT - \int_0^T c_P'dT}{T^2 R}\right] dT + I\right),$$

and I is an integration constant. Sometimes, for example in Smithells (1967) as referenced by Lamy (1974), the full form of Eq. 5.1 must be invoked to provide a sufficiently accurate fit to experimental data, however most often, as in this paper, the assumptions $B \neq B(T)$ and $C = -1$ are made.

Table 5.1: A summary of the dust properties. ($\star$ – not used in the present work, given for completeness.)

Species	Chemical formula	T_{subl} [K]	A (Eq. 5.1)	B (Eq. 5.1)	Reference for A and B	Reference for opacity
Astron. silicate	$MgFeSiO_4$	1300	28030.	12.471	Pollack et al. (1994, P94)	Draine & Lee (1984)
Olivine	$MgFeSiO_4$	1300	28030.	12.471	P94	Dorschner et al. (1995)
Forsterite	Mg_2SiO_4	1150	26091.	13.418	Cameron & Fegley (1982, CF82)	Servoin & Piriou (1973)
Iron	Fe	1400	21542.	6.6715	P94	P94
Iron*	Fe	1150	20686.	9.1134	CF82	
Corundum	Al_2O_3	1500	40720.	18.479	CF82	Koike et al. (1995)
Orthopyroxene*	$MgSiO_3$	...	30478.	14.898	P94	
Quartz*	SiO_2	...	26335.	11.184	Schick (1960); Lamy (1974)	
Water ice*	H_2O	150	2827.7	7.7205	P94	
Troilite*	FeS	680	155.91	-4.9516	P94 (note: T_{subl} = const)	
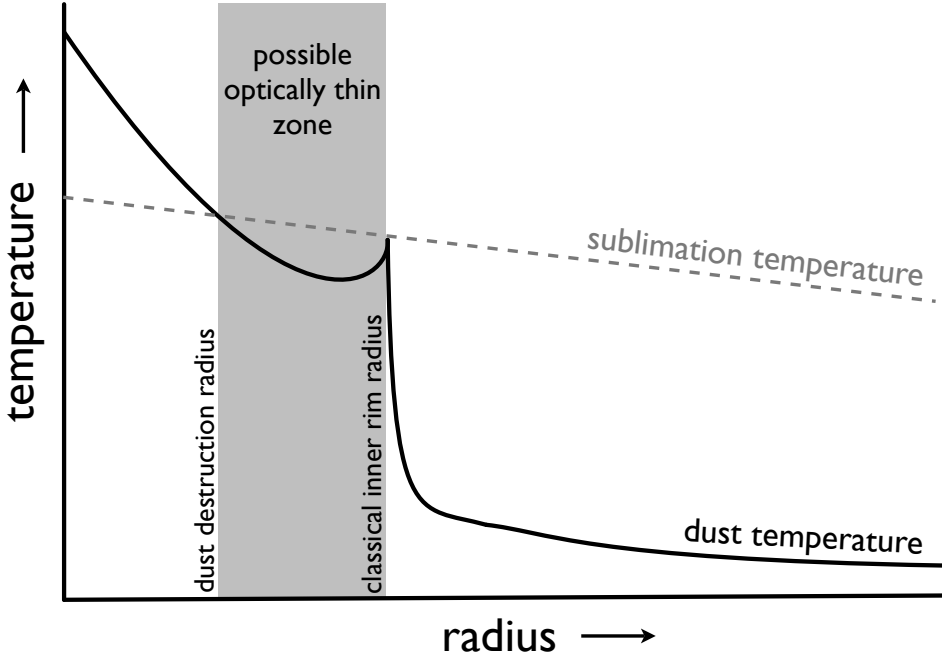
Figure 5.3.2: A schematic midplane dust temperature profile of an efficiently back-warmed rim. In front of the rim, the optically thin equilibrium temperature of the dust grains is plotted. Once this drops below the sublimation temperature, dust can condense. Generally, the sublimation temperature decreases with radius because of the increasing scaleheight and decreasing surface density. Between the dust destruction and classical rim radii, there is a region in which dust may condense but need not be optically thick. Dust in this region is warm, but not close to the sublimation temperature. The dust temperature peaks locally at the optically thick rim location, and then falls rapidly to a low value inside the disc. See also Fig. 5.2.1.

5.3.3   Backwarming

If a dust grain cannot cool into empty space in every direction, its temperature increases due to backwarming. Geometrically, the backwarming factor C_{bw} can be defined as the ratio of a full 4π solid angle to the solid angle subtended by the empty sky seen by the grain. For each photon emitted into the sky area obscured by nearby matter, a similar photon returns, hence the term "backwarming". An estimate of the temperature of a dust grain on the rim surface is obtained from the equation

$$\pi \frac{L_\star}{4\pi R_{rim}^2} = \frac{4\pi}{C_{bw}} \epsilon \sigma T_d^4, \tag{5.2}$$

where the energy absorbed by a grain at a distance R_{rim} from a star of luminosity

$L_\star$ is equated with that emitted by it, assuming a cooling efficiency ϵ. Rigorously, C_{bw} is wavelength-dependent and its value can be obtained by solving a complex radiative transfer and dust sublimation and condensation problem, which is done in the Monte Carlo code we employ. However, as we show later, the description in Eq. 5.2, while simple, is useful in interpreting the results of our more rigorous models, as well as other work on the subject. Other things being constant, the rim location scales as $R_{rim} \propto C_{bw}^{1/2}$.

$C_{bw} = 1$ yields the temperature of a grain in an optically thin environment, and when T_{subl} is considered it gives the smallest possible distance from the star a passive grain may orbit for longer than its sublimation timescale. This limit has been used by e.g. Tuthill (2001) and Monnier & Millan-Gabet (2002) to obtain lower limits on disc inner radii. It must be kept in mind that such limits are derived under assumptions regarding grain opacities, sublimation temperatures and geometry. In assuming the rim was an instantaneously optically thick vertical wall, DDN2001 adopted $C_{bw} = 4$. This illustrates how far backwarming can move the rim. As Monnier et al. (2005) pointed out, the rim is actually between the two limits, depending on over what distance the dust becomes optically thick. The concept of such an optically thin region in front of the rim is illustrated by Figures 5.2.1 and 5.3.2.

On the rim, $C_{bw} > 4$ may also be true for special locations. One can imagine this for a dust grain sitting at the far end of a tunnel which extends into the rim (see also Appendix 5.C).

5.3.4   Monte Carlo radiative transfer with MCMax

Radiative transfer through the complex dust geometries we wish to consider requires a flexible method in terms of density structures and dust composition. In addition, the coupled nature of the dust temperature and the hydrostatic structure also calls for an iterative solution. The required flexibility and speed can be obtained by using Monte Carlo radiative transfer.

We use here the Monte Carlo radiative transfer code MCMax (Min et al. 2009). Because of an efficient implementation of the diffusion approximation for regions with high optical depth, this code is especially suited for fast computations of geometries involving high optical depths.

The radiative transfer is based on the Monte Carlo scheme of continuous reemission developed by Bjorkman & Wood (2001) and optically thin regions are treated with the method of Lucy (1999).

To model the inner rim, dust sublimation was implemented into MCMax according to Eq. 5.1. The density structure of the dust is solved for by iterating the radiative transfer, dust sublimation and recondensation, and vertical hydrostatic equilibrium. After each iteration, the spatial grid is rebuilt in order to properly sample the new density structure. This ensures that in each iteration the radial resolution around $\tau \approx 1$ is sufficient for $\Delta\tau$ through any cell to be less than a fraction of unity.

Condensation, if it can occur, must be treated carefully. An upper limit is to transfer all the gas phase dust into grains, but if done too quickly this may overheat the cell, forcing sublimation and thus a loop. In the rim region, between $C_{bw} = 1$

and 4, the change in solid dust mass in any cell is weighted so that the change is smaller the closer the cell is to the local T_{subl}. The gas fraction of any dust species is constrained to be radially and vertically monotonous in this region. Furthermore, the optical depth added radially in front of the $\tau = 1$ surface cannot exceed 0.1. Some physical solutions might be suppressed by our constraints, but we expect a proper treatment of these to require time-dependent modelling. For a detailed discussion of the numerical aspects of implementing the sublimation physics we refer the reader to Appendix 5.C.

In reality, the sublimation of grains will cause the grains to lose mass, and thereby decrease in size. For practical considerations, and because we want to systematically study the effects of varying the grain size, we keep the size of the grains independent of the sublimation state, but increase or decrease their number density.

5.3.5 Disc parameters

General properties

The disc model is parametrized as follows: a radial dust surface density distribution $\Sigma(R)$ is described by two joined power laws, R^{-p_1} and R^{-p_2}, extending from an inner radius R_{in} out to R_{out}. The power laws are joined at the location R_p. The total dust mass, M_{dust}, gas to dust ratio, and a dust composition are specified.

In general, we assume $R_{\text{in}} = 0.03\text{AU}$, $R_{\text{out}} = 200\text{AU}$, $p_1 = 0.0$, $p_2 = 1.5$ and $R_p = 4\text{AU}$. A flat inner disc surface density makes the interpretation of our results more straightforward, especially for the optically thin zones.

Most of our models assume a dust mass of $M_{\text{dust}} \approx 10^{-4}M_{\odot}$. For a parameter study of the inner disc surface density, this is varied from $10^{-7}M_{\odot}$ to $10^{-2}M_{\odot}$ ($10^{-1}M_{\oplus}$ to $10^{4}M_{\oplus}$).

The gas to dust ratio is 100 everywhere, and the gas and dust scaleheights are coupled. All our models use the star previously employed by IN05, with $T_{\star} = 10000\text{K}$, $L_{\star} = 47L_{\odot}$, and $M_{\star} = 2.5M_{\odot}$.

The IN05 comparison discs are parametrized as $R_{\text{in}} = 0.1\text{AU}$, $R_{\text{out}} = 200\text{AU}$ and $p1 = p2 = 1.5$, with homogeneous spheres (HS) of astronomical silicate as the opacity model.

Dust types

The opacities of the dust grains are sensitive to their size and shape. For modelling the effects of the grain shape on the opacities, we use the statistical approach (Bohren & Huffman 1983; Min et al. 2003). This allows to take the grain shape effects into account properly using computationally favorable grain geometries. We apply the distribution of hollow spheres (DHS; see Min et al. 2005).

For the composition of the grains previous studies have frequently used the so-called astronomical silicate (Draine & Lee 1984). This species is most likely a composite of different materials with different sublimation laws. Its composition is unknown and we are thus unable to derive a proper sublimation law for astronomical silicate.

Therefore, in this paper we focus mainly on well characterized materials which have been measured in the laboratory and are known to exist in meteorites.

We begin by exploring discs with various grain sizes and surface densities of amorphous olivine. Then, models with two olivine grain sizes, and with dust types of different transparency, refractivity and cooling effiency are presented.

The presence of small, $\sim 0.1\mu$m grains in discs is revealed by fitting observed solid state emission bands. We use a model with such grains as a reference point. Large, $\geq 10\mu$m grains have a higher cooling efficiency than small grains, and as grain growth is known to occur in discs, they are also of great interest in modelling. To study the effects of large grains on the inner disc structure, we present models with 10 or 100μm olivine grains added to 0.1μm particles. Discs of 1, 10, 100 and 1000μm olivine are presented in Sections 5.4 and 5.5.

Surface density influences the inner rim in several ways: it sets the sublimation temperature, influences the backwarming efficiency and determines over what radial distance any given optical depth is reached. We vary the dust surface density in the inner disc from $\Sigma_{\rm d} = 10^{-4}$ to 10^3 as a parameter study.

In modelling two grain types, we assume they are not in thermal contact, unless the contrary is explicitly stated. This is to allow more efficiently cooling or refractory species to exist independently of less efficiently cooling or more volatile species. Thermal coupling will arise from the Monte Carlo radiative transfer in sufficiently dense regions, where all species will be in radiative thermal equilibrium. Unless stated otherwise, abundance ratios of 9999/1, 90/10 and 10/90 are used in studying grain mixtures.

Above ~ 1000K, amorphous silicates anneal to form crystalline silicates. The amorphous component is represented by olivine in our models. It has been found that the annealed silicates are often iron-poor and magnesium-rich, e.g. forsterite and enstatite. Observations (van Boekel et al. 2004) and the short timescale of crystallization (Lenzuni et al. 1995) suggest that the crystalline silicate fraction on the inner rim surface approaches unity.

We only present 10μm forsterite grains in this paper. Given the expected high abundance of crystalline particles in the inner disc, we also perform full scattering computations for our olivine and forsterite mixtures. Using a 0.1%, 10% or 90% forsterite abundance allows to follow the transition from an amorphous- to crystalline-dominated rim, assuming the former is represented by olivine and the latter by forsterite.

Iron grains, plausibly a sink of iron left over from forsterite formation, is another component we explore. Small iron grains cool more efficiently than small olivine grains, furthermore iron is significantly more refractory in the high vapour density regime, as seen in Fig. 5.3.1. Abundance ratios of 9999/1 and 90/10 are used in our olivine and iron disc models.

Corundum has been suggested to exist in discs (e.g. Lenzuni et al. 1995). It is very refractory in the low vapour density regime, and forms a "highly refractory envelope" around olivine together with iron in $T_{\rm subl}$-$\rho_{\rm vapour}$ parameter space, as seen in Fig. 5.3.1. We use a trace olivine/corundum mass abundance of 9999/1 and compare it with a model where this ratio is 99/1. The latter is a convenient limit, approaching

one obtained by taking a mixture with cosmic abundances and putting all aluminium into corundum.

Materials such as olivine do not exist in single molecule form and decompose during sublimation (Duschl et al. 1996). Thus, particles transferred to the gas phase from one grain species may contribute to upholding the gas-grain equilibrium of another species (Dominik et al. 1993). We have attempted to take this into account by using the summed partial pressures of amorphous olivine and crystalline forsterite to uphold the gas-grain equilibrium of both. Any pure iron released by the sublimation of olivine is not considered as a separate dust species in these models.

For comparison with previous studies we also present several models using astronomical silicate, in these cases the olivine sublimation law is applied.

5.4   Results

The results of our disc modelling are presented in this section. We first put forward single grain type models with realistic opacities. Then, dependencies on grain size and surface density are discussed. Finally, the effects of adding various amounts of different grain sizes or types are shown. A detailed comparison with the results of IN05 and Tannirkulam et al. (2007) may be found in Appendix 5.B.

The optical depths are computed using the dust Planck mean opacity at the stellar temperature of 10000K.

5.4.1   Olivine grains of various sizes

For the main batch of models, we used opacities of iron-containing olivines, with sublimation properties from P94.

The developing rim

The first important result is that the inclusion of detailed condensation and sublimation physics leads to a rim location which is not entirely stable. This is demonstrated in Fig. 5.4.1, where we show the location and sharpness of the rim as a function of the computational iteration number.

We begin the computation by placing the rim at the $C_{bw} = 1$ location (iteration 0), followed by two backwarming iterations where the location is dictated by an upper limit on C_{bw}. The radiative transfer (temperature determination across the disc), vertical structure of the disc, and dust sublimation and condensation are iterated on 50 to 200 times. For each iteration, we plot a horizontal bar in Fig. 5.4.1, showing the radii where the optical depth radially along the midplane ranges from 0.1 to 10, with a mark on the $\tau = 1$ location. Thus a short, point-like extent of the bar indicates a sharp rim that jumps from low to high optical depth very fast, i.e. the classical structure as proposed by DDN01.

Over 1000 iterations, we see that both the rim location as well as its inward motion are unstable. Around iteration 150, the sublimation temperature is exceeded in a small region in the rim, which becomes very sharp, with the $\tau = 0.1$ and 10
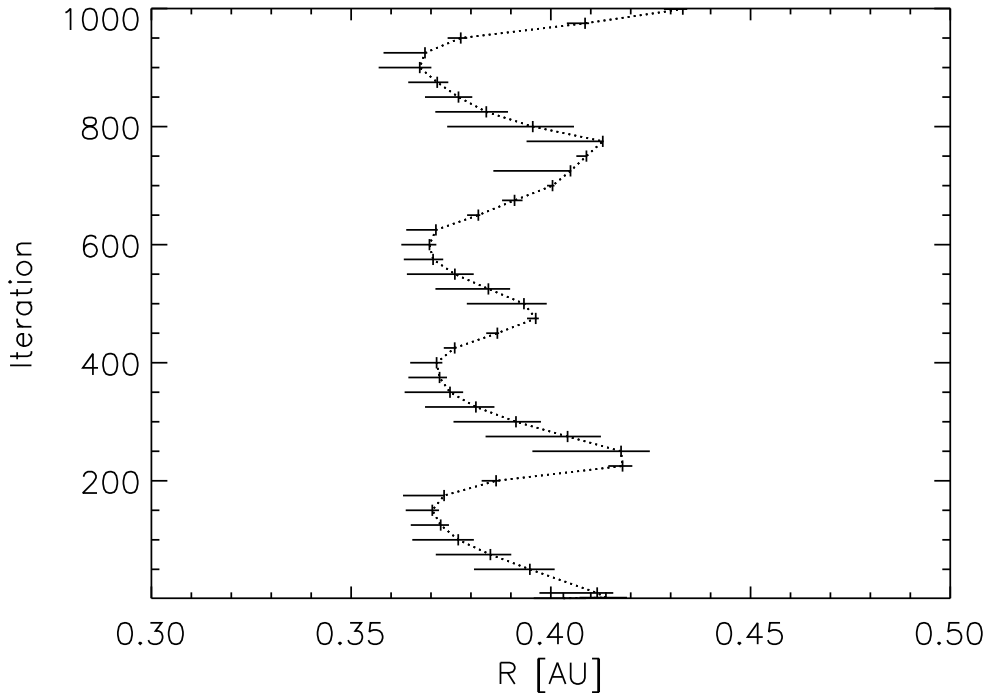
Figure 5.4.1: Distances along the midplane, in AU, where $\tau = 0.1, 1$ and 10 is reached, versus iteration number. The evolution of an $\Sigma_{\mathrm{dust}} = 25\mathrm{g/cm}^2$ inner disc with $10\mu m$ olivine over 10^3 iterations reveals the oscillatory long-term behaviour of our models. Dust is built up over ~ 150 iterations, after which the sublimation temperature is exceeded and a retreat occurs, during which the optically thin zone is narrow. The fractional extent of the rim radius variation is significantly smaller for smaller grains.

locations moving close together. The backwarming efficiency increases and the rim recedes. Around iteration 250, a new cycle begins with optically thin zone formation.

Similar variability in the rim location is evident in models with multiple grain types. The variability in rim structure which we have demonstrated can, in some cases, considerably affect the fractional NIR excess, f_{NIR}, making it difficult to associate illustrative values with a particular model. We are working on clarifying the issue.

It must be emphasized that while we have just described the changes in rim structure as if time-dependent, our modelling has no physical time dependence. Rather, our results seem to indicate that there is no unique, static solution for the dust distribution in the rim, at least when a single grain type is used, and variations should be expected in a proper time-dependent treatment.

Grain size and surface density

As we saw in Section 5.3, both the grain size as well as the surface density influence the rim location. This is demonstrated in the first three panels of the summary diagram in Fig. 5.4.2, which show the rim location and sharpness for models with three different grain sizes and a range of surface densities. For a given total (solid and vapour) dust surface density of 1g/cm^2 (models 0-2), the rim of $0.1\mu m$ grains is at 2.22AU, while $10\mu m$ grains put the rim at 0.43AU and $100\mu m$ grains at 0.29AU. A shift of the rim location towards the star is also evident for surface density variations with a fixed grain size of $10\mu m$ (models 3-8) and of $100\mu m$ (models 9-13). We will return to this point in Section 5.5 and show how this can be understood analytically.

Another feature of the single grain type models is the relative sharpness of the rims. It seems that if enough condensible material is available, the rim will take a sharp form, as assumed in the classical rim models. The low surface density computation in model 3 reveals the situation in discs with low amounts of condensible material available. In model 3, the $\tau = 0.1$ to 10 region extends from 0.67 to 1.88AU because the opacity is too small for the optical depth to rise quickly with radius even if all condensible material is put in the solid phase. A similar effect is seen in models 9-13, where the same parameter study as with models 3-8 is carried out with $100\mu m$ grains.

While in these models, the low surface density or very large grain size might seem artifical, effects similar to those seen here also emerge in multi-grain models with trace species that might be present in the very hot inner regions of discs. We will now turn our attention to these models.

5.4.2   Two sizes of olivine grains

Increasing the grain size generally allows cooling to gain in efficiency compared to heating. We will now present the effects of this in models where small and large grains are mixed.

Models 14-17 of Fig. 5.4.2 contain two different grain sizes of the same material, in this case olivine. How the optically thin region is cooled by the large olivine grains, and then filled up as the abundance is increased, is demonstrated sequentially as temperature maps in Fig. 5.4.3.

In the upper row of Fig. 5.4.3, the $0.1\mu m$ grains (left panel) have a rim at 2.22AU, the $10\mu m$ particles (right panel) at 0.43AU. Differences in dust temperature throughout the inner disc are evident.

Model 14, seen in the middle row, is a disc with a $0.1\mu m$ to $10\mu m$ grain mass ratio of 9999/1. The trace abundance of efficiently cooling large grains is sufficient to give rise to an extended, cool region of low optical depth, which shifts the condensation location of $0.1\mu m$ grains from 2.22AU (model 0) to 1.68AU. The $\tau = 10$ location coincides closely with this point, indicating that a large amount of $0.1\mu m$ grains exists, pushing up the opacity. An optical depth of $\tau = 0.1$ is reached at 0.81AU, indicating the optically thin region covers 50% of the rim radius and around 75% of the surface inside that radius.

N_{mod}	log Σ_0	Olivine 0.1	Olivine 10	Olivine 100	Fors 10	Iron 0.1	Iron 10	Cor 0.1
0	0	1.0						
1	0		1.0					
2	0			1.0				
3	−3	1.0						
4	−2	1.0						
5	−1	1.0						
6	0	1.0						
7	1	1.0						
8	2	1.0						
9	−2			1.0				
10	−1			1.0				
11	0			1.0				
12	1			1.0				
13	2			1.0				
14	0	0.9999	0.0001					
15	0	0.9	0.1					
16	0	0.9999		0.0001				
17	0	0.9		0.1				
18	0		0.9999		0.0001			
19	0		0.9		0.1			
20	0		0.1		0.9			
21	0	0.9999				0.0001		
22	0	0.9				0.1		
23	0		0.9			0.1		
24	0		0.9				0.1	
25	0	0.9999						0.0001
26	0	0.99						0.01

R_{rim} [AU] axis: 0.0, 0.5, 1.0, 1.5, 2.0, 2.5
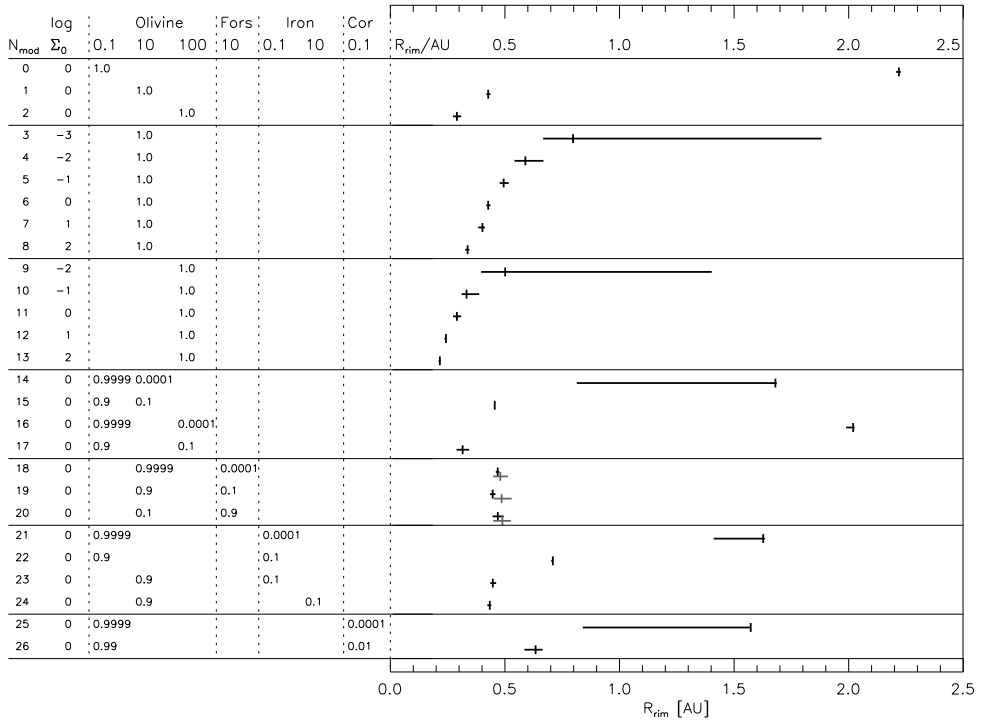
Figure 5.4.2: $\tau = 0.1$, 1 and 10 radii of selected models. Total dust surface densities are given, and normalized abundances are tabulated. Cases with no scattering are given (*black, upper lines*), with isotropic scattering indicated for forsterite (18-20, *dark gray, lower lines*). The horizontal bars indicate the $\tau = 0.1$ and 10 radii. Models $0 \ldots 2$ provide a comparison to surface density $(3 \ldots 13)$, size $(14 \ldots 17)$ and composition $(18 \ldots 26)$ variations.

The effect of pulling in the rim is more pronounced in model 15, seen in the bottom row of Fig. 5.4.3, where 10% of the dust mass is in 10μm olivine grains and the rest in 0.1μm grains. The inner rim is now at 0.45AU. The large grains dominate the structure, which is close to that of the disc with only large grains (model 1). The smaller, 0.1μm grains exist all the way to the new rim location, in a region where they could never condense without the presence of the larger particles.

Model 16 shows that a fractional mass abundance of 10^{-4} of 100μm grains has very little effect on the small grain rim, for their low abundance is insufficient to contribute to the optical depth. Model 17 demonstrates that a 10% abundance of 100μm grains is sufficient for them to dominate the rim location at a total dust surface density of 1g/cm^2.

5.4.3   Olivine and forsterite

Forsterite is expected to be very abundant in the inner rim region. We now present modelled disc structures obtained with no scattering (our usual assumption) and with isotropic scattering for mixtures of 10μm olivine and forsterite.

Since relative to olivine, forsterite grains are highly transparent to stellar radiation, one might imagine them to exist very close to the star. In addition to having a low heating efficiency in the stellar radiation field, however, forsterite grains cool very inefficiently at temperatures of 1300...1500K. This causes them to sublimate at approximately the same radius as the iron-rich silicates, leading to no difference between the rim structure of model 1 and models 18 to 20 in the case with no scattering, as seen in Fig. 5.4.2. Including isotropic scattering (lower, dark gray lines of models 18 to 20) slightly increases the rim radius because of the increased backwarming efficiency. Note that at temperatures of a few hundred kelvin, the forsterite grains will cool much more efficiently and be much cooler than the iron-containing silicate grains.

5.4.4   Small amounts of efficiently cooling or ultra-refractory material

Small, 0.1μm grains of iron and corundum are more efficiently cooling than olivine of the same size, and may exist significantly closer to the star. The high refractivity of corundum and iron provides another mechanism that allows grains to survive near the star.

A mass abundance of 0.0001 in 0.1μm iron grains pulls the rim of similarly sized olivine from 2.22AU to 1.63AU and gives rise to an optically thin zone covering $\approx 10\%$ of the rim radius (model 21). While 0.1μm iron is cooler than olivine, it does not cool the inner disc as efficiently as corundum does (see below and Fig. 5.4.4). A 10% abundance of small iron pulls the rim to 0.71AU, but now the rim is very sharp (model 22), and the structure resembles that obtained with a 90/10 mass ratio of small and large olivine grains (model 15, see Fig. 5.4.3)

Adding an abundance as large as 10% of either 0.1 or 10μm iron particles to 10μm olivine (models 23 and 24) has little effect on the rim location (model 1), as the cooling efficiency of larger olivine grains is similar to that of iron.

Model 25 shows the effects of a mass abundance of 0.0001 of 0.1μm corundum grains in a disc of olivine of the same size. The corundum is significantly cooler than the olivine, as seen in Fig. 5.4.4. The rim has moved from 2.22AU (the 0.1μm olivine rim in model 0) to 1.57AU, with an optically thin zone beginning already at 0.84AU, i.e. covering $\approx 45\%$ of the radial distance and 70% of the surface area inside the $\tau = 1$ radius.

Allocating corundum a mass fraction of 0.01 (model 26), a rough upper limit based on the assumption that the cosmic abundance of aluminium is all in corundum, demonstrates that this species can draw the rim in considerably. Small, 0.1μm corundum grains draw the rim in more efficiently than iron of the same size, both because they are relatively more refractory at the low densities they have in these

models (as low as 10^{-17}g/cm^3, see Fig. 5.3.1), and because they cool more efficiently at temperatures typical of dust sublimation.

A comparison of how small abundances of 0.1μm corundum and iron in a disc of identically sized olivine cool the inner disc, and how their refractivity allows them to exist closer to the star, is presented as temperature maps of models 25, 21 and 22 in Fig. 5.4.4. Corundum (top row) cools more efficiently than iron (e.g. middle row), and with a further contribution from its high refractivity, it moves the rim to 1.57AU, closer to the star than an identical mass abundance of iron, which is at 1.63AU. A 10% mass abundance of small iron grains is sufficient for them to dominate the rim structure and decrease the radius considerably, to 0.71AU. Due to the similar cooling properties of 0.1μm iron and 10μm olivine grains, models 15 and 22 are similar.

5.5 Discussion

5.5.1 Modelling summary

We have successfully employed the Monte Carlo radiative transfer code MCMax (Min et al. 2009) in modelling the inner rim structures of dusty passive protoplanetary discs.

Results in Section 5.4 show that, especially for larger grains, a rigorous treatment of dust sublimation and condensation, together with other rim physics in MCMax, may not always lead to a stable solution for a solid dust density and temperature distribution in a passive, static disc framework.

5.5.2 Where is the rim?

The rims of MCMax disc models are generally between the optically thin destruction and the backwarmed wall radii (the $C_{bw} = 1$ and 4 radii, respectively). Grains can begin to attenuate the stellar radiation field from the $C_{bw} = 1$ location outward, allowing the rim to exist closer than a fully backwarmed estimate. That the rim location could vary like this has been pointed out earlier (e.g. Monnier et al. 2005), but we have explored the phenomenon in detail for the first time.

For a given dust species, larger grains will generally cool more efficiently and thus will set the rim location, but only if they are present in sufficient abundance, as shown in Figures 5.4.2 and 5.4.3. Large grains of olivine can exist much closer to the star than small grains. A small, 0.0001 abundance of 10μm grains is enough to create an extended, cool optically thin region in front of the rim, which is still determined by 0.1μm grains. Allocating a fraction 0.1 of the mass to large grains is sufficient for them to determine the rim location.

It was noted by IN05 that the most refractory species would determine the rim location, if it was also able to build up enough optical depth. They also pointed out that for one species, the largest grains would position the rim under the same assumption. We add the generalization that refractivity and cooling efficiency combine to determine the species which sets the rim radius. A very high cooling efficiency may
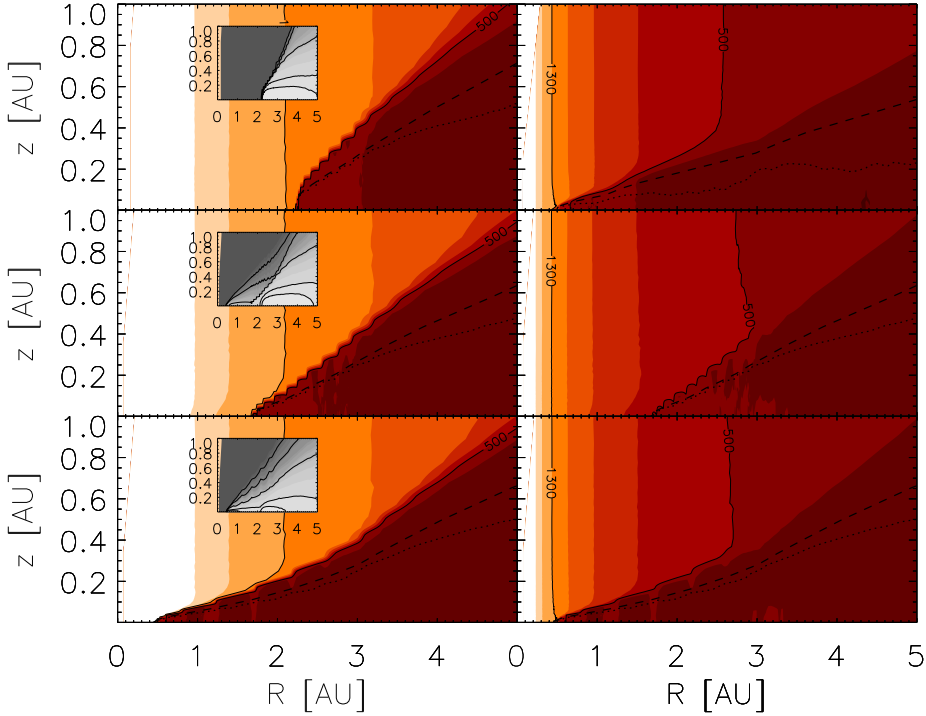
Figure 5.4.3: Temperature (main) and density (insets) maps of disc inner regions for various olivine mixtures. The axes show radial distance from the star along the midplane and vertical height from it. The colour levels represent the dust temperature in steps of 100K, for reference we give solid lines at 500K and 1300K. Also shown are the radial (dashed) and vertical (dotted) $\tau = 1$ surfaces for the stellar radiation. The inset maps have total solid dust density contours at factors 2.7, 10, 10^4, 10^7 and 10^{10} below the maximum. The dust surface density in these models is $\Sigma_g \approx 1g/cm^2$. A typical midplane dust density is $3 \cdot 10^{-13} g/cm^3$. In models with several dust species, the species are thermally decoupled, but radiative thermal equilibrium arises naturally deep inside the disc. Non-uniformities in the temperature maps reflect Monte Carlo noise and the resolution of the angular grid. **Top row:** Models of discs with one grain size. Shown is the dust temperature for discs with 0.1 (left panel) and 10μm (right panel) olivine grains (models 0 and 1 in Fig. 5.4.2). **Middle row:** A disc with a small to large grain mass ratio of 9999/1 (model 14). Given are the temperatures of the small, 0.1μm grains (left) and the larger, 10μm grains (right). **Bottom row:** A disc with a mass abundance ratio of 90/10 in small/large grains (model 15). We again give the temperatures of the 0.1μm grains (left) and 10μm grains (right) that co-exist in this disc.
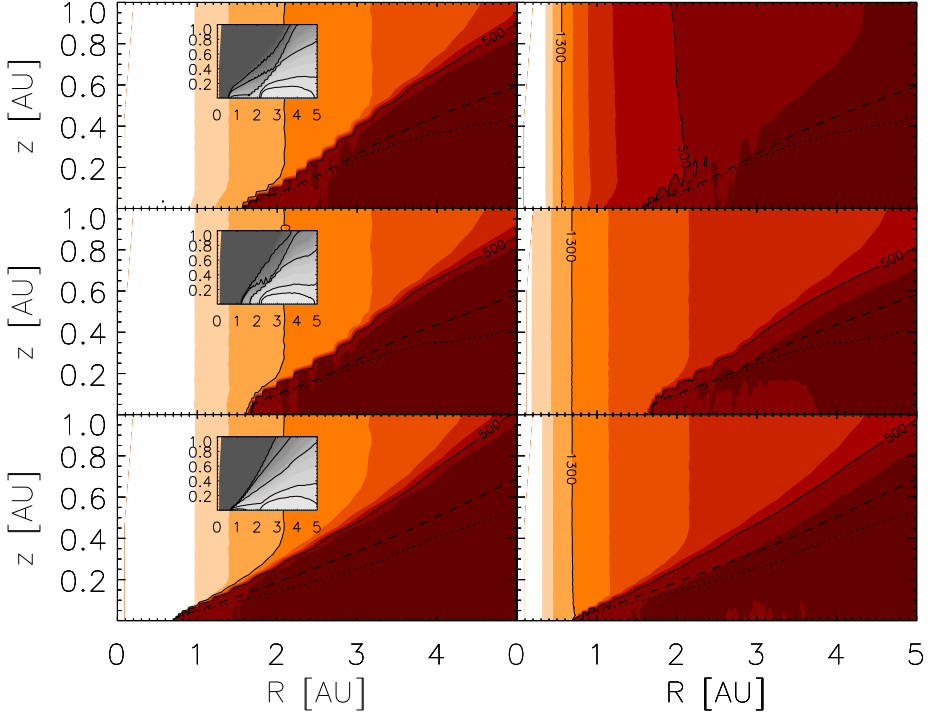
Figure 5.4.4: Temperature (main) and density (insets) maps of disc inner regions for various grain mixtures. See Fig. 5.4.3 for a detailed legend. **Top row:** A disc with an olivine to corundum mass abundance ratio of 9999/1. Shown are the temperatures of the 0.1μm olivine (left) and the 0.1μm corundum (right) grains. (Model 25 of Fig. 5.4.2, compare with model 0.) **Middle panel:** A disc with an olivine/iron mass abundance ratio of 9999/1 (model 21). Shown are the temperatures of the 0.1μm olivine (left) and iron (right) grains. **Lower panel:** A disc with an olivine/iron mass abundance ratio of 90/10 (model 22). Given are the temperatures of the 0.1μm olivine (left) and iron (right) grains.

allow a species which does not have the highest sublimation temperature to determine the rim location.

For a given cooling efficiency, the species with the highest sublimation temperature will determine the rim location, again assuming a sufficient abundance of it is present. Corundum has been considered an ultra-refractory condensate in discs, which it is if one assumes that all species have equal partial pressures. However, if the dust vapour densities are taken equal, as in vertical slices in Fig. 5.3.1, corundum is more refractory at vapour densities $\rho_{\text{vapour}} < 10^{-10}$, but at $\rho_{\text{vapour}} > 10^{-10}$, the sublimation temperature of iron is higher and increases rapidly. Hence, iron is the most likely dust
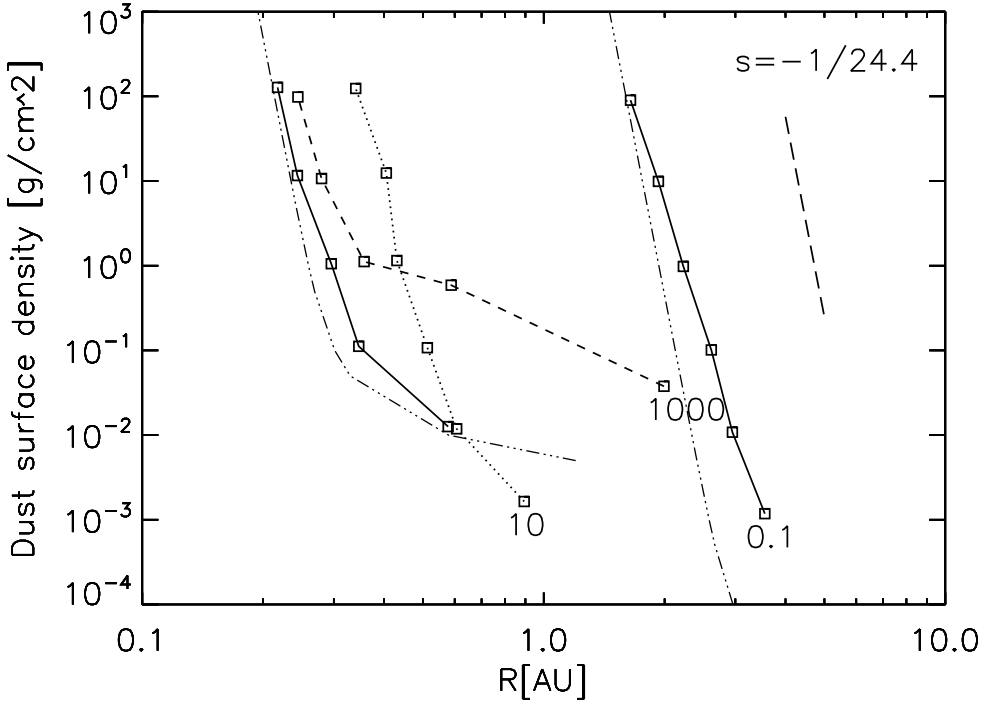
Figure 5.5.1: Midplane rim locations and dust surface densities for various sizes of olivine. *Boxes* represent the final computed MCMax iteration, usually between 50 and 200. The left *solid* line connects models with 100μm grains, and the right 0.1μm. *Dash-dotted* lines represent analytical computations for the same grain sizes with Eq. 5.3 for $C_{bw} = 1$ and a dust temperature of 1500K. The *dotted* line connects models with 10μm grains, and the *dashed* one 1000μm. **Grain size variations:** The rim radius R_{rim} changes by almost an order of magnitude for olivine grain size variations. **Surface density variations:** For a given grain size, increasing the surface density decreases R_{rim}, in one limit as a power law (shown by the *long-dashed* line). Models for a given grain size follow irregular lines due to variations between iterations (see Fig. 5.4.1).

species to be responsible for rim temperatures above 1500K [2].

The above points to the fact that if grain growth proceeds steadily and the dust has a complex composition featuring efficiently cooling and refractory metal oxides such as iron or corundum, the rim will exist close to the star, at 0.4AU or closer for

---

[2]This is subject to the validity of the thermodynamic data for iron from P94. Sublimation temperatures more than 200K lower than this are found with data from Cameron & Fegley (1982). However, P94 considered a protoplanetary nebula environment, where iron-rich silicates and other species contribute to the vapour pressure of iron. They assumed a silicate to iron mass ratio similar to ours, therefore we use their results with confidence but state that a full treatment of the multi-species gas-grain equilibria is desired.

a $47L_\odot$ Herbig star if $\Sigma_d \geq 10^0 \mathrm{g/cm^2}$ (see Figures 5.4.2 and 5.5.1). Evidence for grain growth is presented in e.g. van Boekel et al. (2004) and Herbst et al. (2008). Relatively large rim radii, for a star of the type used here $R_{rim} > 2AU$, are likely to arise as the inner disc is cleared of gas by the magneto-rotational instability (Chiang & Murray-Clay 2007) or a planet, lowering the sublimation temperature. Dust may also be dynamically cleared.

Surface density controls the rim location for a given grain size. This is described by a $R_{rim} \propto \Sigma_{dust}^{s=-1/24.4}$ power law in the sublimation-controlled regime and is illustrated in Fig. 5.5.1. The low density ends of lines in Fig. 5.5.1 branch off from the power law as there is insufficient mass to reach $\tau = 1$ at the dust evaporation location. An analytical description of the rim location as a function of surface density for both the sublimation-controlled and optical depth controlled regimes is given in Eq. 5.3. It is a curve which branches from the power law and asymptotically becomes parallel to the x-axis.

$$
R_{rim} = \left[C_1^{-p} \left(22.09 \Sigma_{subl}^{0.020} S_1 \left(\frac{C_{bw}}{\epsilon} \right)^{-0.252} - \right.\right.
$$
$$
\left.\left. C_2 \frac{1+4p}{\kappa'} \Sigma_{subl}^{-1-0.078p} S_2 \left(\frac{C_{bw}}{\epsilon} \right)^{\frac{1+8.080p}{8}} \right) \right]^{-\frac{4}{1+4p}} \text{[cm]} \tag{5.3}
$$

This equation, derived in Appendix 5.A, yields the curves seen in Fig. 5.5.1. κ' is the dust opacity at $0.55\mu m$, in $\mathrm{cm^2/g}$. Note that the surface density profile is anchored to Σ_{subl}, its value at the sublimation radius, with a radial dependence of $\Sigma \propto R^{-p}$. The properties of the central star are hidden in $S_1 = M_\star^{0.010} L_\star^{-0.252}$ and $S_2 = M_\star^{-\frac{1+0.078p}{2}} L_\star^{\frac{1+8.080p}{8}}$. The constants are given by $C_1 = 4.1982 \cdot 10^{-6}$ and $C_2 = 4.84 \cdot 10^8$.

The good correspondence of the analytical curves described by the above equation with our numerical results shows that Eq. 5.3 captures the processes that are thought to dominate the rim location in dusty discs, and we propose it as an aid in interpreting more sophisticated numerical models, but also observations.

The sublimation properties of olivine were used in the above derivation. To use the presented formalism for any dust species, a power law fit to Pollack et al. (1994) data should be obtained ($T_{subl} = G_K (\rho_{gas} / [1\mathrm{g/cm^3}])^\gamma$, see also IN05 and compare with Eq. 5.1).

Omittances in the above analytical approach include the temperature dependence of the cooling efficiency, $\epsilon(T_{dust})$, and the fact that partial condensation of dust occurs in front of the $\tau = 1$ location, i.e. the rim is always somewhat diffuse. These two effects are the main culprits in the discrepancies between the numerical and analytical curves seen in Fig. 5.5.1.

We use a flat dust surface density profile $\Sigma \propto R^{-p}$, where $p = 0$, in the inner disc, however Eq. 5.3 is generic and allows to use the canonical $p = 1 \ldots 1.5$. Furthermore, the sublimation location for a given surface density and grain type is independent of the surface density power law.

Used with observed rim radii, Eq. 5.3 may prove useful in estimating the surface

density in the inner disc. For this, the equation should be solved numerically for Σ_{subl}, inserting the stellar properties and adopting constraints on the grain opacity and the surface density power law.

5.5.3   Is the rim diffuse or sharp?

The optically thin inner disc region is an important concept. A $\tau < 1$ region between $C_{\text{bw}} = 1$ and 4 is supported by any of three conditions: 1) a low surface density, 2) a high surface density but very low opacity, and 3) early stages of dust condensation in a cool region.

Condition 1 can be met by a low-abundance of a species which is more refractory than the bulk of the dust, such as corundum (see model 25 in Fig. 5.4.2), or which can cool relatively efficiently, such as large grains or iron (models 14 and 21 in Fig. 5.4.2).

Condition 2 could be met by a dust type which is very transparent in the optical, but cools efficiently in the NIR. If the scattering phase function of such a species is not strongly forward-peaked, a population of grains closer to the star than the rim (determined in this case by the sublimation of another, more opaque species) could further give rise to an extended hot radiation zone through scattering.

Condition 3 is met as a transient phenomenon in our models, which allow dust to slowly condense into an initially empty inner disc, creating and then filling in an optically thin region, as illustrated by Fig. 5.4.1. Transient heating events such as a powerful flares may destroy dust in an inner disc region, which will subsequently go through a similar cycle of a transient extended optically thin zone during dust re-condensation. It would be surprising to observe long-lived sharp rims composed of only large grains. However, our modelling also indicates that adding several types of dust to a model makes the rim structure much more stable.

5.5.4   Dust differentiation

Differentiation of dust types can occur in the optically thin region, where highly refractory or very efficiently cooling species can exist independently of more volatile or less efficiently cooling species. Maintaining such an extensive optically thin region in a disc with a diverse and broad distribution of grain sizes and compositions requires considerable fine-tuning, thus sublimation-based differentiation in a static disc is unlikely.

5.5.5   Observational implications

The smallest observed characteristic rim radii for $L_\star \approx 50 L_\odot$ stars are around 0.2AU (Millan-Gabet et al. 2007). These come from ring model fits to visibility curves. In the framework of our models, such small radii require grains of around 100μm to be present at dust surface densities of $\Sigma_{\text{d}} \approx 10^{0\ldots2}$g/cm^2 (Fig. 5.4.2, in particular models 11 to 13).

It may be feasible to put a lower limit on the inner rim surface density Σ_{rim} of a system with Eq. 5.3, under the assumptions that a measured R_{rim} corresponds

to $C_{bw} \approx 1$, and that R_{rim} is determined by the sublimation of grains with $\epsilon \approx 1$. The former is suggested by comparison of the Monte Carlo and analytical results in Fig. 5.5.1, and the latter reflects the assumption that large, efficiently cooling grains will dominate the inner disc. One could then use a measured R_{rim} with the stellar luminosity and mass to obtain a simple lower limit on the surface density.

Furthermore, it is interesting to assume that the largest grains needed to satisfactorily fit the mid- to far-infrared SED of a system provide a lower limit on the size of the grains setting the location of the inner rim. Under this assumption, an upper limit for Σ_{rim} could be obtained by using the cooling efficiency ϵ of these grains in Eq. 5.3. If we further assume that these grains dominate the rim location instead of $\epsilon \approx 1$ grains, we are again left with a lower limit on Σ_{rim}.

Comparing these limits with observed disc masses and canonical $\Sigma \propto R^{-1...-1.5}$ power laws will constrain the difference between the inner and outer disc surface density profiles.

Our results hold if the optical depth of gas in the inner hole to stellar radiation is $\tau_{g,\star} \ll 1$ and, relatedly, if accretion can be neglected. If the gas continuum opacity in the inner hole is $\tau_{gas,\star} \approx 1$, shielding will decrease the dust destruction radius by $[\exp(-1)]^{1/2} \approx 20\%$, if the gas itself does not approach stellar temperatures. A hot gaseous component may give rise to NIR emission observed inside the dust destruction radius in some systems (Eisner et al. 2007; Tannirkulam et al. 2008b,a; Kraus et al. 2008; Isella et al. 2008).

As Najita et al. (2009) have pointed out, modelling indicates that gas in the inner hole of a Herbig Ae/Be star should produce spectral features of CO and H_2O, but instead a continuum process was found necessary to explain the compact NIR excess of MWC480. Potentially relevant opacity sources inside the classical dust sublimation radius include H_2O, H^-, free-free emission and highly refractory or transparent dust species (e.g. Najita et al. 2009). However, even the most refractory species hypothesized to exist in discs, such as corundum, are not expected to have a significant solid fraction inside the classical silicate dust sublimation radius.

If a dust species is responsible for a extended hot emission component reaching from a few stellar radii to the optically thick dust rim, it is likely to have low absorption in the visible range and a high cooling efficiency in the NIR. Moreover, species with small absorption cross-sections and relatively isotropic scattering phase functions in the visible or NIR regimes may play a role in creating an extended radiating zone in the inner disc by scattering stellar or rim emission.

Forsterite meets some of the above requirements, however it is not able to cool efficiently in the NIR and thus differs little from olivine in terms of rim structure, as seen in Fig. 5.4.2.

5.5.6 Looking ahead

To make full use of our work, observed SEDs and interferometric visibilities (as opposed to rim radii derived from them under various assumptions) need to be fitted simultaneously with MCMax or a similarly capable code. A paper focussing on the observational applications of our models is in preparation. We are performing a study

of the extreme values of observables that can be obtained with static dust models, as well as simultaneously fitting the SEDs and visibilities of specific objects.

We are actively exploring whether the fractional NIR excesses of our models provide a source of additional information about the inner disc surface density and/or grain type. As f_{NIR} varies with iteration as well as grain, disc and stellar properties, a better handle on the variability of the rim is needed before this fraction is useful.

Rim temperatures obtained from NIR SED-fitting and limits on inner disc gas densities would increase the usefulness of Eq. 5.3 in constraining the amount and type of dust in the rim region.

We support the conclusion, overlapping in part with Monnier et al. (2005), that detailed modelling of multi-species condensation and sublimation processes, as well as simultaneous treatment of radiative transfer in the gas and dust components, is needed to make further progress on the numerical side, and encourage gas and dust modellers to join efforts.

5.6   Conclusions

We have demonstrated a wide range of possible inner rim structures in a parameter study of grain size, composition and dust surface density, as well as multiple grain type models. To do this, we implemented dust sublimation and condensation physics into a fast Monte Carlo radiative transfer code. Here, we outline our main conclusions:

1. The inner rim in dusty discs is not an infinitely sharp wall. Backwarming effects combine with sublimation and condensation in leading to a diffuse region that can extend over a significant fraction of the rim radius. In our treatment, dust generally begins to condense near the $C_{bw} = 1$ location and the $\tau = 1$ surface is closer to the star than in previous models.

2. The inner disc surface density of a given species is an important parameter, because it determines the highest possible temperature where the species can be stable. High surface densities move the rim closer to the star.

3. The dust component (species or size) which determines the rim location by building up an optical depth of unity closest to the star need not have the highest sublimation temperature, it may instead cool very efficiently.

4. If large particles are abundant enough to produce optical depth, then the rim location will be dominated by silicates. If large particles are not abundant enough, corundum and iron grains will likely set the rim location. In either case, for our standard star, the rim location is typically around 0.4 AU, much smaller than models for 0.1μm silicate grains would predict.

5. For any given grain material and size, the rim location can be analytically expressed as a function of stellar properties and of surface density. We give this expression in full form for a silicate-dominated rim.

6. The optically thin region can cover 70% of the surface inside the rim radius in cases where a very efficiently cooling or highly refractory species is present in low abundance compared to the less efficiently cooling or more volatile bulk of the dust.

7. In the case of very low surface densities, the build-up of optical depth will be slow, and the rim region will be very diffuse.

Acknowledgments

5.A   Analytical relation between rim radius and surface density

The rim location for a given grain type is a function of surface density at the rim location, as seen in Fig. 5.5.1. At high surface densities, this dependence is a power law. This power law relation is a limiting case of a more general relation describing the $\tau = 1$ location as a function of surface density. At low surface densities, the rim location moves away from the dust sublimation radius as not enough dust is available there to reach an optical depth of unity.

The calculations that follow use the `cgs` system of units. This is important to keep in mind when using the final expressions, where everything is implicit except the relevant characteristics of the dust, the disc and the star.

5.A.1   Sublimation-controlled regime

We assume initially that the rim is at the dust destruction location, $R_{\mathrm{rim}} \equiv R_{\mathrm{subl}}$, and wish to describe this radius as a function of dust surface density, $\Sigma_{\mathrm{d}} = \Sigma_{\mathrm{gas}}/f_{\mathrm{gd}}$, where $f_{\mathrm{gd}} = 100$ is the gas to dust ratio. Assuming the minimal rim radius is at the dust sublimation location, with $C_{\mathrm{bw}} = 1$, we first express the temperature of a grain at the rim radius from Eq. 5.2:

$$T_{\mathrm{d}} = \left(\frac{C_{\mathrm{bw}}}{\epsilon}\right)^{\frac{1}{4}} \left(\frac{L_{\star}}{16\pi\sigma}\right)^{\frac{1}{4}} R_{\mathrm{subl}}^{-\frac{1}{2}}, \tag{5.4}$$

where C_{bw} is the backwarming factor, ϵ the cooling efficiency of the grain and $L_{\star}$ the luminosity of the star. This expression assumes the disc is optically thin until the rim radius.

Further assuming that the gas and dust are in thermal equilibrium, their scaleheights will be the same and we can relate the midplane dust density ρ_{d} to the dust surface density via

$$\Sigma_d(R_{rim}) = \int_{-\infty}^{\infty} \rho_d(R_{rim}) \exp\left(-\frac{z^2}{2h^2}\right) dz, \qquad (5.5)$$

where z is the vertical distance from the midplane and h is the scaleheight, $h \propto T_d^{1/2} R_{rim}^{3/2}$. Integrating Eq. 5.5 and replacing the temperature with Eq. 5.4, we obtain a relation connecting $\Sigma_d(R_{rim})$, $\rho_d(R_{rim})$ and R_{rim}.

Using the IN05 power law fit to the sublimation law of olivine, we can write

$$T_d \equiv T_{subl} = 2000 \left(\frac{\rho_d f_{gd}}{a_d \cdot 1g/cm^3}\cdot\right)^{0.0195} \qquad (5.6)$$

Here, the bulk gas density, used by IN05 in fitting, has been broken into the dust density ρ_d, abundance of the species a_d and the gas to dust ratio f_{gd}. Taking the appropriate abundance from P94, we obtain the relation:

$$R_{subl} = C_1 \frac{L_\star^{0.53}}{\Sigma_d^{0.04} M_\star^{0.02}} \left(\frac{C_{bw}}{\epsilon}\right)^{0.53} [cm] \qquad (5.7)$$

This power law, where $C_1 = 4.198 \cdot 10^{-6}$, describes the minimum radius where dust can condense as a function of the surface density at that location. Note that if one assumes full condensation of the dust, backwarming will move the rim further, an effect which can be explored by varying C_{bw}. A more general expression for the rim location is formulated below.

5.A.2 Optical depth controlled regime

The inner rim is defined as the radial $\tau = 1$ location for a stellar photon at $\lambda = 0.55\mu m$. For high surface densities and under the assumptions of full condensation and $C_{bw} = 1$, this corresponds closely to the dust destruction radius. However, the lower the surface density, the longer the distance along the midplane that photons have to travel to reach an optical depth of unity. Thus, at relatively low surface densities, one predicts (and our numerical results show) a turn-off from the power law of Eq. 5.7.

We begin by integrating the optical depth through dust radially along the midplane:

$$\tau = \kappa' \int_{R_{subl}}^{R_{rim}} \rho_d(R) dR. \qquad (5.8)$$

Here, R_{subl} is the dust destruction radius of Eq. 5.7, R_{rim} is the rim radius, for which one assumes $\tau = 1$, and κ' is the mass absorption coefficient of the dust at $0.55\mu m$. $\rho_d(R)$, the radial run of dust density, is obtained by multiplying Eq. 5.5 with a factor $\Sigma_{subl}(R_{subl}/R)^{-p}$. This is a surface density power law fixed at the sublimation location, i.e. Σ_{subl} and R_{subl} obey Eq. 5.7. Assuming some power p relates the rim radius to the surface density at the sublimation location.

Employing Eq. 5.7 for R_{subl} and inserting physical constants, we are left with the following description of the rim location:

$$R_{rim} = \left[C_1^{-p} \left(22.09 \Sigma^{0.020} S_1 \left(\frac{C_{bw}}{\epsilon} \right)^{-0.252} - \right. \right.$$

$$\left. \left. C_2 \frac{1+4p}{\kappa'} \Sigma^{-1-0.078p} S_2 \left(\frac{C_{bw}}{\epsilon} \right)^{\frac{1+8.080p}{8}} \right) \right]^{-\frac{4}{1+4p}} \text{[cm]} \tag{5.9}$$

This equation yields the curves seen in Fig. 5.5.1. P relates to the surface density power law as $P = (1 + 4p)/4$ and the properties of the central star are hidden in $S_1 = M_\star^{0.010} L_\star^{-0.252}$ and $S_2 = M_\star^{-\frac{1+0.078p}{2}} L_\star^{\frac{1+8.080p}{8}}$. The constants are given by $C_1 = 4.198 \cdot 10^{-6}$ and $C_2 = 4.84 \cdot 10^8$. It is important to keep in mind that the sublimation properties of olivine were used in the above derivation.

5.B   Differences from IN05 and T07

In modelling discs parametrized identically with those of Isella & Natta (2005, IN05), we find systematically smaller rim radii. The main reasons are that the IN05 formalism yields a higher optically thin dust temperature and a lower sublimation temperature than the treatment used in this work, as discussed below. A similar study by Tannirkulam et al. (2007, T07), which we also comment on, found results different from both this work and IN05.

We find rim radii smaller than those of both IN05 and T07 and for all modelled grains, i.e. 0.1, 0.5 and 1.3μm astronomical silicate. As seen in Fig. 5.B.1, the relative difference increases with grain size, from $\Delta R_{rim} \approx 10\% R_{IN05}$ for 0.1μm grains to $\Delta R_{rim} \approx 35\% R_{IN05}$ for 1.3μm.

The IN05 disc model uses the radiative transfer equation given by Calvet et al. (1991) for a semi-infinite slab to get a radial temperature structure inside the rim, and then calculates the vertical structure as in CG97 and DDN01. A gas to dust ratio of 100 is used, and the total disc mass is distributed according to a $\Sigma \propto R^{-1.5}$ surface density power law extending from $R_{in} = 0.1$AU to $R_{out} = 200$AU. The dust opacity determines the temperature and vertical structures, and the gas density is used to compute the dust sublimation temperature and thus governs dust sublimation.

To obtain a law for the dependence of the dust sublimation temperature on gas density, IN05 fitted Eq. 5.6 to data from P94. The fitted points were T_{subl} of olivine (olivine is used interchangeably with astronomical silicate in this appendix, as the two are assumed to differ in optical, and not in sublimation properties) and ρ_{gas}, the bulk gas density. Because the grain-gas equilibrium is maintained by the partial pressure of olivine, this approach yields a $T_{subl} = T(\rho_{gas})$ law which is applicable only to gas of the same composition as that of P94. By applying this law to a disc with a purely olivine dust composition, IN05 obtained lower sublimation temperatures than us, as discussed next.

P94 supplied the fractional mass abundances of the species in their gas. For olivine, it is 0.00264, i.e. 26.4% of the dust mass, assuming a gas to dust ratio of 100. Thus, in the IN05 approach, olivine contributes 100% of the dust mass, but the sublimation
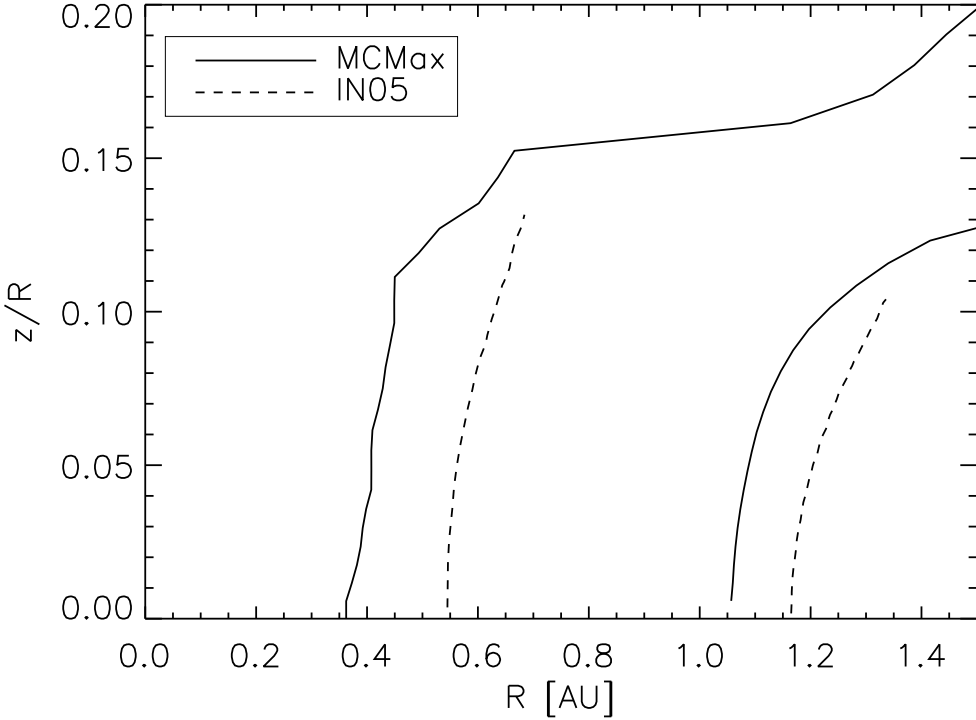
Figure 5.B.1: Radial $\tau = 1$ results for the IN05 disc models (*dashed lines*) and the same discs modelled with MCMax (*solid lines*). Grain size goes from left to right as 1.3 and 0.1μm. A systematic difference in radius is evident.

temperature is computed from the bulk gas density under the assumption that there is 100/26.4 times less olivine present, leading to a correspondingly lower T_{subl}. This underlies our choice to reduce the sublimation law to a dependence of T_{subl} on the vapour density of the species, ρ_{vapour}, and not the bulk gas – by doing so, we may use the law for all nebular compositions[3].

   Fitting the P94 data for the olivine gas density removed its abundance from our T_{subl} law, allowing us to compute the olivine sublimation temperature for any mass abundance. In an identical disc with pure olivine dust and $f_{gd} = 100$, we obtain higher sublimation temperatures than IN05, because for the same bulk gas density, pure olivine can maintain equilibrium at a higher temperature than that given by the law IN05 used.

   The above is illustrated by Fig. 5.B.2, which gives various temperatures in the rim region of an IN05 comparison disc with 0.1μm grains, modelled with MCMax. The dash-dotted line is the sublimation temperature computed and used in MCMax,

---

[3]This is valid under the assumption that olivine is the only species contributing to its own gas pressure. While this is not the case as there is no gas phase olivine molecule, it is the best we can do at present if we wish to model discs with a composition different from the P94 nebula.
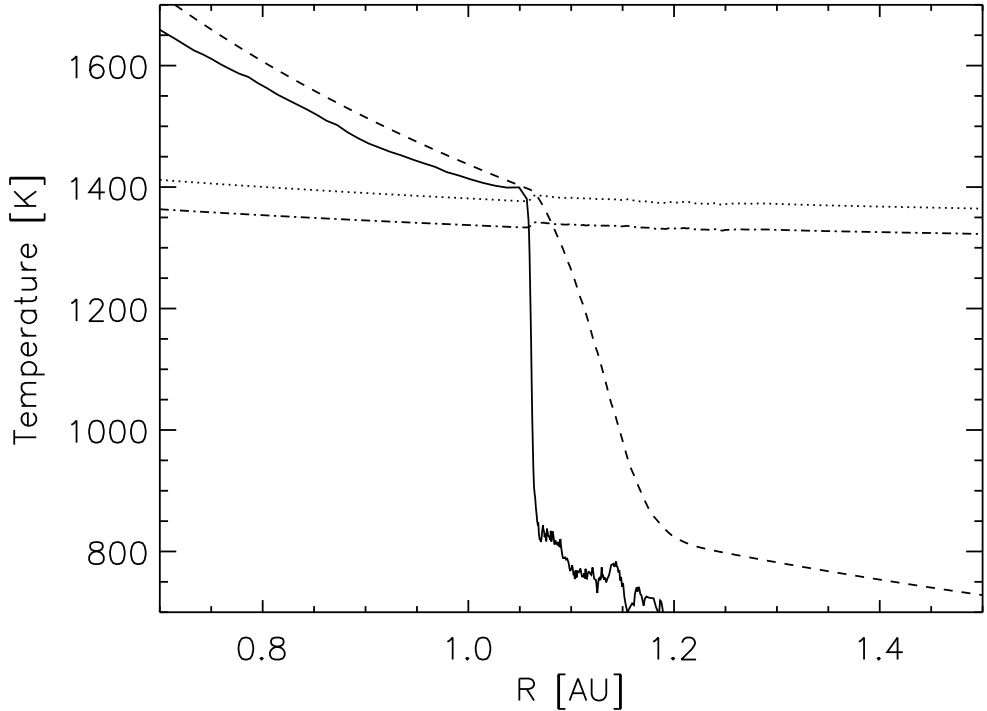
Figure 5.B.2: Midplane dust temperature structures for an MCMax model of the IN05 disc with 0.1μm astronomical silicate grains. The MCMax dust temperature structure (solid line) is seen to drop more rapidly, and is significantly cooler, in the rim region than the estimate obtained for the same density structure with the radiative transfer equation used by IN05 (dashed line). The ~ 50K difference between our estimate of the dust sublimation temperature (dotted line) and that of IN05 (dash-dotted line) is also clear. In the MCMax model, the rim radius is at 1.05AU. The intersection of the extrapolated optically thin temperature curves and the T_{subl} computed by IN05 is at ~ 1.16AU. Inside the rim, the MCMax dust temperature and that computed using the IN05 radiative transfer equation coincide better in later iterations, when more dust has condensed there and made the rim structure more similar to a wall.

according to our fit to P94 data. The dotted line, seen to lie ~ 50K below the previous, shows T_{subl} calculated from the same density structure using the IN05 sublimation law.

To use the IN05 law generally, a "dummy" bulk gas density can be calculated from an olivine density using both the P94 olivine abundance of 0.00264 and $f_{gd} = 100$. This density can be used in Eq. 5.6 to obtain T_{subl}. We do this when using Eq. 5.6 in Appendix 5.A, obtaining results which match our numerical models very well.

For radiative transfer, IN05 adopted the approach of Calvet et al. (1991). The disc is assumed to be an irradiated semi-infinite slab. A temperature structure derived

from this overestimates the disc temperature, because a semi-infinite slab can only cool in one direction, but a disc has a finite height. Two dust temperature profiles are given in Fig. 5.B.2, one from MCMax (solid line) and the other computed for the same density structure using Eq.1 of IN05 (dashed line). The IN05 approach overestimates the temperature inside the rim compared to a Monte Carlo computation. The backwarming factor as defined in Sec. 5.3.3 is useful in understanding this, as we will now discuss.

The expression derived by IN05 (their Eq.6) from C91 for the optically thin dust temperature is

$$\mathrm{T}^4(\tau_\mathrm{d} = 0) \equiv \mathrm{T}_0^4 = \left(2\mu + \frac{1}{\epsilon} \right) \left(\frac{\mathrm{R}_\star}{2\mathrm{r}} \right)^2 \mathrm{T}_\star^4, \qquad (5.10)$$

where T_0 is the dust and T_star the stellar temperature, r the distance from the star, $\mathrm{R}_\star$ the stellar radius, μ is the sine of the incidence angle of starlight on the rim, and ϵ the cooling factor as defined before.

Comparing Eq.5.10 to Eq.5.2, taking $\mu \approx 1$, we see that a backwarming factor of $\mathrm{C}_\mathrm{bw} = 2\epsilon + 1$ is implicit in the IN05 calculation. Because $\mathrm{R}_\mathrm{rim} \propto \sqrt{\mathrm{C}_\mathrm{bw}}$, the IN05 sublimation locations can be further than our estimates by up to a factor $\sqrt{2\epsilon + 1}$ for any given grain type (to relate this to rim radii derived from interferometry, see Eq.5 and 6 of Isella et al. 2006). Using $\mathrm{C}_\mathrm{bw}(\epsilon)$ in Eq. 5.9 decreases differences with IN05 considerably (from 10% to 4% of R_IN05 for $0.1\mu\mathrm{m}$ grains). However, as the comparison of results from such a C_bw and our Monte Carlo calculations has shown, this assumption generally overestimates the backwarming factor at the sublimation location.

Midplane temperatures of a disc parametrized like an IN05 model with $0.1\mu\mathrm{m}$ astronomical silicate are presented in Fig. 5.B.2. Extrapolating the optically thin dust temperature curves (solid and dashed lines) to an intersection with the IN05 sublimation temperature curve for the same density structure (dotted line), and taking into account the overestimated backwarming at the sublimation location, one sees how in MCMax, the inner rim is situated at 1.04AU and how it would be close to 1.16AU under the radiative transfer and dust sublimation assumptions of IN05.

Monte Carlo radiative transfer was used by T07 to model discs parametrized like those of IN05, obtaining rim radii larger than the MCMax results in all cases, but smaller than IN05 for $1.2\mu\mathrm{m}$ grains, and larger than IN05 for $0.1\mu\mathrm{m}$. The T07 shift from MCMax seems to be due mostly to their use of the IN05 dust sublimation law, i.e. a low T_subl, and a more basic treatment of dust sublimation and the associated numerical instabilities (A.Tannirkulam, personal communication; see also Appendix 5.C). It is not clear whether the latter accounts for the changed order of rim radii for small and large grains between IN05 and TORUS (used by T07).

In summary, compared to the treatment in the present work, the IN05 formalism leads to higher optically thin temperatures because of the assumptions implicit in the radiative transfer, and lower sublimation temperatures for pure olivine or astronomical silicate dust because of an inconsistent use of the dust density. These factors explain their comparatively larger inner rim radii. The work of T07 adopted the IN05 sublimation law with its implications for the rim radii, and the treatment of sublima-

tion and condensation in TORUS is more basic than in MCMax, leading to further variations in rim location which we are presently unable to quantify.

5.C   Numerical implementation

In this appendix we discuss the numerical implementation of the sublimation physics described previously. We find that great care has to be taken in order to avoid instabilities or incorrect results. The iterative scheme described below is accompanied by a careful regridding of the spatial grid after each iteration to make sure that the optical depth through the disc is always sampled properly, allowing for accurate radiative transfer. Although the negative effects of a somewhat less optimized spatial grid are not always evident at first sight, we find that the influence on the temperature structure is significant and a proper spatial grid is of crucial importance for a proper implementation of the sublimation physics.

5.C.1   Iterative method

A straightforward iterative implementation of dust evaporation and recondensation does not always result in a stable solution for the dust density structure. This is because of the high optical depths through the disc and the highly nonlinear radiative transfer effects resulting from it. In addition, changing the dust density in one region of the disc affects the temperature structure at other places, making the problem highly non-local. For example, the condensation of a tiny fraction of the available dust material in the inner region can already make the region in which this material was condensed optically thick, enhancing the effects of backwarming and thereby lifting the temperature of the grains above the evaporation temperature again. At the same time, the region behind it is shielded and there dust can condense. This causes situations where the density flips between two configurations which are both not the equilibrium solution. Thus, care has to be taken not to condense too much material in a single iterative step. However, the other extreme, condensing only so much material such that the change in optical depth is smaller than unity, requires a massive number of iterations which is unfeasible given the computation time required per iteration.

   Therefore, one must take care that the amount of material condensed or evaporated in a single iteration is not too small or too large. We have considered several different schemes for deciding how much dust to add or remove. The scheme we found to be the best tradeoff between stability and speed decides how much dust to condense or evaporate according to how close the temperature of the dust species is to its evaporation temperature. In this way, it is possible to take large steps when the solution is far from equilibrium, while the size of the steps is automatically decreased when the solution is locally approached. The method is outlined below.

   The parameter we want to determine at every location in the disc is the *gas fraction* of each species i, γ_i. The gas fraction is defined as the fraction of the total available material for forming dust grains of species i that is in the gas phase. Thus

$\gamma_i = 1$ means dust species i is totally evaporated, while $\gamma_i = 0$ means all the material is in the solid phase.

In order to determine γ_i at each location in the disc we first compute the temperature structure for the initial guess of the dust density structure (see section 5.C.2 below). From this we compute using Eq. (1) the partial gas pressure needed to counter the evaporation at each location in the disc. This gives the equilibrium gas fraction at this temperature, $\gamma_{i,0}$. We also compute the sublimation temperature at each location, T_{subl} and the temperature of the grains in the optically thin approximation, T_{thin}. The new gas fraction is then given by,

$$\gamma_{i,\mathrm{new}} = f_w \gamma_{i,0} + (1 - f_w)\gamma_{i,\mathrm{old}}, \tag{5.11}$$

where the weighting factor f_w is taken as,

$$f_w = \begin{cases} \left| \dfrac{T - T_{\mathrm{subl}}}{T + T_{\mathrm{subl}}} \right|^q \left| \dfrac{T_{\mathrm{thin}} - T_{\mathrm{subl}}}{T_{\mathrm{thin}} + T_{\mathrm{subl}}} \right|^q & \text{for } T < T_{\mathrm{subl}} \\[2ex] 1 - \exp\left\{ -400 \left[\dfrac{T_{\mathrm{subl}} - T}{T_{\mathrm{subl}}} \right]^2 \right\} & \text{for } T > T_{\mathrm{subl}} \end{cases} \tag{5.12}$$

The parameter q determines how fast the condensation of dust can take place and is adjusted such that the increase in optical depth up to the $\tau = 1$ surface as seen by direct stellar radiation is always less than 10% (i.e. $\Delta\tau < 0.1$). The second term in the equation for f_w for $T < T_{\mathrm{subl}}$ ensures that in the region just outside the first few optical depths the condensation of material is not too fast. The temperature in these regions is quite low and if this term is not taken into account, the shielded regions will form so much dust that it will again start heating the region in front of it, causing another instability. By adding dust slowly also in these regions, the overall stability of the method is increased significantly. Removal of dust grains when the temperature is too high is done much faster than recondensation. This ensures that during the iterative process only a tiny fraction of the dust grains has a temperature above the sublimation temperature.

Together with the sublimation and recondensation of dust in the disc, we also determine the vertical density profile of the disc from hydrostatic equilibrium.

5.C.2   Initial guess

The success of most iterative schemes depend heavily on the initial guess. This is also true for the iterative scheme described above. Especially the estimate for the location of the start of the inner rim as a function of height above the midplane is of crucial importance for the success of the computation. We compute the initial guess for the dust density structure using analytic consideration as described below.

First we take the temperature structure as obtained by Eq. (3) with an initial guess for C_{bw} (usually unity), ignoring the thermal radiation and extinction of the stellar radiation by other dust grains. This temperature structure can then be used to compute the gas fraction at each location in the disc, and from this we setup

the first estimate for the density structure. We then do a full radiative transfer run through this density structure obtaining a temperature at each location. We use this to determine C_{bw} at the inner rim. Again we use Eq. (3) to determine the temperature at each location in the disc using the new value for C_{bw}. This will result in a slightly different location of the inner rim. We iterate this procedure several times to get a proper value for C_{bw} and thereby a good estimate for the location of the inner rim. After this we proceed with the iterative scheme as described in the previous section.

5.C.3   Restrictions on the gas fraction gradients

The location of the inner rim as a function of height in the disc is to a large extend determined by the local backwarming efficiency and the density of dust forming material. In the midplane of the disc the density is highest which causes the sublimation temperature to be highest and the rim radius to be small at this height. However, due to the heigh density the backwarming efficiency at the midplane is also highest, which causes the rim to retreat to larger radii. When this retreating effect of backwarming wins from the effect of a higher sublimation temperature, the rim radius at the midplane will be slightly larger than just above it causing a 'hole' in the disc. Inside this hole the dust is irradiated from almost all sides, causing the effect of backwarming to increase even further and the rim to retreat even further. This is a runaway effect which, in the end, causes the entire disc to retreat to large radii. When this has happened, in front of this rim the temperatures are low and dust can start forming again. This cycle repeats and no stable solution is found.

The above instability might be a physical effect which can emerge in a time-dependend treatment of the problem. However, we do not pursue this in this paper. Therefore, we restrict the gas fraction gradient to avoid triggering this instability. We restrict the gas fraction to be monotonously increasing with increasing height above the midplane. In this way we avoid the formation of a hole in the disc.

Another problem which might arise from the iterative procedure explained above is that the destruction of dust proceeds faster in the region which is effectively backwarmed than in the optically thin region in front of it. This might cause the fraction of condensed material to decrease with increasing radius. This solution turns out to be unstable, and in addition we consider it to be an unlikely physical solution. Thus, to avoid this we restrict the gas fraction to be monotonously decreasing with increasing radius.

Note that by restricting the gas fraction in the ways described above we force the rim to have the curved shape we see in the paper. However, other structures we have found have in all cases turned out to be unstable, thus we consider the curved rim a robust solution.

Samenvatting

Het onderwerp van dit proefschrift is het ontstaan van sterren, en van de planeten die om sterren heen draaien. Door onderzoek te doen op deze gebieden, kunnen we niet alleen de oorsprong van de vele sterren en planeten in het Universum beter leren begrijpen, maar ook die van de Zon, de Aarde, en ons zelf. Verder kan dit onderzoek ons helpen om de kans in te schatten dat we elders in het Universum vergelijkbare plekken voor leven kunnen vinden.

In het bijzonder heb ik het microgolf spectrum bestudeerd van een gaswolk waarin sterren vormen, waarbij ik in Hoofdstuk 2 de complexiteit laat zien van de chemische en fysische structuur van deze wolk, en in Hoofdstukken 3 en 4 de eigenschappen van zijn meest extreme componenten bestudeer. Om verder te gaan met ster- en planeetvorming, Hoofdstuk 5 is het verslag van een theoretische en numerieke studie van de heetste stoffige gebieden van planeetvormende schijven rondom jonge sterren. Deze studie laat een grote diversiteit zien aan mogelijke stofverdelingen, en werpt licht op algemene principes van modellen van zulke systemen.

Het ontstaan van sterren en planeten

Gigantische complexen van moleculaire wolken, die zich tientallen tot honderden lichtjaren uitspreiden door de ruimte, zijn de kraamkamers waarin nieuwe sterren worden gevormd. De chaotische bewegingen die voortdurend worden aangemaakt in dergelijke wolken door grootschalige gasstromen, supernova explosies en andere mechanismen, zorgen ervoor dat de wolken variaties in dichtheid krijgen. Sommigen van deze variaties zijn zo groot dat de zwaartekracht die ze op zichzelf uitoefenen de thermische expansie en andere dissipatieve krachten tegen kan gaan. Een dergelijke kern die zwaartekrachtsgebonden is, trekt langzaam samen. Daarbij vormt zich een centraal object van hoge dichtheid, waar materiaal naartoe wordt gebracht via een accretieschijf. Het centrale object groeit totdat de druk in zijn centrum hoog genoeg wordt om het mogelijke maken dat waterstofkernen fuseren, waarbij helium wordt gevormd en energie vrij komt. Op dat moment is er een nieuwe ster geboren.

De nieuwgevormde ster verhit het binnendeel van de mantel van gas die om de ster heen zit. Dit leidt tot een verhoging van infrarood straling, en ook van atomaire en moleculaire lijnemissie, omdat er nu hogere rotationele energieniveaus gevuld kunnen

Figure S.1: Een gedeelte van het complex van moleculaire reuzenwolken in Orion, gezien in nabij infrarood licht met de *Spitzer* ruimtetelescoop. Sterren die momenteel aan het ontstaan zijn, leiden tot de rode gloed in de anderszins donkere gebieden links van het midden. Het materiaal waaruit nog geen sterren ontstaan straalt in golflengtes die langer zijn dan wat hier wordt getoond. De uitgespreide blauwe en witte gloed is gas dat wordt bestraald met hoog-energetische fotonen van pasgeboren heldere sterren. Het noorden is naar links in deze foto en de horizontale omvang van het beeld is ~ 30 lichtjaar. Foto: NASA/JPL-Caltech/J. Stauffer (SSC/Caltech).

worden. De uitgebreide mantel van kouder gas rondom de protoster verhult de ster in het zichtbare licht.

Omdat het ontstaan van sterren gebeurt in materiaal waarin willekeurige, grootschalige bewegingen voorkomen, en omdat impulsmoment behouden blijft tijdens het ineenstorten van de gaswolk, zal het object in wording doorgaans een draaiing hebben. Het ineenstorten is gemakkelijker langs de rotatie-as, en dus zal het gas rondom de pasgeboren ster afplatten tot een draaiende schijf. Wat er nog over is van de gasmantel wordt in de loop van tienduizenden jaren weggedreven door een uitstroom van gas langs de rotatie-as, waardoor de ster zichtbaar wordt. Binnen de protoplanetaire schijf die om de ster heen zit, zijn stofkorrels aanwezig – de microscopische mineraaldeeltjes die overal in het interstellaire gas voorkomen. Deze korrels groeien door onderlinge botsingen, wat in de loop van miljoenen jaren leidt tot de vorming van rotsplaneten.

De chemie van stervorming

Naarmate de temperatuurs- en dichtheidsstructuur, en ook de bewegingen, van een ineenstortende gaswolk zich ontwikkelen, doet het chemische samenstelling dat ook. Bijvoorbeeld, waar het gas erg koud is, bevriezen veel atomen en moleculen op stofkorrels. Daar kunnen ze reacties uitvoeren die in de gasfase niet mogelijk zijn. Andere processen kunnen alleen plaatsvinden op hoge temperaturen. Dit is het geval in de binnenmantel, die wordt verhit door de protoster. Hier kunnen chemische stoffen die
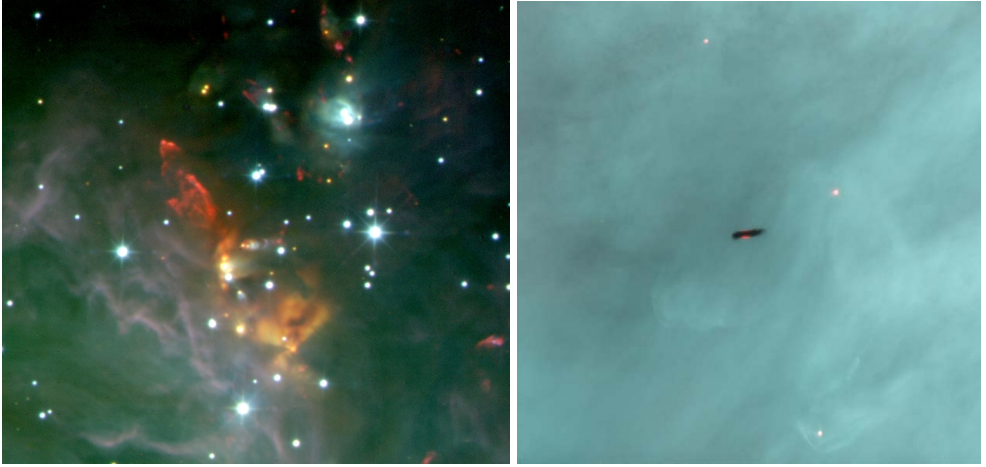
Figure S.2: *Linker paneel:* Het OMC-2 gebied, een deel van de stellaire kraamkamer in Orion die in Fig. S.1 wordt getoond. Pasgeboren sterren zijn gemengd met nog groeiende, geel- en roodachtige tegenhangers. Slierten interstellair materiaal gaan diagonaal door het beeld. Tevens te zien zijn enkele uitstromen, en de schaduw van een schijf-systeem dat van de zijkant wordt waargenomen. OMC-2 FIR 4, de protoster die in dit proefschrift wordt bestudeerd, bevindt zich vlak onder het midden. Foto: UKIRT/JAC. *Rechter paneel:* Een protoplanetaire schijf, gezien als een donker silhouet tegen uitgebreid stralend gas in Orion. De schijf van planeetvormend materiaal is vanaf de zijkant waargenomen, en de gloed van de centrale ster is zichtbaar net onder het midden van de schijf. Foto: J. Bally (University of Colorado) en H. Throop (SWRI).

zijn uitgevroren op de stofkorrels, of daarop gevormd zijn, verdampen en deelnemen aan de chemie in de gasfase. Schokgolven die voortkomen uit de uitstroom van de protoster brengen atomen van het oppervlak van de stofkorrels naar het gas, en verhitten ook het gas, waarvan één resultaat het efficiënt vormen van water is. Daarom vertegenwoordigt de chemische opbouw van een stervormende gaswolk de diversiteit aan fysische omstandigheden en bewerkingsgeschiedenissen van zijn verschillende delen.

Moleculair waterstof is het meest voorkomende stofje in het gas van stervormende gebieden. Het wordt gevolgd door koolstofmonoxide, dat 10 000 tot 100 000 keer minder vaak voorkomt. Door het gebrek aan dipoolmoment, echter, kan H_2 zelf doorgaans niet worden gezien in het betrekkelijk koude gas waaruit sterren vormen, terwijl de rotatie-overgangen van CO gemakkelijk te observeren zijn op microgolf golflengtes. De meeste andere moleculen komen ten minste 100 keer minder vaak voor dan CO, maar veel verbindingen kunnen toch nog worden waargenomen, omdat ze sterke overgangen hebben in het microgolfgebied. Hieronder vallen CS, HCN en methanol, die vaak worden gezien, en ook de gedeutereerde isotopologen van verscheidene verbindingen.
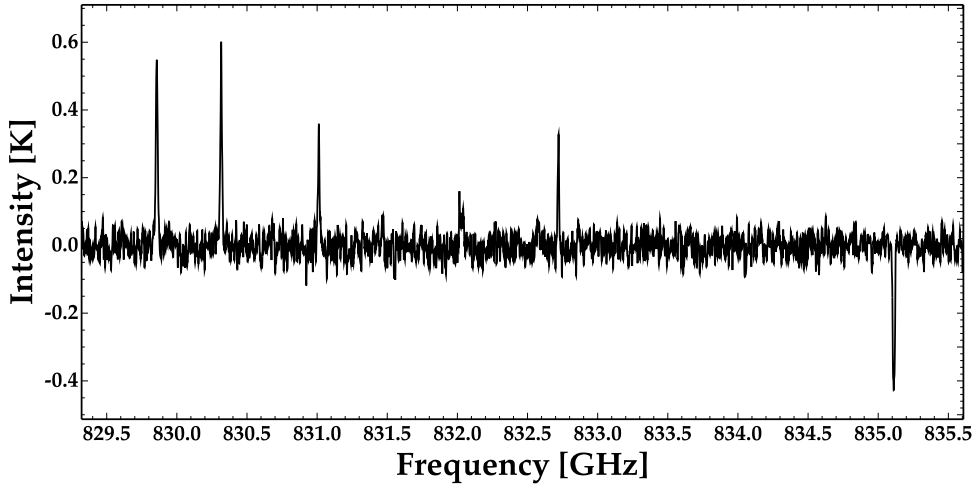
Figure S.3: Een klein segment van het breedband microgolf spectrum van OMC-2, dat wordt geanalyseerd in Hoofdstukken 2, 3 en 4 van dit CH^+ absorptie lijn. Zelfs dit korte spectrum geeft informatie over de chemische samenstelling van het stervormende gas en de detectie van meerdere overgangen van methanol maakt het mogelijk om andere eigenschappen te bepalen, zoals dichtheid en temperatuur.

Spectraallijnen als diagnostische middelen

Atomen en moleculen kunnen zich in tal van discrete energetische toestanden bevinden. Voor moleculen zijn de toestanden die relevant zijn voor dit onderzoek de rotationele energieniveaus. Wanneer een deeltje spontaan overgaat van een rotationele toestand met een hogere energie naar één met een lagere energie, dan wordt er een foton uitgezonden om het verschil in energie en impulsmoment af te voeren. De verzameling van energieniveaus en de verschillen daartussen is uniek voor elk atoom en molecuul, en zodoende heeft elk soort deeltje zijn eigen spectrale vingerafdruk. Bovendien is de fractie van deeltjes van een gegeven stof die zich in een specifiek energieniveau bevindt, en dus kan stralen op een bepaalde frequentie, een functie van omgevingsomstandigheden zoals de dichtheid en de temperatuur van het gas. Een lijnspectrum van een volume aan gas is een indicator voor de samenstelling en de parameters van dit gas.

De gecombineerde straling van tientallen betrekkelijk veelvoorkomende moleculen, en de diversiteit aan fysieke omstandigheden die het mogelijk maakt zowel laag- als hoogliggende energieniveaus aan te slaan, zorgen ervoor dat protostellaire kernen zeer rijke en informatieve microgolf spectra hebben. Een krachtige manier om een protostellaire kern te kenschetsen, is daarom het observeren van zijn microgolf spectrum over een groot golflengtebereik, en dit is de aanpak die in Hoofdstukken 2, 3 en 4 is gebruikt. Dergelijke spectra verschaffen een uitgebreid overzicht van het chemische inventaris, van de diversiteit aan fysische omstandigheden en van de kinematische

componenten in een stervormende gaswolk. Figuur 3 toont een typisch gedeelte van het spectrum van een ster in wording. De figuur toont enkele emissielijnen, die wijzen op betrekkelijk warm en dicht gas, en één absorptielijn, die wijst op een laag gas op de voorgrond die bestaat uit betrekkelijk koud materiaal met een lage dichtheid. Dit kleine gedeelte van de dataset bevat al detecties van drie moleculen en, omdat er meerdere lijnen van methanol zijn gedetecteerd, maakt het mogelijk om de dichtheid en temperatuur van het gas in te perken.

Dit proefschrift

Veel moleculaire spectraallijnen zijn moeilijk of onmogelijk waar te nemen vanaf het aardoppervlak door sterke absorptie van infrarood straling in de atmosfeer. Onlangs heeft de HIFI spectrometer aan boord van het *Herschel Space Observatory* van de Europese ruimtevaartorganisatie ESA ons toegang gegeven tot een ongekende combinatie van frequentie bereik, spectrale resolutie en gevoeligheid. Het spectrale bereik omvat een groot scala aan frequenties die geheel onmogelijk te zien zijn met instrumenten op de grond. Onder andere kunnen voor het eerst de hogere rotationele overgangen van menig veelvoorkomend molecuul regelmatig worden waargenomen in protosterren. Verschillende moleculaire hydriden en hydride-ionen zijn voor het eerst waarneembaar. Met behulp van deze mogelijkheden, streeft het CHESS Key Programme team ernaar om een van de eerste uitgebreide systematische vergelijkingen te maken van protosterren in de terahertz frequenties die waarneembaar zijn met HIFI. Onze vraag is verkennend: hoe variëren de chemische samenstelling en het spectrum van protosterren met massa, leeftijd en omgeving?

Een van de meest beroemde en nabijgelegen stellaire kraamkamers bevindt zich op veertienhonderd lichtjaar afstand, in de richting van het sterrenbeeld Orion. In dit wolkencomplex, waarvan een deel is afgebeeld in Fig. 1, worden duizenden sterren worden gevormd. Een zoom-in van de regio rond de protostellaire kern OMC-2 FIR 4 wordt weergegeven in het linker paneel van Fig. 2. Dit jonge object, een onopvallende donkere vlek net onder het midden van de afbeelding, is de focus van Hoofdstukken 2 tot en met 4.

In Hoofdstuk 2 presenteer en karakteriseer ik het *Herschel*/HIFI spectrum van OMC-2 FIR 4, waarvan 0.4% wordt weergegeven in Fig. S.3. Deze dataset is het eerste volledige spectrum van een protoster met een middelgrote massa in het terahertz frequentie regime, en bevat meer dan zevenhonderd lijnen van 41 chemische stoffen. De diversiteit aan stoffen, overgangen en lijnprofielen die zijn gedetecteerd brengt een nieuw niveau van complexiteit ten toon van de structuur, chemie en kinematica van de bron, dat we nu pas beginnen te begrijpen. Op basis van hun profielen wijzen de gedetecteerde chemische verbindingen op ten minste vier verschillende, en vooral nieuwe, kinematische en fysieke componenten.

In Hoofdstuk 3 wordt een subset van een honderdtal methanol lijnen geanalyseerd uit de HIFI census van OMC-2 FIR 4. Deze analyse brengt een compacte, hete, centrale regio aan het licht, ter grote van het Zonnestelsel, die zich binnen in de grootschalige, koude, protostellaire gasmantel bevindt. De regio is waarschijnlijk de hete kern, die direct wordt verhit door de nieuw gevormde protoster.

In Hoofdstuk 4 doe ik verslag van een studie naar de hoge-snelheid vleugels van H_2O en CO emissie-lijnen die worden waargenomen in de richting van OMC-2 FIR 4. De straling blijkt afkomstig te zijn van zeer compacte, waterrijke gebieden die vergelijkbaar in grootte zijn met de hete component uit Hoofdstuk 3, en wat hun eigenschappen betreft consistent zijn met gas dat is bewerkt door sterke schokgolven. De analyse duidt sterk op de aanwezigheid van een compacte uitstroom van gas vanuit de protoster, die voorheen nog niet is waargenomen.

In Hoofdstuk 5 beschrijf ik het modelleren van de binnenste regionen van planeet-vormende schijven – zoals de schijf die is weergegeven in het rechter paneel van Fig. 2 – rondom sterren in de latere fasen van hun ontstaan. Hierbij heb ik een scala van mogelijke verdelingen gevonden voor de microscopische mineraalkorrels die zullen uit-groeien tot planeten. Verder geef ik een algemeen toepasbare analytische beschrijving van de numerieke resultaten.

Vooruitzicht

Het rijke HIFI spectrum van OMC-2 FIR 4 stelt ons ertoe in staat om deze proto-stellaire kern in ongekend detail te karakteriseren, en levert bewijs voor een centrale hete kern, een compacte uitstroom, en verdere substructuur van onduidelijke aard. De weg is vrijgemaakt voor verdere uitvoerige analyses en voor vergelijkingen met andere protosterren. We verwachten dat er in de komende paar jaar een schat aan ontdekkingen en nieuwe vragen voortkomt uit dit werk. Gerichte vervolg-observaties van geselecteerde moleculen door interferometers met een hoge ruimtelijke resolutie, zoals ALMA, zullen een belangrijk punt zijn in het testen van de aard van de sub-structuur die is gevonden in OMC-2 FIR 4 met HIFI.

Summary

The subject of this thesis is the birth of stars, and of the planets around them. Work in these areas can help us to better understand the origin of the myriad stars and planets in the Universe, but also of our own Sun, Earth and selves, as well as to estimate the probability of finding similar abodes for life elsewhere.

Specifically, I have studied the microwave spectrum of a star-forming gas clump, revealing the complexity of its chemical and physical structure in Chapter 2 and studying the properties of its most extreme components in Chapters 3 and 4. Moving on through star and planet formation, in Chapter 5 I have presented a theoretical and numerical study of the hottest dusty regions in planet-forming disks around young stars, revealing the great diversity of possible dust distributions and elucidating general principles in models of such systems.

The formation of stars and planets

Giant complexes of molecular gas clouds, stretching through space for tens or hundreds of light-years, are the nurseries in which new stars are formed. Chaotic motions that are constantly generated in such clouds by large-scale gas flows, supernova explosions and other mechanisms cause them to have variations in density. Some of these variations are large enough for self-gravity to make them stable against thermal expansion and other dissipative forces. Such a bound core slowly contracts, forming a central dense object onto which material is fed through an accretion disk. The central object grows until the pressure at the centre becomes sufficient to make it possible for hydrogen nuclei to fuse together, forming helium and releasing energy. A star is born.

The freshly minted star heats the inner part of its surrounding envelope, leading to an increase in thermal infrared radiation and, because many higher rotational energy levels can now be populated, in molecular line emission. The extended envelope of colder gas around the protostar hides the star from view in visible light.

As starbirth occurs in material with random large-scale motions and angular momentum is conserved in collapse, the forming object will generally be rotating. It is easier to collapse along the rotation axis, so the gas around the newborn star flattens into a spinning disk. Over tens of thousands of years, an outflow of gas along the

Figure S.1: A part of the Orion giant molecular cloud complex, as seen in near-infrared light with the *Spitzer* space telescope. Currently forming stars give rise to the red glow in the otherwise dark areas left of centre. The material not yet forming stars emits at wavelengths longer than shown here. The extended blue and white glow is gas irradiated by high-energy photons from newborn bright stars. North is left in this image and the horizontal extent is ~ 30 light years. Credits: NASA/JPL-Caltech/J. Stauffer (SSC/Caltech).

rotation axis dissipates what remains of the envelope, and the star becomes visible. Within the protoplanetary disk (see Fig. S.2) around it, dust grains – the microscopic mineral particles that are present everywhere in interstellar gas – undergo collisional growth, which over millions of years leads to the formation of rocky planets.

The chemistry of star formation

As the temperature and density structure, as well as the motions, of a collapsing gas cloud evolve, so does its chemical composition. For example, where the gas is very cold, many atoms and molecules freeze onto the dust grains, where they can carry out reactions that are not possible in the gas phase. Other processes can only occur at high temperatures. For example, in the inner envelope, which is heated by the protostar, chemical species frozen onto or formed on dust grains can evaporate and participate in the gas-phase chemistry. Shockwaves originating in the outflow from the protostar sputter atoms from the dust into the gas, and also heat the gas, one result being the efficient formation of water. Thus, the chemical makeup of a star-forming gas clump represents the diversity of physical conditions and processing histories of its different parts.

Molecular hydrogen is the dominant gas species in star-forming regions. It is followed by carbon monoxide, which is $10\,000$ to $100\,000$ times less abundant. However, due to a lack of dipole moment H_2 itself cannot usually be seen in the relatively cool gas from which stars form, while the rotational transitions of CO are easily ob-
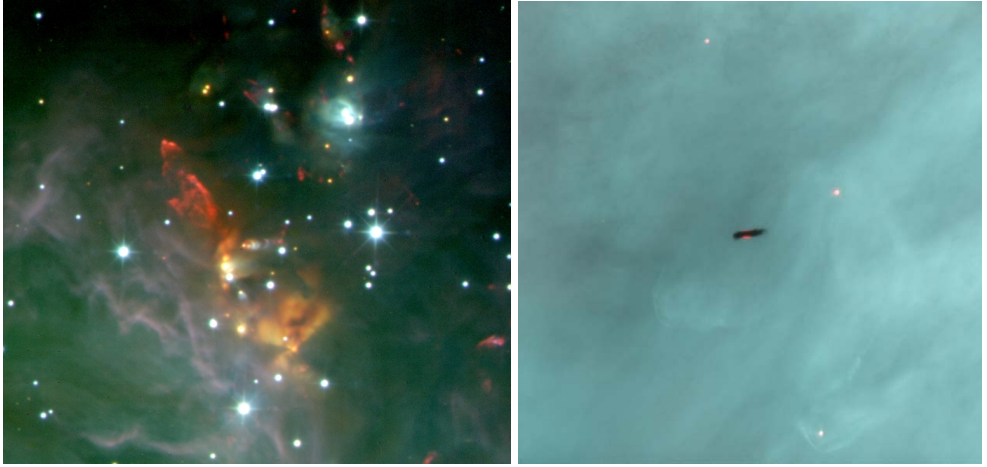
Figure S.2: *Left panel:* The OMC-2 region, a part of the Orion stellar nursery shown in Fig. S.1. Newborn stars intermingle with their still growing yellowish and reddish counterparts. Wisps of interstellar material are visible diagonally across the image. Also seen are several outflows and the shadow of an edge-on disk system. OMC-2 FIR 4, the protostar studied in this thesis, is below centre. Credits: UKIRT/JAC. *Right panel:* A protoplanetary disk seen as a dark silhouette against extended glowing gas in Orion. The disk of planet-forming material is edge-on, the glow of its central star is visible below the centre of the disk. Credits: J. Bally (University of Colorado) and H. Throop (SWRI).

servable at microwave wavelengths. Most other molecules are at least 100 times less abundant than CO, but many are still detectable due to strong transitions in the microwave regime. These include the commonly seen CS, HCN and methanol, as well as deuterated isotopologues of various species.

Spectral lines as diagnostic tools

Molecules can be in various discrete energetic states. The states relevant to this thesis are the rotational energy levels. When a particle spontaneously transitions from a higher energy rotational state to a lower one, a photon is emitted to carry away the energy and angular momentum diference. The set of energy levels and their differences is unique to a given molecule and thus each has its own spectral fingerprint. Furthermore, the fraction of particles of a given species that are in a specific state, and thus able to emit at a particular frequency, is a function of ambient conditions such as the density and temperature of the gas. A line spectrum of a volume of gas is a tracer of its composition and properties.

The combined radiation from dozens of relatively abundant molecules, and the diversity of physical conditions which allows to excite both low- and high-lying energy levels, leads to protostellar cores having very rich and informative microwave
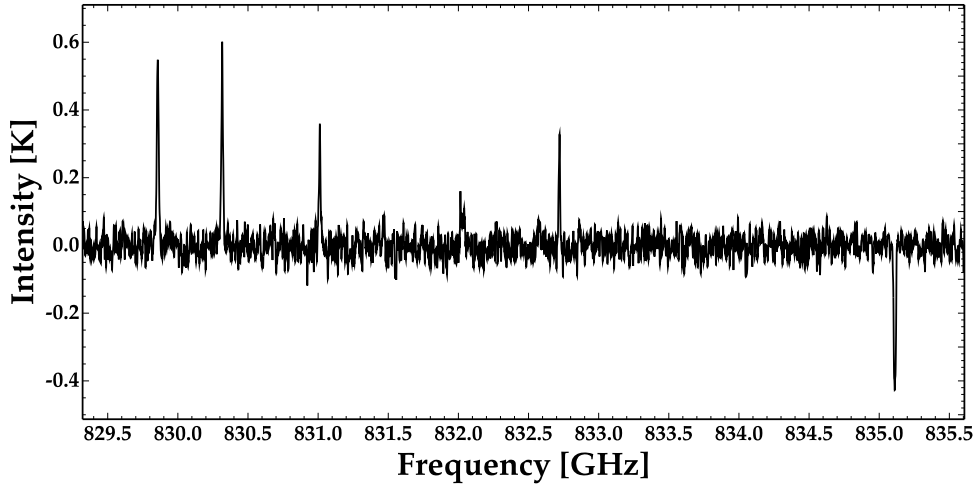
Figure S.3: A small segment of the broadband microwave spectrum of OMC-2 analyzed in Chapters 2, 3 and 4 of this thesis. Several emission lines – mostly transitions of methanol, with a single CS line at 832.057 GHz – and a CH^+ absorption line are visible. Even this short spectrum provides information about the chemical composition of the star-forming gas and the detection of multiple transitions of methanol allows to determine other properties, such as density and temperature.

spectra. A powerful way to characterize a protostellar core, then, is to observe its microwave spectrum over a large range of wavelengths, and this is the approach used in Chapters 2, 3 and 4. Such spectra provide a comprehensive overview of the chemical inventory, of the diversity of physical conditions and of the kinematical components in a star-forming gas clump. Figure S.3 shows a typical part of the spectrum of a forming star. Several emission lines, indicative of relatively warm and dense gas, and one absorption feature, indicative of a foreground layer of relatively cold and low-density material, are visible. This small fraction of the dataset already provides detections of three molecules and, as multiple lines of methanol are detected, allows to constrain the density and temperature of the gas.

This thesis

Many molecular spectral lines are difficult or impossible to observe from the surface of the earth due to strong infrared absorbtion in the atmosphere. Recently, the HIFI spectrometer on the European Space Agency's *Herschel Space Observatory* has given us access to an unprecedented combination of frequency coverage, spectral resolution and sensitivity, including a large range of frequencies entirely impossible to see with ground-based instruments. Among other things, for the first time, the higher rotational transitions of many common molecules can be regularly observed in protostars. Several molecular hydrides and hydride ions are observable for the first time. Using

these capabilities, the CHESS Key Programme team aims to make one of the first comprehensive systematic comparisons of protostars at the terahertz frequencies observable with HIFI. The question is exploratory: how do the chemical composition and spectrum of protostars vary with mass, age and environment?

One of the most famous and nearby stellar nurseries is located fourteen hundred light years away, in the direction of the Orion constellation. Thousands of stars are forming in this cloud complex, a part of which is shown in Fig. S.1. A zoom-in of the region around the protostellar core OMC-2 FIR 4, one of the objects in the CHESS programme, is shown in the left panel of Fig. S.2. This young object, an unremarkable dark patch below the image centre, is the focus of Chapters 2 through 4.

In Chapter 2, I present and characterize the *Herschel*/HIFI spectrum of OMC-2 FIR 4, 0.4% of which is shown in Fig. S.3. This dataset is the first full spectrum of an intermediate-mass protostar (meaning it will form a star of a few solar masses) in the terahertz frequency regime and contains more than seven hundred lines from 41 chemical species. The diversity of species, transitions and line profiles detected reveals a new level of complexity of the structure, chemistry and kinematics of the source, that we are only beginning to understand. Based on their profiles, the detected chemical species trace at least four different, and mostly new, kinematical and physical components.

In Chapter 3, a hundred-strong subset of methanol lines from the HIFI survey of OMC-2 FIR 4 is analyzed, revealing a compact, hot, Solar System sized central region within the the large-scale, cold protostellar envelope. This is likely the hot core, directly heated by the newly formed protostar.

In Chapter 4, I present a study of the high-velocity wings of H_2O and CO emission lines observed towards OMC-2 FIR 4. The emission is found to originate in very compact, water-rich regions of similar size to the hot component presented in Chapter 3 and consistent in its properties with gas processed by strong shockwaves. The analysis strongly suggests the presence of a previously unseen compact outflow from the protostar.

In Chapter 5, I describe the modeling of the innermost regions of planet-forming disks – such as that shown in the right panel of Fig. S.2 – around stars in their late phases of formation, finding a range of possible distributions of the microscopic mineral grains that will grow into planets and giving a generally applicable analytical description of the numerical results.

Outlook

The rich HIFI spectrum of OMC-2 FIR 4 is allowing us to characterize this protostellar core in unprecedented detail and is providing evidence for a central hot core, a compact outflow, and further substructure of an unclear nature. The stage is set for further detailed analyses and for comparisons with other protostars. We expect a wealth of discoveries and new questions to emerge from this work in the coming few years. Targeted follow-up observations of selected molecules with high spatial resolution interferometers, such as ALMA, will be a key point in testing the nature of the substructure found in OMC-2 FIR 4 with HIFI.

Kokkuvõte

Käesoleva doktoritöö teemaks on tähtede ja nende ümber tiirlevate planeetide sünd. Nende protsesside uurimine aitab meil paremini mõista Universumis leiduvate loendamatute tähtede ja planeetide, aga ka Päikese, Maa ja meie endi päritolu. Samuti aitab see meil hinnata eluks sobivate paikade leidmise tõenäosust kosmoses.

Tähed tekivad väikestes, tihedates gaasipilvedes, mida nimetatakse tuumadeks. Oma uurimistöös keskendusin ühe sellise tuuma, OMC-2 FIR 4, mikrolaine-spektri analüüsile. Peatükis 2 paljastasin selle objekti keemilise koostise ja füüsikalise struktuuri keerukuse, peatükkides 3 ja 4 aga uurisin antud gaasitombu kõige ekstreemsemate osade omadusi. Peatükis 5 käsitlesin tähe- ja planeeditekke hilisemat etappi, uurides erakordselt kuumi tolmurikkaid piirkondi noorte tähtede ümber olevates planeeditekke ketastes. Näitasin, et aine võib sellistes piirkondades omada väga erinevaid jaotusi ning esitasin mõned selliste süsteemide modelleerimise üldprintsiibid.

Tähtede ja planeetide tekkimine

Tähtede sünnipaigad on hiiglaslikud molekulaarse gaasi pilvede kompleksid, mis laiuvad kosmoses üle kümnete ja sadade valgusaastate. Kaootilised liikumised, mis neis pilvedes suuremastaabiliste gaasivoolude, supernoovade ja teiste mehhanismide läbi pidevalt tekivad, põhjustavad ebaühtlusi gaasi tiheduses. Mõned ebaühtlused on piisavalt suured, et gravitatsiooni kokkutõmbav jõud ületab soojuspaisumise ja teised hajutavad jõud. Säärane stabiilne tuum tõmbub aeglaselt kokku, moodustades enda keskele tiheda objekti, millele langeb läbi akretsiooniketta järjest uut ainet. Keskse objekti kasvades lubab rõhu tõus tema sees vesiniku tuumadel ühinema hakata, vabastades nii energiat. Täht on sündinud.

Värskelt vermitud täht, mida esialgu nimetatakse prototäheks, kuumutab end ümbritseva gaasituuma siseosa, põhjustades infrapunase soojuskiirguse ja molekulide joonkiirguse kasvu. Tähte ümbritsev tohutu külma gaasi ümbris varjab ta välise vaatleja eest nähtavas valguses esialgu täielikult.

Kuna täheteke toimub juhuslike liikumistega aines ning pöördimpulss kokkutõmbel säilib, pöörleb üldjuhul ka tekkiv objekt ise. Kokkutõmbumine mööda pöörlemistelge on lihtsam ning seetõttu koguneb gaas vastsündinud tähe ümber pöörlevasse kettasse. Kümnete tuhandete aastate vältel ajab piki pöörlemistelge toimuv aine väljavool

Figure S.1: Osa Orioni hiiglaslikust molekulaarsete pilvede kompleksist vaadelduna kosmoseteleskoobi *Spitzer* abil. Praegu tekkivad tähed põhjustavad pildi keskosast vasakul olevas tumedas piirkonnas punast kuma. Tähetekkes veel mitte osalev aine kiirgab lainepikkustel, mida käesolev pilt ei näita. Hajus sinine ja valge kuma pärineb vasttekkinud tähtede ultraviolett-footonitega kiiritatud gaasilt. Põhi on pildil vasakul ning horisontaalne ulatus on ~ 30 valgusaastat. Allikas: NASA/JPL-Caltech/J. Stauffer (SSC/Caltech).

ülejäänud gaasümbrise laiali ning täht muutub ka nähtavas valguses vaadeldavaks. Teda ümbritsevas protoplanetaarses kettas (joonise S.2 parem paneel) kasvavad tolmuterad – kõikjal kosmilises gaasis leiduvad mikroskoopilised mineraalosakesed – läbi kokkupõrgete üha suuremaks, kuni pärast miljoneid aastaid on tekkinud kiviplaneedid.

Tähetekke keemia

Koos kokkutõmbuva gaasipilve füüsikalise ja kinemaatilise struktuuri arenguga muutub ka pilve keemiline koostis. Pilve osades, kus gaas on väga külm, jäätuvad paljud aatomid ja molekulid tolmuterade pinnale, kus võivad seejärel osaleda reaktsioonides, mis gaasifaasis on võimatud. Paljud teised reaktsioonid leiavad aset vaid kõrgetel temperatuuridel. Gaasituuma sisemuses, mida kuumutab keskne prototäht, hakkavad tolmuteradele jäätunud osakesed aurustuma, misjärel osalevad nad gaasifaasis toimuvates reaktsioonides. Prototähelt lähtuv aine väljavool põhjustab lööklaineid, mis samuti gaasi kuumutavad. Kui temperatuur ületab ligikaudu 50 tselsiuskraadi, algab aga väga tõhus veemolekulide moodustumine. Niisiis esindab tähetekkelise gaasitombu keemiline koostis selle füüsikaliste komponentide mitmekesisust ja ka erinevaid minevikke.

Tähetekke piirkondades on gaasi peamiseks komponendiks molekulaarne vesinik, millele järgneb 10 000 kuni 100 000 korda haruldasem süsinikmonoksiid. Kuna H_2 molekulil puudub dipoolmoment, ei ole teda antud gaasipilvedes enamasti otseselt
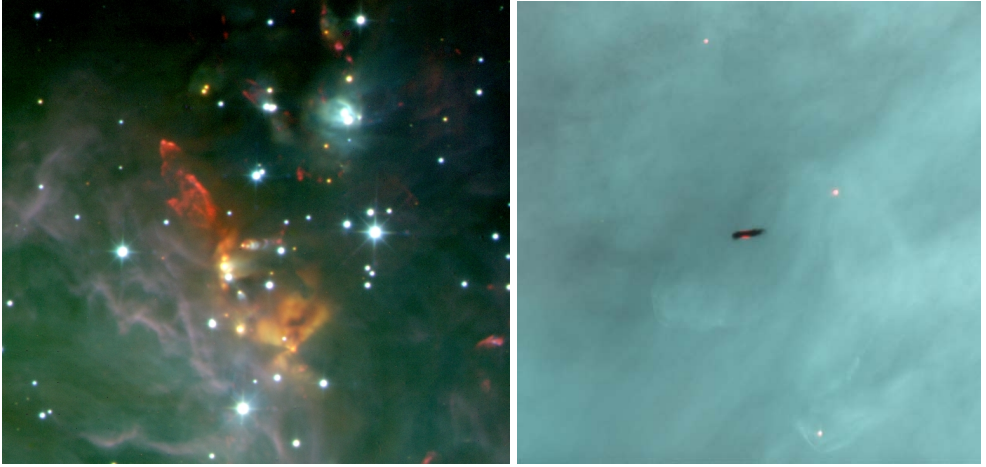
Figure S.2: *Vasak paneel:* OMC-2, piirkond joonisel S.1 kujutatud Orioni tähetekke kompleksis. Näha on vasttekkinud tähed ja nende veel kasvavad kollakad ja punakad kaaslased. Diagonaalselt laiuvad üle pildi tähtedevahelise aine tuustid. Samuti on pildil mitu aine väljavoolu ning ühe serviti oleva protoplanetaarse ketta vari. OMC-2 FIR 4, käesolevas töös uuritud objekt, on pildi keskosa all. Allikas: UKIRT/JAC. *Parem paneel:* Hõõguva gaasi taustal tumeda siluetina paistev protoplanetaarne ketas Orionis. Planeeditekke ketas paistab meile serviti, ta keskosa ülal ja all on näha ketta sees oleva tähe kuma. Allikas: J. Bally (Colorado ülikool) ja H. Throop (SWRI).

vaadelda võimalik, samas kui CO pöörlemisspekter on mikrolainekiirguses kergesti nähtav. Enamus molekule on CO'st vähemalt sada korda väiksema kontsentratsiooniga, kuid paljud neist on tänu tugevatele üleminekutele mikromeetrises laine-alas siiski samuti leitavad. Mõned näited on CS, HCN, metanool ning mitmete molekulide deutereeritud isotopoloogid.

Spektrijooned kui diagnostilised töövahendid

Molekul võib olla ühes paljudest diskreetsetest energeetilistest olekutest. Käesoleva töö jaoks on olulised pöörlemisolekute vahelised üleminekud. Kui osake läheb spontaanselt kõrgemast pöörlemisolekust madalamasse, kiirgub footon, mis kannab ära üleliigse energia ja pöördimpulsi. Et energiaolekute ja nende vahede hulk on igale keemilisele ühendile ainulaadne, on igal molekulil oma spektraalne sõrmejälg. See, kui palju teatud ühendi molekule parajasti mingis olekus on ja ka vastavalt kiirata suudavad, sõltub aga tingimustest nagu gaasi tihedus ja temperatuur. Gaasi joonspekter võimaldab niisiis sondeerida nii tema koostist kui ka tingimusi.

Paljude erinevate molekulide olemasolu ja füüsikaliste tingimuste mitmekesisus, mis võimaldab ergastada nii madalaid kui kõrgeid olekuid, tekitavad tähe-tekkelistes gaasituumades väga rikkalikke kaug-infrapuna spektreid. Laia sagedusribaga ja kõrge lahutusega spektraalvaatlused on niisiis väga võimas tööriist sääraste tuumade ise-
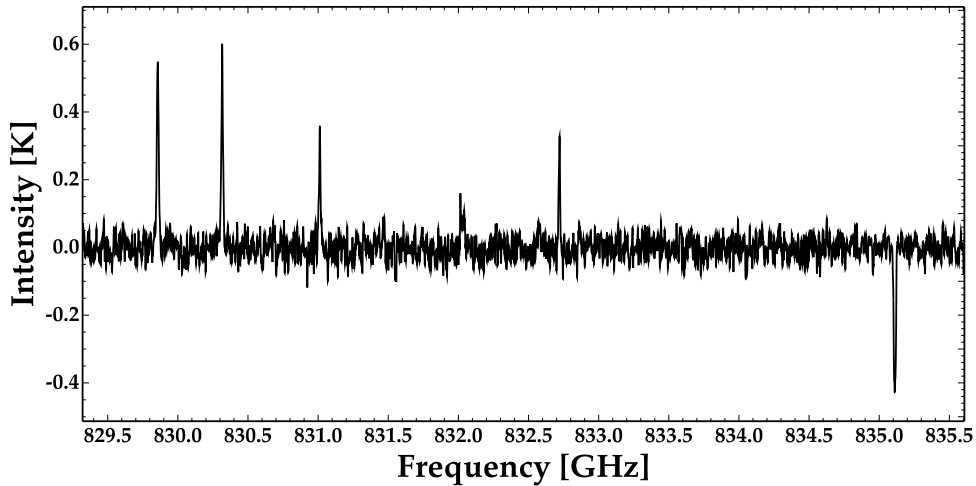
Figure S.3: Väike osa OMC-2 mikrolaine-spektrist, mida analüüsitakse peatükkides 2 kuni 4. Näha on mitu emissioonijoont – enamik neist on metanooli üleminekud, sagedusel 832.057 GHz on ka üks CS molekuli joon – ning üks CH^+ neeldumisjoon. Juba see lühike spekter annab informatsiooni tähetekkelise gaasi koostise kohta, mitme metanooli joone detekteerimine võimaldab aga hinnata ka gaasi tihedust ja temperatuuri.

loomustamiseks ja seda meetodit kasutan käesoleva töö peatükkides 2, 3 ja 4. Sellised spektrid võimaldavad luua põhjaliku ülevaate tähti sünnitavate gaasipilvede keemilisest koostisest, füüsikalistest tingimustest ja kinemaatilistest komponentidest. Joonis S.3 kujutab tüüpilist juppi tekkiva tähe spektrist. Näha on mitu emissioonijoont, mis pärinevad võrdlemisi soojast ja tihedast gaasist, ning üks neeldumisjoon, mis paljastab prototähe ja meie vahel asuva külma ja hõreda gaasi kihi. Ainuüksi selline väike osa andmestikust võimaldab leida kolm erinevat molekuli ning, kuna näha on mitu erinevat metanooli joont, võimaldab määrata ka gaasi tihedust ja temperatuuri.

Käesolev doktoritöö

Paljud molekulide kiirgusjooned ei ole atmosfääris toimuva infrapunakiirguse neeldumise tõttu maapinnalt vaadeldavad. Hiljuti jõudis aga astronoomide kasutusse Euroopa Kosmoseagentuuri kosmoseteleskoobi *Herschel* pardal olev spektromeeter HIFI, millel on ennenägematult lai sagedusriba, hea lahutusvõime ja tundlikkus. Nüüd on vaadeldav suur sagedusulatus, mis on maapealsetele instrumentidele kättesaamatu. Esimest korda on korrapäraselt vaadeldavad paljude levinud molekulide kõrged pöörlemisülemineku, samuti paljud hüdriidid ja hüdriidioonid. Neid võimalusi kasutades on võtmeprogramm CHESS (*Chemical HErschel Surveys of protostarS*) seadnud eesmärgiks viia läbi üks esimesi prototähtede mikrolaine-spektrite võrdlusi. Põhiküsimus seisneb avastamises: kas ja kuidas sõltub prototähe keemiline koostis ja spekter ta

massist, vanusest ja keskkonnast?

üks kuulsamaid ja meile lähemaid tähetekke piirkondi on tuhande neljasaja valgusaasta kaugusel, Orioni tähtkuju suunas. Selles pilvekompleksis, millest osa on kujutatud joonisel S.1, on tekkimas tuhandeid tähti. Joonise S.2 vasakul paneelil on suurendatult näidatud piirkond prototähe OMC-2 FIR 4 ümber. See noor täht, pildi keskmest allpool olev tähelepandamatu tume laik, on üks programmi CHESS uurimisobjekte ja asub peatükkide 2 kuni 4 fookuses.

Peatükis 2 esitan ja iseloomustan OMC-2 FIR 4 *Herschel*/HIFI spektrit, millest 0.4% hõlmav lõik on kujutatud joonisel Fig. S.3. See on esimesena vaadeldud keskmise massiga prototähe spekter vastavatel lainepikkustel. "Keskmine mass" tähendab siinkohal, et antud tuumast tekib Päikesest paar korda massiivsem täht. Spektris on näha enam kui seitsesada joont 41 erinevalt keemiliselt ühendilt. See ühendite, spektrijoonte ja nende kujude rikkus paljastab antud prototähe ehituses, keemias ja kinemaatikas uue keerukuse tasandi, mille lahtiharutamises teeme alles esimesi samme. Spektrijoonte profiilides kajastub vähemalt neli erinevat ja suuresti uut kinemaatilist ja füüsikalist komponenti.

Peatükis 3 analüüsin enam kui sadat metanooli kiirgusjoont OMC-2 FIR 4 HIFI spektrist. Töös paljastub prototähe suure ja jaheda gaasümbrise keskel olev väike, kuum, Päikesesüsteemi-suurune piirkond. See on tõenäoliselt nn. "kuum tuum", vasttekkinud prototähe poolt kuumutatud piirkond.

Peatükis 4 esitan OMC-2 FIR 4 suunas vaadeldud H_2O ja CO molekulide spektrijoonte tiibade analüüsi. Osutub, et kiirgus pärineb väga väikestest ja veerikastest piirkondadest, mille suurus sarnaseb peatükis 3 esitatud kuuma tuuma suurusele ning mille omadused on kooskõlas tugevate lööklainete mõju all olnud gaasiga. Analüüsi tulemused viitavad seniavastamata ülikompaktsele aine väljavoolule uuritavalt prototähelt.

Peatükis 5 kirjeldan planeeditekke ketaste sisepiirkondade modelleerimist. Sellised kettad, millest ühte võib näha joonise S.2 paremal paneelil, asuvad hilises tekkestaadiumis olevate tähtede ümber. Näitan, et planeetideks kasvavad mikroskoopilised mineraaliterad võivad protoplanetaarsetes ketastes omada väga erinevaid ruumilisi jaotusi ning annan numbrilise modelleerimise tulemustele ka üldise analüütilise kirjelduse.

Väljavaade tulevikuks

OMC-2 FIR 4 rikkalik mikrolaine-spekter võimaldab meil antud tähetekke tuuma enneolematult täpselt kirjeldada. Oleme näinud tõendeid, et tuumas on hulgaliselt komponente, mille uurimine on alles algusjärgus – sealhulgas keskne kuum piirkond ja ülikompaktne aine väljavool. Rajatud on vundament järgmistele üksikasjalikele analüüsidele ja võrdlustele teiste prototähtedega. Võib eeldada, et antud tööst kerkib lähiaastatel veel rikkalikult avastusi ja uusi küsimusi. Järgmine võtmesamm OMC-2 FIR 4 ehituse uurimisel on HIFI andmete põhjal planeeritud kõrge ruumilise lahutusega vaatlused tuleva põlvkonna interferomeetritega nagu ALMA.

Acknowledgments

Astronomers and stars have something in common – most of both are born in populous clusters. Each is shaped in its details by countless influences from sources long gone, as well as from coeval comrades, and so writing the acknowledgments is every bit as difficult as figuring out what caused a particular gas cloud to collapse. Who is to tell what made a little boy fascinated with everything from ancient civilizations to dinosaurs to ships to space? What is clear, however, is the support many unique people have given me over the years. There are too many to name them all. For example, I have uncle Ain to thank for the book "100 spacecraft" that I got for Christmas when I was not even ten years of age, that I read to shreds, and that still sits on my bookshelf now. Among the people that shaped and supported my intellectual development are many dedicated teachers, of whom Jaak Saukas deserves particular emphasis.

Now I am finishing a PhD degree in astrophysics. It seems incredible. Thank you, Carsten. You played an instrumental part in making this project possible, and provided me with all the encouragement and resources I needed to complete it. Above all, thank you for your openness and understanding during times of sailing calmer and rockier waters. Cecilia, your help and energy were invaluable, and the times we spent working together in Grenoble all led to leaps in results. Xander, your wise words, timely involvement and pinch of pressure kept me on track and moving. You three carried me through this project – thank you for everything. Ana, it has been great to share science, fun and frustrations with you, and I hope we can continue doing so!

There are a number of other collaborators, colleagues and mentors who deserve a special mention for various reasons, among them Sébastien, Emmanuel, Asunción, Rens, Alex, Michiel, Floris, Sylvie, Charlotte, Sandrine, Valentine, Ronan, Lars and Yoshito. Over the past four years, I was also involved in a number of exciting side projects, for which particular thanks go to Malcolm, Conny, Pieter, Jonas, Rik, Jérémy, Jean-Charles and Sjoert. In addition, many wonderful people at API in Amsterdam, at IPAG in Grenoble, at IRAP in Toulouse, at Leiden Observatory, at the Kapteyn Institute in Groningen, at HIFI ICC at SRON Groningen, at the ESA Herschel Science Centre, at Caltech/IPAC in Pasadena, in Leuven, and within CHESS and several other Herschel Key Programmes each deserve more thanks than

space allows here. All of you who this paragraph pertains to, thank you for the many discussions, for your efforts in helping a confused student, for hosting me and for being such enjoyable characters.

I would like to take a detour here to thank the Dutch people, government, and the funding agency, NWO, for their efforts to keep science strong in the Netherlands, and for their acceptance of large numbers of foreign researchers. Academics worldwide complain about poor funding and about the low priority of science in their societies, but I think the situation in the Netherlands is remarkably good. Astronomy is doing very well here, and I still hold the view I had when I arrived, that this is one of the Homes of Astronomy. And, speaking of homes, I have been lucky to have a great one in Amsterdam. Pieter & Corinne, thank you for being the best landlords in the Universe.

Working at the Astronomical Institute "Anton Pannekoek" has been a pleasure. Thank you, everyone with whom I crossed paths here. Most importantly, there is a special group of people without whom we would all surely perish: Lidewijde, Minou, Milena, Marieke, Natalie, Esther, Eva, Nicole – you have all been amazing in your efficiency, persistence and patience. I also appreciated the open doors of staff members, and the conversations about science and academia, most memorably with Alex, Rens, Sera, Ralph and Joop. For useful advice, fun commentary and for being brilliant, thank you Daan, Diego, Ale, Hugues and Saskia. My first officemates at API, Nathalie and Ramesh, thank you for easing me into the PhD life and for those walks for tea. Our current office – Maithili, Danai, Daniela, we've become friends, you've made this place feel like home, and it has been so very wonderful. In developing my physical and intellectual squash form, and in general, Rik & Theo, you've been great amigos. Samia, Kostas, Ben, Lucas, Koen, Eduardo, Gerrit, Gijs – I've also enjoyed your company and our various exploits greatly.

Dancing has enriched my life, and several excellent teachers deserve credit: Ben & Nel, Robert, Arjan & Marjanne and Sebastian & Marijke. And Josephine, Kim and Anneli, thank you – I really was dancing with the stars.

Allan, Andy and Marko, it is great to have your blue capes to rely on. Martin, thanks for not letting me turtle. I've been fortunate to have friends as great as you for housemates, Paula and Jürgen, enriching gray days with discussions, good food and music. Thank you for never failing to inspire and aspire, Mari. Nele, thank you for always being there. And thank you also in particular, for many particulars, but in no particular order, Tiit, Rainer, Silva, Little and Big Andre, Nele, Allan-Hermann, Mihkel, Jaan, Juhan, Renate, Hanna, Daniel & Hanna, Umberto, Josephine, Denija and *reaalikad*.

The final word is intended to those to whom I owe most of everything. For her encouragement and support in my reaching for the stars, I thank my mother, Aiki. For reminding me to keep my feet on the ground, I thank my grandmother, Asta. And Oskar, thanks for being the most inspiring little brother.

Curriculum Vitae

I was born in 1984 in Tallinn, Estonia. Already interested in the physical sciences, I went to high school at Tallinn Secondary Science School (*Tallinna Reaalkool*).

From 2003 to 2006, I completed a Bachelor's degree in Physics at the University of Tartu, with a thesis on the spectral energy distributions of T Tauri stars, supervised by Indrek Kolka. The following summer I spent as an intern with Gail Schaefer and Howard Bond at the Space Telescope Science Institute in Baltimore, Maryland, working on optical stellar spectral classification. In 2008, I graduated *cum laude* with a Master's degree in Astronomy & Astrophysics from the University of Amsterdam. My thesis work, on dust sublimation in the inner regions of protoplanetary disks, was done under the supervision of Carsten Dominik and Michiel Min. During my studies, I was funded by the Huygens Scholarship programme.

In 2008, I got awarded both a Fulbright Fellowship and an NWO Toptalent grant. The former I declined and the latter funded my stay in Amsterdam as a PhD student. I focussed on a *Herschel*/HIFI spectral study of an intermediate-mass protostar, but also developed projects related to dust sublimation in protoplanetary and debris disks, and maintained a strong interest in extrasolar planetary systems.

As of March 1st, 2013, I will be a postdoctoral researcher at Leiden Observatory, in the group of Ewine van Dishoeck. My main project will focus on the gas-phase carbon-to-oxygen ratio in protoplanetary disks.

The unifying theme of my interests in astrophysics is life in the Universe.

Instrument and software experience

I have observed on-site with the following telescopes: IRAM 30m (30m millimetre), Anton Pannekoek Observatory (0.5m optical), Mercator at Roque de los Muchachos (1.2m optical), Tartu Observatory (1.5m optical). Additionally, I have experience with data from the Herschel Space Observatory, the James Clerk Maxwell Telescope, APEX, the Caltech Submillimeter Observatory and the Wisconsin Indiana Yale NOAO (WIYN) observatory 3.5m telescope.

The operating system I am most comfortable with is OS X, but I have also worked with Windows and Linux. Most of my programming is done in Python or Jython, and I am also familiar with Fortran. I am an advanced user of the *Herschel* data

processing software, HIPE, and have worked with the spectral data packages CASSIS and CLASS. The modeling codes I have used include the Meudon PDR code, RADEX, RATRAN and MCMax.

Teaching and public outreach

During the years 2008 to 2011, I was a regular teaching assistant for various astronomy Master's courses at the University of Amsterdam. I have also lectured to chemistry Bachelor's students on the topic of interstellar chemistry as part of a general course. My outreach experience includes popular talks at schools in Estonia, blog entries and magazine articles related to astronomy, and several interviews to news media. In 2012, I gave the talk "Life in the Universe" at a TEDx conference in Tallinn.

Professional memberships and organizatorial experience

I am a member of the Planetary Society, the Estonian Astronomical Society and the Estonian Physics Society. From 2010 through 2011, I was a founding member of the Faculty of Science PhD Council at the University of Amsterdam. Previously, I have participated in the founding and operation of the non-profit astronomy outreach organization Ridamus, and have been a member and president of the Tallinn Secondary Science School student self-government.

List of publications

1. "An interferometric study of the Fomalhaut inner debris disk. Detailed model ling of the exozodiacal dust morphology", Lébréton et al., submitted to A&A

2. "High angular resolution observations towards OMC-2 FIR 4: Dissecting an intermediate-mass protocluster", López-Sepulcre et al., submitted to A&A

3. "*Herschel* CHESS discovery of the fossil cloud that gave birth to the Trapezium and Orion KL", López-Sepulcre, **Kama**, Ceccarelli, Dominik, Caux, Fuente & Alonso-Albi, 2012, A&A, 1211, 5772

4. "In-orbit performance of *Herschel*/HIFI", Roelfsema et al., 2012, A&A, 537, 17

5. "The thermal structure and the location of the snow line in the protosolar nebula: Axisymmetric models with full 3-D radiative transfer", Min, Dullemond, **Kama** & Dominik, 2011, Icarus, 212, 416

6. "Nitrogen hydrides in the cold envelope of IRAS 16293-2422", Hily-Blant et al., 2010, A&A, 521, L52

7. "*Herschel*/HIFI observations of spectrally resolved methylidyne signatures toward the high-mass star-forming core NGC 6334I", van der Wiel et al., 2010, A&A, 521, L43

8. "First detection of ND in the solar-mass protostar IRAS16293-2422", Bacmann et al., 2010, A&A, 521, L42

9. "The methanol lines and hot core of OMC2-FIR4, an intermediate-mass protostar, with *Herschel*/HIFI", **Kama** et al., 2010, A&A, 521, L39

10. "Ortho-to-para ratio of interstellar heavy water", Vastel et al., 2010, A&A, 521, L31

11. "The distribution of water in the high-mass star-forming region NGC 6334 I", Emprechtinger et al., 2010, A&A, 521, L28

12. "*Herschel* spectral surveys of star-forming regions. Overview of the 555-636 GHz range", Ceccarelli et al., 2010, A&A, 521, L22

13. "*Herschel*/HIFI discovery of interstellar chloronium (H_2Cl^+)", Lis et al., 2010, A&A, 521, L9

14. "The CHESS spectral survey of star forming regions: Peering into the protostellar shock L1157-B1. II. Shock dynamics", Lefloch et al., 2010, A&A, 518, L113

15. "The CHESS spectral survey of star forming regions: Peering into the protostellar shock L1157-B1. I. Shock chemical complexity", Codella et al., 2010, A&A, 518, L112

16. "Detection of interstellar oxidaniumyl: Abundant H_2O^+ towards the star-forming regions DR21, Sgr B2, and NGC6334", Ossenkopf et al., 2010, A&A, 518, L111

17. "The lunar phases of dust grains orbiting Fomalhaut", Min, **Kama**, Dominik & Waters, 2010, A&A, 509, L6

18. "The inner rim structures of protoplanetary discs", **Kama**, Min & Dominik, 2009, A&A, 506, 1199

19. "Emission Line Stars in the Framework of Gaia", Kolka, Eenmäe, Hirv, Tuvikene & **Kama**, 2005, in proc. *Emission Line Stars in the Framework of Gaia*

Bibliography

Adams, F. C., Lada, C. J., & Shu, F. H. 1987, ApJ, 312, 788

Adams, J. D., Herter, T. L., Osorio, M., et al. 2012, ApJL, 749, L24

Alonso-Albi, T., Fuente, A., Crimier, N., et al. 2010, A&A, 518, A52

Alonso-Albi, T. et al. 2013, A&A, in preparation

Alves, J., Lombardi, M., & Lada, C. J. 2007, A&A, 462, L17

Alves, J. F., Lada, C. J., & Lada, E. A. 2001, Nature, 409, 159

André, P., Men'shchikov, A., Bontemps, S., et al. 2010, A&A, 518, L102

Andre, P., Ward-Thompson, D., & Barsony, M. 2000, Protostars and Planets IV, 59

Araki, M., Furuya, T., & Saito, S. 2001, Journal of Molecular Spectroscopy, 210, 132

Arce, H. G. & Sargent, A. I. 2006, ApJ, 646, 1070

Arce, H. G., Shepherd, D., Gueth, F., et al. 2007, Protostars and Planets V, 245

Aso, Y., Tatematsu, K., Sekimoto, Y., et al. 2000, ApJS, 131, 465

Bachiller, R. 1996, ARAA, 34, 111

Bachiller, R., Martin-Pintado, J., Tafalla, M., Cernicharo, J., & Lazareff, B. 1990, A&A, 231, 174

Bachiller, R. & Perez Gutierrez, M. 1997, ApJL, 487, L93

Bally, J., Lanber, W. D., Stark, A. A., & Wilson, R. W. 1987, ApJL, 312, L45

Bally, J., Licht, D., Smith, N., & Walawender, J. 2006, AJ, 131, 473

Bally, J., Reipurth, B., & Davis, C. J. 2007, Protostars and Planets V, 215

Barsony, M. 1994, in Astronomical Society of the Pacific Conference Series, Vol. 65, Clouds, Cores, and Low Mass Stars, ed. D. P. Clemens & R. Barvainis, 197

Baulch, D. L. 1972, Evaluated kinetic data for high temperature reactions

Belov, S. 1995, Journal of Molecular Spectroscopy, 173, 380

Bergin, E. A., Phillips, T. G., Comito, C., et al. 2010, A&A, 521, L20

Bergin, E. A. & van Dishoeck, E. F. 2012, Royal Society of London Philosophical Transactions Series A, 370, 2778

Bjorkman, J. E. & Wood, K. 2001, ApJ, 554, 615

Blake, G. A., Farhoomand, J., & Pickett, H. M. 1986a, Journal of Molecular Spectroscopy, 115, 226

Blake, G. A., Masson, C. R., Phillips, T. G., & Sutton, E. C. 1986b, ApJS, 60, 357

Bogey, M., Civiš, S., Delcroix, B., et al. 1997, Journal of Molecular Spectroscopy, 182, 85

Bohren, C. F. & Huffman, D. R. 1983, Absorption and scattering of light by small particles (New York: Wiley, 1983)

Bottinelli, S., Ceccarelli, C., Lefloch, B., et al. 2004, ApJ, 615, 354

Bottinelli, S., Ceccarelli, C., Williams, J. P., & Lefloch, B. 2007, A&A, 463, 601

Brown, J. M. & Müller, H. S. P. 2009, Journal of Molecular Spectroscopy, 255, 68

Bruderer, S., Benz, A. O., Doty, S. D., van Dishoeck, E. F., & Bourke, T. L. 2009, The Astrophysical Journal, 700, 872

Bruderer, S., Benz, A. O., Stäuber, P., & Doty, S. D. 2010, ApJ, 720, 1432

Brünken, S., Fuchs, U., Lewen, F., et al. 2004, Journal of Molecular Spectroscopy, 225, 152

Burrows, C. J., Stapelfeldt, K. R., Watson, A. M., et al. 1996, ApJ, 473, 437

Calvet, N., Magris, G. C., Patino, A., & D'Alessio, P. 1992, Revista Mexicana de Astronomia y Astrofisica, 24, 27

Calvet, N., Patino, A., Magris, G. C., & D'Alessio, P. 1991, ApJ, 380, 617

Cameron, A. G. W. & Fegley, M. B. 1982, Icarus, 52, 1

Caratti o Garatti, A., Giannini, T., Nisini, B., & Lorenzetti, D. 2006, A&A, 449, 1077

Cardelli, J. A., Meyer, D. M., Jura, M., & Savage, B. D. 1996, ApJ, 467, 334

Castets, A. & Langer, W. D. 1995, A&A, 294, 835

Caux, E., Kahane, C., Castets, A., et al. 2011, A&A, 532, A23

Caux, E. et al. 2012, A&A, in preparation

Cazaux, S., Tielens, A. G. G. M., Ceccarelli, C., et al. 2003, ApJL, 593, L51

Cazzoli, G. & Puzzarini, C. 2005, Journal of Molecular Spectroscopy, 233, 280

Cazzoli, G., Puzzarini, C., & Lapinov, A. V. 2004, ApJ, 611, 615

Ceccarelli, C., Bacmann, A., Boogert, A., et al. 2010, A&A, 521, L22

Ceccarelli, C., Caselli, P., Herbst, E., Tielens, A. G. G. M., & Caux, E. 2007, Protostars and Planets V, 47

Ceccarelli, C., Caux, E., Loinard, L., et al. 1999, A&A, 342, L21

Cernicharo, J., Barlow, M. J., Gonzalez-Alfonso, E., et al. 1996, A&A, 315, L201

Cernicharo, J., Guélin, M., & Kahane, C. 2000, AAPS, 142, 181

Chavarría, L., Herpin, F., Jacq, T., et al. 2010, A&A, 521, L37

Chiang, E. & Murray-Clay, R. 2007, Nature Physics, 3, 604

Chiang, E. I. & Goldreich, P. 1997, ApJ, 490, 368

Chini, R., Reipurth, B., Ward-Thompson, D., et al. 1997, ApJL, 474, L135

Comito, C. & Schilke, P. 2002, A&A, 395, 357

Comito, C., Schilke, P., Phillips, T. G., et al. 2005, ApJS, 156, 127

Cooksy, A. L., Blake, G. A., & Saykally, R. J. 1986a, ApJL, 305, L89

Cooksy, A. L., Saykally, R. J., Brown, J. M., & Evenson, K. M. 1986b, ApJ, 309, 828

Crimier, N., Ceccarelli, C., Lefloch, B., & Faure, A. 2009, A&A, 506, 1229

Crockett, N. et al. 2012, ApJ, in preparation

Crockett, N. R., Bergin, E. A., Wang, S., et al. 2010, A&A, 521, L21

Crovisier, J. 1989, A&A, 213, 459

Davis, C. J., Froebrich, D., Stanke, T., et al. 2009, A&A, 496, 153

de Graauw, T., Helmich, F. P., Phillips, T. G., et al. 2010, A&A, 518, L6+

Di Francesco, J., Myers, P. C., Wilner, D. J., Ohashi, N., & Mardones, D. 2001, ApJ, 562, 770

Dickinson, R. E. & Cicerone, R. J. 1986, Nature, 319, 109

Dominik, C., Dullemond, C. P., Waters, L. B. F. M., & Walch, S. 2003, A&A, 398, 607

Dominik, C., Sedlmayr, E., & Gail, H.-P. 1993, A&A, 277, 578

Dorschner, J., Begemann, B., Henning, T., Jaeger, C., & Mutschke, H. 1995, A&A, 300, 503

Doty, S. D., van Dishoeck, E. F., & Tan, J. C. 2006, A&A, 454, L5

Draine, B. T. 1980, ApJ, 241, 1021

Draine, B. T. & Lee, H. M. 1984, ApJ, 285, 89

Dubernet, M.-L., Daniel, F., Grosjean, A., & Lin, C. Y. 2009, A&A, 497, 911

Dullemond, C. P. & Dominik, C. 2004, A&A, 417, 159

Dullemond, C. P., Dominik, C., & Natta, A. 2001, ApJ, 560, 957

Dullemond, C. P., Hollenbach, D., Kamp, I., & D'Alessio, P. 2007, in Protostars and Planets V, ed. B. Reipurth, D. Jewitt, & K. Keil, 555–572

Duschl, W. J., Gail, H.-P., & Tscharnuter, W. M. 1996, A&A, 312, 624

Eisner, J. A., Chiang, E. I., Lane, B. F., & Akeson, R. L. 2007, ApJ, 657, 347

Eisner, J. A., Graham, J. R., Akeson, R. L., & Najita, J. 2009, ApJ, 692, 309

Eisner, J. A., Lane, B. F., Hillenbrand, L. A., Akeson, R. L., & Sargent, A. I. 2004, ApJ, 613, 1049

Faure, A. & Josselin, E. 2008, A&A, 492, 257

Fich, M., Johnstone, D., van Kempen, T. A., et al. 2010, A&A, 518, L86+

Flores-Mijangos, J., Brown, J. M., Matsushima, F., et al. 2004, Journal of Molecular Spectroscopy, 225, 189

Flower, D. R. & Pineau Des Forêts, G. 2010, MNRAS, 406, 1745

Franklin, J., Snell, R. L., Kaufman, M. J., et al. 2008, ApJ, 674, 1015

Fusina, L., di Lonardo, G., Johns, J. W. C., & Halonen, L. 1988, Journal of Molecular Spectroscopy, 127, 240

Garrod, R. T., Weaver, S. L. W., & Herbst, E. 2008, ApJ, 682, 283

Gatley, I., Becklin, E. E., Mattews, K., et al. 1974, ApJL, 191, L121

Godard, B., Falgarone, E., Gerin, M., et al. 2012, A&A, 540, A87

Goicoechea, J. R., Cernicharo, J., Karska, A., et al. 2012, ArXiv e-prints

Goldsmith, P. F. 2001, ApJ, 557, 736

Goldsmith, P. F. & Langer, W. D. 1999, ApJ, 517, 209

Gullbring, E., Hartmann, L., Briceno, C., & Calvet, N. 1998, ApJ, 492, 323

Haisch, Jr., K. E., Lada, E. A., & Lada, C. J. 2001, ApJL, 553, L153

Herbst, W., Hamilton, C. M., Leduc, K., et al. 2008, Nature, 452, 194

Herczeg, G. J., Karska, A., Bruderer, S., et al. 2012, A&A, 540, A84

Herrmann, F., Madden, S. C., Nikola, T., et al. 1997, ApJ, 481, 343

Higgins, R. 2011, Advanced optical calibration of the Herschel HIFI heterodyne spectrometer

Higgins, R. D., Pearson, J. C., Lord, S. D., & Teyssier, D. 2009, in 64th International Symposium On Molecular Spectroscopy

Hirota, T., Bushimata, T., Choi, Y. K., et al. 2007, PASJ, 59, 897

Hogerheijde, M. R. & van der Tak, F. F. S. 2000, A&A, 362, 697

Huang, X., Schwenke, D. W., & Lee, T. J. 2011, JChPh, 134, 044321

Isella, A. & Natta, A. 2005, A&A, 438, 899

Isella, A., Tatulli, E., Natta, A., & Testi, L. 2008, A&A, 483, L13

Isella, A., Testi, L., & Natta, A. 2006, A&A, 451, 951

Johansson, L. E. B., Andersson, C., Elder, J., et al. 1985, AAPS, 60, 135

Johns, J. W. C. 1985, Journal of the Optical Society of America B Optical Physics, 2, 1340

Johnstone, D., Boonman, A. M. S., & van Dishoeck, E. F. 2003, A&A, 412, 157

Johnstone, D., Fich, M., McCoey, C., et al. 2010, A&A, 521, L41

Jørgensen, J. K., Bourke, T. L., Myers, P. C., et al. 2005, ApJ, 632, 973

Jørgensen, J. K., Johnstone, D., van Dishoeck, E. F., & Doty, S. D. 2006, A&A, 449, 609

Kama, M., Dominik, C., Maret, S., et al. 2010, A&A, 521, L39

Kama, M. et al. 2012, ApJ, in preparation

Kaufman, M. J. & Neufeld, D. A. 1996, ApJ, 456, 611

Kennicutt, R. C. & Evans, N. J. 2012, ARAA, 50, 531

Kenyon, S. J. & Hartmann, L. 1987, ApJ, 323, 714

Kim, E. & Yamamoto, S. 2003, Journal of Molecular Spectroscopy, 219, 296

Klapper, G., Lewen, F., Gendriesch, R., Belov, S. P., & Winnewisser, G. 2001, Zeitschrift Naturforschung Teil A, 56, 329

Klapper, G., Surin, L., Lewen, F., et al. 2003, ApJ, 582, 262

Klisch, E., Klaus, T., Belov, S. P., Winnewisser, G., & Herbst, E. 1995, A&A, 304, L5+

Koike, C., Kaito, C., Yamamoto, T., et al. 1995, Icarus, 114, 203

Kraus, S., Preibisch, T., & Ohnaka, K. 2008, ApJ, 676, 490

Kristensen, L. E., van Dishoeck, E. F., Bergin, E. A., et al. 2012, A&A, 542, A8

Kristensen, L. E., van Dishoeck, E. F., Tafalla, M., et al. 2011, A&A, 531, L1

Kristensen, L. E., Visser, R., van Dishoeck, E. F., et al. 2010, A&A, 521, L30

Krumholz, M. R., Leroy, A. K., & McKee, C. F. 2011, ApJ, 731, 25

Kurtz, S., Cesaroni, R., Churchwell, E., Hofner, P., & Walmsley, C. M. 2000, Protostars and Planets IV, 299

Lada, C. J. 2006, ApJL, 640, L63

Lada, C. J. & Adams, F. C. 1992, ApJ, 393, 278

Lada, C. J. & Lada, E. A. 2003, ARAA, 41, 57

Lamy, P. L. 1974, A&A, 35, 197

Langer, W. D. & Penzias, A. A. 1993, ApJ, 408, 539

Lattanzi, V., Walters, A., Drouin, B. J., & Pearson, J. C. 2007, ApJ, 662, 771

Lefloch, B., Cabrit, S., Busquet, G., et al. 2012, ApJL, 757, L25

Lefloch, B., Cabrit, S., Codella, C., et al. 2010, A&A, 518, L113

Lenzuni, P., Gail, H.-P., & Henning, T. 1995, ApJ, 447, 848

Leurini, S., Schilke, P., Menten, K. M., et al. 2004, A&A, 422, 573

Leurini, S., Schilke, P., Wyrowski, F., & Menten, K. M. 2007, A&A, 466, 215

Liszt, H. S. & Ziurys, L. M. 2012, ApJ, 747, 55

Lucy, L. B. 1999, A&A, 344, 282

Mannings, V. & Sargent, A. I. 1997, ApJ, 490, 792

Maret, S., Ceccarelli, C., Tielens, A. G. G. M., et al. 2005, A&A, 442, 527

Marseille, M. G., van der Tak, F. F. S., Herpin, F., et al. 2010, A&A, 521, L32

Martin-Pintado, J., Bachiller, R., & Fuente, A. 1992, A&A, 254, 315

Maury, A., Ohashi, N., & André, P. 2012, A&A, 539, A130

Mayor, M., Marmier, M., Lovis, C., et al. 2011, ArXiv e-prints

McCarthy, M. C., Mohamed, S., Brown, J. M., & Thaddeus, P. 2006, Proceedings of the National Academy of Science, 103, 12263

McCaughrean, M. J. & O'dell, C. R. 1996, AJ, 111, 1977

McKee, C. F. & Ostriker, E. C. 2007, ARAA, 45, 565

Meeus, G., Waters, L. B. F. M., Bouwman, J., et al. 2001, A&A, 365, 476

Melnick, G. J., Tolls, V., Neufeld, D. A., et al. 2010, A&A, 521, L27

Menten, K. M., Reid, M. J., Forbrich, J., & Brunthaler, A. 2007, A&A, 474, 515

Mezger, P. G., Zylka, R., & Wink, J. E. 1990, A&A, 228, 95

Millan-Gabet, R., Malbet, F., Akeson, R., et al. 2007, in Protostars and Planets V, ed. B. Reipurth, D. Jewitt, & K. Keil, 539–554

Min, M., Dullemond, C. P., Dominik, C., de Koter, A., & Hovenier, J. W. 2009, ArXiv e-prints

Min, M., Hovenier, J. W., & de Koter, A. 2003, A&A, 404, 35

Min, M., Hovenier, J. W., & de Koter, A. 2005, A&A, 432, 909

Molinari, S., Swinyard, B., Bally, J., et al. 2010, A&A, 518, L100

Monnier, J. D., Millan-Gabet, R., Billmeier, R., et al. 2005, ApJ, 624, 832

Motte, F., Andre, P., & Neri, R. 1998, A&A, 336, 150

Müller, H. S. P. 2010, A&A, 514, L6

Müller, H. S. P., Farhoomand, J., Cohen, E. A., et al. 2000a, Journal of Molecular Spectroscopy, 201, 1

Müller, H. S. P., Klein, H., Belov, S. P., et al. 1999, Journal of Molecular Spectroscopy, 195, 177

Müller, H. S. P., Menten, K. M., & Mäder, H. 2004, A&A, 428, 1019

Müller, H. S. P., Schlöder, F., Stutzki, J., & Winnewisser, G. 2005, Journal of Molecular Structure, 742, 215

Müller, H. S. P., Winnewisser, G., Demaison, J., Perrin, A., & Valentin, A. 2000b, Journal of Molecular Spectroscopy, 200, 143

Mürtz, P., Zink, L. R., Evenson, K. M., & Brown, J. M. 1998, JChPh, 109, 9744

Myers, P. C., Mardones, D., Tafalla, M., Williams, J. P., & Wilner, D. J. 1996, ApJL, 465, L133

Najita, J. R., Doppmann, G. W., Carr, J. S., Graham, J. R., & Eisner, J. A. 2009, ApJ, 691, 738

Natta, A., Prusti, T., Neri, R., et al. 2001, A&A, 371, 186

Neufeld, D. A. & Dalgarno, A. 1989a, ApJ, 340, 869

Neufeld, D. A. & Dalgarno, A. 1989b, ApJ, 344, 251

Neufeld, D. A. & Wolfire, M. G. 2009, ApJ, 706, 1594

Nisini, B., Benedettini, M., Codella, C., et al. 2010, A&A, 518, L120

Nisini, B., Benedettini, M., Giannini, T., et al. 1999, A&A, 350, 529

Nisini, B., Codella, C., Giannini, T., et al. 2007, A&A, 462, 163

Nolt, I. G., Radostitz, J. V., Dilonardo, G., et al. 1987, Journal of Molecular Spectroscopy, 125, 274

Nummelin, A., Bergman, P., Hjalmarson, Å., et al. 2000, ApJS, 128, 213

Offer, A. R., van Hemert, M. C., & van Dishoeck, E. F. 1994, JChPh, 100, 362

Ott, S. 2010a, in ASP Conf. Ser.: Astronomical Data Analysis Software and Systems XIX, ed. Y. Mizumoto & M. Ohishi, in press

Ott, S. 2010b, in Astronomical Society of the Pacific Conference Series, Vol. 434, Astronomical Data Analysis Software and Systems XIX, ed. Y. Mizumoto, K.-I. Morita, & M. Ohishi, 139

Padoan, P. & Nordlund, Å. 2002, ApJ, 576, 870

Padovani, M., Walmsley, C. M., Tafalla, M., Galli, D., & Müller, H. S. P. 2009, A&A, 505, 1199

Pagani, L., Daniel, F., & Dubernet, M.-L. 2009, A&A, 494, 719

Pendleton, Y., Werner, M. W., Capps, R., & Lester, D. 1986, ApJ, 311, 360

Peterson, D. E. & Megeath, S. T. 2008, The Orion Molecular Cloud 2/3 and NGC 1977

Regions, ed. B. Reipurth, 590

Pickett, H. M., Pearson, J. C., & Miller, C. E. 2005, Journal of Molecular Spectroscopy, 233, 174

Pickett, H. M., Poynter, R. L., Cohen, E. A., et al. 1998, JQSRT, 60, 883

Pilbratt, G. L., Riedinger, J. R., Passvogel, T., et al. 2010, A&A, 518, L1+

Pollack, J. B., Hollenbach, D., Beckwith, S., et al. 1994, ApJ, 421, 615

Reipurth, B., Rodríguez, L. F., & Chini, R. 1999, AJ, 118, 983

Roelfsema, P. R., Helmich, F. P., Teyssier, D., et al. 2010, A&A

Roelfsema, P. R., Helmich, F. P., Teyssier, D., et al. 2012, A&A, 537, A17

Rydgren, A. E. & Zak, D. S. 1987, PASP, 99, 141

Sana, H., de Koter, A., de Mink, S. E., et al. 2012, ArXiv e-prints

Schaye, J. 2004, ApJ, 609, 667

Schick, H. L. 1960, Chemical Reviews, 60, 331

Schilke, P., Comito, C., Thorwirth, S., et al. 2006, A&A, 454, L41

Schilke, P., Groesbeck, T. D., Blake, G. A., & Phillips, T. G. 1997, ApJS, 108, 301

Schöier, F. L., van der Tak, F. F. S., van Dishoeck, E. F., & Black, J. H. 2005, A&A, 432, 369

Servoin, J. L. & Piriou, B. 1973, Phys. Status Solidi (B), 55, 677

Shakura, N. I. & Sunyaev, R. A. 1973, A&A, 24, 337

Shimajiri, Y., Kawabe, R., Takakuwa, S., et al. 2011, PASJ, 63, 105

Shimajiri, Y., Takahashi, S., Takakuwa, S., Saito, M., & Kawabe, R. 2008, ApJ, 683, 255

Smithells, C. J. 1967, Metals Reference Book (Butterworths)

Snell, R. L., Howe, J. E., Ashby, M. L. N., et al. 2000, ApJL, 539, L93

Spaans, M., Hogerheijde, M. R., Mundy, L. G., & van Dishoeck, E. F. 1995, Astrophysical Journal Letters v.455, 455, L167

Stanke, T., McCaughrean, M. J., & Zinnecker, H. 2002, A&A, 392, 239

Takahashi, S. & Ho, P. T. P. 2012, ApJL, 745, L10

Takahashi, S., Saito, M., Ohashi, N., et al. 2008, ApJ, 688, 344

Takano, S., Klaus, T., & Winnewisser, G. 1998, Journal of Molecular Spectroscopy, 192, 309

Tannirkulam, A., Harries, T. J., & Monnier, J. D. 2007, ApJ, 661, 374

Tannirkulam, A., Monnier, J. D., Harries, T. J., et al. 2008a, ApJ, 689, 513

Tannirkulam, A., Monnier, J. D., Millan-Gabet, R., et al. 2008b, ApJL, 677, L51

Thorwirth, S., Müller, H. S. P., Lewen, F., et al. 2003, ApJL, 585, L163

Thorwirth, S., Müller, H. S. P., Lewen, F., Gendriesch, R., & Winnewisser, G. 2000, A&A, 363, L37

Thronson, Jr., H. A., Harper, D. A., Keene, J., et al. 1978, AJ, 83, 492

Tielens, A. G. G. M. 2005, The Physics and Chemistry of the Interstellar Medium

van Boekel, R., Min, M., Leinert, C., et al. 2004, Nature, 432, 479

van der Tak, F. F. S., Black, J. H., Schöier, F. L., Jansen, D. J., & van Dishoeck, E. F. 2007, A&A, 468, 627

van der Tak, F. F. S., Marseille, M. G., Herpin, F., et al. 2010, A&A, 518, L107

van der Tak, F. F. S., van Dishoeck, E. F., & Caselli, P. 2000, A&A, 361, 327

van Dishoeck, E. F. & Black, J. H. 1988, ApJ, 334, 771

van Dishoeck, E. F., Jonkheid, B., & van Hemert, M. C. 2006, Faraday Discussions, 133, 231

van Dishoeck, E. F., Kristensen, L. E., Benz, A. O., et al. 2011, PASP, 123, 138

van Kempen, T. A., Kristensen, L. E., Herczeg, G. J., et al. 2010, A&A, 518, L121+

Visser, R., Kristensen, L. E., Bruderer, S., et al. 2012, A&A, 537, A55

Viti, S., Jimenez-Serra, I., Yates, J. A., et al. 2011, ApJL, 740, L3

Wakelam, V., Caselli, P., Ceccarelli, C., Herbst, E., & Castets, A. 2004, A&A, 422, 159

Wakelam, V., Ceccarelli, C., Castets, A., et al. 2005, A&A, 437, 149

Walker, C. K., Narayanan, G., & Boss, A. P. 1994, ApJ, 431, 767

Wampfler, S. F., Bruderer, S., Kristensen, L. E., et al. 2011, A&A, 531, L16

Wampfler, S. F., Herczeg, G. J., Bruderer, S., et al. 2010, A&A, 521, L36

Wang, S., Bergin, E. A., Crockett, N. R., et al. 2010, A&A, submitted

Wardle, M. 1999, ApJL, 525, L101

Williams, J. P., Plambeck, R. L., & Heyer, M. H. 2003, ApJ, 591, 1025

Wilson, B. A., Dame, T. M., Masheder, M. R. W., & Thaddeus, P. 2005, A&A, 430, 523

Wilson, T. L. & Rood, R. 1994, ARAA, 32, 191

Winnewisser, G., Belov, S. P., Klaus, T., & Schieder, R. 1997, Journal of Molecular Spectroscopy, 184, 468

Wyrowski, F., van der Tak, F., Herpin, F., et al. 2010, A&A, 521, L34

Xu, L., Fisher, J., Lees, R. M., et al. 2008, Journal of Molecular Spectroscopy, 251, 305

Yang, B., Stancil, P. C., Balakrishnan, N., & Forrey, R. C. 2010, ApJ, 718, 1062

Yu, K. C., Bally, J., & Devine, D. 1997, ApJL, 485, L45

Yu, S., Pearson, J. C., Drouin, B. J., et al. 2010, JChPh, 133, 174317

Zemansky, M. W. 1968, Heat and Thermodynamics (McGraw-Hill Kogakusha, Ltd.), 346–356

Zhang, Q., Hunter, T. R., Brand, J., et al. 2005, ApJ, 625, 864